

UNIVERSITY OF CALIFORNIA
SANTA CRUZ

VACUUM TRANSITIONS AND ETERNAL INFLATION

A dissertation submitted in partial satisfaction of the
requirements for the degree of

DOCTOR OF PHILOSOPHY

in

PHYSICS

by

Matthew C. Johnson

June 2007

The Dissertation of Matthew C. Johnson
is approved:

Anthony Aguirre, Chair

Tom Banks

Michael Dine

Lisa C Sloan
Vice Provost and Dean of Graduate Studies

Copyright © by
Matthew C. Johnson
2007

Table of Contents

List of Figures	vi
List of Tables	ix
Abstract	x
Dedication	xii
Acknowledgments	xiii
1 Introduction	1
I Vacuum Transitions	7
2 Classical Dynamics of Thin-Wall Bubbles	8
2.1 Israel Junction Conditions	9
2.2 Bubbles with zero mass	11
2.3 Bubbles with nonzero mass	20
2.4 Conformal diagrams and classification	26
2.4.1 Application of the Penrose singularity theorem	31
2.5 The instability of bubbles with a turning point	34
2.5.1 Wall Equation of Motion	35
2.5.2 Perturbation equations of motion	38
2.6 Application to tunneling mechanisms	40
2.6.1 Dynamics of the Perturbation Field	41
2.6.2 Initial Conditions and Evolution to the Turning Point	43
2.6.3 Thick Walls and Radiation	49
2.7 Conclusions	49
3 Tunneling: Zero Mass	52
3.1 Introduction	52
3.2 CDL Formalism	55
3.2.1 Neglecting gravity	55
3.2.2 Thin-wall approximation: without gravity	57
3.2.3 Deep-well approximation: without gravity	57

3.2.4	Including gravity	58
3.2.5	Thin-wall approximation including gravity	62
3.3	Approximate analytic solutions	70
3.4	The $V_F \rightarrow 0$ limit	72
3.4.1	Small ϵ	72
3.4.2	Numerical results for small ϵ	76
3.4.3	Large ϵ	78
3.5	The Great Divide	80
3.6	Below the great divide	82
3.7	Connections with eternal inflation	84
3.8	Conclusions	87
4	Tunneling: Non-Zero Mass	89
4.1	Introduction	89
4.2	Hamiltonian formalism	92
4.2.1	An example from 1-D quantum mechanics	92
4.2.2	Full semiclassical calculation	95
4.2.3	Calculating tunneling rates	97
4.2.4	High- and low-mass limits	101
4.3	Comparison of the Tunneling Exponents	106
4.4	The bottom line	110
4.5	Conclusions	111
II	Eternal Inflation	115
5	Measures for Eternal Inflation	116
5.1	Desirable measure properties: a scorecard	120
5.2	False Vacuum Eternal Inflation	123
5.2.1	The Measures and their Properties	123
5.2.2	Relations between the measures	131
5.3	Some Sample Landscapes	132
5.3.1	Coupled pairs dominate in terminal landscapes	135
5.3.2	Coupled pairs dominate in cyclic landscapes	138
5.3.3	Splitting vacua	138
5.3.4	Continuity of predictions	139
5.4	Consequences for predictions in a landscape	140
5.5	Observers in Eternal Inflation	142
5.6	Discussion and Conclusions	148
6	Measures on transitions for cosmology from eternal inflation	153
6.1	Introduction	153
6.2	Transitions rather than vacua	154
6.3	Transitions on a single worldline	157
6.3.1	Recovery of one-point statistics	159
6.3.2	Higher moments and longer histories	160
6.4	Counting total transition numbers	161
6.5	Conclusions	162

7	Towards observable signatures of other bubble universes	163
7.1	Introduction	163
7.2	Setting up the problem	166
7.3	Computations	172
7.3.1	Angles according to the unboosted observer	173
7.3.2	The boosted view	175
7.3.3	Angles according to the boosted observer	178
7.3.4	Angular distribution function	184
7.3.5	Behavior of the distribution near $\psi \simeq 2\pi$ and $\psi \simeq 0$	188
7.4	Summary of results and implications	191
7.4.1	Properties of the distribution function	191
7.4.2	A classification of collision events	192
7.4.3	Observational implications	195
7.5	Discussion	197
A	Spacetimes with a cosmological constant	200
A.1	The FRW metric	200
A.1.1	Friedmann Equations	201
A.2	de Sitter Space	203
A.3	Anti-de Sitter space	209
A.4	Schwarzschild de Sitter	212
A.5	Schwarzschild Anti-de Sitter	216
B	Covariant Entropy Bound and Singularity Theorems	219
B.1	Covariant Entropy Bound	219
B.2	Penrose Singularity Theorems	223
C	Matrix Calculations and Snowman Diagrams	225
D	Triple intersection in the unboosted frame	229
E	Effects of boosts on the bubble	232
	Bibliography	234

List of Figures

2.1	The full causal structure of the one-bubble spacetime.	12
2.2	The zero mass one-bubble spacetime.	13
2.3	Shown on the left are the true and false vacuum de Sitter hyperboloids, both centered on the origin. Shown on the right is the geometry of a zero-mass bubble.	15
2.4	The causal structure of a true-vacuum bubble spacetime with $(\Lambda_+ > 0, \Lambda_- < 0)$	18
2.5	The causal structure of a true-vacuum bubble spacetime with $(\Lambda_+ > 0, \Lambda_- = 0)$	19
2.6	The causal structure of a true-vacuum bubble spacetime with $(\Lambda_+ = 0, \Lambda_- < 0)$	20
2.7	The potential for various Y	22
2.8	Potential for false-vacuum bubbles with $B < 3(A - 1)$	24
2.9	Potential for false-vacuum bubbles with $B > 3(A - 1)$	25
2.10	Potential for true-vacuum bubbles with $A > \frac{B}{3} + 1$	25
2.11	Potential for true-vacuum bubbles with $(A = .6, B = .5)$, corresponding to the case where $A < \frac{B}{3} + 1 < B + 3$	26
2.12	Conformal diagrams for the one-bubble spacetimes which do not lie behind a worm hole.	27
2.13	Conformal diagrams for the one-bubble spacetimes which lie behind a worm hole.	29
2.14	Solutions can be to the right of region I instead of behind the wormhole.	30
2.15	Solutions which are in unstable equilibrium between the bound and unbound solutions of Fig. 2.12 and 2.13.	31
2.16	Conformal diagrams for three representative one-bubble spacetimes.	32
2.17	Contour plot of $\text{Log}_{10}[f(l = 1, z_0, Q, T_{\max})]$ (left) and $\text{Log}_{10}[g(l = 1, z_0, Q, T_{\max})]$ (right) for $M_I = 10^{14}$ GeV (top) and $M_I = 100$ GeV (bottom).	42
2.18	$f(l, z_0 = .5, Q = -10^{-4}, T)$ for various l	43
3.1	The potential $V(\phi)$, with the true vacuum x_T , the false vacuum x_F and the “Hawking-Moss” point x_H labeled.	53
3.2	Shown on the left is a potential which satisfies the thin-wall approximation. Shown on the right is a potential which satisfies the deep-well approximation.	56
3.3	The evolution of $\rho(z)$ (top) and $\phi(z)$ (bottom) for a single-pass (left), multiple-pass (center), and Hawking-Moss (right) instanton.	59
3.4	The Euclidean instanton for zero mass thin wall bubbles in the embedding space.	64
3.5	Euclidean de Sitter in the (z, χ) coordinatization (top) and the (t_E, R) coordinatization (bottom) on slices of constant (θ, ϕ) in the (X_0, X_1, X_4) embedding space.	65

3.6	The analytic continuation of the instanton defining the initial conditions for the lorentzian evolution of true or false vacuum bubbles.	65
3.7	The instanton in the (t_E, R) coordinatization.	66
3.8	The gravitational factor, Eq. 3.39, for thin-wall vacuum bubble nucleation with gravity.	68
3.9	The potential, $v(x)$, used for the numerics.	76
3.10	Evolution of $r(s)$ for $\epsilon = .72$ and $z = (.01, .008, .006)$ from bottom to top.	77
3.11	The evolution of $x(s)$ for $\epsilon = .85$ and $z = (1, .1, .01, .001, .0001)$ from bottom to top.	79
3.12	The evolution of $r(s)$ for $\epsilon = .85$ and $z = (1, .1, .01, .001, .0001)$ from bottom to top.	79
3.13	The evolution of $r(s)$ for $z = 0$ on either side of ϵ_c	81
3.14	It can be seen in this plot of δ_T vs ϵ for the case where $z = 0$ that there is an ϵ_c for which $\delta_T \rightarrow 0$	81
4.1	Tunneling spacetime	91
4.2	Tunneling from a bound solution to an unbound solution which exists outside the cosmological horizon.	98
4.3	Tunneling exponent as a function of Q for $(A = 1, B = 6)$ (false vacuum bubbles).	102
4.4	The exponent for the creation of a false-vacuum bubble from empty de Sitter as a function of Q for $(A = 1, B = 6)$	109
4.5	Tunneling exponent as a function of Q for $(A = 9, B = 20)$ (true-vacuum bubbles).	109
5.1	A depiction of the cutoff scheme imposed in the CHC method for a two-well landscape.	128
5.2	A summary of the connections between the various measures.	132
5.3	Some sample landscapes.	133
5.4	A picture of an eternally inflating universe which takes into account both L and R tunneling geometries.	146
6.1	A simple potential landscape	155
7.1	On the left is the embedding of two dS spaces of different vacuum energy in 5-D Minkowski space (three dimensions suppressed).	168
7.2	The conformal diagram for a bubble universe.	169
7.3	A time lapse picture of the null rays reaching an observer from the boundary of the region affected by a collision event in the Poincaré disk representation.	174
7.4	The effects of the boost.	178
7.5	A spatial slice in the global foliation of the background de Sitter space, and its stereographic projection.	180
7.6	The three cases of bubble intersection in the plane of projection.	181
7.7	The foliation of the exterior de Sitter space into surfaces of constant ψ for junctions with $H_T \sim H_F$ (left) and $H_T \ll H_F$ (right).	183
7.8	The distribution function Eq. 7.25 for an observer at $\xi_o = 0$ with varying T_{co} (corresponding to a varying H_T), factoring out the overall scale λH_F^{-4}	186
7.9	The distribution function Eq. 7.25 for an observer at $\xi_o = 25$, with $T_{co} = \frac{\pi}{4}$, for $\theta = \frac{\pi}{10}, \frac{\pi}{15}, \frac{\pi}{20}$, factoring out the overall scale λH_F^{-4}	187

7.10	The distribution function Eq. 7.25 with $\theta_n = 0$ and $\tau_{co} = \frac{3\pi}{8}$ for $\xi_o = (1.5, 2, 100)$, factoring out the overall scale λH_F^{-4}	187
7.11	The distribution function Eq. 7.25 with $\theta_n = 0$ and $\xi_o = 2$ for $T_{co} = (\frac{\pi}{4}, \frac{3\pi}{8}, \frac{7\pi}{16})$, factoring out the overall scale λH_F^{-4}	188
7.12	A log-log plot (calculated numerically) of the total angular area on the sky taken up by late-time collisions with $\psi \simeq 0$	190
7.13	A general set of situations which might involve collisions between two bubbles in an eternally inflating spacetime.	193
A.1	4 dimensional de Sitter space can be visualized as a hyperboloid embedded in 5 dimensional Minkowski space.	203
A.2	A projection in the X_0 - X_4 plane of the embedding for de Sitter space.	207
A.3	Conformal diagram for the de Sitter geometry.	209
A.4	Conformal diagram for the Anti de Sitter geometry.	211
A.5	Conformal diagram of the Schwarzschild de Sitter geometry for $3M < \Lambda_+$	216
A.6	Conformal diagram for the Schwarzschild de Sitter geometry when $3M = \Lambda_+$	217
A.7	Conformal diagram for the Schwarzschild Anti de Sitter geometry.	218
B.1	Shown in this figure is the conformal diagram for Minkowski space.	221
B.2	The conformal diagram for the time symmetric Schwarzschild spacetime.	221
C.1	Examples of “snowman diagrams” summarizing relative transition probabilities μ_{NM}	226

List of Tables

4.1	$F_I [R_2 - R_1]$ and $F_O [R_2 - R_1]$ for the tunneling geometries with the unbound final state lying to the left of the bound initial state (L tunneling geometries). . .	105
4.2	$F_I [R_2 - R_1] + F_O [R_2 - R_1]$ for the tunneling geometries with the unbound final state lying to the <i>right</i> of the bound initial state (R tunneling geometries).	106
5.1	Properties of bubble counting measures.	148

Abstract

Vacuum Transitions and Eternal Inflation

by

Matthew C. Johnson

In this thesis, we focus on aspects of inflation and eternal inflation arising in scalar field theories coupled to gravity which possess a number of metastable states. Such theories contain instantons that interpolate between the metastable potential minima, corresponding to the nucleation of bubbles containing a new phase in a background of the old phase. In the first part of this thesis, we describe the classical dynamics and quantum nucleation of vacuum bubbles. We classify all possible spherically symmetric, thin-wall solutions with arbitrary interior and exterior cosmological constant, and find that bubbles possessing a turning point are unstable to aspherical perturbations. Next, we turn to the quantum nucleation of bubbles with zero mass. Focusing on instantons interpolating between positive and negative energy minima, we find that there exists a "Great Divide" in the space of potentials, across which the lifetime of metastable states differs drastically. Generalizing a semi-classical Hamiltonian formalism to treat the nucleation of bubbles with nonzero mass, we show that a number of tunneling mechanisms can be unified in the thin-wall limit, and directly compare their probabilities. In the second part of this thesis, we discuss the measure problem in eternal inflation. We give a detailed analysis of the prospects for making predictions in eternal inflation, and describe the existing probability measures and the connections between them. We then show that all existing measures exhibit a number of rather generic phenomena, for example strongly weighting vacua that can undergo rapid transitions between each other. It is argued that making predictions will require a measure that weights histories as opposed to vacua, and we develop a formalism to address this. Finally, we assess

the prospects for observing collisions between vacuum bubbles in an eternally inflating universe. Contrary to conventional wisdom, we find that under certain assumptions most positions inside a bubble should have access to a large number of collision events. We calculate the expected number and angular size distribution of such collisions on an observer's "sky", finding that for typical observers the distribution is anisotropic and includes many bubbles, each of which will affect the majority of the observer's sky.

Cheers!!!

Acknowledgments

Thanks first and foremost to Anthony Aguirre for being an excellent advisor and collaborator. I also would like to acknowledge the invaluable role that Tom Banks has played in my thesis research. In addition, I owe a debt of gratitude to Assaf Shomer (whose unique sense of humor I will miss very much) and Steven Gratton for collaboration on a number of projects.

Equally important has been the role that my friends and family have played. Mom, dad, Greg, Lisa, and Joanna, grad school and life in general would be very hard without you! Much credit is also owed to my cohort, especially Ingrid Anderson, Mike Griffo, Jan Haerter, Trieu Mai, and John Mason. Aside from being excellent sources of inspiration and guidance during my work, they have been the best friends I have known! Many thanks also to Carmen and countless other friends who have made my time in Santa Cruz wonderful!

I would like to acknowledge support from the ARCS Foundation, the Hierarchical Systems Research Foundation, and a Foundational Questions in Physics and Cosmology grant.

The text of this dissertation includes reprints of the following previously published material: A. Aguirre and M.C. Johnson, *Phys. Rev. D* **72**, (2005) 103525, A. Aguirre and M.C. Johnson, *Phys. Rev. D* **73**, (2005) 123529, A. Aguirre, T. Banks, and M.C. Johnson, *JHEP* **08** (2006) 065, A. Aguirre, S. Gratton, and M.C. Johnson, *Phys. Rev. Lett.* **98**, 131301 (2007). A. Aguirre directed and supervised the research which forms the basis for this dissertation.

Chapter 1

Introduction

In the absence of extremely fine tuned initial conditions and correlations over causally disconnected parts of the early universe, the universe as we see it today cannot be explained by the standard big bang cosmology. The theory of inflation [3] was introduced to explain some of these long standing problems, and has subsequently become a key ingredient of the standard cosmological model. Inflation postulates a period of super-accelerated expansion at some time in the past of our universe. The standard lore posits that this epoch generically produces an isotropic, homogenous, flat universe in which regions that are now causally disconnected could at some time in the past have been in causal contact. It does all of this by stretching: inhomogeneities and anisotropies are diluted, curvature is stretched flat, and causally connected regions are stretched out to produce many causally disconnected regions.

The basic idea is simple, but its implementation has a surprisingly rich phenomenology. Literally hundreds of models of inflation have been postulated. There is old inflation, new inflation, open inflation, hybrid inflation, chaotic inflation, racetrack inflation....the list goes on and on. All of these models share some very basic characteristics, most importantly that somehow a region of space finds itself with an equation of state in which the pressure is negative,

and equal in magnitude to the energy density. This negative pressure (which can be caused by the vacuum expectation value of a scalar field, a fundamental cosmological constant, or perhaps by other means), causes the exponential expansion known as inflation. However, this epoch must end, and inflation must "gracefully exit" to the standard post-big bang cosmological evolution.

In fact, inflation does much more than just sweep a few outstanding problems with Big-Bang cosmology under the rug. There are small inhomogeneities produced during inflation, which are predicted to have a nearly scale-invariant spectrum. Inhomogeneities in the temperature of the cosmic microwave background (CMB) with just such a spectrum have been detected. Eventually, these inhomogeneities grow, and serve as the seeds for the formation of galaxies and large scale structure. The departure from scale invariance is model-specific, and the fact that many models of inflation can be constructed which agree with observations can be viewed as a dramatic theoretical success.

At the end of inflation, copious amounts of particles are produced, and the universe is "reheated" to some very high temperature. It is thought that at this time the matter and energy which fills our universe is created, and some mechanism operates which produces much more matter than antimatter. The production of light elements during this epoch, known as Nucleosynthesis, can be modeled very accurately, and compared with the observed abundances. Many models of inflation have the ability to reheat the universe to sufficiently high temperatures to explain the observed elemental abundances, and perhaps provide the correct environment to generate the matter-antimatter asymmetry.

Using constraints from observational cosmology, we can estimate the energy scale at which inflation must occur. This is of course model dependent, but present understanding dictates that inflation must occur at scales normally associated with particle-physics (energies of order TeV and higher). Complementing this is the fact that inflation takes very small scales and blows them up to cosmological sizes (the observed inhomogeneities in the CMB are thought

to have been produced by quantum fluctuations in the field responsible for inflation), which effectively renders it a cosmic microscope into the realm of high energy physics. We are therefore presented with an arena in which we can probe physics at energy scales much higher than will be accessible in any conceivable future particle accelerator.

However, all of this excitement must be taken with a grain of salt: for all of its explanatory power, inflation suffers from a number of discontents [4, 5, 6, 7]). Since inflation does such a good job of diluting unwanted initial conditions, it leaves us very little observational information about the *actual* state of the universe before the inflationary epoch. Because of this, there is little hope of directly determining if the initial conditions for inflation in our universe were "generic" (as the standard lore of inflation posits), or in some way very special.

As the story goes, inflation must begin from a horizon-sized patch (this statement must be made more precise, and we will discuss locally inflating patches in great detail in Chapter 2). Our entire observable universe will arise from this proto-inflationary patch, whose entropy content can be bounded by applying the covariant entropy bound (discussed in Appendix B) $S_I < \frac{m_{pl}^2}{m_I^2}$. The current entropy of our observable universe is dominated by black holes in the centers of galaxies [8], and can be estimated as $S_0 \sim 10^{90}$ (the next largest contribution is entropy in the CMB, which can be estimated by $S_{CMB} \sim 10^{88}$ [9]). For any reasonable inflationary energy scale, we see that our universe started in a state of *fantastically* low entropy. How did this state of affairs arise, and are the the initial conditions for such evolution in some way "generic"?

We can make these questions more concrete by considering a specific model, related to Guth's original model of inflation [3], consisting of a scalar field theory coupled to gravity which has two local minima separated by a barrier. The energy density of the scalar field in one of the minima is larger than the other, and we will refer to the minimum with the higher energy density as the false vacuum and the vacuum with the lower energy density as the true vacuum.

If the false vacuum energy density is large enough, it can drive a period of inflation (though there will be no generation of density perturbations, yielding a phenomenologically implausible universe). In this false vacuum dominated universe, a phase transition can occur, which proceeds by the nucleation of bubbles of true vacuum in the background false vacuum [10, 11, 12]. When the nucleation rate out of the false vacuum is smaller than a false vacuum Hubble time, then most bubbles will grow to be extremely large before they undergo a collision, and the phase transition will never complete. Such models can be fairly described as "eternal" because a time foliation exists in which the physical volume in the false vacuum expands exponentially forever, and inflation only ends *locally* in regions where the field settles into the true vacuum. Even those regions which fall into the true vacuum can be recycled, since it is possible to form bubbles of false vacuum in a background of true [13], though this process will be strongly suppressed.

This simple model may have direct relevance for *our* universe, since developing understanding of metastable states in string theory seems to be pointing towards a vast, interconnected, many-dimensional web or "landscape" of many, many vacua. If it is possible to locate a vacuum where low-energy physics resembles our own, then, considering that such a vacuum is metastable, a natural question is: where did we come from, and where are we going? Our cosmological evolution will depend on where we came from (discussed in detail in Chapter 6), and so the question of the initial conditions for inflation can now be re-phrased as: how did the universe end up in the false vacuum? This thesis will discuss a number of subjects related to answering this question.

In Part I of the thesis, we will discuss bubble nucleation: the mechanism by which the vacua of an eternally inflating landscape might be populated. We begin in Chapter 2 by describing the classical evolution of spherically symmetric thin-wall vacuum bubbles. A full classification of bubbles allowed by the Israel junction conditions with zero mass is presented, and a number of properties of the construction and causal structure of these spacetimes are

summarized. We also find the allowed junctions for non-zero mass bubbles with positive vacuum energy. Then, relaxing the assumption of spherical symmetry, we show that bubbles with a turning point are unstable to aspherical perturbations, and present a quantitative analysis of this instability for a particular model. The material in this chapter includes and supplements Ref. [14].

In Chapter 3, we describe the nucleation of bubbles with zero mass. After introducing the instanton formalism for bubble nucleation with and without gravitational effects, we focus on the analysis of bubbles whose true vacuum has a negative vacuum energy. In the limit where the positive false vacuum energy goes to zero, we find a "Great Divide" in the space of potentials (of codimension one, since only one parameter is tuned), above which tunneling becomes very suppressed. We conclude by commenting on the implications of this phenomenon for theories of quantum gravity. The material in this chapter includes and supplements Refs. [15] and [16].

Bubble nucleation for massive bubbles is described in Chapter 4. We show that a number of bubble nucleation mechanisms can be unified in the thin-wall limit, allowing for a direct comparison of their nucleation probabilities. The zero-mass limit is shown to be the most probable in all cases. The dominant channel for production of false vacuum bubbles is the creation of an inhomogenous universe "from nothing," while the most probable mechanism for the production of true vacuum bubbles is by the Coleman-de Luccia instanton [12]. This chapter reproduces Ref. [17], with a small amount of supplementary material.

Having described, compared, and classified all of the known mechanisms for bubble nucleation, Part II addresses the question of how to make predictions in eternal inflation as driven by bubble nucleation. Chapter 5 describes a number of measures for eternal inflation. We outline the properties of and connections between these measures, and then highlight a number of generic predictions. For example, *pairs* of vacua that undergo fast transitions between themselves will be strongly favored. The resultant implications for making predictions in a generic potential

landscape are discussed. We also raise a number of issues concerning the types of transitions that observers in eternal inflation are able to experience. This chapter reproduces Ref. [18].

In Chapter 6, we argue that making predictions for cosmological – and possibly particle physics – observables in eternal inflation requires a measure on the possible cosmological histories as opposed to one on the vacua themselves. If significant slow-roll inflation occurs, the observables are generally determined by the history after the last *transition* between metastable vacua. Hence we start from several existing measures for counting vacua and develop measures for counting the transitions between vacua. This chapter reproduces Ref. [19].

We include a number of appendices which supplement the material presented in the main text. Appendix A provides a detailed description of spacetimes with a cosmological constant, including de Sitter, Schwarzschild-de Sitter, Anti de Sitter, and Schwarzschild-Anti de Sitter. The conformal structure is displayed, and a number of coordinate systems are constructed. In Appendix B, a brief presentation of the covariant entropy bound and Penrose singularity theorems is given.

Note on units: unless otherwise stated, we work in units where $\hbar = c = G_N = 1$.

Part I

Vacuum Transitions

Chapter 2

Classical Dynamics of Thin-Wall

Bubbles

In this chapter we consider the classical dynamics of thin-wall vacuum bubbles. These are solutions where regions of differing vacuum energy are matched across an infinitesimally thin wall with some associated surface tension. In later chapters we will see that many of these solutions are the Lorentzian continuations of Euclidean instantons which describe the transition between minima of different energy in a scalar field theory coupled to gravity. As such, they are relevant for early universe cosmology as described in the introduction, and outlined in greater detail in later chapters.

We discuss the Israel junction conditions, from which we will construct a comprehensive catalogue of all thin-wall bubble solutions with arbitrary surface tension and interior and exterior cosmological constant that satisfy Einstein's equations. After detailing the causal structure and properties of a number of these solutions, we discuss a classical instability towards aspherical perturbations which exists in all solutions with a turning point. Finally, a detailed analysis of the growth of such perturbations is presented, which will find relevance in the discussion of

tunneling mechanisms described in Chapters 3 and 4.

All of the solutions described in this chapter will be parametrized by a mass M , surface tension k , interior cosmological constant Λ_- , and exterior cosmological constant Λ_+ . If $\Lambda_- > \Lambda_+$ we will refer to the configuration as a false-vacuum bubble, otherwise it will be denoted a true-vacuum bubble.

2.1 Israel Junction Conditions

In this section, we develop the formalism for the junction conditions between an interior and exterior spacetime matched across a bubble wall of some tension. We will restrict our attention to interior and exterior spacetimes which are spherically symmetric, and can be fully specified by an interior and exterior cosmological constant and one mass parameter. The bubble wall worldsheet has metric:

$$ds^2 = -d\tau^2 + R(\tau)^2 d\Omega^2, \quad (2.1)$$

where τ is the proper time in the frame of the wall, and (θ, ϕ) are the usual angular variables.

The coordinates in the full $4D$ spacetime are chosen to be Gaussian normal coordinates constructed in the neighborhood of the bubble wall worldsheet. Three of the coordinates are (τ, θ, ϕ) on the worldsheet, and the fourth, η , is defined as the proper distance along a geodesic normal to the bubble worldsheet, with η increasing in the direction of the exterior spacetime.

The transformation from a static coordinate system (ie for dS, SdS, AdS, and SAdS) to the Gaussian normal system can be constructed in closed form using the methods of [20], and the full metric takes the form:

$$ds^2 = g_{\tau\tau}(\tau, \eta) d\tau^2 + d\eta^2 + r(\tau, \eta)^2 d\Omega^2, \quad (2.2)$$

where $\eta = 0$ defines the wall and therefore $g_{\tau\tau}(\tau, 0) = -1$ and $r(\tau, 0) = R(\tau)$.

The energy momentum tensor on the wall is:

$$T_{\text{wall}}^{\mu\nu} = -\sigma\gamma^{\mu\nu}\delta(\eta) \quad (2.3)$$

where $\gamma^{\mu\nu}$ is the metric on the worldsheet of the wall for $\mu = \nu = \tau, \theta, \phi$ and zero otherwise, and σ is the energy density of the wall.

Using the metric 2.2 and the energy-momentum tensor 2.3 together with the contributions from the interior and exterior spacetimes in Einstein's equations yields an equation of motion for the bubble wall of [20, 21] :

$$K_j^i(\eta_+) - K_j^i(\eta_-) = -4\pi\sigma R\delta_j^i, \quad (2.4)$$

where $K_j^i(\eta_{\pm})$ is the extrinsic curvature tensor in the exterior and interior spacetimes respectively. In the Gaussian normal coordinates, this takes the form:

$$K_{ij} = \frac{1}{2} \frac{d}{d\eta} g_{ij} \quad (2.5)$$

Evaluating this in metric 2.2, the $\theta\theta$ and $\phi\phi$ components of Eq. 2.4 reduce to:

$$\beta_- - \beta_+ = kR, \quad (2.6)$$

where $k \equiv 4\pi\sigma$

$$\beta_- \equiv -a_- \frac{dt_-}{d\tau}, \quad \beta_+ \equiv a_+ \frac{dt_+}{d\tau}. \quad (2.7)$$

Here, a_{\pm} is the metric coefficient in the static slicing of the exterior or interior spacetimes. The sign of β is fixed by the trajectory because $dt/d\tau$ could potentially be positive or negative (motion can be with or against the direction of increasing static-slicing coordinate time).

For this class of metrics, it is possible to cast Eq. 2.6 as the equation of motion for a massless particle with unit energy in a 1-D potential. This is accomplished by squaring Eq. 2.6, solving for β_+ ,

$$\beta_+ = \frac{a_- - a_+ - k^2 R^2}{2kR} \quad (2.8)$$

and squaring again

$$\dot{R}^2 + V(R, M) = -1 \quad (2.9)$$

where

$$\begin{aligned} -V(R, M) &= \frac{1}{R} \left(2M + \frac{M}{3k^2} (\Lambda_+ - \Lambda_- - 3k^2) \right) + \frac{M^2}{k^2 R^4} \\ &+ R^2 \left(\frac{\Lambda_+}{3} + \frac{1}{36k^2} (\Lambda_+ - \Lambda_- - 3k^2)^2 \right). \end{aligned} \quad (2.10)$$

As a byproduct, we can now solve for β_-

$$\beta_- = \frac{a_- - a_+ + k^2 R^2}{2kR} \quad (2.11)$$

2.2 Bubbles with zero mass

We will concentrate on the zero mass case first, where only the quadratic term in Eq. 2.10 is nonzero. In this case, it will be possible to construct an analytic solution for the wall equation of motion. The motion is governed by the equation

$$\left(\frac{dR}{d\tau} \right)^2 - R_0^{-2} R^2 = -1 \quad (2.12)$$

where

$$R_0^{-2} = \frac{1}{36k^2} \left[(\Lambda_+ + \Lambda_- + 3k^2)^2 - 4\Lambda_+ \Lambda_- \right]. \quad (2.13)$$

The solution for $R(\tau)$ in the presence of this potential is given by

$$R(\tau) = R_0 \cosh(R_0^{-1} \tau). \quad (2.14)$$

The constant R_0 is the (minimal) size of the bubble at $\tau = 0$. Note that in these coordinates, the wall's velocity is unbounded (though this does not mean that the wall goes past null).

It is possible to use the information at hand to construct the full causal structure of the matched spacetime. We will first consider a situation where the interior and exterior

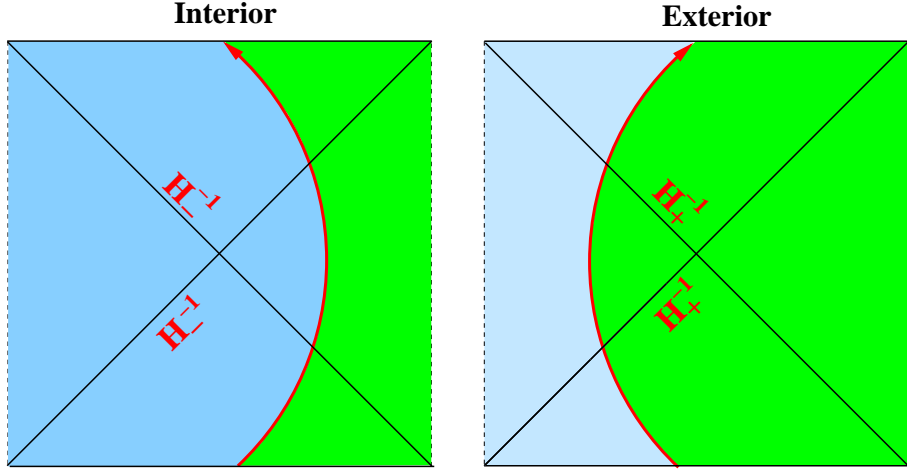


Figure 2.1: The full causal structure of the one-bubble spacetime. The two diagrams are matched across the wall. For false vacuum bubbles ($H_+ < H_-$), only the regions shaded blue are physical. For true vacuum bubbles ($H_+ > H_-$), only the regions shaded green are physical.

cosmological constants are positive. From Eq. 2.14, we see that the radius of the bubble collapses from $R(\tau = -\infty) = \infty$, reaches a turning point at $\tau = 0$, and then expands to $R(\tau = \infty) = \infty$. By looking at the functions β_{\pm} , we can determine qualitatively where to locate the bubble wall on a de Sitter conformal diagram of the interior and exterior spacetimes. For $M = 0$, the functions β_{\pm} are positive definite as can be seen from Eq. 2.8 and 2.11. From Eq. 2.7, this means that the interior coordinate time decreases as the proper time increases and the exterior coordinate time increases as the proper time increases. Therefore, the bubble wall will circulate in consistent but opposite directions on the interior and exterior de Sitter conformal diagrams.

The conformal diagram for the matched one-bubble spacetime is shown in Fig. 2.1. On the left is the conformal diagram for the interior de Sitter spacetime and on the right is the conformal diagram for the exterior de Sitter spacetime. The two diagrams are matched across the wall. For false vacuum bubbles ($H_+ < H_-$), only the regions shaded blue are physical. For true vacuum bubbles ($H_+ > H_-$), only the regions shaded green are physical.

Since we have already set up the problem in terms of the static coordinates, it is

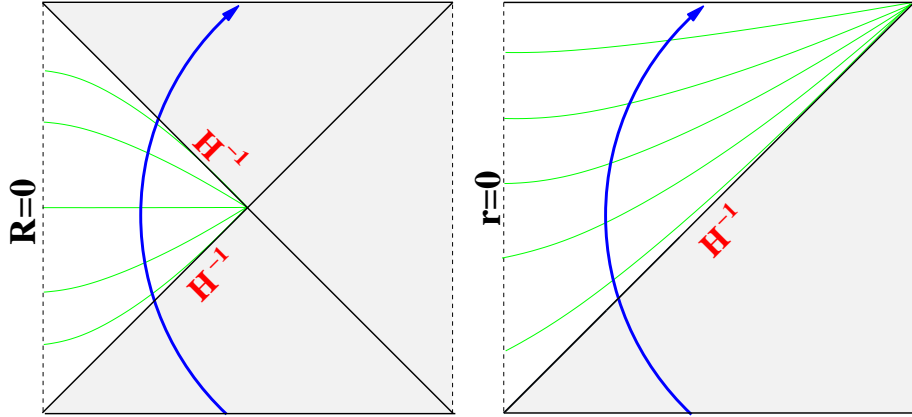


Figure 2.2: The zero mass one-bubble spacetime. Shown on the left is the region of the wall's motion which is described by one static patch (the unshaded region of the conformal diagram). The foliation of the spacetime in surfaces of constant t_+ is shown as light green lines. On the right is the same one-bubble spacetime, with the coverage of one of the flat slicing patches indicated (the unshaded region), and the foliation of the spacetime in surfaces of constant T_+ indicated by the light green lines.

straightforward to convert the time variable in Eq. 2.12 to the static slicing time. Exploiting the definition of β_{\pm} (see Eq. 2.7), we find

$$\left(\frac{dR}{dt_{\pm}} \frac{\beta_{\pm}}{a_{\pm}}\right)^2 - R_0^{-2} R^2 = -1. \quad (2.15)$$

Note that the evolution is different according to the interior and exterior observers. This arises because we chose to match R across the wall, and there will then necessarily exist a discontinuity in t . Solving the above equation for $R(t_{\pm})$, we must be careful since the static coordinates do not cover the entire region over which the bubble wall propagates. This can be seen in the left cell of Fig. 2.2, where the unshaded region corresponds to the area of the exterior (or interior if the south and north poles of the diagram are exchanged) conformal diagram over which our static patch is valid, and the light green lines indicate how the spacetime is foliated into constant t slices.

To cover its entire range of motion, we need to use three of the coordinate patches described in Appendix A.2 (each corresponding to one of the triangular wedges in Fig. 2.2).

The full solution is given by

$$R(t_{\pm}) = H_{\pm}^{-1} \left[1 - (1 - H_{\pm}^2 R_0^2) \operatorname{sech}^2 \left(H_{\pm} t_{\pm} + \frac{in\pi}{2} \right) \right]^{1/2} \quad (2.16)$$

where $n = 0$ will cover the unshaded region in Fig. 2.2. In detail, this patch will cover $H_{\pm}^{-1} < R < 0$ (corresponding to $-\infty < t_{\pm} < 0$) and $0 < R < H_{\pm}^{-1}$ (corresponding to $0 < t_{\pm} < \infty$). As the bubble grows past the cosmological horizon, we must take $n = 1$ for $H_{\pm}^{-1} < R < \infty$ (corresponding to a range in t_{\pm} of $-\infty < t_{\pm} < 0$). To the past of the turning point, as the bubble retreats behind the cosmological horizon, we must take $n = -1$ for $H_{\pm}^{-1} < R < \infty$ (corresponding to a range in t_{\pm} of $\infty > t_{\pm} > 0$).

In these coordinates, the asymptotic size of the bubble at $t_{\pm} \rightarrow \infty$ in the $n = 0$ patch is H_{\pm}^{-1} . It can be seen from Eq. 2.16 that evolution in terms of the true vacuum time variable (which could be either t_+ or t_-) covers a larger range of R , and will encompass the time of false vacuum horizon-crossing. The evolution in terms of the false vacuum time variable will not cover the time of true vacuum horizon-crossing. An observer riding on the bubble wall will see true vacuum bubbles cross the exterior de Sitter horizon before the interior de Sitter horizon. This means that an observer in the interior of the true vacuum bubble will have causal access to a larger than horizon region of the exterior spacetime.

To further understand the geometry, we can go to the embedding coordinates in Eq. A.19, and solve for R in terms of T and X_4

$$R = H^{-1} \left[1 - X_4^2 \operatorname{sech}^2(HT) \right]^{1/2}. \quad (2.17)$$

This is very similar to the bubble wall equation of motion Eq. 2.16, from which it can be seen that the bubble wall trajectory corresponds to $X_4 = \text{constant}$. To determine this value of X_4 , we must choose either the interior or exterior de Sitter hyperboloid to be centered about the origin of the embedding coordinates. We will choose the true vacuum de Sitter space, in which

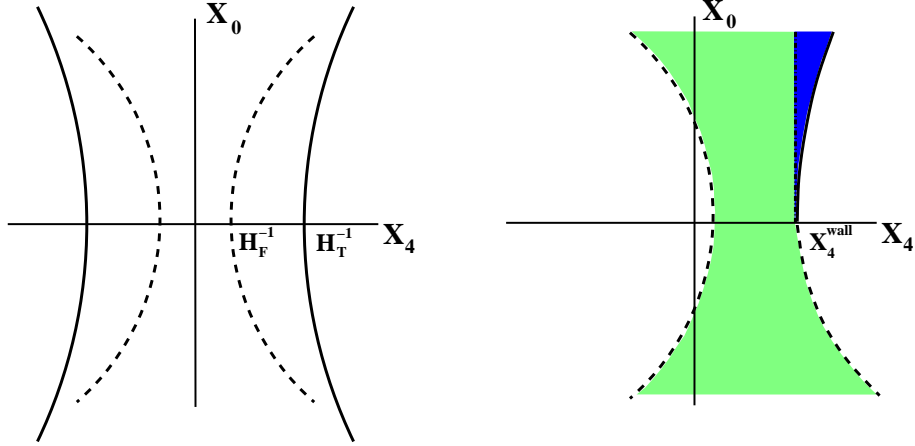


Figure 2.3: Shown on the left are the true and false vacuum de Sitter hyperboloids, both centered on the origin. Shown on the right is the geometry of a zero-mass bubble. The true vacuum de Sitter hyperboloid is centered on the origin, and matched to a displaced false vacuum de Sitter hyperboloid along a surface of constant X_4^{wall} . The true vacuum region of the full matched solution is shaded.

case

$$X_4^{wall} = \pm H_{true}^{-1} (1 - H_{true}^2 R_0^2)^{1/2}. \quad (2.18)$$

Note that in the case of true vacuum bubbles $H_{true} = H_-$, and in the case of false vacuum bubbles $H_{true} = H_+$. Shown in Fig. 2.3 is the bubble geometry in the embedding coordinates, which corresponds to two hyperboloids of different curvature attached along a surface of constant X_4 .

We can now use the description of the wall in the embedding coordinates to find the motion of the wall in a variety of coordinate systems. We will be particularly interested in the description of the bubble's evolution in the flat slicing (defined by the metric Eq. A.30). The range of evolution covered by this coordinate system is shown on the right of Fig. 2.2. The coordinates for the true vacuum side of the bubble can be found from the expression for X_4 in Eq. A.31

$$X_4^{wall} = (1 - H_{true}^2 R_0^2)^{1/2} = H_{true}^{-1} \cosh(H_{true} T_{true}) - \frac{H_{true}}{2} \mathbf{x}^2 e^{H_{true} T_{true}}. \quad (2.19)$$

Solving for the physical radius, $R = |\mathbf{x}|e^{H_{true}T_{true}}$, we find that

$$R(T_{true}) = H_{true}^{-1} \left[e^{2H_{true}T_{true}} - 2(1 - H_{true}^2 R_0^2)^{1/2} e^{H_{true}T_{true}} + 1 \right]^{1/2}. \quad (2.20)$$

To find the radius as a function of the false vacuum flat slicing time variable, we must take into account that the center of the false vacuum hyperboloid is not at the origin of the embedding coordinates, but shifted to:

$$X_4^{false} = H_T^{-1}(1 - H_T^2 R_0^2)^{1/2} - H_F^{-1}(1 - H_F^2 R_0^2)^{1/2}. \quad (2.21)$$

Solving for the intersection of the wall with the false vacuum hyperboloid, we find that

$$R(T_{false}) = H_{false}^{-1} \left[e^{2H_{false}T_{false}} - 2(1 - H_{false}^2 R_0^2)^{1/2} e^{H_{false}T_{false}} + 1 \right]^{1/2}. \quad (2.22)$$

We can also consider cases where the interior and exterior cosmological constants are less than or equal to zero. In this category of solutions we can have true vacuum bubbles with $(\Lambda_+ > 0, \Lambda_- < 0)$ as shown in Fig. 2.4, $(\Lambda_+ > 0, \Lambda_- = 0)$ as shown in Fig. 2.5, and $(\Lambda_+ = 0, \Lambda_- < 0)$ as shown in Fig. 2.6. Expanding false vacuum bubbles are only possible for $(\Lambda_+ > 0, \Lambda_- > 0)$. The pressure gradient always points from the true to the false vacuum, and therefore the only way to avoid the collapse of false vacuum bubbles is to rely on the background expansion of the true vacuum. Further, the collapse of zero mass false vacuum bubbles formed in Minkowski or AdS space would seemingly produce a naked singularity (the end-point of the collapse would certainly involve singular energy densities, which, since the total mass of the solution is zero, would not be shielded by an event horizon), and so would violate cosmic censorship (for a recent discussion of cosmic censorship, see [22]). Indeed, the junction conditions forbid such matchings (requiring $\beta_+ < 0$, which cannot occur in Minkowski space).

Looking at the solution in Fig. 2.4, the turning point radius in Eq. 2.13 approaches the size of the exterior cosmological horizon when $\Lambda_- = \Lambda_+ - 3k^2$ (which is the maximum value R_0 can attain if a time symmetric solution exists). If we now take $\Lambda_+ \rightarrow 0$ in this region of

parameter space, $R_0 \rightarrow \infty$, and it can be seen from Eq. 2.12 that the bubble wall radius becomes constant in time. Thus, we have found a static domain wall, which exists along a surface of codimension one in the parameter space of (Λ_-, k) . When $\Lambda_+ \leq 3k^2$ it is impossible to find a solution where $R_0 = H_+^{-1}$ with a negative Λ_- , and $R_0 < H_+^{-1}$ for all values of (k, Λ_-) , reaching a maximum value of $R_0^{max} = 6k(\Lambda_+ + 3k^2)^{-1}$ at $\Lambda_- = 0$.

A number of features of the matched solution shown in Fig. 2.4 should be noted. In the interior of the bubble, the spacetime is not truly AdS. Generic perturbations in the interior will cause a big crunch to the future (in the time symmetric solution, initial conditions will also generically be singular), and any observer entering the bubble will encounter a singularity in finite proper time. For geometries corresponding to the Lorentzian continuation of CDL vacuum bubbles (where the interior of the bubble is a perturbed AdS), this was rigorously shown by Abott and Coleman in [23] using the Penrose singularity theorems [24] (see Appendix B for a brief discussion).

The dashed blue lines in Fig. 2.4 represent the boundary of the causal diamond of an eternal observer located at the origin. They also represent the light sheet corresponding to the S^2 located at the point labeled B. We can therefore apply the covariant entropy bound (see Appendix B), and limit the statistical entropy of any system inside the bubble by the area of this S^2 . Note that the maximal area is given by the area of the exterior cosmological horizon, since B lies on the $t = 0$ surface. Applying the Holographic Principle, this implies that the number of degrees of freedom required to describe the interior of the bubble is always less than or equal to the number fundamental degrees of freedom describing the exterior de Sitter space. We will discuss the implications of this observation in Chapter 3.

The causal diamond of the observer at the origin who exists from $t = 0$ until the crunch ¹ is indicated in Fig. 2.4 by the area between the dashed blue line and the dashed red

¹This will be identified as the observer who lives the longest in the nucleation of a CDL true vacuum bubble

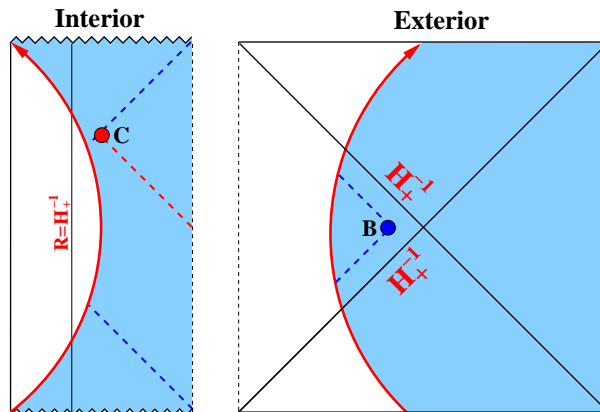


Figure 2.4: The causal structure of a true-vacuum bubble spacetime with $(\Lambda_+ > 0, \Lambda_- < 0)$. The singularities to the past and future of the wall’s evolution in the interior space of negative cosmological constant indicate that the interior of the bubble is unstable to collapse into a big crunch.

line in the interior of the bubble. This causal diamond will always be located entirely within the AdS space (since the wall is asymptotically null), and the observer will have a lifetime of $t_{crunch} = \pi H_-^{-1}$. These null rays also form the light sheet corresponding to the surface labeled C, and therefore we can apply the covariant entropy bound: $S[L(C)] < A(C)/4 = \pi H_-^{-2}$.

We now turn to true vacuum bubbles with $(\Lambda_+ > 0, \Lambda_- = 0)$, as depicted in Fig. 2.5. The red dashed line indicates a past directed null ray emanating from the origin. A cauchy surface in this spacetime is drawn through the $t = 0$ slice. The entirety of this cauchy surface will lie within the causal diamond of an observer at the origin, denoted by the blue dotted lines. This led Freivogel and Susskind to propose the existence of an S-matrix relating asymptotic states at early and late times inside of the bubble [25]². However, it was subsequently shown by Bousso and Freivogel [27] that the contracting portion of the geometry is violently unstable to perturbations, and generically leads to a big crunch in the bubble interior.

The red dashed line in Fig 2.5 forms the light sheet of the point P located on the

of negative energy density, and will be discussed further in Chapter 3.

²Given the difficulty in constructing observables in cosmological spacetimes [26], this would be an important development.

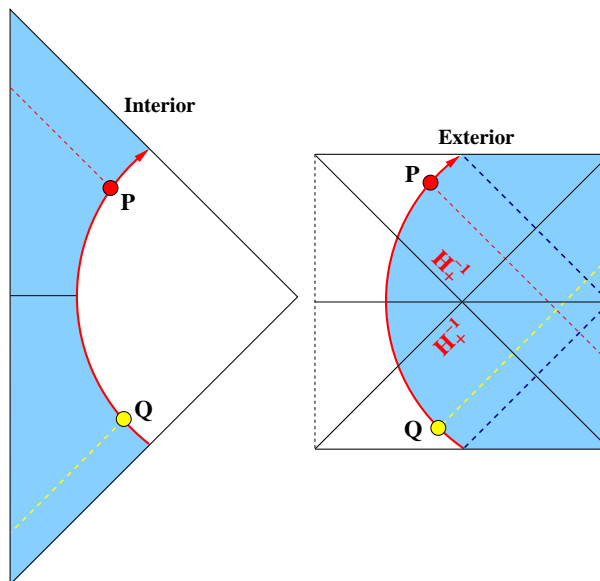


Figure 2.5: The causal structure of a true-vacuum bubble spacetime with $(\Lambda_+ > 0, \Lambda_- = 0)$. Shown in the red dotted line is a past directed null ray from the origin inside the true vacuum bubble.

bubble wall. We can apply the covariant entropy bound to this surface, and since the light sheet forms a Cauchy surface itself, we can bound the total entropy moving through a cauchy surface in the one-bubble spacetime [27]. The strictest bound is obtained by moving the point P to the location where the bubble wall crosses the exterior de Sitter horizon: $S < \pi H_+^{-2}$. Performing the same analysis for the point Q , it appears as though at early times there is a very large entropy allowed by the bound (becoming arbitrarily large as Q is slid down the bubble wall to the past). There appears to be a contradiction: since any entropy moving across this light sheet will move across the light sheet associated with P what happens to the allowed entropy in the asymptotic past? The resolution [27] lies in the fact that only a small set of the microstates allowed in the past will correspond to the bubble geometry: most will correspond to a spacetime which undergoes a big crunch.

Finally, we cover the case of true vacuum bubbles with $(\Lambda_+ > 0, \Lambda_- = 0)$, as depicted in Fig. 2.6. The causal diamond of an observer at the origin is enclosed by the dashed red lines.

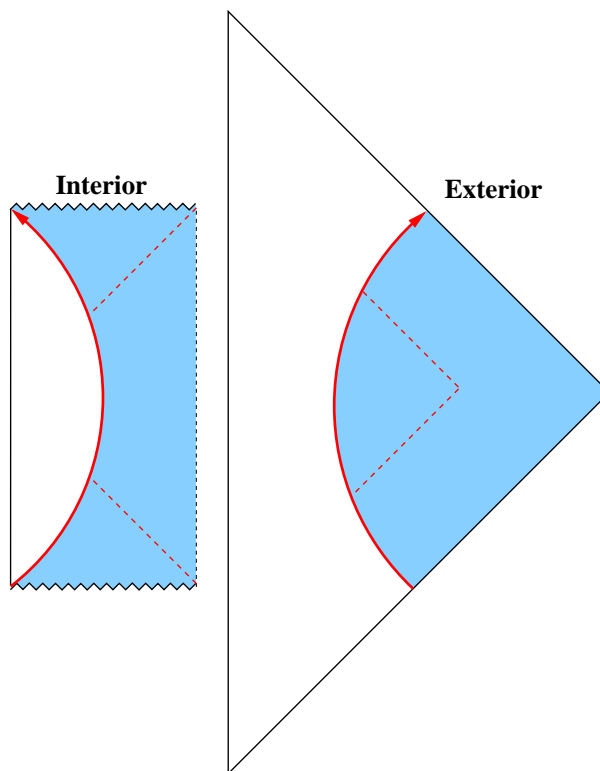


Figure 2.6: The causal structure of a true-vacuum bubble spacetime with $(\Lambda_+ = 0, \Lambda_- < 0)$. Enclosed in the dotted red lines is the causal diamond of an observer at the origin inside the true vacuum bubble.

It can be seen that the area of this causal diamond is finite. Like the spacetime depicted in Fig 2.5, there are observers in this spacetime for whom an S-matrix is well defined.

2.3 Bubbles with nonzero mass

In this section, we will describe the classical dynamics of bubbles with a nonvanishing mass parameter in the exterior metric coefficient. Returning to the bubble wall equation of motion in Eq. 2.9, it will be useful to define a set of dimensionless variables which will help us to classify the allowed junctions. Let:

$$z = \left(\frac{L^2}{2M} \right)^{\frac{1}{3}} R, \quad T = \frac{L^2}{2k} \tau, \quad (2.23)$$

and

$$L^2 = \frac{1}{3} \left[\left[(\Lambda_- + \Lambda_+ + 3k^2)^2 - 4\Lambda_+\Lambda_- \right] \right]^{\frac{1}{2}}. \quad (2.24)$$

With these definitions, Eq. 2.9 becomes

$$\left[\frac{dz}{dT} \right]^2 = Q - V(z), \quad (2.25)$$

where the potential $V(z)$ and energy Q are

$$V(z) = - \left[z^2 + \frac{2Y}{z} + \frac{1}{z^4} \right], \quad (2.26)$$

with

$$Y = \frac{1}{3} \frac{\Lambda_+ - \Lambda_- + 3k^2}{L^2}, \quad (2.27)$$

and

$$Q = - \frac{4k^2}{(2M)^{\frac{2}{3}} L^{\frac{8}{3}}}. \quad (2.28)$$

Note that a small negative Q corresponds to a large mass, so that even between $-1 < Q < 0$ the mass can be arbitrarily large.

We now consider solutions which have $\Lambda_{\pm} \geq 0$, where $-1 \leq Y \leq 1$. The maximum V_{\max} of the potential $V(z)$ then satisfies $-2^{5/3} - 2^{-4/3} \leq V_{\max} \leq 0$. The potential curves over the entire range of Y are shown in Fig.2.7. The fact that the potential function is essentially unchanged over the entire parameter space will prove to be a very useful property for classifying the various solutions, and is the main motivation for the change of variables introduced above.

The interior and exterior cosmological constants can be expressed in terms of k^2 as $\Lambda_+ = Ak^2$ and $\Lambda_- = Bk^2$. With these choices, the dynamics of the bubble wall are entirely determined by A , B , and Q .

To get a feel for the values these parameters might take, consider a false vacuum bubble with $\Lambda_+ \gg \Lambda_-$. The interior cosmological constant ($\Lambda_- = M_-^4/M_{pl}^4$) and the bubble wall surface

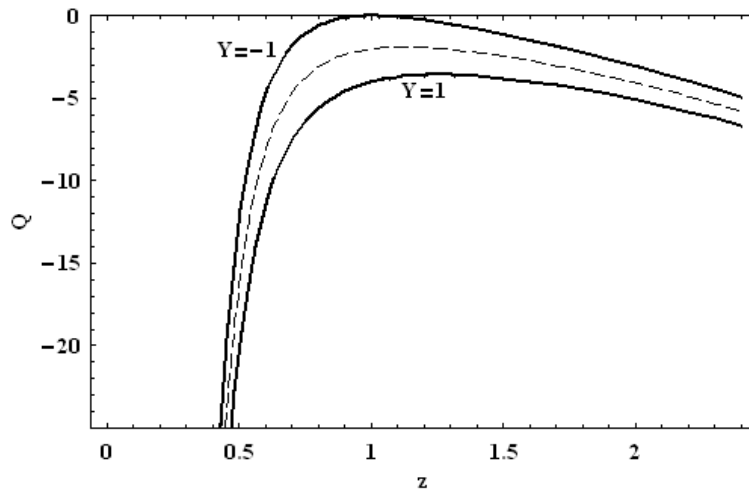


Figure 2.7: The potential for various Y .

energy density ($k = 4\pi M_-^3/M_{\text{pl}}^3$) will be set by a scale M_- . The exterior cosmological constant ($\Lambda_+ = M_+^4/M_{\text{pl}}^4$) will be set by a scale M_+ . These yield

$$A = \frac{M_+^4 M_{\text{pl}}^2}{(4\pi)^2 M_-^6}, \quad B = \frac{M_{\text{pl}}^2}{(4\pi)^2 M_-^2}. \quad (2.29)$$

We might now consider three representative energy scales M_- , covering the interesting range of energy scales for inflation³. For weak scale inflation (100 GeV), $k \simeq 4\pi \times 10^{-51}$, $A \simeq 0$, and $B \simeq 10^{32}$. For an inflation scale near the GUT scale (10^{14} GeV), we have $k \simeq 4\pi \times 10^{-15}$, $A \simeq 0$, and $B \simeq 10^7$. Near-Planck scale inflation (10^{17} GeV) yields $k \simeq 4\pi \times 10^{-6}$, $A \simeq 0$, and $B \simeq 63$. The mass scale corresponding to the maximum of the potential is given by converting from Q to M using Eq. 2.28. This maximal mass is very different in each case, ranging from an ant-mass of $M_{\text{max}} \simeq 10^3 M_{\text{pl}} \simeq 10^{-2}$ grams for $M_- = 10^{17}$ GeV to an Earth-mass of $M_{\text{max}} \simeq 10^{33} M_{\text{pl}} \simeq 10^{28}$ grams, for $M_- = 100$ GeV.

A bubble wall trajectory is characterized by $Q = \text{const.}$, and there are three general types:

³This is in anticipation of later discussions of false vacuum bubbles, the formation of which might have corresponded to the initial conditions for inflation.

- Bound solutions with $Q < V_{\max}$. These solutions start at $z = 0$, bounce off the potential wall and return to $z = 0$.
- Unbound solutions with $Q < V_{\max}$. These solutions start at $z = \infty$, bounce off the potential wall and return to $z = \infty$.
- Monotonic solutions with $Q > V_{\max}$. These solutions start out at $z = 0$ and go to $z = \infty$, or execute the time-reversed motion.

From the constant- Q trajectories in the presence of the potential of Eq. 2.26, one can construct the full one-bubble spacetimes [21, 20, 14, 17]. Shown in Fig. 2.8 is an example of two of the possible potential diagrams. In addition to the potential Eq. 2.26, there are other landmarks in Fig. 2.8:

- As one follows a line of constant Q , every intersection with the dashed line Q_{sds} (which is obtained by solving $a_{\text{sds}} = 0$ for Q) represents a horizon crossing in the SdS spacetime (this could represent either the past/future black hole or cosmological horizons).
- Intersections with the dashed line Q_{ds} (which is obtained by solving $a_{\text{ds}} = 0$ for Q) as one moves along a line of constant Q represent the crossing of the interior dS horizon.
- The vertical line on the right (in the left panel of Fig. 2.8) denotes the position at which β_{ds} changes sign. β_{ds} is a monotonic function of z , which will have a zero where Q_{ds} intersects the potential. Recall that $\beta_{\text{ds}} > 0$ if t_{ds} is decreasing along the bubble wall trajectory and is negative if t_{ds} is increasing.
- The vertical dotted line on the left denotes the radius at which β_{sds} changes sign. β_{sds} is also a monotonic function of z , with a zero where Q_{sds} intersect the potential. $\beta_{\text{sds}} > 0$ if t_{sds} is increasing along the bubble wall trajectory, and $\beta_{\text{sds}} < 0$ if it is decreasing.

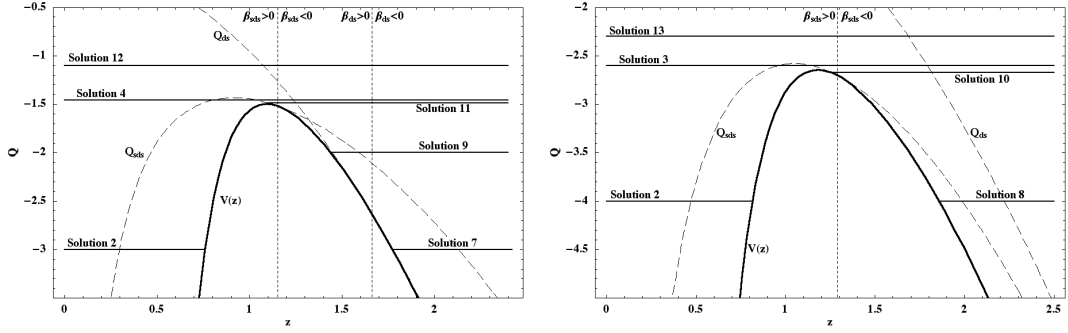


Figure 2.8: Potential for false-vacuum bubbles with $B < 3(A - 1)$. The diagram on the left is for $(A = 9, B = 15)$. The diagram on the right is for $(A = 2.9, B = 3)$, which is an example of a case where there is no β_{ds} sign change ($B < A + 3 < 3(A - 1)$). The two dashed lines labeled Q_{sds} and Q_{ds} represent the exterior and interior horizon crossings respectively. The vertical dotted lines denote the regions in which β_{sds} and β_{ds} are positive and negative. Various trajectories are noted.

For there to be a β_{ds} sign change, Y in Eq. 2.27 must be in the range $-1 \leq Y < 0$ [28], which yields the condition that $B > A + 3$ if a sign change is to occur. This inequality shows that β_{ds} does not change sign for true vacuum bubbles ($A > B$). For there to be a β_{sds} sign change, the function

$$\tilde{Y} = \frac{1}{3} \frac{\Lambda_+ - \Lambda_- - 3k^2}{L^2} \quad (2.30)$$

must be in the range $-1 \leq \tilde{Y} < 0$ [28], which yields the condition that $B > A - 3$ if a β_{sds} sign change is to occur. If a β_{sds} sign change does exist, it can occur to the left (if $B > 3(A - 1)$) or right ($B < 3(A - 1)$) of the maximum in the potential [14]. Given these conditions, there are a total of seven qualitatively different potential diagrams to consider, examples of which are shown in Figs. 2.8, 2.9, 2.10, and 2.11.

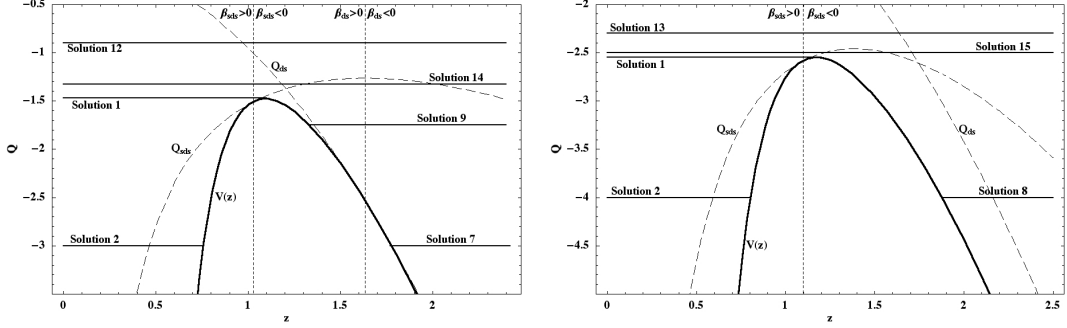


Figure 2.9: Potential for false-vacuum bubbles with $B > 3(A - 1)$. The diagram on the left is for $(A = 1, B = 6)$. The diagram on the right is for $(A = 1, B = 2)$, which is an example of a case where there is no β_{ds} sign change ($3(A - 1) < B < A + 3$). For these choices of parameters, the sign change in β_{sds} occurs to the left of the maximum in the potential. Various trajectories are noted.

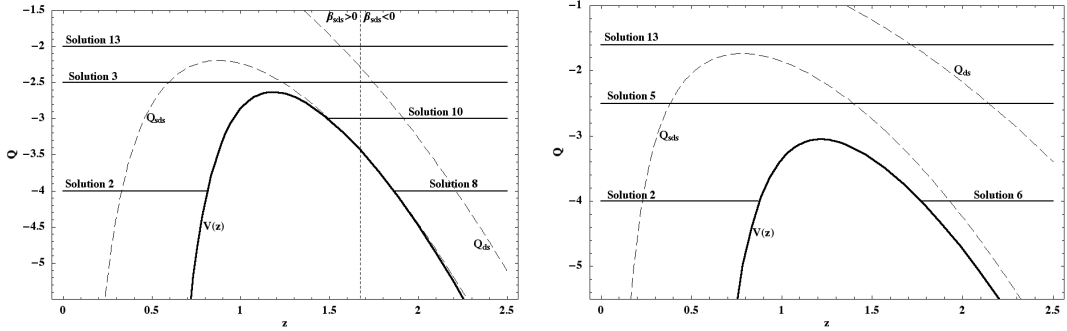


Figure 2.10: Potential for true-vacuum bubbles with $A > \frac{B}{3} + 1$. The diagram on the left is for $(A = 7, B = 6)$, which is an example of a case where there is a β_{sds} sign change ($A < B + 3$). The diagram on the right is for $(A = 14, B = 8)$, which contains no β_{sds} sign change ($A > B + 3$). Various trajectories are noted.

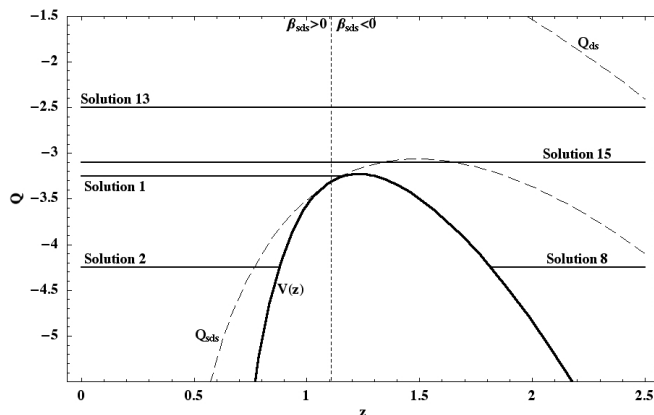


Figure 2.11: Potential for true-vacuum bubbles with $(A = .6, B = .5)$, corresponding to the case where $A < \frac{B}{3} + 1 < B + 3$. Various trajectories are noted.

2.4 Conformal diagrams and classification

The one-bubble spacetimes, represented by lines of constant Q on the junction condition potential diagrams, are shown in Figs. 2.12, 2.13, and 2.15⁴. The shaded regions of the conformal diagrams shown in the left column cover the interior of the vacuum bubble. The shaded regions of the diagrams in the right column cover the spacetime outside the bubble. The conformal diagrams in each row are matched along the bubble wall (solid line with an arrow). For solutions with qualitatively similar SdS diagrams, the various options for the dS interior are connected by labeled solid lines.

The conformal diagrams shown in Fig. 2.12 are all solutions in which the bubble wall remains to the right of the wormhole of the SdS conformal diagram. The bound solutions, Solutions 1 and 2, exist for both true- and false-vacuum bubbles. For false-vacuum bubbles, they represent a regime in which the inward pressure gradient and bubble wall tension dominate the dynamics, causing the bubble to ultimately contract. In the case of true-vacuum bubbles,

⁴Many of these solutions have appeared in previous work [21, 29, 30, 28, 31, 32, 14], but with specific assumptions about the mass and/or the interior and exterior cosmological constants.

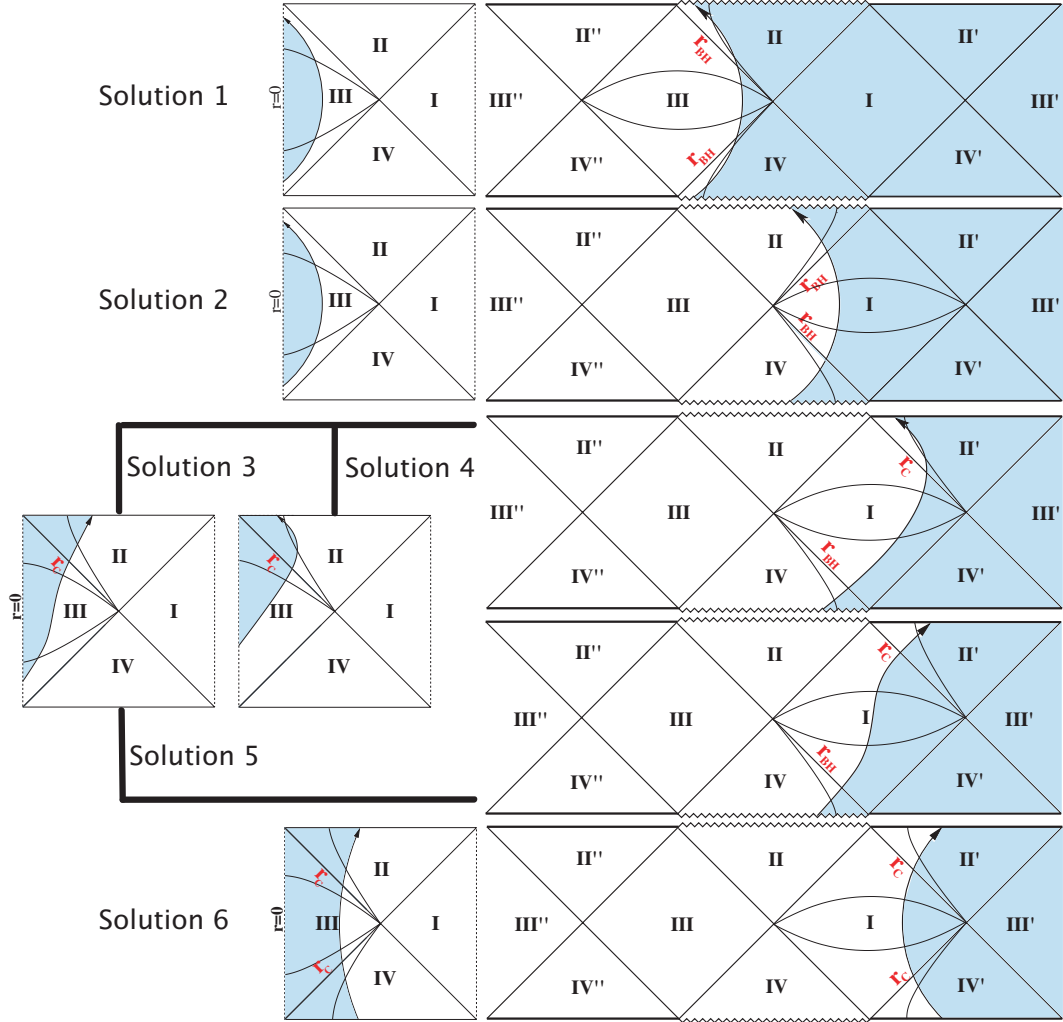


Figure 2.12: Conformal diagrams for the one-bubble spacetimes which do not lie behind a worm hole. The global one-bubble spacetimes are constructed by matching the interior (shaded regions of the dS conformal diagrams in the left column) to the exterior (shaded regions of the SdS conformal diagrams in the right column) across the bubble wall (solid line with an arrow). For solutions with qualitatively similar SdS diagrams, the various options for the dS interior are shown.

this corresponds to cases where the wall tension overwhelms the outward pressure gradient.

In the monotonic Solutions 3-5 of Fig. 2.12 the bubble wall has enough kinetic energy to reach curvatures comparable to the exterior horizon size, at which time the bubble cannot collapse. Solutions 3 and 4 represent either true- or false-vacuum bubbles where the wall tension and/or the inward pressure gradient causes the wall to accelerate towards $r = 0$, but which are saved from collapse by the expansion of the exterior spacetime. Solution 5 exists only for true-vacuum bubbles, and describes a solution which accelerates away from the origin due to the outward pressure gradient while also being pulled out of the cosmological horizon by the expansion of the exterior spacetime.

The unbound Solution 6 also exists only for true-vacuum bubbles. Here, the bubble expands, all the while accelerating towards the false-vacuum. The zero mass limit ($M \rightarrow 0$, or $Q \rightarrow -\infty$) of this solution reproduces the solution for de Sitter–de Sitter junctions with $\Lambda_+ > \Lambda_-$ presented in Sec. 2.2.

The solutions shown in Fig. 2.13 are all behind the wormhole in the SdS spacetime, save Solutions 12 and 13, which correspond to evolution in a spacetime without horizons. The false-vacuum bubble solutions 7 and 9, and true- or false-vacuum bubble solution 8 are unbound solutions which exist to the left of the worm hole on the SdS conformal diagram. It can be seen that at turnaround, each of these bubbles will be larger than the exterior horizon size. Observers in region III of the SdS conformal diagram will see themselves sandwiched between a black hole and a bubble wall which encroaches in from the cosmological horizon. Observers inside the bubble are also surrounded by a bubble wall, and so we are faced with the rather odd situation that both observers will perceive themselves inside bubbles of opposite phase.

Solutions 7 and 8 have interesting zero mass limits. Since these solutions involve both sides of the wormhole, the zero mass limit corresponds to an exactly dS universe consisting of regions I, II', III', and IV' (encompassed by the vertical dashed lines shown on the right side of

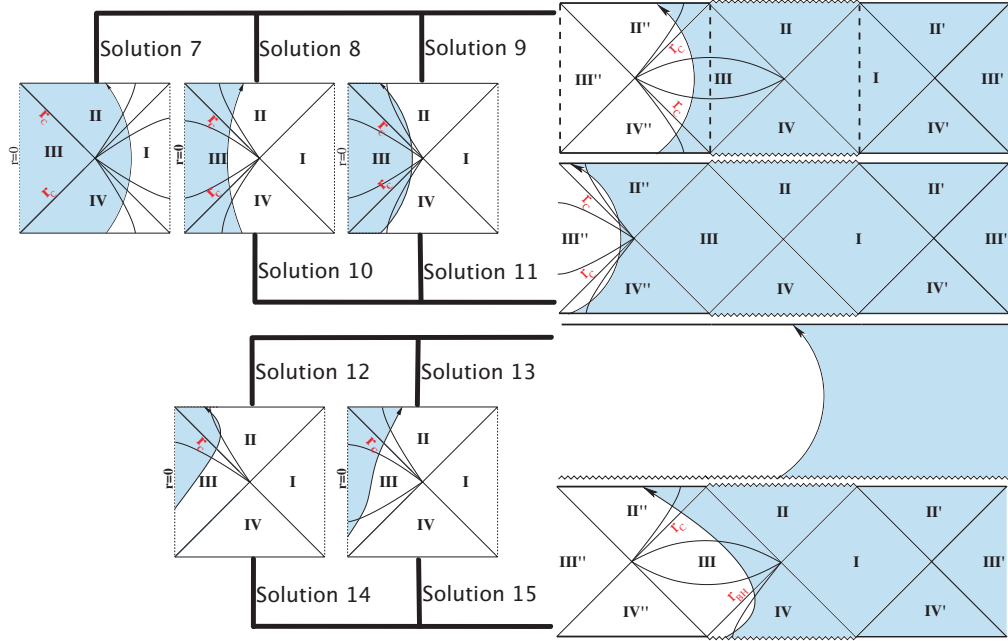


Figure 2.13: Conformal diagrams for the one-bubble spacetimes which lie behind a worm hole. The global one-bubble spacetimes are constructed by matching the interior (shaded regions of the dS conformal diagrams in the left column) to the exterior (shaded regions of the SdS conformal diagrams in the right column) across the bubble wall (solid line with an arrow). For solutions with qualitatively similar SdS diagrams, the various options for the dS interior are shown.

the first diagram of Fig. 2.13) of the SdS diagram (in which nothing happens), and a dS universe consisting of regions III, II', and IV'' (encompassed by the other set of vertical dashed lines) which contains a CDL true- or false-vacuum bubble. The radius at the turning point is still given by Eq. 2.13, and so the bubble to the left of the wormhole is the analytic continuation of the true- or false-vacuum CDL instanton. However, note that the Lorentzian evolution of the true-vacuum bubbles is very different from the canonical zero mass true vacuum bubbles discussed in Sec. 2.2. As seen from the outside (region III of the SdS diagram on the right), the bubble wall accelerates towards the true-vacuum (driven by the wall tension); in the absence of the cosmic expansion of the false-vacuum, this solution would be bound.

Because the SdS manifold is non-compact (see the discussion in Sec. A.4), there are

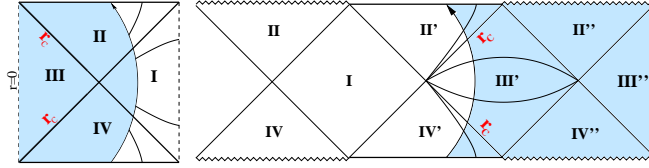


Figure 2.14: Solutions can be to the right of region I instead of behind the wormhole. This solution is identical to Solution 7 of Fig. 2.13.

actually many more options. We have so far placed special significance on the singularities in regions II and IV of the SdS diagram. However, there will be other singularities both to the left and right of these regions which can also be viewed as the origin of coordinates. It is perfectly legitimate to construct bubble wall solutions using any origin of coordinates one wishes, and therefore each of the solutions in Fig. 2.12 and 2.13 represents only one of an infinity of possible solutions. An example of an alternative solution is shown in Fig. 2.14, which is identical to the Solution 7 in Fig. 2.13 in every way, except different regions of the conformal diagram are physical. This observation is key for the tunneling mechanisms we will describe in Chapter 4.

Moving on to the other solutions in Fig. 2.13, Solution 10 (corresponding to either true- or false-vacuum bubble) and Solution 11 (corresponding to a false-vacuum bubble) are massive unbound solutions which lie outside the cosmological horizon of a region III observer. Solution 12 (corresponding to a false-vacuum bubble) and Solution 13 (corresponding to either a true- or false-vacuum bubble) are monotonic solutions with mass greater than the Nariai mass of the SdS spacetime. This can be seen by noting that these constant Q trajectories never cross the Q_{sds} line in the potential diagrams. The false-vacuum bubble Solution 14, and the true- or false-vacuum bubble solution 15 are monotonic solutions which must lie to the left of the wormhole.

There is one more class of solutions, shown in Fig. 2.15, which exist in unstable equilibrium between the bound and unbound solutions of Fig. 2.12 and 2.13. Solution 16 corresponds

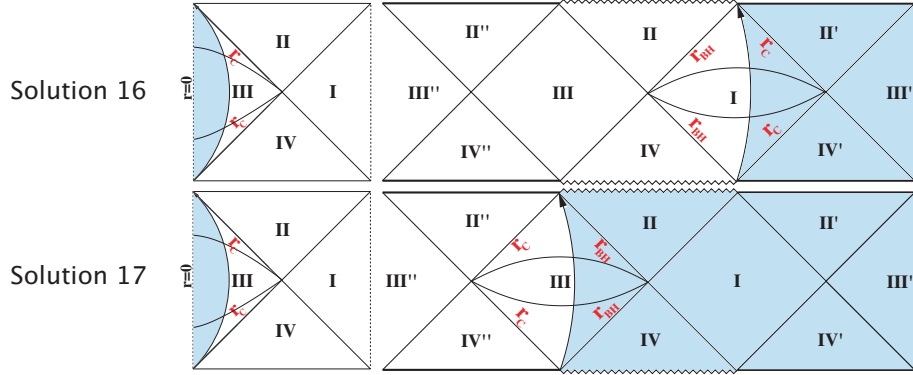


Figure 2.15: Solutions which are in unstable equilibrium between the bound and unbound solutions of Fig. 2.12 and 2.13. These solutions correspond to the time symmetric spacetimes of thermally activated bubbles.

to true- or false-vacuum bubbles with $B < 3(A - 1)$, while Solution 17 corresponds to true- or false-vacuum bubbles with $B > 3(A - 1)$. These solutions can be identified as the spacetimes of the thermal activation mechanism of Garriga and Megevand [32], which we will discuss further in Sec. 4.2.4 and 4.3.

2.4.1 Application of the Penrose singularity theorem

In a series of papers, Farhi et. al. [33, 20] discussed the application of the Penrose singularity theorems [22] (see Appendix B) to the one-bubble spacetimes discussed above. Since the null energy condition is satisfied on the junction and in both the interior and exterior spacetimes, and there exists a non-compact cauchy surface, then the existence of a closed anti-trapped surface in the spacetime implies the presence of an initial singularity. The 2-sphere represented by point P_1 shown in Fig. 2.16, Solution 2, is a closed anti-trapped surface. This can be seen by noting that both the ingoing and outgoing past directed null rays in Fig. 2.16 are diverging. An initial singularity is therefore necessary for this solution to exist at and near P_1 . This spacetime also, however, contains regions without anti-trapped surfaces. The point

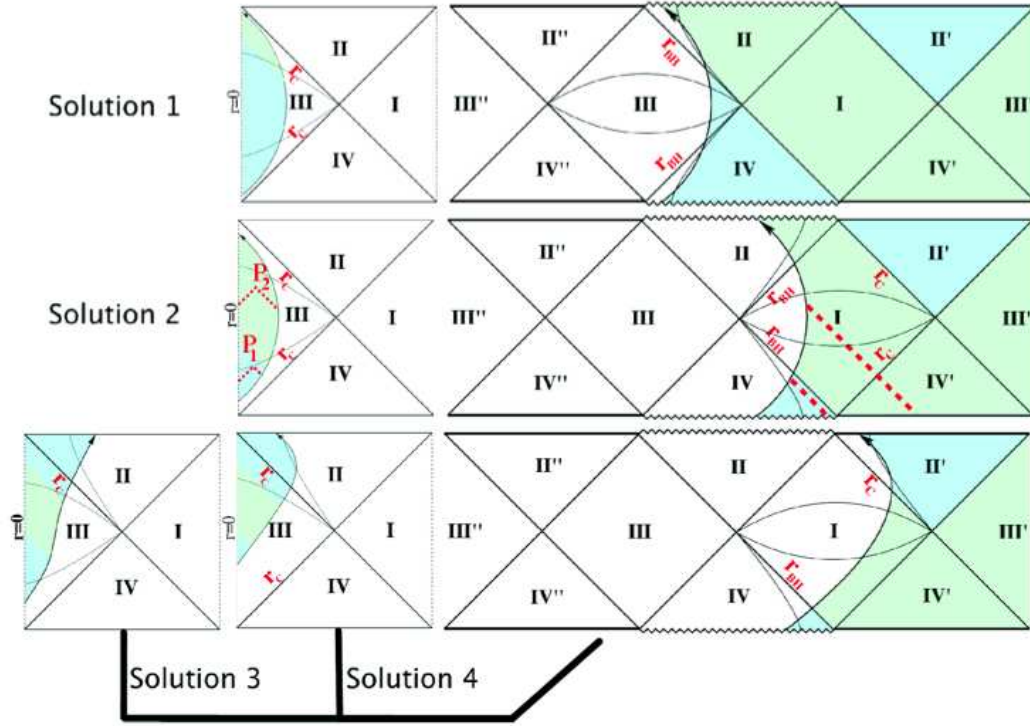


Figure 2.16: Conformal diagrams for three representative one-bubble spacetimes. Regions which do not contain anti-trapped surfaces are shaded green, regions which do are shaded blue.

P_2 , for example is a normal surface. In Fig. 2.16, regions which contain anti-trapped surfaces are shaded blue (dark) and the regions which do not are shaded green (light).

If we imagined constructing the bubble shown in Solution 2 in its expanding phase at a time where the radius of the bubble wall satisfies $r > r_{BH}$, then the future evolution of the spacetime would not necessarily require an initial singularity⁵. We can remove the initial singularity from Solution 3 and 4 as well by forming the bubble on the same spacelike

⁵There are anti-trapped surfaces in region II' of the SdS diagram, and there is a noncompact Cauchy surface C for it, so the Penrose theorem applies, but only indicates that geodesics are incomplete in region II' because they reach its edge (the past Cauchy horizon of C .) The region is thus extendible (into regions I, III' and IV') rather than singular. Full dS has only compact Cauchy surfaces so the theorem does not apply.

surface. Solutions 2,3, and 4 are therefore classically buildable. Solutions 3 and 4 are the only examples where it is possible to form an inflationary universe from classically buildable initial conditions, but only exists when the interior and exterior cosmological constant are almost equal ($B < 3(A - 1)$). This solution might be of interest in understanding transitions between nearly degenerate vacua, for example in the context of eternal inflation.

Our full catalog of solutions is also interesting in regards to a recent proposal [34, 35] that false vacuum regions, assumed to be larger than the interior horizon, must at all times be larger than the exterior, true vacuum, horizon. The basis of this conjecture is the condition that the divergence of a congruence of future directed null geodesics (defined as θ) must satisfy

$$\frac{d\theta}{dT} \leq 0, \tag{2.31}$$

where T is an affine parameter, if the NEC holds for all T . Null rays in the dS and SdS spacetimes satisfy this inequality (in dS, the inequality is exactly zero), but we should check that the junction conditions do not violate it. One requirement imposed by Eq. 2.31 is that the divergence of the null rays does not increase at the position of the wall as they go from a true vacuum region into a false vacuum one. Along any given null geodesic in the bubble interior or exterior, the value of r is either increasing or decreasing monotonically as a function of T . We can therefore state the condition Eq. 2.31 as: one cannot have a null ray along which $dr/dT \leq 0$ outside the bubble and $dr/dT \geq 0$ inside the bubble. Surveying the allowed solutions, we see that Eq. 2.31 is indeed always satisfied.

The authors of Ref. [34, 35] intended to demonstrate that if one requires the false vacuum region to be larger than the interior horizon size at all times (so that inflation is un-stoppable), it is necessarily larger than the exterior horizon size. Although all of the allowed one-bubble spacetimes satisfy the condition Eq. 2.31, there are observers that will see only a *black hole* horizon sized volume removed from the true vacuum phase. We therefore conjecture

that if one requires the false vacuum region to be larger than the interior horizon size at all times, then it will replace a volume larger than the exterior horizon size according to *only some* observers. If one relaxes this requirement, then the monotonic solutions 3 and 4, which grow from an arbitrarily small size, could also contain an inflationary universe.

2.5 The instability of bubbles with a turning point

The solutions described in Sec. 2.4 assume that the bubble is spherically symmetric. The stability of these solutions against aspherical perturbations has important consequences for building plausible cosmologies inside a vacuum bubble. That there might be an instability in domain walls was first discussed by Adams, Freese and Widrow [36]. The bubble wall can trade volume energy for surface energy and wall kinetic energy locally as well as globally, and so the bubble wall will become distorted if different sections of the wall have different kinetic energies. As long as the local distortions of the wall remain small compared to the size of the background solution's radius, this process can be formulated quantitatively as perturbation theory around a background spherically symmetric solution.

Previous authors [36, 37, 38] have considered perturbations on zero mass expanding bubbles of true-vacuum, which can expand asymptotically. As was first pointed out by Garriga and Vilenkin [37], even though local observers on the bubble wall see perturbations grow, external observers see them freeze out because they do not grow faster than bubble radius.

The story is different for bubbles that reach a turning point, since the perturbations have a chance to catch up to the bubble's expansion and become nonlinear. Aside from the monotonic solutions 3–5, 14, and 15, all of the full time symmetric solutions discussed in Sec. 2.4 have a turning point⁶. This also presumably has implications for the thermal decay mechanism

⁶This includes the zero mass true and false vacuum bubble solutions. Perturbations (not necessarily aspherical) of the full time symmetric solution were found to be catastrophic in [27].

of Garriga and Megevand [32], depending on the duration of time the bubble wall sits in unstable equilibrium between expansion and collapse (see discussion in Sec. 2.4).

The remainder of this section will focus on the instability of the bound Solution 2, since physically plausible initial conditions may be clearly formulated. There is no obvious set of initial conditions for the perturbations on the unbound solutions, and so we simply observe that the results we will obtain for the bound solutions apply qualitatively here as well.

To simplify the problem, we assume that the full gravitational problem described in the previous sections can be treated as motion of the bubble wall in a fixed SdS background. This assumption must be validated (as we do below), but we are mainly interested in the low-mass bound solutions for which we might expect the gravitational contributions to be small. Assuming that a thin spherically symmetric bubble wall separates an internal dS from an external SdS spacetime, we can employ the action [36, 37, 38] :

$$S = -\sigma \int d^3\xi \sqrt{-\gamma} + \epsilon \int d^4x \sqrt{-g}, \quad (2.32)$$

where σ is the surface energy density on the bubble wall, γ_{ab} ($a, b = 1, 2, 3$) is the metric on the worldsheet of the bubble wall, ϵ is the difference in volume energy density on either side of the bubble wall:

$$\epsilon = \frac{\Lambda_+ - \Lambda_-}{8\pi}, \quad (2.33)$$

and $g_{\alpha\beta}$ is the metric of the background spacetime.

2.5.1 Wall Equation of Motion

The equation of motion resulting from Eq. 2.32 is [38]:

$$g^{ab} K_{ab} = -\frac{\epsilon}{\sigma}, \quad (2.34)$$

where K_{ab} is the extrinsic curvature tensor of the worldsheet of the bubble wall,

$$K_{ab} = -\partial_a x^\mu \partial_b x^\nu D_\nu n_\mu, \quad (2.35)$$

where D_ν is the covariant derivative and n_μ is the unit normal to the bubble wall worldsheet.

We will use the static foliation of the SdS spacetime (see Eq. A.68) as the coordinates x^μ for the background spacetime. The world sheet is given coordinates (τ, θ, ϕ) as in Eq. 2.1, and has metric:

$$\gamma_{ab} = g_{\mu\nu} \partial_a x^\mu \partial_b x^\nu, \quad (2.36)$$

with the gauge freedom in choosing τ fixed by

$$\frac{dt}{d\tau} \equiv t' = \frac{\sqrt{a_{\text{sds}} + R'^2}}{a_{\text{sds}}}, \quad (2.37)$$

so that $\gamma_{\tau\tau} = -1$. Here and henceforth primes will denote derivatives with respect to τ . The other non-zero components of γ_{ab} are $\gamma_{\theta\theta} = R^2$ and $\gamma_{\phi\phi} = R^2 \sin^2 \theta$.

The first task at hand is to find the worldsheet's unit normal, which by spherical symmetry has only R and t components. Requiring orthogonality to the worldsheet ($g_{\mu\nu} n^\nu \partial_a x^\mu = 0$) and unit norm ($g_{\mu\nu} n^\mu n^\nu = 1$) yields its components:

$$n_t = -R', \quad n_R = t'. \quad (2.38a)$$

The components of K_{ab} are given by

$$K_{\tau\tau} = \left[R'' + \frac{1}{2} \frac{da_{\text{sds}}}{dR} \right] (a_{\text{sds}} + R'^2)^{-1/2}, \quad (2.39a)$$

$$K_{\phi\phi} = -R a_{\text{sds}} t' \sin^2 \theta = K_{\theta\theta} \sin^2 \theta. \quad (2.39b)$$

Substituting Eq. 2.39 into Eq. 2.34 gives the equation of motion for the bubble wall:

$$R'' = \frac{\epsilon}{\sigma} \sqrt{a_{\text{sds}} + R'^2} - \frac{2}{R} (a_{\text{sds}} + R'^2) - \frac{1}{2} \frac{da_{\text{sds}}}{dR}. \quad (2.40)$$

Eq. 2.26 supplies the velocity of the bubble at some position along its trajectory

$$z' = [Q - V(z_0)]^{1/2}. \quad (2.41)$$

Choosing this boundary condition is effectively restricting ourselves to Solutions 1 and 2. Since the solutions to Eq. 2.40 approximate the dynamics of the junction condition problem, we should parametrize by A , B , and Q . This can be done by using the conversions defined in Sec. 2.3, and gives:

$$z'' = -\frac{3(B-A)}{c} \sqrt{a_{\text{sds}}(-Q) + z'^2} - \frac{2}{z} (a_{\text{sds}}(-Q) + z'^2) - \frac{(-Q)}{2} \frac{da_{\text{sds}}}{dz}, \quad (2.42)$$

where a_{sds} is written in terms of z as

$$a_{\text{sds}} = 1 - \frac{12}{cz(-Q)} - \frac{12A}{c^2(-Q)} z^2, \quad (2.43)$$

and

$$c \equiv [(A+B+3)^2 - 4AB]^{1/2}. \quad (2.44)$$

To justify the use of the simplified dynamics described above, Eq. 2.42 was numerically integrated, and the position of the turning point compared to the corresponding point on the full junction condition potential. Over the range of Q corresponding to the bound solutions, we find excellent quantitative agreement (well within 1%) between the turning points of the solutions to Eq. 2.42 and the junction condition potential. This was repeated with equally good results for the weak, GUT, and Planck scale potentials and also for various initial positions between the black hole radius and the potential wall (turning point). This shows that to zeroth order, dynamics as motion in a background is valid, and strongly suggests that it will be at higher orders as well.

2.5.2 Perturbation equations of motion

We are now in a position to discuss the first-order perturbations on the spherically-symmetric background solutions discussed in Sec. 2.5.1. Physical perturbations are normal to the worldsheet of the (background) bubble wall, and can be described by scalar field $\phi(x)$ by taking the position of the perturbed worldsheet to be

$$\bar{x}^\mu = x^\mu + \phi(x)n^\mu, \quad (2.45)$$

where x^μ is the spherically symmetric solution, and n^μ is the unit normal to the worldsheet. It is assumed that ϕ is much smaller than the bubble wall radius, so that a perturbative analysis can be made.

The equation of motion for the perturbation field $\phi(x)$ in a curved spacetime background can be derived from the action Eq. 2.32 after expanding to second order in $\phi(x)$ [38]

$$\Delta\phi - \left[-R_{\mu\nu}h^{\mu\nu} + R^{(3)} - \frac{\epsilon^2}{\sigma^2} \right] \phi = 0, \quad (2.46)$$

where

$$\Delta\phi = \frac{1}{\sqrt{-\gamma}} \partial_a (\sqrt{-\gamma} \gamma^{ab} \partial_b \phi), \quad (2.47)$$

and $h^{\mu\nu}$ is

$$h^{\mu\nu} = g^{\mu\nu} - n^\mu n^\nu. \quad (2.48)$$

To solve the equation of motion, we can decompose $\phi(x)$ into spherical harmonics

$$\phi(x) = \sum_{l,m} \phi_{lm}(\tau) Y_{lm}(\theta, \phi), \quad (2.49)$$

and separate variables to get an equation for $\phi_{lm}(\tau)$. The geometrical factors in Eq. 2.46 become dependent on θ or ϕ only at second order, so we will always be able to make this decomposition.

$\Delta\phi$ is then given by:

$$\Delta\phi_{lm} = - \left(\partial_\tau^2 + \frac{2R'}{R} \partial_\tau + \frac{l(l+1)}{R^2} \right) \phi_{lm}. \quad (2.50)$$

The components of $h^{\mu\nu}$ are:

$$h^{tt} = -\frac{a_{\text{sds}} + R'^2}{a_{\text{sds}}^2}, \quad h^{RR} = -R'^2, \quad (2.51a)$$

$$h^{\theta\theta} = h^{\phi\phi} \sin^2 \theta = \frac{1}{R^2}. \quad (2.51b)$$

The components of the Ricci tensor are given by:

$$R_{tt} = \frac{a_{\text{sds}}}{2} \partial_R^2 a_{\text{sds}} + \frac{a_{\text{sds}}}{R} \partial_R a_{\text{sds}} = -a_{\text{sds}}^2 R_{RR}, \quad (2.52a)$$

$$R_{\phi\phi} = R_{\theta\theta} \sin^2 \theta = (1 - a_{\text{sds}} - R \partial_R a_{\text{sds}}). \quad (2.52b)$$

Contracting equations 2.51 and 2.52 gives:

$$R_{\mu\nu} h^{\mu\nu} = \frac{2(1 - a_{\text{sds}})}{R^2} - \frac{3\partial_R a_{\text{sds}}}{R} - \frac{\partial_R^2 a_{\text{sds}}}{2} = 3\Lambda_+. \quad (2.53)$$

The Ricci scalar on the world sheet is

$$R^{(3)} = \frac{2}{R^2}(1 + R'^2 + 2RR''), \quad (2.54)$$

where R'' is given by Eq. 2.40.

After substituting Eq. 2.50, Eq. 2.53, and Eq. 2.54 into Eq. 2.46, the equation of motion for $\phi_{lm}(\tau)$ is

$$\begin{aligned} \phi_{lm}'' &= \left[\frac{\epsilon^2}{\sigma^2} - \frac{4\epsilon}{\sigma R} (a_{\text{sds}} + R'^2)^{1/2} + 3\Lambda_+ + \frac{2}{R} \frac{da_{\text{sds}}}{dR} + \frac{6R'^2}{R^2} \right. \\ &\quad \left. - \frac{2(1 - 4a_{\text{sds}})}{R^2} - \frac{l(l+1)}{R^2} \right] \phi_{lm} - \frac{2R'\phi_{lm}'}{R}. \end{aligned} \quad (2.55)$$

In terms of the dimensionless variables of the junction condition problem this reads:

$$\begin{aligned} \Phi_{lm}'' &= -\frac{2z'}{z} \Phi_{lm}' \\ &+ \left\{ \frac{108A}{c^2} + \frac{9(A-B)^2}{c^2} + \frac{12(B-A)}{cz} (a_{\text{sds}}(-Q) + z'^2)^{1/2} + \right. \\ &\quad \left. \frac{2(-Q)}{z^2} (4a_{\text{sds}} - 1) + \frac{6z'^2}{z^2} + \frac{2(-Q)}{z} \frac{da_{\text{sds}}}{dz} - \frac{l(l+1)(-Q)}{z^2} \right\} \Phi_{lm}, \end{aligned} \quad (2.56)$$

where Φ is the dimensionless perturbation field defined similarly to z (see Eq. 2.23). The first term acts as a (anti)drag on (shrinking) growing perturbations. The last term in this equation is always negative, acting as a restoring force. Perturbations will grow when the other terms (which are positive over most of the trajectory in the expanding phase) in this equation dominate. Further, the last term indicates that lower l modes will experience the largest growth. The full details of the solutions, however, require a numerical approach, to which we now turn.

2.6 Application to tunneling mechanisms

Classical trajectories exist on either side of the potential diagrams of Figs. 2.8, 2.9, 2.10, and 2.11, and so one can ask if there is any quantum process that connects two solutions of the same mass through the classically forbidden region under the potential. This would correspond to transitions from the bound spacetimes shown in Fig. 2.12 (Solutions 1 and 2) to the unbound spacetimes shown in Figs. 2.12 and 2.13 (Solutions 6-11). Such processes do seem to occur [20, 39, 40, 41, 42], at least within the framework of semi-classical quantum gravity, and we will discuss them in great detail in Chapter 4.

This problem has been investigated only under the assumption of spherical symmetry, which would be grossly violated if perturbations on the bubble wall before tunneling become nonlinear. In this section, we investigate the circumstances for which this is the case, under the assumption that the pre-tunneling spacetime is described by Solution 2, and that the tunneling event occurs at its turning point. The two basic questions at issue are: first, when do perturbations go nonlinear for some given set of initial perturbations, and second, what initial perturbations can be expected.

2.6.1 Dynamics of the Perturbation Field

Let us begin with the first issue. Since Eq. 2.56 is a second order ODE, it can be decomposed into the sum of two linearly independent solutions

$$\begin{aligned}\Phi_{\text{lm}}(T) &= \Phi_{\text{lm}}(T=0)f(l, z_0, Q, T) \\ &+ \Phi'_{\text{lm}}(T=0)g(l, z_0, Q, T).\end{aligned}\tag{2.57}$$

The functions $f(l, z_0, Q, T)$ and $g(l, z_0, Q, T)$ can be found numerically by alternately setting $\Phi_{\text{lm}}(T=0)$ and $\Phi'_{\text{lm}}(T=0)$ to zero, then evolving the coupled Eq. 2.56 and Eq. 2.42 numerically for a time T with initial conditions for Q , z_0 , and l . If the bubble is to tunnel, it will do so at the time T_{max} , when the bubble reaches its maximum radius and begins to re-collapse. Given f and g at time T_{max} , the size of the perturbations at the turning point for any z_0 , Q , l , $\Phi_{\text{lm}}(T=0)$, and $\Phi'_{\text{lm}}(T=0)$ can be determined. An RK4 algorithm with adaptive step size was used to solve for f and g , with numerical errors well within the 1% level.

The results of this analysis for $l = 1$ and for the low (weak) and intermediate (GUT) inflation scales discussed below Eq. 2.29 are shown in Fig. 2.17. The solid lines show contours of constant (log) amplification factor f (left) and g (right) versus the bubble starting radius z_0 and mass parameter Q , with bubble mass increasing toward the top. The shaded regions indicate regions which we have disallowed as bubble starting radii because the bubble would not be classically buildable for $R < R_{\text{BH}}$ (marked as $Q > Q_{\text{BH}}$), or the bubble is in the forbidden region $Q < V(z)$ of the effective 1D equation of motion Eq. 2.25, or the bubble would be too small to be treated classically. We choose the latter radius as fifty times the Compton wavelength z_{compton} of a piece of the bubble wall ⁷. The choice of fifty Compton wavelengths is rather arbitrary; the effect of a larger bound would be to exclude more of the parameter space in Fig. 2.17. This (unshaded) parameter space includes all classical initial conditions which could

⁷The mass of a piece of wall of scale s is $M \simeq s^2 \sigma$, where σ is the wall surface energy density; the Compton wavelength is then found by setting $M = s^{-1}$, yielding $s = z_{\text{compton}} \simeq \sigma^{-1/3}$.

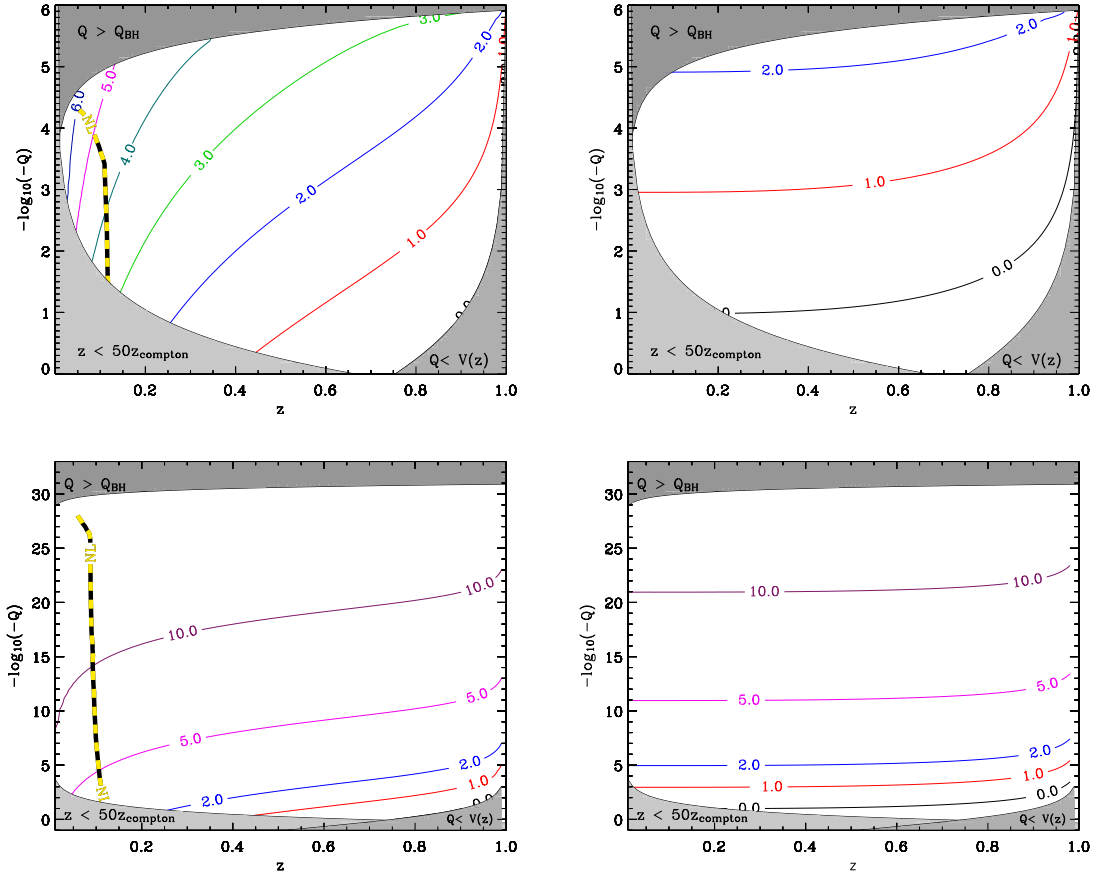


Figure 2.17: Contour plot of $\text{Log}_{10}[f(l = 1, z_0, Q, T_{\text{max}})]$ (left) and $\text{Log}_{10}[g(l = 1, z_0, Q, T_{\text{max}})]$ (right) for $M_I = 10^{14}$ GeV (top) and $M_I = 100$ GeV (bottom).

be set up by the observer in region I of the SdS conformal diagram.

It can be seen in Fig. 2.17 that the growth of the perturbations is in general larger for higher-mass bubbles (smaller $|Q|$, larger $-\log_{10}(-Q)$). The lower the inflation scale, the closer to zero the peak in the potential function becomes, and the smaller $|Q|$ (higher mass) bubbles are allowed, so at low inflation scales f and g can be very large. Growth for the Planck-scale inflation bubbles is very small, with f of order 10 and g of order 1, and is not plotted.

The enhanced growth at small $|Q|$ is due to the suppression of the term in Eq. 2.56 proportional to $l(l + 1)(-Q)$, which always acts to stabilize the perturbations. Another con-

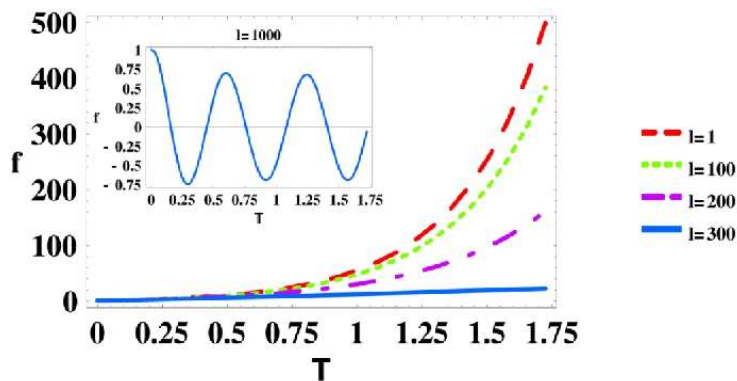


Figure 2.18: $f(l, z_0 = .5, Q = -10^{-4}, T)$ for various l . The inset shows the oscillatory behavior of f for large l .

sequence of this suppression is that the range in l over which solutions are unstable depends on Q ; as a general rule of thumb, approximately a few times $(-Q)^{-1/2}$ l -modes are unstable (note that this is unlike the case of zero mass bubbles, for which only the $l = 0, 1$ modes are unstable). An example of the f function for $Q = -10^{-4}$ with the intermediate (GUT) inflation scale parameters is shown in Fig. 2.18. The f functions for very large l modes are stable and approach sinusoids with amplitudes less than one (see the inset of Fig. 2.18), meaning that the perturbations are never larger than their initial size.

2.6.2 Initial Conditions and Evolution to the Turning Point

Having fully characterized the growth of the perturbations, we now require an estimate for their initial values when the bubble is formed. There is no reason to expect that a region of false vacuum will fluctuate into existence with anything near spherical symmetry, nor is it likely to have thin walls (there is no instanton or other mechanism to enforce these symmetries). Since low- l (relative to $(-Q)^{-1/2}$) modes are unstable, an initially aspherical bubble will only become more aspherical; this is in marked contrast to zero mass true vacuum bubbles, which both start spherical, and tend to become more spherical as they expand.

Suppose, however, that we consider the best-case scenario in which a bubble *is*, by chance or design, spherically symmetric. It will nevertheless inevitably be dressed with zero-point quantum fluctuations of the perturbation field. We may then check whether these fluctuations alone, considered as initial values for the perturbations of a bubble starting with a given Q and z_0 , suffice to make the bubble nonlinearly aspherical by turnaround.

We assume that the ensemble average of the quantum fluctuations at the time of nucleation is zero; but the ensemble average of the square of the field (the space-like two-point function $\langle \Phi(\theta, \phi)\Phi(\tilde{\theta}, \tilde{\phi}) \rangle \equiv \langle \Phi\tilde{\Phi} \rangle$) will not generally vanish. We can write the mode functions (Eq. 2.49) in terms of it as:

$$\langle \Phi_{lm}^2 \rangle = \int d\Omega d\tilde{\Omega} \langle \Phi\tilde{\Phi} \rangle Y_{lm}(\theta, \phi) Y_{lm}^*(\tilde{\theta}, \tilde{\phi}). \quad (2.58)$$

By spherical symmetry, the two-point function can be written as a function of the angular separation Ψ between (θ, ϕ) and $(\tilde{\theta}, \tilde{\phi})$, and decomposed into Legendre polynomials:

$$\langle \Phi\tilde{\Phi} \rangle = \sum_l C_l P_l(\cos \Psi). \quad (2.59)$$

Using the addition theorem for spherical harmonics, we can write this as

$$\langle \Phi\tilde{\Phi} \rangle = \sum_{l', m'} \frac{4\pi}{2l'+1} C_{l'} Y_{l'm'}^*(\theta, \phi) Y_{l'm'}(\tilde{\theta}, \tilde{\phi}). \quad (2.60)$$

Substituting this into Eq. 2.58 and using the orthogonality of the spherical harmonics yields the relation:

$$\langle \Phi_{lm}^2 \rangle = \frac{4\pi C_l}{2l+1}. \quad (2.61)$$

Given some space-like two point function at the time the bubble is nucleated, we can obtain the C_l from

$$C_l = \frac{2l+1}{4\pi} \int_{-1}^1 d(\cos \Psi) \langle \Phi\tilde{\Phi} \rangle P_l(\cos \Psi) \quad (2.62)$$

and therefore set the typical initial amplitudes of the mode functions as the r.m.s. value $\langle \Phi_{lm}^2 \rangle^{1/2}$ from Eq. 2.61. The velocity field can be decomposed into spherical harmonics just as Φ was,

and the analysis performed above carries over exactly. The typical initial size of the velocity mode functions is then given by

$$\langle \Phi_{1m}'^2 \rangle = \frac{4\pi A_l}{2l+1}. \quad (2.63)$$

with

$$A_l = \frac{2l+1}{4\pi} \int_{-1}^1 d(\cos \Psi) \langle \Phi' \tilde{\Phi}' \rangle P_l(\cos \Psi). \quad (2.64)$$

The initial amplitudes in Eq. 2.61 and Eq. 2.63 can now be evolved to the turning point, and the mode functions re-summed. The ensemble average of the r.m.s. fluctuations in Φ at any time at a given point will then be:

$$\begin{aligned} \langle \Phi(T)^2 \rangle &= \sum_l \frac{2l+1}{4\pi} \langle \Phi_{1m}(T)^2 \rangle \\ &= \sum_l \left[C_l^{1/2} f(l, z_0, q, T) + A_l^{1/2} g(l, z_0, q, T) \right]^2, \end{aligned} \quad (2.65)$$

which can be evaluated at $T = T_{\max}$.

A full model of the two-point functions $\langle \Phi \tilde{\Phi} \rangle$ and $\langle \Phi' \tilde{\Phi}' \rangle$ would involve quantizing the mode functions on the curved spacetime of the bubble wall worldsheet, which has a metric depending on $z(T)$. Further, to treat large fluctuations, we would need to include non-linear terms in the equation of motion. The exact two-point function is therefore a rather formidable object to compute. As a simplified model, we will employ the two-point functions of a massless scalar field in flat spacetime, and replace the spatial distance r with the distance along the bubble wall $r_0 \Psi$. This massless scalar corresponds to the perturbations on a flat wall separating domains of equal energy density in Minkowski space [43]. Corrections to this picture in the presence of curvature should be small over small regions of the bubble wall. We are also neglecting the large difference in energy densities across the bubble wall, which will give the field a (negative) mass to first order. The apparent divergence of the correlator due to this negative mass will be rendered finite by the non-linear terms which must be introduced to discuss large fluctuations.

In light of all these difficulties, and several more approximations we will make below, this should be considered as a first, rough estimate of the amplitude of the quantum fluctuations on the bubble at the time of nucleation.

The space-like two-point function in Minkowski space at large separations is given by

$$\langle \phi(\mathbf{x})\phi(\mathbf{y}) \rangle = \frac{\sigma^{-1}}{4\pi r}, \quad (2.66)$$

where $r \equiv |\mathbf{x} - \mathbf{y}|$. As in the work of Garriga and Vilenkin [43], we introduce a smeared field operator to obtain a well-defined answer at close separations

$$\phi_s \equiv \frac{1}{\pi s^2} \int_{|\mathbf{y}-\mathbf{x}|<s} d^2 y \phi(\mathbf{y}), \quad (2.67)$$

where s is a smearing length, chosen to be the Compton wavelength $s = \sigma^{-1/3}$ of a piece of wall, which is a physically reasonable lower bound on the size of a measurable region. The smeared correlator will then be given by

$$\langle \phi_s(\mathbf{x})\phi_s(\mathbf{y}) \rangle = \frac{1}{\pi^2 s^4} \int_{|\mathbf{z}-\mathbf{x}|<s} d^2 z \int_{|\mathbf{q}-\mathbf{y}|<s} d^2 q \langle \phi(\mathbf{z})\phi(\mathbf{q}) \rangle, \quad (2.68)$$

which evaluates at $\mathbf{x} = \mathbf{y}$ to

$$\langle \phi_s^2 \rangle = \left(\frac{1}{2} + \mathcal{G}\right) \sigma^{-2/3}, \quad (2.69)$$

where $\mathcal{G} = .916\dots$ is Catalan's constant. We have been unable to integrate Eq. 2.68 to obtain the exact form of the smeared two-point function for all r . However, it must smoothly interpolate between the value at $r = 0$ in Eq. 2.69 to the functional form at $r \gg s$ given by Eq. 2.66. We therefore employ the following 'toy model' smeared field correlator

$$\langle \phi(\mathbf{x})\phi(\mathbf{y}) \rangle = \frac{\sigma^{-1}}{4\pi s} \left[(2\pi + 4\pi\mathcal{G} - 1) e^{-r^2/2s^2} + \frac{1}{r/s + 1} \right], \quad (2.70)$$

which has the correct asymptotics. With $r = r_0\Psi$, the dimensionless form of the toy correlator is given by:

$$\langle \Phi\tilde{\Phi} \rangle = \frac{(-Q)}{(24\pi)^2} \left[(2\pi + 4\pi\mathcal{G} - 1) e^{-(\xi^2/2)\Psi^2} + \frac{1}{\xi\Psi + 1} \right], \quad (2.71)$$

where $\xi \equiv r_0/s$.

The velocity-velocity correlator can be calculated using the Hamiltonian approach. For spacelike separations, this is given by

$$\begin{aligned}\langle \phi'(\mathbf{x})\phi'(\mathbf{y}) \rangle &= \sigma^{-1} \int \frac{|p|d^2p}{2(2\pi)^2} \exp[i\mathbf{p}(\mathbf{x} - \mathbf{y})] \\ &= \sigma^{-1} \int_0^\Lambda \frac{dp}{4\pi} p^2 J_0(pr)\end{aligned}\tag{2.72}$$

where we have introduced a hard momentum cut-off Λ to obtain a finite answer. This cutoff will correspond to the inverse smearing length, with higher momentum scales accounted for in the smeared operator. The integral can be evaluated in terms of generalized hypergeometric functions as

$$\langle \phi'(\mathbf{x})\phi'(\mathbf{y}) \rangle = \frac{\Lambda^3 \sigma^{-1}}{12\pi} {}_1F_2\left(\frac{3}{2}; 1, \frac{5}{2}; -\frac{\Lambda^2 r^2}{4}\right).\tag{2.73}$$

At close separations, we construct a smeared operator ϕ'_s . The expectation value of this operator at zero separation is

$$\langle \phi'^2_s \rangle = \frac{\log(64) + 2\gamma - 4}{2\pi^2},\tag{2.74}$$

where $\gamma = .577\dots$ is the Euler-Mascheroni constant. Smoothly connecting the small r (Eq. 2.74) and large r (Eq. 2.73) behavior as in Eq. 2.70, the Φ' (defined similarly to z') correlator on the bubble at the time of nucleation is:

$$\begin{aligned}\langle \Phi'\tilde{\Phi}' \rangle &= \frac{(-Q)}{12\pi} \left[{}_1F_2\left(\frac{3}{2}; 1, \frac{5}{2}; -\frac{\xi^2 \Psi^2}{4}\right) \right. \\ &\quad \left. + \left(\frac{12\gamma - 6\log(64) - 24}{\pi} - 1\right) e^{-(\xi^2/2)\Psi^2} \right]\end{aligned}\tag{2.75}$$

The integrals Eq. 2.62 and Eq. 2.64 for the correlators Eq. 2.71 and Eq. 2.75 must be evaluated numerically. Calculation of the coefficients for every l and ξ is unfortunately unfeasible because of the highly oscillatory behavior of the integrands and sheer number of mode functions that must be considered. However, we have been able to deduce sufficiently good approximate

fits for C_l and A_l as a function of both l and ξ . In both cases, the power is dominated by a peak at $l \simeq \xi$.

The C_l are nicely fit by the function

$$C_l = \frac{(-Q)}{(24\pi)^2} \frac{83}{100} \frac{\sqrt{2}l + 1}{\sqrt{2}\xi + 1} \exp \left\{ \frac{-1}{4\xi^2 - 2} \left[(\sqrt{2}l + 1)^2 - (\sqrt{2}\xi + 1)^2 \right] \right\}. \quad (2.76)$$

The proposed fit for the A_l consists of two power laws matched at the $\xi = l$ peak. For $l \leq \xi$, the best fit is $A_l = (-Q)l^{5/4}/(10\xi^{9/4})$ and for $l > \xi$, the fit is $A_l = 3(-Q)\xi^{1.8}/(200l^{2.6})$. Because these power law indices are slightly uncertain, we only count the modes with $l \leq \xi$ in the A_l . This is conservative, and also justified because these modes will not contribute significantly to the sum in Eq. 2.65.

With these initial conditions, we can now evolve each mode function using Eq. 2.57 and then re-sum in Eq. 2.65 to find the average size of the fluctuations at the turning point. We have calculated f and g up to the l corresponding to the last unstable mode of the smallest $|Q|$, for all three inflation scales ($M_I = 100$ GeV, $M_I = 10^{14}$ GeV, and $M_I = 10^{17}$ GeV). The results for weak- and GUT-scale inflation are shown in Fig. 2.17, where the dotted line indicates the boundary of the region over which the perturbations become non-linear (non-linear to the left of the line). It can be seen that in this model, even just quantum perturbations of the bubble wall grow nonlinear in bubbles that start at radii less than about one-tenth of the turnaround radius; this grossly violates the assumption of spherical symmetry used in tunneling calculations. On the other hand, none of the parameter space in the high inflation scale case went non-linear, and at all scales there is *always* a region of initial bubble radii near the turnaround radius, for which nonlinearity never occurs.

2.6.3 Thick Walls and Radiation

Just as we have no reason to expect a fluctuated region to be spherically symmetric, we have no reason to assume that it will have thin walls. An analysis of thick-walled true vacuum bubbles was undertaken in Ref. [43, 44], where it was found that the instabilities found in thin-walled case are still present in the form of deformations normal to the bubble profile. In the case of small false vacuum bubbles, there is no obvious consideration (such as a corresponding instanton) to supply the profile of the bubble wall, and so we can merely conjecture by precedent that the instability would be retained in the thick-walled case as well.

Another consideration, applying to bubbles smaller than the false vacuum horizon size, is whether inflation is spoiled by non-vacuum contributions to the energy density. The perturbations on the bubble wall translate into gravitational waves [45, 46], and since the bound bubble solutions remain relatively close to their gravitational radius and become distorted over many different length scales on a relatively short time scale (see the quasi-exponential growth in Fig. 2.18), they will be emitters of copious gravitational radiation. Another problem arises if the kinetic and gradient energy of the field becomes appreciable in the bubble interior, either from intrusion of the wall (for example, imagine a bubble being pinched in half by some non-linear perturbation), or from particle production or other scalar modes propagating in from the wall. If the emission of energy into the interior of the bubble from any combination of these modes makes a significant contribution to the equation of state, then inflation will not occur.

2.7 Conclusions

In this chapter we have examined the classical dynamics and instability of thin wall vacuum bubbles. We first outlined the construction of bubbles which have zero mass, considering positive, negative, and zero cosmological constant in the interior and exterior. The causal

structure of these spacetimes was presented, and in the case of junctions between two de Sitter spaces, the matching was demonstrated in a number of different coordinate systems. In the case of junctions between a positive or zero cosmological constant exterior and a negative cosmological constant interior, we demonstrated the existence of a static domain wall solution, and found that the measurable entropy of any observer entering the bubble is bounded. These results will be applied further in Chapter 3

We then used the Israel Junction conditions to classify all allowed matchings between a de Sitter interior and Schwarzschild de Sitter exterior. A total of 17 qualitatively different solutions were found of four basic types: bound, unbound, monotonic, and static. These allowed junctions included a number of bubble solutions discussed in previous literature. For instance, zero mass bubbles correspond to the lorentzian continuation of the Coleman-de Luccia [12] true vacuum and Lee-Weinberg [13] false vacuum bubbles. On the other end of the mass spectrum, we have found that static solutions correspond to the lorentzian continuation of the thermal activation mechanism [32].

Examining these classical solutions, we have shown that an instability to linear aspherical perturbations exists in those solutions which possess a turning point. This includes the bound (solutions 1 and 2), unbound (solutions 6-13), and static solutions (solutions 16 and 17). For the unbound case, there is no clear way to set an initial radius or initial perturbation amplitude, so we can say only that collapsing bubbles are violently unstable. Static solutions will be similarly unstable, though the details depend on how long the wall remains in unstable equilibrium between expansion and collapse. The bound solutions are amenable to quantitative investigation, and we have focused on the growth of perturbations in the expanding phase. This evolution precedes a possible tunneling mechanism between bound and unbound solutions, which we will discuss in more detail in Chapter 4.

For bound expanding bubbles formed by the fluctuations of a scalar field in de Sitter

space, there is no instanton to enforce spherical symmetry, so we would expect initial aspherical perturbations to be relatively large. Since there is no detailed model for the fluctuating scalar field to see *how* large, we have instead calculated an estimate of the minimal deviations from spherical symmetry in light of quantum fluctuations, and present this as an extremely rare, best case scenario for spherical symmetry. These minimal fluctuations were then evolved to the turning point of the bound solutions, which is the point where there is a chance for tunneling to an unbound solution to occur. Of the three representative energy scales for false vacuum energy densities (imagined to correspond to the scale of inflation occurring inside a bubble) we have studied, the evolved minimal perturbations on a Planck scale bubble remain small over most of the allowed parameter space, while the perturbations on GUT and weak scale bubbles can grow nonlinear if they start at a sufficiently small ($\sim 10\%$) fraction of the turnaround radius. Thus even in the best-case scenario some bubbles become nonlinear, but on the other hand there will always in principle be some that do not.

Chapter 3

Tunneling: Zero Mass

3.1 Introduction

In this chapter, we will consider a scalar field theory with a potential possessing two minima, one corresponding to a high energy false vacuum and one corresponding to a lower energy true vacuum. An example of such a potential is shown in Fig. 3.1. It was shown long ago by Coleman and collaborators [10, 12] that the false vacuum will in many cases decay to the true vacuum. This proceeds by the nucleation of bubbles of true vacuum in the background false vacuum, and the nucleation rate can be calculated by solving the coupled Euclidean Einstein and scalar field equations under the assumption of $O(4)$ symmetry with the appropriate boundary conditions. It was later conjectured by Lee and Weinberg [13] that the reverse process could occur as well: the nucleation of false vacuum bubbles in a background of true vacuum.

When the scalar field potential satisfies a set of criteria, the nucleated bubble will have a wall which is thin compared to its total radius. The vacuum energy will undergo a sharp jump as one moves through the wall. When this thin-wall approximation is valid, the bubble wall radius becomes a collective coordinate for the bubble configuration, and the Euclidean Israel

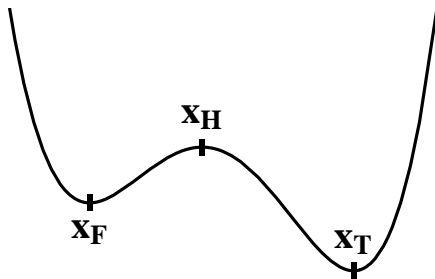


Figure 3.1: The potential $V(\phi)$, with the true vacuum x_T , the false vacuum x_F and the “Hawking-Moss” point x_H labeled.

junction conditions for a thin shell can be used to construct the instanton. The nucleation of true and false vacuum bubbles in this picture corresponds to the quantum tunneling of the bubble wall from zero radius to the radius of the critical bubble configuration, which provides the initial data for the subsequent lorentzian evolution.

In a recent paper [15], a picture of a large class of eternal inflation models was presented that greatly simplifies their analysis by viewing the eternally inflating universe as a finite system comprised of the causal diamond of a single observer.

This picture, which has consequences for the Landscape idea as well as for models of low-energy supersymmetry breaking, both suggested and gained support from an interesting new result in the dynamics of true-vacuum bubble nucleation as described by Euclidean instanton techniques. In particular, it was found that in a certain class of potentials, the instanton action for a transition from positive (false) to negative (true) vacuum energy did *not* tend to infinity as the false vacuum energy V_F was reduced to zero, as would be required to give a finite nucleation probability¹ and hence accord with intuition regarding the decay of Minkowski space to a negative vacuum (“big crunch”) space. This result was supported by general analytic arguments, as well as numerical results for $\epsilon \sim 1$, where ϵ controls the scale in field value over

¹As $V_F \rightarrow 0$, the required background subtraction becomes infinite, requiring an infinite instanton action to cancel it and leave a finite decay probability.

which the potential varies. On the basis of these results it was conjectured that

1. The same behavior holds at $\epsilon \ll 1$, and
2. for $V_F \equiv 0$, a second (non-compact) instanton, like the one found in the absence of gravity, exists which allows much faster decay, so that
3. for all ϵ there is a discontinuity in the decay rate as $V_F \rightarrow 0$.

We will demonstrate that while the specific calculations presented in [15] are correct, the above conjecture is not². Instead we find that the space of potentials is partitioned by a *Great Divide*, into one class where Minkowski space is unstable, and a second class where the tunneling rate is indeed suppressed – as argued in [15] – by the factor $e^{-\pi(RM_F)^2}$ (where R is the de Sitter radius corresponding to the false vacuum), and hence vanishes at $V_F = 0$. The stability, for some potentials, of a seemingly metastable Minkowski vacuum was noted long ago by Coleman and De Luccia [12] in the thin-wall limit and subsequently discussed by several authors [48, 49] outside of that limit.

In Sections 3.2–3.4 we will review the instanton formalism, give approximate analytic solutions, then examine the behavior of the instanton solutions in the limit where $V_F \rightarrow 0$, using both analytic and numerical techniques. After elucidating the actual behavior of the instantons, we will argue in Sec. 3.5 that the Great Divide consists precisely of those potentials which, in the $V_F \rightarrow 0$ limit, have static domain walls interpolating between the true and false stationary points of the potential³; we also argue that the Great Divide is appropriately named because its codimension in the space of potentials is one. In Sections 3.5 and 3.6, we will discuss our results in connection with the picture of eternal inflation put forward in [15]. In Sec. 3.6, we will argue that it is inappropriate to think of potentials describing unstable Minkowski space as having

²R. Bousso, B. Freivogel and M. Lippert, have discovered this fact independently [47].

³This observation is related to the work of Cvetic et. al. on singular domain walls and their relation to CDL bubbles [50, 51, 52, 53]

to do with quantum gravity in asymptotically flat space, then discuss what they may, instead, correspond to. In Sec. 3.7, we comment on the implications of potentials above the Great Divide for the string theory landscape. A brief summary of our conclusions is given in Sec. 3.8.

3.2 CDL Formalism

3.2.1 Neglecting gravity

We will begin by briefly reviewing the formalism for constructing Euclidean instantons describing the nucleation of true vacuum bubbles in a false vacuum background. True vacuum bubbles will in general be of micro-physical size, and so, neglecting the vacuum energy of the field, it is appropriate to neglect the backreaction of the scalar field on the spacetime as a first approximation [10]. In this case, one looks for solutions to the Euclidean equation of motion which go from the false vacuum to the basin of attraction of the true vacuum in infinite Euclidean time. Under the assumption of $O(4)$ invariance, the field is a function of the Euclidean radius, $\rho^2 = \mathbf{x}^2 + t^2$, alone and has the equation of motion

$$\phi'' + \frac{3}{\rho}\phi' = \frac{dV}{d\phi} \quad (3.1)$$

The boundary conditions on the field are

$$\phi(\rho \rightarrow \infty) = \phi_F, \quad \phi(\rho = 0) = \phi_0 \simeq \phi_T \quad \left. \frac{d\phi}{d\rho} \right|_{\rho=0} = 0 \quad (3.2)$$

essentially specifying that the field is in the true vacuum only in a very localized region, and as one goes to large distances/times the false vacuum remains undisturbed by the nucleation event.

The decay probability per unit 4-volume of the false vacuum is given by

$$\Gamma = Ae^{-S_E}, \quad (3.3)$$

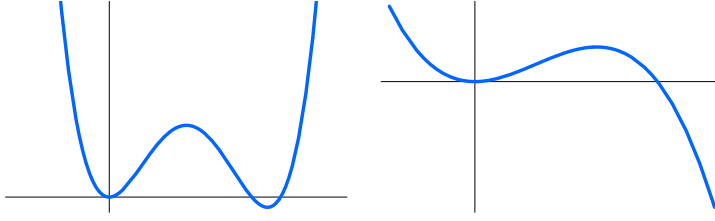


Figure 3.2: Shown on the left is a potential which satisfies the thin-wall approximation. Shown on the right is a potential which satisfies the deep-well approximation.

where S_E is the Euclidean action of the field configuration that interpolates between the true and false vacuum wells, and A is a pre-factor that encodes the first quantum corrections. Under the assumption of $O(4)$ invariance, the euclidean action is given by

$$S_E = 2\pi^2 \int_0^\infty d\rho \rho^3 \left[\frac{\phi'^2}{2} + V \right]. \quad (3.4)$$

The pre-factor is a functional determinant, given by [11]

$$A = \left(\frac{S_E}{2\pi} \right)^2 \left(\frac{\det' [-\square + V''(\phi)]}{\det [-\square + V''(\phi_F)]} \right)^{-1/2}, \quad (3.5)$$

where \det' indicates that the determinant should be computed with the zero modes omitted (there are 4 in this case, corresponding to the 4 possible translations in Euclidean space). The prefactor has mass-dimension 4, and is calculated using quantities such as $R_0, |\phi_F - \phi_T|, V''$ (which will in general lie within an order of magnitude of one another [54] for "typical" values over the instanton), and so we can roughly estimate it to be

$$A \sim O(R_0^{-4}, |\phi_F - \phi_T|^4, V''^2). \quad (3.6)$$

It is also possible to calculate the prefactor numerically [55], yielding an exact expression for Eq. 3.3.

3.2.2 Thin-wall approximation: without gravity

In the limit where the size of the bubble is much larger than the thickness of the wall, we can find an approximate solution to the Euclidean equations of motion. This will occur for potentials with $|V_F - V_T| \ll 1$, as in the example on the left of Fig. 3.2. The Euclidean action and critical radius for the nucleation of a thin-wall bubble are given by

$$S_E = \frac{27\pi^2\sigma^4}{2(V_F - V_T)^3}, \quad R_0 = \frac{3\sigma}{V_F - V_T} \quad (3.7)$$

where the surface tension σ is

$$\sigma = \int_{\phi_0}^{\phi_F} d\phi \sqrt{2(V(\phi) - V(\phi_F))} = 2 \int d\rho (V(\phi) - V(\phi_F)). \quad (3.8)$$

At non-zero temperature T , in the limit where $T \gg R_0^{-1}$, the Euclidean action and critical radius for bubble nucleation are given by [54]

$$S_E = \frac{16\pi\sigma^3}{3(V_F - V_T)^2 T}, \quad R_0 = \frac{2\sigma}{V_F - V_T} \quad (3.9)$$

3.2.3 Deep-well approximation: without gravity

In the limit where the true vacuum well is very deep, we can approximate the potential around the barrier and false vacuum minimum as

$$V(\phi) = \frac{M}{2}\phi^2 - \frac{\delta}{3}\phi^3. \quad (3.10)$$

An example of such a potential is shown on the right of Fig. 3.2. It is possible to obtain an exact solution to the Euclidean field equation for this potential [54], which yields an action of

$$S_E \simeq 205 \frac{M^2}{\delta^2} \quad (3.11)$$

For non-zero temperature, with $T \gg M$, the Euclidean action can be written as

$$B \simeq 44 \frac{M^3}{\delta^2 T}. \quad (3.12)$$

3.2.4 Including gravity

With the inclusion of gravity, the nature of the problem changes drastically. One must now solve the coupled Euclidean scalar field and Einstein equations for solutions that travel between the basins of attraction of the minima at ϕ_T and ϕ_F . Again, assuming $O(4)$ invariance, the instanton is described by an Euclidean manifold of the form

$$ds^2 = dz^2 + \rho^2(z)d\Omega^2, \quad (3.13)$$

where $d\Omega^2$ is the surface element of a unit 3-sphere. The equations of motion are given by

$$\phi'' + \frac{3\rho'}{\rho}\phi' = \frac{dV}{d\phi}, \quad (3.14)$$

$$\rho'^2 = 1 + \frac{8\pi}{3}\rho^2 \left(\frac{\phi'^2}{2} - V \right). \quad (3.15)$$

The nucleation probability is still given by Eq. 3.3. The total Euclidean action, S_E , is the difference between the action of the instanton, S_I , (which is negative due to the positive curvature of the instanton) and the action of the background spacetime, S_{BG} (which is negative and larger in magnitude than the instanton action)

$$S_E = S_I - S_{BG}. \quad (3.16)$$

The instanton action is given by

$$S_I = 4\pi^2 \int dz \left(\rho^3 V - \frac{3\rho}{8\pi} \right). \quad (3.17)$$

The background subtraction term (for an end-point of the evolution in x near x_F) is given by

$$S_{BG} = -\frac{3}{8V_F}. \quad (3.18)$$

When the true or false vacuum has zero energy density, the manifold is noncompact:

$$\begin{aligned} \rho(z=0) = 0, \quad \rho(\infty) = \infty, \quad \dot{\phi}(z=0) = 0, \quad \dot{\phi}(\infty) = 0, \\ \phi(z=0) = \phi_0 \simeq \phi_{F,T}, \quad \phi(\infty) = \phi_{T,F}. \end{aligned} \quad (3.19)$$

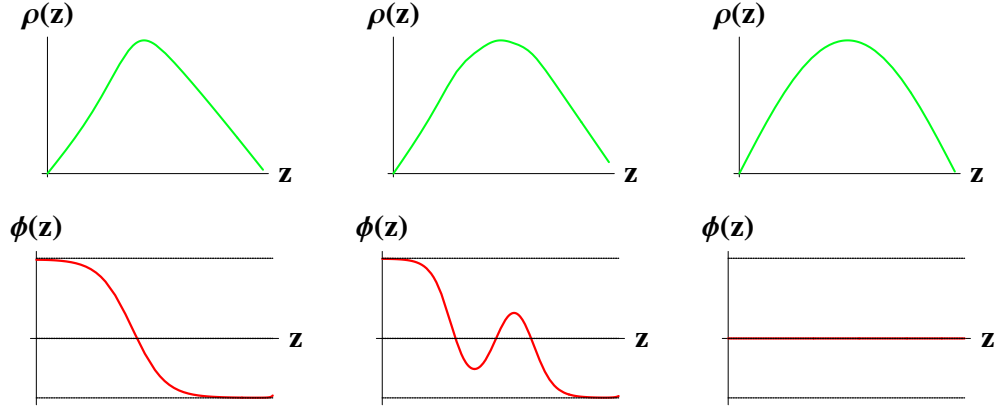


Figure 3.3: The evolution of $\rho(z)$ (top) and $\phi(z)$ (bottom) for a single-pass (left), multiple-pass (center), and Hawking-Moss (right) instanton.

where the initial conditions at $z = 0$ are set near the vacuum with *non-zero* energy density.

When the false vacuum has positive energy density, we can consider a positive or negative energy true vacuum. In either case the Euclidean manifold Eq. 3.13 is necessarily compact, spanning an interval between $z = 0$ and $z = z_{max}$. The solution must then satisfy

$$\begin{aligned} \rho(z = 0) = 0, \quad \rho(z_{max}) = 0, \quad \dot{\phi}(z = 0) = 0, \quad \dot{\phi}(z_{max}) = 0, \\ \phi(z = 0) = \phi_0 \simeq \phi_T, \quad \phi(z_{max}) = \phi_e \simeq \phi_F. \end{aligned} \quad (3.20)$$

Solutions with two zeros in $\dot{\phi}$ will be referred to as “single-pass” instantons. An example of the evolution in is shown in the left cell of Fig. 3.3. It is also possible to have a number of other qualitatively different solutions to the field equations with the above boundary conditions. The Hawking-Moss instanton [56] is the solution where the field remains at the maximum of the potential (with $\dot{\phi} = 0$) over the entire evolution between $z = 0$ and $z = z_{max}$. This is shown in the right cell of Fig. 3.3. The solution for $\rho(z)$ is

$$\rho(z) = \left(\frac{8\pi}{3}V_H\right)^{-1/2} \sin \left[\left(\frac{8\pi}{3}V_H\right)^{1/2} z \right], \quad (3.21)$$

where V_H is the value of the maximum of the potential (the Hawking-Moss point indicated in

Fig. 3.1). The instanton action is

$$S_I^H = \frac{3}{8V_H} \quad (3.22)$$

The physical interpretation of this instanton is the fluctuation of a horizon-sized region up to the top of the potential [57] from either the true or false vacuum minima. The field is then left in an unstable equilibrium, and after the Euclidean instanton is analytically continued, it will roll down to one of the wells. In this sense, the Hawking-Moss instanton can be thought of as mediating a transition between the true and false vacuum wells.

There are also solutions with more than two zeros in $\dot{\phi}$. We will refer to these as multiple-pass instantons [58]. An example is shown in the middle panel of Fig. 3.3. The interpretation of these instantons is rather unclear (having to do with the number of negative modes in fluctuations about the semiclassical solution), but it can be shown that their Euclidean action is always larger than the single-pass instanton.

In the remainder of this chapter, we will study a single scalar field, with a potential that scales with two dimensionful constants M and μ :

$$V(\phi) = \mu^4 v(\phi/M), \quad (3.23)$$

The general scaling form of the potential is motivated by considerations of naturalness. Typical potentials which cannot be fit into this form have fine-tuned dimensionless coefficients and are not stable to radiative corrections.⁴

Defining the following dimensionless variables:

$$x \equiv \phi/M, \quad (3.24)$$

$$r \equiv \frac{\mu^2 \rho}{M}, \quad (3.25)$$

⁴The major exception we know of is the case of moduli in string theory near singular points in moduli space: while the typical potential for moduli depends on ϕ/m_P or ϕ/m_S , near singular points (where other degrees of freedom become light) the potential can have more rapid variation.

$$s \equiv \frac{\mu^2 z}{M}, \quad (3.26)$$

$$\epsilon^2 \equiv \frac{8\pi M^2}{3M_P^2}, \quad (3.27)$$

the coupled Euclidean scalar field and Einstein's equations are

$$\ddot{x} + \frac{3\dot{r}}{r}\dot{x} + u' = 0, \quad (3.28)$$

$$\dot{r}^2 = 1 + \epsilon^2 r^2 E, \quad (3.29)$$

where $u(x) \equiv -v(x)$, primes and dots, respectively, refer to x - and s -derivatives, and E is the Euclidean energy of the field, defined as

$$E = \frac{1}{2}\dot{x}^2 + u(x). \quad (3.30)$$

For future reference, the dynamics of the Euclidean energy are determined by the equation

$$\dot{E} = -3\frac{\dot{r}}{r}\dot{x}^2. \quad (3.31)$$

For compact instantons, there will be a non-singular solution to the Euclidean equations of motion if the boundary conditions (equivalent to Eq. 3.20)

$$r(0) = 0, \quad r(s_{max}) = 0, \quad \dot{x}(0) = 0, \quad \dot{x}(s_{max}) = 0, \quad (3.32)$$

can be met for some set of endpoints in the evolution of x near x_T and x_F . We also note [49] that multifield models can be studied using these methods as well, as long as we restrict attention to instantons for which $\dot{\phi}^i = 0$ only at two points. In that case, however, one might be interested in potentials with more minima and maxima.

In terms of the dimensionless variables, the instanton action is given by

$$S_I = -4\pi^2 \left(\frac{M^4}{\mu^4} \right) \int_{s=0}^{s=s_{max}} ds \left(r^3 u + \frac{r}{\epsilon^2} \right). \quad (3.33)$$

The background subtraction term (for an end-point of the evolution in x near x_F) is given by

$$S_{BG} = \frac{8\pi^2}{3\epsilon^4 u_F}. \quad (3.34)$$

Returning to the equations of motion, we can attempt to determine how including gravitational effects has changed the calculation of the instanton action. Most importantly, the set of boundary conditions that must be satisfied is completely different than in the non-gravitational problem. Since we are solving for both the (compact) geometry and the field configuration, it is impossible to impose a constraint on the solution which says that asymptotically far away from the nucleation event, the field remains undisturbed in the false vacuum. Indeed, since the instanton does not interpolate exactly between the true and false vacuum minima, there is *no* part of the instanton which is in either the true or false vacuum states. Since the true vacuum bubbles are typically of microphysical size, one can approximately apply the zero-gravity picture of a small nucleated bubble whose walls asymptotically approach the speed of light. However, when one works outside the thin-wall limit [59] or considers the nucleation of false vacuum bubbles, this picture becomes misleading.

3.2.5 Thin-wall approximation including gravity

If the field makes the transition between the basins of attraction in a relatively (to the entire range of z) short span of z , the wall will be thin. In this limit, the field must loiter near the true and false vacuum maxima, during which time the solution for $\rho(z)$ will be given by

$$\rho(z) = H_F^{-1} \sin(H_F z); \quad z < z^* \tag{3.35}$$

$$\rho(z) = H_T^{-1} \sin(H_T z); \quad z > z^* \tag{3.36}$$

where z^* denotes the value of z at which the bubble wall (the transition region between the wells) is located. We therefore see that the instanton is constructed in the thin wall limit by matching two four-spheres across the bubble wall (for example, see [60, 13, 61, 12]).

We can understand this geometry by looking at the CDL instanton embedded in 5D Euclidean space. Since in the thin-wall limit the instanton is composed of de Sitter spheres, we

can utilize the catalog of de Sitter embeddings enumerated in Sec. A.2. Focusing on the closed foliation, the Euclidean embedding for one de Sitter sphere is found by analytically continuing $\chi \rightarrow i\chi$ in Eq. A.45. The metric then becomes

$$ds^2 = dz^2 + H^{-2} \sin^2(Hz) [d\chi^2 + \cos^2 \chi d\Omega_2^2], \quad (3.37)$$

where the angles cover ranges $0 \leq Hz \leq \pi$, $-\pi/2 \leq \chi \leq \pi/2$, $0 \leq \theta \leq \pi$, and $0 \leq \phi \leq 2\pi$. The instanton will in general be composed of a large portion of the false vacuum de Sitter sphere, with the bubble wall located on a constant- z slice. On the other side of the bubble wall is a small cap of the true vacuum de Sitter sphere. The slice defined by $(\theta = \pi/2, \phi = 0)$ in the (X_0, X_1, X_4) coordinate system is shown in the left-hand portion of Fig. 3.4, where constant z surfaces describe longitudes and constant χ surfaces describe latitudes on the hemisphere. Slices of different (θ, ϕ) in these coordinates are shown in the top portion of Fig. 3.5, where it can be seen that the volume of a sphere will be foliated by the allowed slices. Importantly, the position of the spherically symmetric bubble wall is independent of θ and ϕ .

Shown in Fig. 3.6 is the analytic continuation of the CDL instanton on a constant- χ slice. The field values on this slice provide initial conditions for the subsequent lorentzian evolution. The conformal diagram shown on the right is identical to the $t > 0$ portion of the full-time symmetric solution shown in Fig. 2.1.

An alternative embedding of de Sitter space yields the Euclidean static coordinates. This can be obtained from Eq. A.19 by analytically continuing $t \rightarrow it_E$, and is shown in the right portion of Fig. 3.4. The pole of the hemisphere is in this case located on the X_1 -axis and corresponds to the radius of the cosmological horizon. Longitudes with respect to this pole correspond to surfaces of constant R , where the equator is at $R = 0$. Latitudes describe slices of constant t_E . Shown in the bottom portion of Fig. 3.7 are slices of different (θ, ϕ) , which again foliate the volume of a sphere.

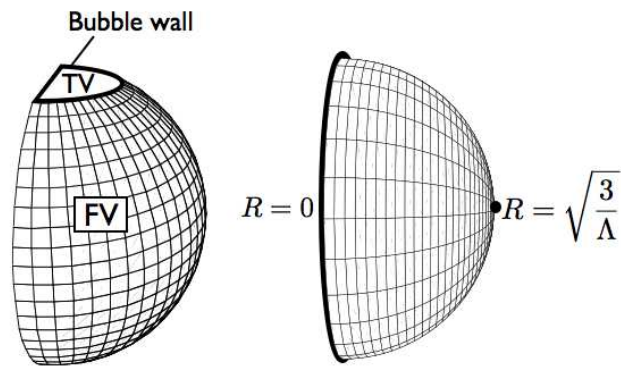


Figure 3.4: The Euclidean instanton for zero mass thin wall bubbles in the embedding space. On the left is the instanton in the (z, χ) coordinatization on a surface of constant (θ, ϕ) . The majority of the space is covered by the false vacuum de Sitter sphere, save a small cap of the true vacuum sphere around the north pole. The bubble wall is located on a constant ξ slice. Euclidean de Sitter in the (t, R) coordinatization, on a surface of constant (θ, ϕ) , is shown on the right.

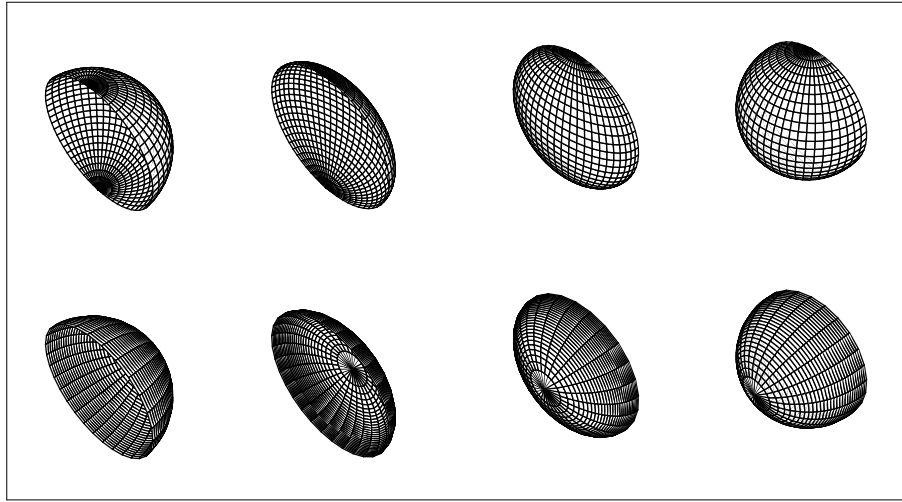


Figure 3.5: Euclidean de Sitter in the (z, χ) coordinatization (top) and the (t_E, R) coordinatization (bottom) on slices of constant (θ, ϕ) in the (X_0, X_1, X_4) embedding space. These slices will foliate the volume of a sphere as (θ, ϕ) traverse their allowed ranges.

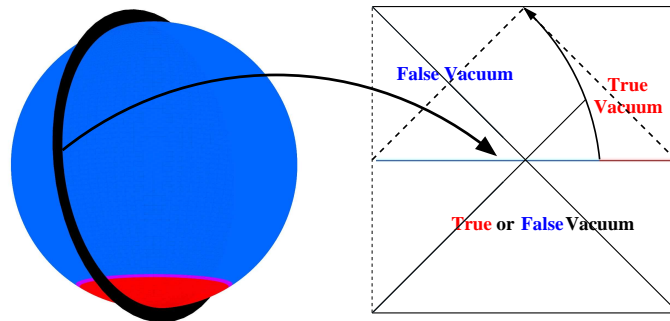


Figure 3.6: The analytic continuation of the instanton defining the initial conditions for the lorentzian evolution of true or false vacuum bubbles.

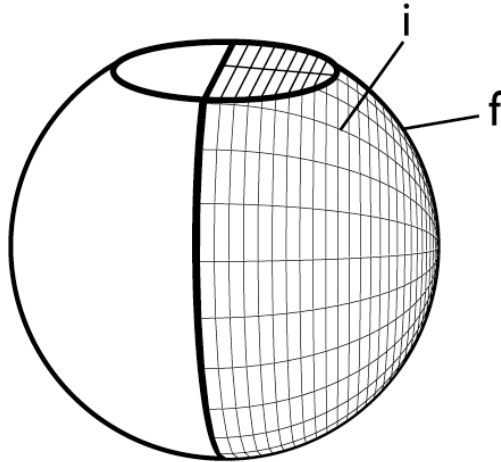


Figure 3.7: The instanton in the (t_E, R) coordinatization. The initial spacelike hypersurface is indicated, and ranges from $R = 0$ (the position of the bubble wall) to the false vacuum cosmological horizon. The final spacelike hypersurface ranges from the critical radius of the true vacuum bubble (see Eq. 2.13) to the false vacuum cosmological horizon. Also shown is the continuation of the final hypersurface and slices of constant R in the true-vacuum portion of the instanton. Values of R in the false-vacuum portion of the instanton match those in the true-vacuum region across the bubble wall.

Shown in Fig. 3.7 is the bubble wall trajectory in the (t_E, R) coordinatization, where it can be seen that the wall will evolve from $R = 0$ to the radius of the bubble at the time of nucleation as the angle χ is evolved from $-\pi/2$ to 0. The initial and final hypersurfaces in the Euclidean space exterior to the bubble wall are indicated in Fig. 3.7, and these slices can be continuously evolved into each other.

From this perspective, the nucleation of thin-wall true and false vacuum bubbles can be described using a collective coordinate, the bubble radius, and we should seemingly be able to map this onto the original description in terms of the field and gravitational degrees of freedom. In the case of true vacuum bubbles this is indeed possible, and by slicing the CDL instanton in the correct way, it is possible to locate the initial and final configurations of the Euclidean interpolating manifold in the collective coordinate description. Indeed, this picture has been

known to exist for some time, and to the author's knowledge appeared for the first time in Ref. [62].

The situation is much different when we turn to discuss CDL false vacuum bubbles. Here, it is impossible to locate on the CDL instanton the initial configuration in the collective coordinate description. There are no initial value hypersurfaces that encompass a region of order the true vacuum horizon size. Of course, as soon as deviations from the thin wall approximation are included, the instanton does not contain any regions where the field is in the true or false vacuum, and it will never be possible to locate the initial value surface. In both the thick-wall and false vacuum bubble, gravitational effects are important, and our inability to use the collective coordinate picture seems to be tied to the fact that including gravity completely changes the description and construction of the instanton.

Following Parke [63], the bounce action for thin-wall bubbles including gravitational effects is given by

$$S_E = \frac{27\pi^2\sigma^4}{2(V_F - V_T)^3} r(x, y) \quad (3.38)$$

where $r(x, y)$ measures the effect of gravitational corrections to the bounce action

$$r(x, y) = \frac{2[(1 + xy) - (1 + 2xy + x^2)^{1/2}]}{x^2(y^2 - 1)(1 + 2xy + x^2)^{1/2}} \quad (3.39)$$

with

$$x = \frac{6\pi\sigma^2}{(V_F - V_T)}, \quad (3.40)$$

$$y = \frac{V_F + V_T}{V_F - V_T}. \quad (3.41)$$

A contour plot of the function $r(x, y)$ is shown in Fig. 3.8. The unshaded region corresponds to the portion of the parameter space where $|r| < 1$, and the tunneling rate is enhanced by gravitational effects. The region with $y > 0$, in which the tunneling rate is always enhanced, corresponds to $|V_F| > |V_T|$. The region with $y < 0$ corresponds to $|V_F| < |V_T|$, and in this

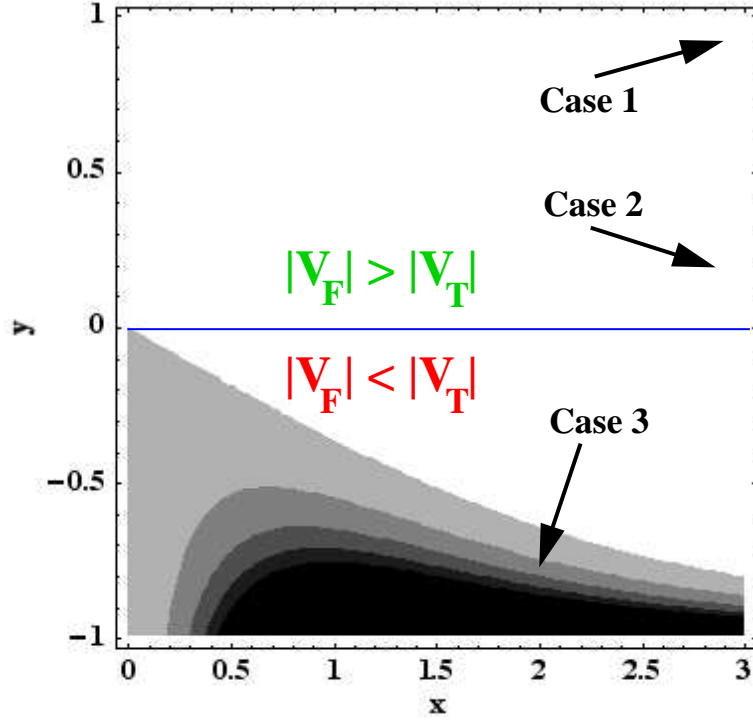


Figure 3.8: The gravitational factor, Eq. 3.39, for thin-wall vacuum bubble nucleation with gravity. The unshaded region corresponds to $r(x, y) < 1$, where tunneling is enhanced by gravitational effects. Contours for $r(x, y) = 1, 1.5, 2, 2.5, 3$ are shown.

parameter space the tunneling rate can either be enhanced or suppressed. In the thin-wall approximation, the critical radius is given by the turning-point, Eq. 2.13, found in the zero-mass solutions of Chapter 2.

There are a few limiting cases [63], where we can discuss the behavior of $r(x, y)$.

Case 1: $y \ll x \ll 1/y$

In the limit where $y \ll x$ (corresponding to $V_F + V_T \ll 6\pi\sigma^2$), Eq. 3.39 becomes

$$r(x, y) = \sqrt{2} \left(\frac{y}{x} \right)^{3/2}. \quad (3.42)$$

The relevant parameter space is indicated in Fig. 3.8.

Case 2: $x \gg 1/y, 1$

In the limit where $x \gg 1/y, 1$, Eq. 3.39 becomes

$$r(x, y) = \frac{2}{x^2(1+y)}, \quad (3.43)$$

which is a more steep decreases with x than the case where $x \ll 1/y$. The relevant parameter space is indicated in Fig. 3.8.

Case 3: $y < -1$

At $(x = 1, y = -1)$, corresponding to $V_F \rightarrow 0$ and $6\pi\sigma^2 = V_T$, Eq. 3.39 blows up. In Chapter 2 (see the discussion surrounding Fig. 2.4), we found that the turning point radius diverges in this limit, explaining the behavior of the action. If we also consider cases where $y < -1$ (corresponding to $V_F < 0$), gravitational effects always act to stabilize the false vacuum. The gravitational factor will diverge for

$$x \geq -y - (y^2 - 1)^{1/2} \quad (3.44)$$

corresponding to a limit on the tension of

$$\sigma \leq \sqrt{\frac{|V_T|}{6\pi}} - \sqrt{\frac{|V_F|}{6\pi}}. \quad (3.45)$$

From Eq. 2.13, the critical radius of the bubble diverges when the equality holds.

In theories of slightly broken supersymmetry [64], the tension of the bubble wall can be approximated by the tension of BPS domain walls in the supersymmetric theory. In this case, one is able to relate the scale of SUSY breaking ($m_{3/2}$ —the mass of the gravitino) to the tunneling rate between an uplifted dS vacuum and a negative CC supersymmetric vacuum:

$$B = \frac{8\pi^2}{m_{3/2}^2} \frac{(C-1)^4}{C^2(2C-1)^2} \quad (3.46)$$

where $C \equiv \frac{|V^{susy}_F|}{|V^{susy}_T|}$ is the ratio of the (negative) vacuum energy in the false and true vacuum prior to the uplifting. For low-energy SUSY, this tunneling rate can be appreciable, perhaps indicating a connection between eternal inflation and SUSY breaking. It would be interesting to analyze such theories in more detail using the methods outlined below.

3.3 Approximate analytic solutions

For the remainder of this chapter, we will consider a dimensionless potential $v(x)$ given by

$$v(x) = f(x) - (1+z)f(x_F), \quad (3.47)$$

where

$$f(x) = \frac{1}{4}x^4 - \frac{b}{3}x^3 - \frac{1}{2}x^2. \quad (3.48)$$

We will tune the parameter b such that the potential has three extrema as shown in Fig. 3.1, and has variations of order 1 between x_F and x_T . The non-negative parameter z controls the false vacuum cosmological constant V_F , so that $V_F \rightarrow 0$ as $z \rightarrow 0$.⁵

We can solve Eq. 3.28 and 3.29 exactly when the Euclidean energy remains approximately constant for a period of time. This can only occur in the neighborhood of the extrema of the potential. The focus of this study is on transitions from a positive Euclidean energy well at x_T to a negative Euclidean energy well at x_F , but the results we present below can be used to study arbitrary combinations of positive and negative energy wells. The approximate solution to the instanton equations near x_H (see Fig. 3.1) was presented in [58], and is relevant for the study of oscillating solutions.

Consider the evolution of the field in the neighborhood of x_T or x_F . The field will begin/end with zero velocity and some displacement, $\delta_{T,F}$, from x_T or x_F . If the variable $\delta_{T,F}$ is small, then the field will loiter in the neighborhood of the maximum. During this time, the Euclidean energy of the field will remain roughly constant and, if the velocity remains small, equal to the value of u at the maximum. Equation 3.29, for the cases of loitering near the true

⁵The way in which we have chosen to tune the vacuum energy is not really appropriate in many supergravity models. There, one tunes a constant in the superpotential. If there are excursions in field space of order m_P , this changes the potential in a more complicated way than a simple subtraction. We hope to return to a study of supergravity models in a future publication.

or false vacuum maxima, then reduces to

$$r^2 \simeq 1 + \epsilon^2 r^2 u_{T,F}, \quad (3.49)$$

which can be integrated to yield

$$r(s) = \frac{1}{\epsilon \sqrt{-u_{T,F}}} \sin(\epsilon \sqrt{-u_{T,F}} s). \quad (3.50)$$

If we take the false vacuum maximum to have $u_F < 0$, then we can recognize this as the metric for Euclidean de Sitter space (the four sphere). Substituting Eq 3.50 into Eq. 3.28 yields:

$$\ddot{x} + 3\epsilon \sqrt{-u_{T,F}} \cot(\epsilon \sqrt{-u_{T,F}} s) \dot{x} + u'(x) = 0. \quad (3.51)$$

Since we are trying to find solutions only in the vicinity of the true and false vacuum maxima, we may Taylor expand the potential about $x_{T,F}$, keeping only the constant and quadratic terms.

After making the change of variables $y = \cos(\epsilon \sqrt{-u_{T,F}} s)$ and $\delta = x - x_{T,F}$, we then obtain

$$(1 - y^2) \frac{d^2 \delta}{dy^2} - 4y \frac{d\delta}{dy} + \frac{\omega^2}{\epsilon^2 u_{T,F}} \delta = 0, \quad (3.52)$$

where $\omega^2 \equiv |u''_{T,F}|$. This can be recognized as the hyperspherical differential equation, the solution of which is given in terms of Legendre functions. After imposing the boundary conditions $\dot{\delta}(y = 1) = 0$ and $\delta(y = 1) = \delta_{T,F}$, we obtain

$$\delta(y) = \frac{-2i\delta_{T,F}}{\nu(\nu + 1)} (y^2 - 1)^{-1/2} P_\nu^1(y), \quad (3.53)$$

with

$$\nu = -\frac{1}{2} \left(1 + \sqrt{9 + \frac{4\omega^2}{\epsilon^2 u_{T,F}}} \right). \quad (3.54)$$

For $s \ll \epsilon \sqrt{|u_{T,F}|}$, this solution can be written in terms of Bessel functions.

We have found an approximate analytic solution near the true and false vacuum maxima. However, in order to construct the entire single-pass instanton we must evolve across regions of the potential in which our approximations break down. This requires a numerical approach, which will be presented in Sec. 3.4.2.

3.4 The $V_F \rightarrow 0$ limit

We are now in a position to re-examine some of the conclusions of [15]. It was conjectured that for all ϵ the instanton describing a transition from a positive energy false vacuum to a negative energy true vacuum approaches a finite size as $z \rightarrow 0$, and therefore the instanton action would not scale with the background subtraction term. We argued (to ourselves) that there would also be a flat space instanton which existed for $z = 0$, by a version of Coleman's overshoot/undershoot argument. This implied a discontinuous limit as the false vacuum energy was sent to zero.

Here, we will present numerical and analytical arguments that below some (potential dependent) ϵ_c there are in fact large dS instantons that asymptote as $z \rightarrow 0$ to the flat space instanton. Above ϵ_c , there are finite-size instantons with finite action as $z \rightarrow 0$, but no flat space instanton. At ϵ_c (on the Great Divide), we will find that the instanton for $z = 0$ is a static domain wall solution of the coupled Euclidean Einstein and field equations.

3.4.1 Small ϵ

Let us explore the small ϵ case first, and argue that if a single-pass instanton exists, it *must* resemble the dimensionless de Sitter metric, Eq. 3.50, over most of its volume. From Eq. 3.29, we see that the Euclidean energy, which is bounded from below by the value $u(x_H)$ of the potential at the Hawking-Moss maximum, must be negative for a turn-around in r to occur. If there is a turn-around, the value of r at this point, r_m , will be

$$r_m = \frac{1}{\epsilon\sqrt{-E_m}}. \quad (3.55)$$

Since the Euclidean energy is bounded, as ϵ is decreased, r_m must increase. If there is a compact nonsingular instanton, the field must evolve in such a way to facilitate this growth in r . When the field is not in the vicinity of the extrema of the potential, it will move between the potential

wells in a time of order one. During this time, r will grow to some ϵ independent size. Thus, for r to become large enough to find a turn-around in the small ϵ limit, the field must loiter in the vicinity of one of the extrema of the potential.

Loitering near the Hawking-Moss maximum leads to an oscillatory motion, because this is a minimum of the Euclidean potential. There are non-singular solutions which make of order $\frac{1}{\epsilon}$ oscillations before ending up in the basin of x_F . These are not single pass instantons. Loitering near the true vacuum maximum will cause r to grow as in Eq. 3.50 (linearly if $s \ll \epsilon\sqrt{u_T}$). However, because the friction term decays during the loitering phase, these solutions will in general have too much energy and overshoot the false vacuum maximum. For intermediate values of ϵ , the growth in r near the true vacuum becomes important, as we will see below.

The only viable option is then that the field be near x_F at the turn-around in r . If we take the end-point near x_F to be at $s = 0$, the field must remain near x_F until $r = r_m$. This evolution should be well described by the analytic solution Eq. 3.53 derived in the previous section. The Euclidean energy at r_m will be given by

$$E_m \simeq u_F + \frac{1}{2}\dot{\delta}_m^2 - \frac{\omega^2}{2}\delta_m^2. \quad (3.56)$$

We can write δ_m and $\dot{\delta}_m$ in terms of Gamma functions

$$\delta_m = \delta(s = \pi/2\epsilon\sqrt{v_F}) = \delta_F \frac{\sqrt{\pi}}{\Gamma(1 - \frac{\nu}{2}) \Gamma(\frac{3}{2} + \frac{\nu}{2})}, \quad (3.57)$$

and

$$\dot{\delta}_m = \dot{\delta}(s = \pi/2\epsilon\sqrt{v_F}) = -\delta_F \epsilon \sqrt{\pi v_F} \frac{2 + \nu}{\Gamma(\frac{1}{2} - \frac{\nu}{2}) \Gamma(2 + \frac{\nu}{2})}. \quad (3.58)$$

This limit will be an important component of the numerical scheme presented in the following section. We note that δ_m and $\dot{\delta}_m$ are of the same order of magnitude, and must be much smaller in magnitude than v_F for our approximation scheme to remain self-consistent. This can always be arranged by making δ_F of order $\exp(\frac{-1}{\epsilon\sqrt{v_F}})$. Thus, we can see that there is a self-consistent solution in the vicinity of x_F which tracks the de Sitter solution until r_m .

In fact, it is necessary, for small ϵ , to choose δ_F small enough that the de Sitter/Legendre approximation remains valid until $s = \frac{\pi}{\epsilon\sqrt{v_F}} - o(1)$. If we do not do this, then $x(s)$ moves rapidly away from x_F on a time scale of $o(1)$, while $r(s)$ is still $\gg 1$. It will either overshoot x_T or stop and fall back, long before the second zero of $r(s)$ is reached. In neither case do we get a single pass instanton. The rest of the instanton consists of a traverse from the vicinity of the false vacuum, to the basin of attraction of the true vacuum, in a time of $o(1)$ (ϵ -independent for small ϵ). It is important that, since $r \ll 1/\epsilon$ during this traverse, Eq. 3.49 indicates that $r(s)$ is approximately linear in this period, and indeed also linear for a long period before $x(s)$ leaves the vicinity of the false vacuum.

It is convenient to think of the rest of the instanton as a function of a new time variable t which starts at $t = 0$ near the true vacuum and increases toward the false vacuum so that $d/dt \equiv -d/ds$. Since $r(t) \approx t$ when $r \ll 1/\epsilon$, we have

$$\frac{d^2x}{dt^2} + \frac{3}{t} \frac{dx}{dt} = -u'(x), \quad (3.59)$$

with the boundary conditions $\frac{dx}{dt}(t=0) = 0$ and $x_H < x(t=0) < x_T$.

This equation is just the equation for an instanton in quantum field theory, neglecting gravitational effects. Coleman [10] showed that one can find solutions which start in the basin of attraction of the true minimum, and get arbitrarily close to (or even overshoot) the false minimum. Eq. 3.59 is ϵ -independent, but as ϵ goes to zero, the range of t over which it is a good approximation to the real instanton solution grows as $1/\epsilon$. Thus, for small enough ϵ , we can use Coleman's argument to show that there are solutions of Eq. 3.59, which are non-singular at $t = 0$ and penetrate into the region where the Legendre approximation is valid. By varying the initial position $x(t=0)$ among all such solutions, we can tune the logarithmic derivative of x at a given point t^* where both approximations are valid, within a finite range.

The conditions that the two solutions match at some point (t^*, s^*) are

$$t^* = \frac{1}{\epsilon\sqrt{v_F}} \sin(\epsilon\sqrt{v_F}s^*), \quad (3.60)$$

$$\frac{1}{x(s^*)} \frac{dx}{ds} = -\frac{1}{x(t^*)} \frac{dx}{dt}, \quad (3.61)$$

$$x(s^*) = x(t^*), \quad (3.62)$$

where functions of s^* are in the de Sitter/Legendre approximation and functions of t^* are in the zero-gravity approximation. Once we know that there is a range of $x(t=0)$ for which $x(t)$ penetrates into the range where the Legendre approximation is valid, we can tune $x(s=0)$ to satisfy the last condition. We know that s^* is large for very small ϵ , of order $\frac{\pi}{\epsilon\sqrt{v_F}} - o(1)$, in which case the first condition becomes $t^* = s^*$.

$x(t=0)$ is then tuned to match the logarithmic derivatives. Although there is a range of s over which $x(s)$ is rapidly varying, its logarithmic derivative is roughly constant over that range. The only place where the logarithmic derivative is large, is near the second zero of the sine, but for small ϵ the matching occurs far from that region (t^* large but $\ll \frac{1}{\epsilon\sqrt{v_F}}$). It is thus plausible that by varying s^* and $x(t=0)$ we can satisfy both of Equations 3.60 and 3.61. If this is the case, then a non-singular, large radius instanton exists. As $v_F \rightarrow 0$, this goes over smoothly to an “instanton for the decay of asymptotically flat space”.

The argument above indicates the possibility of a true asymptotic matching of solutions of the non-gravitational equations to solutions of the de Sitter/Legendre approximation over a range of s which grows as $\epsilon \rightarrow 0$. Since we cannot exhibit solutions of the non-gravitational equations exactly, our argument is not completely rigorous. In the next section we will present numerical calculations, which show that it is correct.

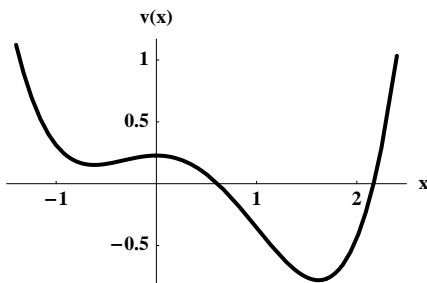


Figure 3.9: The potential, $v(x)$, used for the numerics. The parameter b is fixed at $b = 1$, and z will be allowed to vary (this plot shows $z = 1$).

3.4.2 Numerical results for small ϵ

To confirm the validity of the conclusions above, we have undertaken a semi-analytic search for single pass instantons in a potential with a positive false vacuum and a negative true vacuum. Here, we will focus on the potential shown in Fig. 3.9, though qualitatively our results are potential independent (we have confirmed this by studying a variety of potentials).

The strategy is to use the matching scheme discussed in Section 3.4.1. We will relax the zero-gravity approximation for the evolution from the true vacuum well to the false vacuum well, and numerically evolve Eqs. 3.29 and 3.28. To fix the initial conditions of the numerical evolution from the true vacuum side of the potential, we will use an analytic solution to evolve for the first time step. If it is near x_T , we use Eq. 3.53; if not, we approximate the potential as linear, yielding a $\delta(s) \propto s^2$. We then evolve and attempt to match onto the de Sitter/Legendre approximation (Eq. 3.50 and 3.53) when the field approaches x_F . Of course, we are not guaranteed to find a match for all ϵ . It was shown by Coleman and De Luccia [12], that in the thin-wall limit there are cases where the transition from a positive (Euclidean) energy well to a zero energy well is forbidden. This occurs when the positive energy at the true vacuum maximum becomes too small, so that an over-shoot solution becomes impossible. This would prevent the instanton from ever entering a regime where the de Sitter/Legendre approximation was valid.

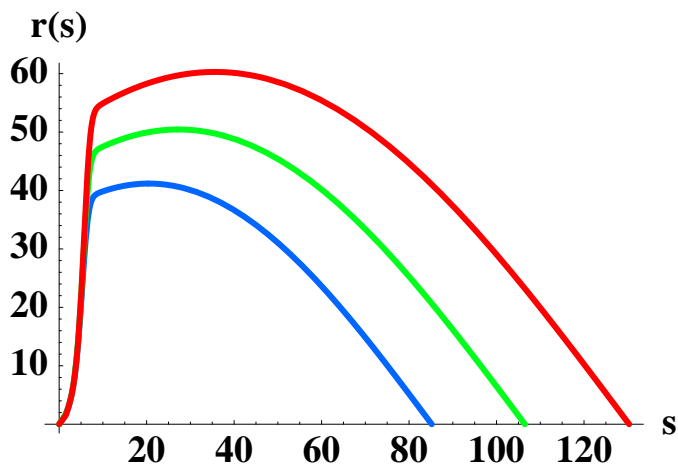


Figure 3.10: Evolution of $r(s)$ for $\epsilon = .72$ and $z = (.01, .008, .006)$ from bottom to top. The matching between the analytic and numeric solutions occurs at the maximum of r , r_m .

The need for a semi-analytic approach is evident from the fantastically small displacement from the false vacuum required to find solutions with large r_m . Numerically evolving the solution over the entire trajectory would become impossible as the field approaches x_F . Also for reasons of numerical tractability, we match the solutions at r_m , where $s = \pi/(2\epsilon\sqrt{v_F})$, and the Legendre function can be written in terms of (calculable) Γ - functions as in Eq. 3.57 and 3.58.

This method also has its limitations. For small enough $\epsilon\sqrt{v_F}$, we may be trying to compare field velocities at a precision that is not achievable by the numerical integrator. Despite these difficulties, we have been able to construct a number of instantons in the intermediate ϵ regime, examples of which are shown in Fig. 3.10. It can be seen in this plots that as $z \rightarrow 0$, these instantons are growing. Since we have shown that a matching is possible at r_m , as $v_F \rightarrow 0$, by the argument given in Sec. 3.4.1, these instantons must scale with the background subtraction term.

3.4.3 Large ϵ

To study large⁶ values of ϵ , where the approximations introduced above are not necessarily valid, we must take an entirely numerical approach. We choose to begin the evolution from the true vacuum side of the potential, varying δ_T until a solution is found. To fix the initial conditions of the numerics, we will again use an analytic solution to evolve for the first time step as described in the previous section.

Shown in Fig. 3.11 is the evolution in x for $\epsilon = .85$ as $z \rightarrow 0$. Shown in Fig. 3.12 is the evolution in r with the same parameters. It can be seen that as $z \rightarrow 0$, the instanton approaches a constant, finite size. Therefore, for large ϵ , the instanton action will not scale with the background subtraction term.

To discuss the continuity of the limit $V_F \rightarrow 0$, we must first determine in which cases there is an instanton for $V_F = 0$. If this instanton describes the decay of a spacetime with exactly zero cosmological constant, then the evolution in r must be from $r(s=0) = 0$ to $r(s=\infty) = \infty$. The field will be moving from some initial position near x_T at $s=0$ to *exactly* x_F at $s=\infty$. If, starting near x_T , there is a region of δ_T -space in which over-shoot occurs, then there must be a second zero in \dot{x} . The question is then what value r takes at the second zero of \dot{x} .

In all of the numerical examples we have studied with $z=0$, we find that $r=0$ at the second zero of \dot{x} . The turn-around in r in these cases is not caused by loitering in the vicinity of a negative energy extremum of the potential. Instead, as the field is climbing towards x_F , the negative potential energy comes to dominate over the kinetic energy. Since ϵ is rather large, r does not need to grow very large to cause a turn-around in r . Since the end-points of this instanton are on the boundaries of the unique over- and under-shoot regions of the potential, there is no other single-pass instanton with $r(s=\infty) = \infty$.

⁶By large we mean of order one. While the formalism will accommodate arbitrarily large values of ϵ , there will be an ϵ after which only the Hawking-Moss instanton exists.

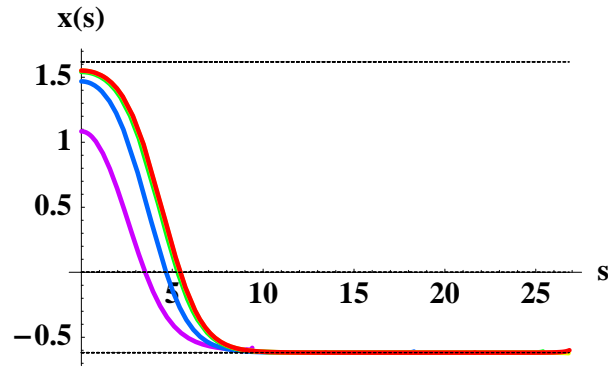


Figure 3.11: The evolution of $x(s)$ for $\epsilon = .85$ and $z = (1, .1, .01, .0001)$ from bottom to top. The dashed horizontal lines indicate the positions x_T (top) and x_F (bottom) .

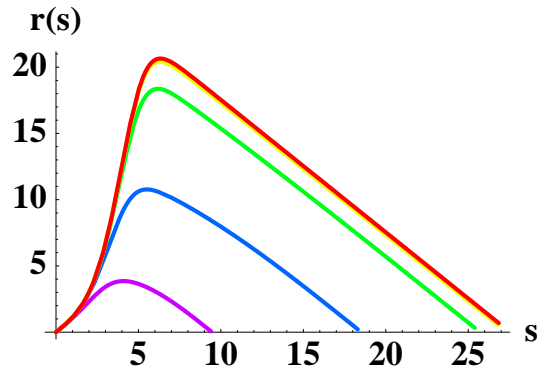


Figure 3.12: The evolution of $r(s)$ for $\epsilon = .85$ and $z = (1, .1, .01, .0001)$ from bottom to top.

3.5 The Great Divide

In this section we show that, for any potential $v(x)$, there is a critical value of ϵ for which planar domain wall solutions exist. As one goes from the small to the large ϵ regime, there is a transition point between the two behaviors discussed in Section 3.4. We will define ϵ_c as the transition point in the case where $z = 0$ (when the false vacuum well has zero energy).

We have found instantons (with $z = 0$) for a variety of ϵ near ϵ_c as shown in Fig. 3.13. The evolution of the field is from the vicinity of x_T at $s = 0$ to x_F at $s = \infty$. Of course, we cannot track the entire evolution, but we can follow it for some finite time scale by tuning δ_T to approach the boundary between the under- and over-shoot solutions. It can be seen from these numerical examples that r is growing very large in the vicinity of the true vacuum.

As we approach ϵ_c , the initial displacement on the true vacuum side, δ_T , is decreasing as shown in Fig. 3.14. Because we are starting with more energy on the true vacuum side of the potential, we must send $\delta_F \rightarrow 0$ as well. Therefore, at this critical value of ϵ , the instanton interpolates exactly between x_T at $s = -\infty$ and x_F at $s = +\infty$. Also, note that after we analytically continue to the Lorentzian solution, the interior of the CDL bubble will be infinitely large. This solution therefore describes a static domain wall.

We can understand this behavior by looking at the energetics of the evolution from x_T to x_F . The instanton equations in the critical limit approach the static domain wall equations

$$\ddot{x} + \frac{3\dot{r}}{r}\dot{x} + u' = 0, \tag{3.63}$$

$$\dot{r}^2 = \epsilon^2 r^2 E, \tag{3.64}$$

s now runs between $-\infty$ and ∞ , and a domain wall solution asymptotes to the two vacua on opposite sides. The energy is always decreasing along the trajectory from the true to the false vacuum well. The question is whether x can lose just enough energy during its traverse to asymptote to x_F without overshooting. If $\epsilon = 0$ the answer is clearly no, because energy

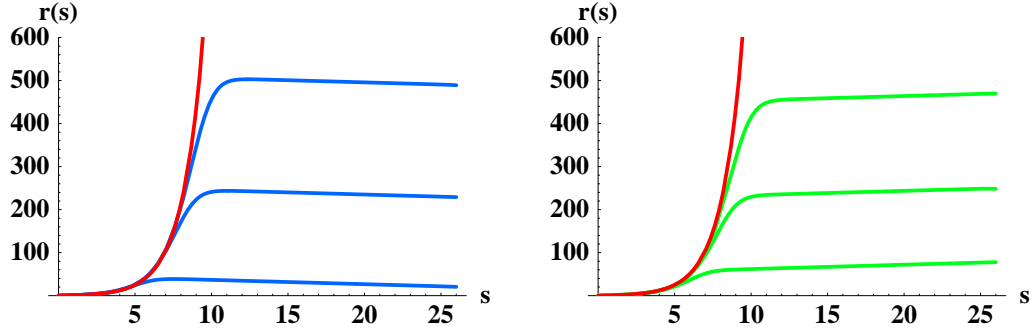


Figure 3.13: The evolution of $r(s)$ for $z = 0$ on either side of ϵ_c . Shown on the left are values of $\epsilon > \epsilon_c$ in blue ($\epsilon = (.8, .75, .745)$ from bottom to top) and $\epsilon_c \sim .74$ in red. The instantons with $\epsilon > \epsilon_c$ are compact, having two zeros in r . On the right are values of $\epsilon < \epsilon_c$ ($\epsilon = (.7, .73, .735)$ from bottom to top) in green and ϵ_c in red. The instantons with $\epsilon < \epsilon_c$ are not compact, with $r \rightarrow \infty$ as $s \rightarrow \infty$.

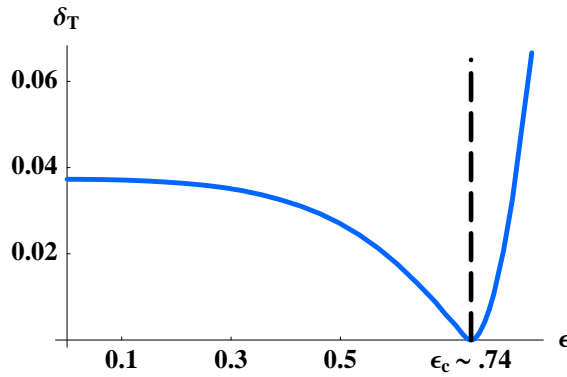


Figure 3.14: It can be seen in this plot of δ_T vs ϵ for the case where $z = 0$ that there is an ϵ_c for which $\delta_T \rightarrow 0$. Below this value, δ_T is approaching the zero-gravity solution, and above it, $\delta_T \rightarrow x_T - x_H$.

is conserved. The solution overshoots the false vacuum. This persists for very small ϵ . On the other hand, in the mathematical limit $\epsilon \gg 1$, the friction term dominates the motion and x undershoots in a finite time. It follows that there is a critical value of ϵ where x indeed asymptotes to x_T and we have a static domain wall solution in the presence of gravity. The critical value is clearly $o(1)$. Since we have found such a solution by tuning a single parameter, the codimension of the subset of potentials which have a domain wall is 1, and the subset forms a Great Divide in the space of potentials.

We have shown both that there is a critical value of ϵ at which domain walls exists, and that the flat space instanton solution, which exists below the Divide, approaches the domain wall solution at this critical value. Above the divide, the flat space instanton and the associated large instantons for small v_F , disappear. Flat space is stable, and the stability of nearly flat dS spaces has a clear entropic explanation.

3.6 Below the great divide

In [15], along with the conjecture of a discontinuity of the tunneling action at $V_F \rightarrow 0$ came a (retrospectively flawed) physical argument to explain the discontinuity, based on the physical picture of quantized dS space adumbrated in [65]. In that picture, quantized dS space is equipped with two operators: the static Hamiltonian H , and the Poincare Hamiltonian P_0 ; these satisfy a finite-dimensional approximation to the commutation relation

$$[H, P_0] \sim \frac{1}{R} P_0, \tag{3.65}$$

where R is the de Sitter radius. The eigenvalues of H are highly degenerate, and bounded by something of order the dS temperature, $T_{dS} = \frac{1}{2\pi R}$. The low-lying eigenstates of P_0 are metastable (when evolved using H), and correspond to states localized in a given horizon volume; the lowest lying eigenstates have small degeneracies, and the ground state is unique. The

conjectured discontinuity in the tunneling probability was alleged to be related to the fact that for finite V_F the CDL instanton describes the decay of the thermal ensemble of H eigenstates (a system of high-entropy), but that for vanishing V_F it describes the decay of a low-entropy system consisting just of the single P_0 ground state.

The flaw in this argument is that it hypothesizes both a stable P_0 eigenstate, and also the decay of that stable system. That is, the existence of the CDL instanton for potentials below the great divide is, in fact, evidence that these low energy effective theories do not correspond to limits of theories describing asymptotically flat space-time.

The conformal boundary of the Lorentzian continuation of the CDL instanton is not the same as that of Minkowski space: in the usual parametrization (u, Ω) of future null infinity, \mathcal{I}^+ , in terms of a null coordinate u and a transverse sphere, the boundary becomes geodesically incomplete because the asymptotic bubble wall hits \mathcal{I}^+ at a finite value of u . Neither the Lorentz group (consisting of the conformal group of the sphere accompanied by a rescaling of u) nor the time translation group (the generator of which is just $P_0 = \frac{\partial}{\partial u}$, in a particular Lorentz frame) is an asymptotic symmetry of this spacetime. Thus, the “explanation” of an hypothetical discontinuity in [15] was based on an equally hypothetical operator P_0 . Neither exists.

If potentials below the Great Divide do not correspond to effective theories of gravity in asymptotically flat space, what do they correspond to? Two possibilities consistent with the authors’ current understanding of quantum gravity are:

1. Nothing. That is, there simply are no theories of quantum gravity which give rise to such potentials.
2. These theories correspond to models of quantum gravity which, in the $V_F \rightarrow 0$ limit under consideration, actually contain only a finite number of excitations of the Minkowski solution. This would remove the apparent contradiction between the infinite number of

states of the would-be asymptotically flat space and the finitely bounded entropy of the maximal-area causal diamond in the Big Crunch.

The confusion may be simplified enormously if the conjecture of [66] is accepted. According to that hypotheses, the only viable quantum theories of asymptotically flat space time are exactly supersymmetric, and all models with a vacuum energy that can be tuned to be arbitrarily small become exactly supersymmetric in that limit. At the moment, this conjecture is valid for all models which have been derived from string theory in a reliable manner. The whole concept of the Great Divide is defined in terms of one-parameter families of potentials, with vacuum energy that can be tuned to zero. The conjecture of [66] thus implies that all valid models of quantum gravity will fall above the Great Divide; which is hypothesis 1 above.

3.7 Connections with eternal inflation

In [15], two of the authors proposed a regulated model of eternal inflation for potential landscapes with only non-vanishing vacuum energies. According to that model the system has a finite number of quantum states, and for most of its time evolution it resembles the dS space of lowest positive vacuum energy⁷. This model remains valid for potentials above the Great Divide. For such potentials, tunneling amplitudes out of dS space are suppressed in a way which may be attributable to the principle of detailed balance, and entropic effects.

To be more precise, for a potential with multiple minima, if the minimum with smallest positive vacuum energy becomes absolutely stable as that vacuum energy is tuned to zero by subtraction, then the CDL tunneling amplitudes are consistent with an interpretation in which eternal inflation on the potential landscape is a finite-dimensional quantum system, most of

⁷If the minimum with lowest absolute value of the vacuum energy is negative, then this statement might be corrected to "for most of the period during which local observers exist it resembles the dS space of lowest positive vacuum energy".

states of which resemble the dS space of smallest positive vacuum energy. “Decays” of this state into negative vacuum energy Big Crunch regions will occur, but in such an interpretation would be viewed as improbable, low entropy fluctuations of a system that spends most of its time as a large radius dS space.

We also want to comment on the remark of [47] that this kind of landscape is ruled out by observation. This is based on the paper of Dyson *et. al* [67], which is itself a variation on the “Boltzmann’s brain” paradox. This paradox arises if we attribute a state in our past to a downward fluctuation from a high-entropy state. It would then be much more probable for our past (given what we observe now) to consist of a *smaller* fluctuation downward in entropy into the universe ten minutes ago. ⁸

References [67] and [47] argue that this paradox is not solved by a model in which the universe is a random fluctuation of a finite system with time-independent Hamiltonian. Even if tunneling to negative vacuum energy is suppressed as above the Great Divide, however, there are a number of possible resolutions to this paradox, some well-developed, which we will enumerate here:

- The transitions rates between vacua may not obey detailed balance [8]. This would be the case if the Farhi-Guth-Guven tunneling mechanism is allowed, and would subvert the paradox by allowing a small inflating region to form, with relatively high probability. This region would then create a large, low-entropy region. Whether the Farhi-Guth-Guven process actually occurs, however, is not clear (see, e.g., [17, 69]).
- The description of the universe as a finite system that can equilibrate is insufficient. Since the region within the horizon *does* apparently approach equilibrium, this would indicate

⁸This paradox is closely related to the observation stressed by Penrose [68] (among others) that there is a contradiction between the claim that the initial conditions for the universe are “generic” (as often claimed is allowed by inflation) and the observation that they are of lower-entropy than the current universe (as demonstrated by the second law of thermodynamics).

that regions outside the horizon must be taken into consideration in the overall predictions of the theory. In this view, inflation, while difficult to start from a low-energy vacuum, would “get credit” for creating a huge number of observers, so that most observers see inflation in their past. The following argument suggests that there is something wrong with the “causal patch” picture. Consider a multi-vacuum system with a vanishing lowest vacuum energy. According to [47], no paradox arises because tunneling out of the zero-energy vacuum is completely suppressed. Then it would be hard to see how, if the minimal vacuum energy were tuned upward by an infinitesimal amount, this could discontinuously change the observables so that the theory would be ruled out. Continuity as $\Lambda \rightarrow 0$ (for which the authors have a greater respect than ever before) implies that either the paradox arises in both cases, or in neither.

- The Hamiltonian of the universe may be time dependent and only asymptote to the static Hamiltonian of the dS observer. A particular model of this is holographic cosmology [70, 71, 72, 73], where, at early times the Hamiltonian does not couple the degrees of freedom within the particle horizon of an observer to those outside it. This is the way in which a non-local, holographic theory can be compatible with the idea of a particle horizon. In such a theory, time has a beginning, and the first recurrence time of an asymptotically dS universe is special since its evolution is not governed by the static dS Hamiltonian. It might be that the explanation of what we see today depends crucially on the time dependence of the dynamics of the early universe. Further recurrences might never produce a universe remotely like our own and might be argued to be irrelevant. The picture of our past as a low entropy fluctuation of a time independent system is what leads to the Boltzmann’s brain paradox. It may simply be wrong. This is not a claim that holographic cosmology has (as yet) solved the Boltzmann’s brain paradox, but merely that

the solution might involve time-dependent dynamics in the early universe.

3.8 Conclusions

We have seen that there is a rich variety of behaviors of instantons describing the transition from positive or zero energy false vacuum to a negative energy Big Crunch. The complete picture is more detailed than was conjectured in [15], and different than the conventional (thin-wall) wisdom suggests. For small values of ϵ , we have shown that there *does* exist an instanton which resembles Euclidean de Sitter over most of its volume. As the false vacuum energy is taken to zero, the instanton action scales with the background subtraction, and there is no discontinuity in the tunneling rate. However, the analytically continued bubble wall removes a section of the conformal boundary of Minkowski space, providing evidence that low energy effective theories with small ϵ do not correspond to limits of theories describing truly asymptotically flat space-time.

We have found that there exists a static domain wall solution at a critical value of ϵ (ϵ_c). The critical value of ϵ corresponds to a Great Divide in the space of potentials, of codimension one. Below ϵ_c , we find the behavior described in the previous paragraph. Above this value of ϵ , we find compact instantons which *do not* resemble Euclidean de Sitter. The instanton action approaches a constant as the false vacuum energy goes to zero, but the discontinuity claimed in [15] does not exist. We find that there is no non-compact instanton describing the decay of the zero-energy false vacuum, and therefore as the false vacuum energy is decreased, the diverging background subtraction will cause an infinite suppression of the tunneling rate.

The other observation of [15] which remains unchanged by our new results is the remark that metastable SUSY violating vacua of flat space field theories can be viable models of the real world, within the context of Cosmological SUSY Breaking. That is, if we assume that the vacuum

energy is tunable and that the limit of vanishing vacuum energy is a supersymmetric theory in asymptotically flat space, then we are above the Great Divide. For finite Λ the probability for the meta-stable vacuum to make a transition to a Big Crunch is of order $e^{-\pi(RM_F)^2}$. This is not a decay, and it has no phenomenological relevance.

Our new results raise interesting questions about the interpretation of models below the Great Divide. The study of these models will be the subject of a future paper.

Chapter 4

Tunneling: Non-Zero Mass

4.1 Introduction

We have seen in previous chapters that in a field theory with multiple vacua – including some models of cosmological inflation – the nucleation of true-vacuum bubbles in a false-vacuum background can and does occur. Real understanding of the *reverse* process, nucleation of false-vacuum (inflating) regions in a background of (non-inflating) true-vacuum, has, however, been somewhat more elusive. It has been proposed that this may occur by the same Coleman-DeLuccia (CDL) instanton responsible for true-vacuum nucleation [13, 49, 74], by the tunneling of a small false-vacuum bubble through a wormhole to become an inflating region (the Farhi-Guth-Guven, or ‘FGG’ mechanism) [20, 40, 39], or by thermal activation [32, 31].

In this chapter we unify the treatment of both false- and true-vacuum bubble nucleations, via the CDL, FGG, and thermal activation mechanisms, in the thin-wall limit. We find that these can all be studied within a single framework based on the junction condition potentials developed in Chapter 2.

Understanding the quantum mechanical ¹ genesis of inflating regions is very important in assembling a picture of spacetimes containing fields with multiple false vacua, and in understanding how inflation might have begun in our past. These are related because if inflation can begin from a non-inflating region like our own, then *our* inflationary past may have nucleated from non-inflation, and this raises troubling questions [67, 8] if spawning inflation is less probable than spawning a large homogeneous big-bang region. This is indeed suggested by singularity theorems showing that inflating false vacuum regions must be larger than the *true* vacuum horizon size [24, 35] according to some observers [14]. The FGG mechanism provides a potential loophole [8] because according to an observer in the background true vacuum spacetime, only a region the size of the black hole event horizon is removed.

There have, however, been lingering questions about whether the Farhi-Guth-Guven [20] “tunneling” process can actually occur. The oldest objection is the fact that the euclidean tunneling spacetime is not a regular manifold [20]. A more modern objection comes from holography: in the FGG mechanism, an observer in the background spacetime only sees a small black hole, whereas the inflating region “inside” should be described by a huge number of states [26, 49]. This entropy puzzle was recently considered by Freivogel et. al. [69], who have used the AdS/CFT correspondence to study thin-walled dS bubbles embedded in a background Schwarzschild-Anti-de Sitter space (Alberghi et. al. have also used the ADS/CFT correspondence to study charged vacuum bubbles [75]). They find that bubbles containing inflating regions which reside behind a wormhole are represented by mixed states in the boundary field theory. This resolves the entropy puzzle, and also implies that inflating regions hidden behind a wormhole cannot arise from a background spacetime by any unitary process, including tunneling. It does not, however, suggest why semi-classical methods break down, nor how we should interpret the seemingly-allowed tunneling.

¹This process cannot occur classically unless the weak energy condition is violated as discussed in Sec. 2.4.1.

The formalism that we outline in this chapter indicates that there are two ways to interpret tunneling through the effective potential of the junction conditions. The existing interpretation (the FGG mechanism) requires that the wall of a false vacuum bubble (and in some cases of true vacuum bubbles) must tunnel through a wormhole to produce an inflating region (see Fig. 4.1). This is a rather strange transition, as an observer in region I would see the bubble expand, reach its turning point, and then disappear, only to be replaced by a black hole. An observer inside the bubble would see the wall expanding away and – just as it is about to turn around and start collapsing – instead disappear behind the cosmological horizon. This observer will be inside an inflationary universe, but forever disconnected from region I. If the black hole in the SdS spacetime then evaporates, the baby universe will become completely topologically disconnected.

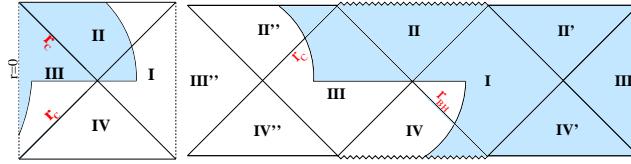


Figure 4.1: Tunneling spacetime

In this chapter, we use the global properties of the Schwarzschild-de Sitter spacetime to show that there is another interpretation corresponding to a mechanism that does not require the existence of a wormhole. In this mechanism, a small bubble of true or false vacuum, which would classically collapse, instead tunnels to a large bubble that exists outside of the *cosmological* horizon of the background spacetime. Consequently, this mechanism exists only in spacetimes with a positive cosmological constant. The zero-mass limit of this mechanism correctly reproduces the tunneling exponent for both true and false vacuum CDL bubbles [12, 13]. In light of the objections to the FGG mechanism, this new process may be an alternative, in which case

the formation of inflating false vacuum regions by tunneling is forbidden in flat spacetime. On the other hand, these may just be two competing processes, and we will directly compare the tunneling exponents under this assumption.

4.2 Hamiltonian formalism

In a pair of papers, Fischler et. al. (FMP) [40, 39] presented a calculation of the probability for transitions between various thin-wall false-vacuum bubble solutions. This calculation was done using Hamiltonian methods in the WKB approximation for the case where the exterior cosmological constant is zero. A similar calculation of such tunneling events was performed by Farhi et. al. [20] using a path integral approach. Both methods encounter the difficulty that the interpolating geometry involves a two-to-one mapping to the exterior spacetime, and thus is *not* a manifold. We will use the Hamiltonian approach, which is the most direct route to a tunneling exponent and temporarily skirts this issue (which we will not have the opportunity to discuss further in this thesis).

Here, we extend the calculation of FMP to include all spacetimes with arbitrary non-negative interior (Λ_-) and exterior (Λ_+) cosmological constants. This formalism, together with the catalog of all classically allowed solutions, will allow us to create a complete listing of the possible tunneling events.

4.2.1 An example from 1-D quantum mechanics

Before undertaking the full semi-classical calculation of the tunneling amplitude, let us formulate the equivalent problem in 1-D quantum mechanics. We will be using the theory of parametrized systems, in which one over-constrains the system to obtain the equations of

motion as a constraint. Consider the action of a particle in the presence of a 1-D potential

$$S[q(t)] = \int_{t_1}^{t_2} dt L \left(q, \frac{dq}{dt} \right). \quad (4.1)$$

The trick is to now define an auxiliary variable, τ , and promote t to a dynamical variable.

Changing variables to τ in the integral above and defining a new Lagrangian $\tilde{L} \equiv \dot{t}L$ (where the dot refers to a derivative with respect to τ), the action becomes:

$$S[q, t] = \int_{\tau_1}^{\tau_2} d\tau \tilde{L} (q, \dot{q}, \dot{t}) \quad (4.2)$$

The Hamiltonian is given by

$$\tilde{H} = \tilde{p}_q \dot{q} + \tilde{p}_t \dot{t} - \tilde{L}, \quad (4.3)$$

where the momenta are defined by

$$\tilde{p}_q \equiv \frac{\partial \tilde{L}}{\partial \dot{q}} = \frac{\partial L}{\partial \left(\frac{dq}{dt} \right)} = p_q, \quad (4.4)$$

and

$$\tilde{p}_t \equiv \frac{\partial \tilde{L}}{\partial \dot{t}} = L - p_q \frac{dq}{dt} = -H. \quad (4.5)$$

Plugging this back into \tilde{H}

$$\tilde{H} = \dot{t} (\tilde{p}_t + H), \quad (4.6)$$

we see that if we fix p_t , then this becomes a constraint:

$$\tilde{H} = 0. \quad (4.7)$$

Dropping the \dot{t} , and promoting H and \tilde{p}_t to operators,

$$H \rightarrow \hat{H} \quad (4.8)$$

$$\tilde{p}_t \rightarrow -i\hbar \frac{\partial}{\partial t} \quad (4.9)$$

if we impose the classical constraint on a wave function Ψ , we recover the Schrodinger equation

$$\left(\hat{H} - i\hbar \frac{\partial}{\partial t} \right) \Psi = 0 \quad (4.10)$$

We now want to discuss applying the WKB approximation, which we will do below. Any classical Hamiltonian can be decomposed into sum over functions of the position multiplied by some power of the momentum

$$H = \sum_{n=0}^{\infty} a_n(q)p^n. \quad (4.11)$$

Promoting the p and q to operators (with $\hat{p} \equiv -i\hbar\partial/\partial q$), we see that

$$\hat{H} = \sum_{n=0}^{\infty} [a_n(\hat{q})\hat{p}^n + O(\hbar) + \dots], \quad (4.12)$$

so to lowest order in \hbar , the Hamiltonian operator is obtained by neglecting operator ordering issues. We now make the ansatz that Ψ is separable, and the q -dependent piece can be written as

$$\Psi(q) = e^{\frac{i\sigma(q)}{\hbar}}. \quad (4.13)$$

plugging this into the Schrodinger equation ($\hat{H}\Psi(q) = E\Psi(q)$), we see that to lowest order in \hbar , we obtain

$$\sum_{n=0}^{\infty} a_n(q) \left(\frac{d\sigma}{dq} \right) = H \left(q, \frac{d\sigma}{dq} \right) = E. \quad (4.14)$$

The solution to lowest order in \hbar is therefore given by

$$\sigma = \int^q p(q')dq' \quad (4.15)$$

with $p(q')$ evaluated under the constraint that $H = E$.

If we are evaluating the wave function in classically un-allowed regions, then the momentum is imaginary, yielding

$$\sigma = i \int dt \dot{q}p. \quad (4.16)$$

Using the fact that at classical turning points, $H = -L_{turn}$, we see that the integral above is equivalent to

$$\sigma = i \int dt [L_E - L_{turn}]. \quad (4.17)$$

4.2.2 Full semiclassical calculation

Following FMP, we begin by making a coordinate transformation to recast the interior and exterior metrics in Eqs. A.68 and A.17 into the form

$$ds^2 = -N^t(t, r)^2 dt^2 + L(t, r)^2 [dr + N^r(t, r) dt]^2 + R(t, r)^2 (d\theta^2 + \sin^2 \theta d\phi^2), \quad (4.18)$$

where $N^t(t, r)$ is the lapse function, $N^r(t, r)$ is the shift, and $L \equiv ds/dr$. The action for a general theory of matter coupled to gravity is then given by

$$S = \int dt p \dot{q} + \int dr dt \left(\pi_L \dot{L} + \pi_R \dot{R} - N^t H_t - N^r H_r \right) \quad (4.19)$$

where π_L is the momentum conjugate to L , and π_R is the momentum conjugate to R . This action, with the four constraints

$$H_{t,r}(q, L, R, p, \pi_L, \pi_R) = 0, \quad (4.20a)$$

$$\pi_{N^t} = \pi_{N^r} = 0, \quad (4.20b)$$

fully determines the classical evolution of the system. For a thin-walled bubble with an arbitrary surface energy density k and interior and exterior cosmological constant (Λ_- and Λ_+), the Hamiltonian densities are given by

$$\begin{aligned} H_t &= \frac{L\pi_L^2}{2R^2} - \frac{\pi_L\pi_R}{R} \\ &+ \frac{1}{2} \left[\left[\frac{2RR'}{L} \right]' - \frac{R'^2}{L} - L + \Lambda_+ LR^2 \right] \\ &+ \Theta(r_w - r) \frac{(\Lambda_- - \Lambda_+)}{2} LR^2 \\ &+ \delta(r_w - r) (L^{-2} p_w^2 + k^2 R_w^4)^{1/2}, \end{aligned} \quad (4.21)$$

$$H_r = R' \pi_R - L \pi_L' - \delta(r_w - r) p_w, \quad (4.22)$$

where a prime denotes a derivative with respect to r and r_w is the position of the bubble wall (quantities with the subscript w are evaluated at this position).

A linear combination of the constraints Eq. 4.21 and 4.22 can be use to eliminate π_R

$$\frac{R'}{L}H_t + \frac{\pi_L}{RL}H_r = 0, \quad (4.23)$$

which, if we define

$$\mathcal{M} \equiv \frac{\pi_L^2}{2R} + \frac{R}{2} \left[1 - \left[\frac{R'}{L} \right]^2 - \frac{\Lambda_{\pm} R^2}{3} \right], \quad (4.24)$$

can be written as

$$\mathcal{M}' = \delta(r_w - r) \left(\frac{R'}{L} (L^{-2} p_w^2 + k^2 R_w^4)^{1/2} + \frac{\pi_L}{RL} p_w \right). \quad (4.25)$$

It can be seen from Eq. 4.25 that \mathcal{M} is zero for $r < r_w$ and independent of r for $r > r_w$. We will define $\mathcal{M}(r > r_w) \equiv M$, which is the mass enclosed by a surface with $r > r_w$. Solving for π_L at $r = 0$ and $r = \infty$ using the conditions on \mathcal{M} yields:

$$\pi_L^2 = -R^2 \left[1 - \left[\frac{R'}{L} \right]^2 - \frac{\Lambda_- R^2}{3} \right], \quad r < r_w \quad (4.26)$$

$$\pi_L^2 = -R^2 \left[1 - \left[\frac{R'}{L} \right]^2 - \frac{\Lambda_+ R^2}{3} - \frac{2M}{R} \right], \quad r > r_w. \quad (4.27)$$

From $H_r = 0$, solving for π_L' , and integrating from $r_w - \epsilon$ to $r_w + \epsilon$, one finds that the discontinuity in π_L across the wall ($\Delta\pi_L$) is

$$\Delta\pi_L = -\frac{p_w}{L_w}, \quad (4.28)$$

From $H_t = 0$, solving for R'' , and integrating from $r_w - \epsilon$ to $r_w + \epsilon$, one finds that the discontinuity in R' across the wall ($\Delta R'$) is

$$\Delta R' = -\frac{1}{R_w} [p_w^2 + k^2 L^2 R_w^4]. \quad (4.29)$$

These discontinuity equations are equivalent to the Israel junction conditions, and can be manipulated to reproduce Eq. 2.6. There are classically allowed and forbidden regions in the space

of R , L , and r , the boundaries between which can be found by looking for where the conjugate momenta are zero. There is, however, only one true degree of freedom, the classically allowed/forbidden region for which is classified by the potential Eq. 2.26. The unphysical degrees of freedom will allow for a variety of physically equivalent paths through the the space of (L, R, r) .

To quantize the system, we impose the constraints of Eq. 4.20 on the wave functional Ψ :

$$\hat{H}_t \Psi = \hat{H}_r \Psi = \hat{\pi}_{N^t} \Psi = \hat{\pi}_{N^r} \Psi = 0. \quad (4.30)$$

The last two constraints restrict the wave functional to depend only upon L , R , and r , which in the WKB approximation is taken to be

$$\Psi(L, R, r) = \exp[i\Sigma_0(L, R, r)/\hbar + O(\hbar)]. \quad (4.31)$$

We explicitly include \hbar here to emphasize the order of our approximation, but note that we use geometrical units in all other cases. Acting with \hat{H}_t and \hat{H}_r , and keeping terms in the Taylor expansion only to leading order in \hbar (which removes any operator ordering ambiguities) yields the Hamilton-Jacobi equations

$$H_{r,t}\left(r, L, R, \frac{\delta\Sigma_0}{\delta r}, \frac{\delta\Sigma_0}{\delta L}, \frac{\delta\Sigma_0}{\delta R}\right) = 0. \quad (4.32)$$

We will integrate

$$\delta\Sigma_0 = \hat{p}\delta\hat{r} + \int_0^\infty dr [\pi_L\delta L + \pi_R\delta R], \quad (4.33)$$

to solve for the exponent of the wave functional Eq. 4.31.

4.2.3 Calculating tunneling rates

The problem that we wish to solve is the tunneling amplitude in the WKB approximation to connect bound solutions with turning point R_1 to equal-mass unbound solutions with

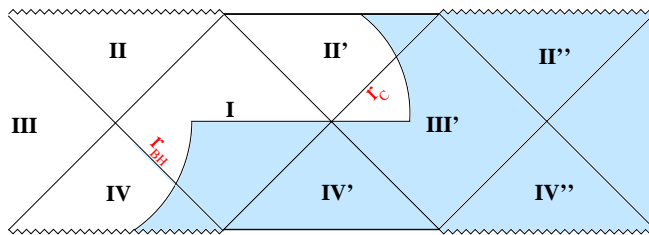


Figure 4.2: Tunneling from a bound solution to an unbound solution which exists outside the cosmological horizon.

turning point R_2 . An example of this is the FGG mechanism [20], which consists of two steps. First, an expanding region of false/true-vacuum, which would classically collapse into a black hole, is formed and evolves to the classical turning point. Here, there is a chance for the bubble wall to tunnel through the wormhole to one of the unbound solutions, as shown in Fig. 4.1. The result of this process is a black hole in the region of the old phase, which is connected by a wormhole to a universe containing an expanding bubble of the new phase.

As we saw in Sec. 2.4, because SdS is non-compact, there are many possible one-bubble spacetimes where region I of the SdS conformal diagram is not physical. We can therefore imagine tunneling from the bound Solution 1 or Solution 2 of Fig. 2.12 to the unbound spacetime shown in Fig. 2.14. This process, which can occur only in the presence of a positive exterior cosmological constant, is depicted in Fig. 4.2. For every transition which goes through the wormhole, as in the FGG mechanism, there is another transition which instead goes out the cosmological horizon.

There are many possible transitions to consider, corresponding to the many qualitatively different spacetimes shown in Figs. 2.12 and 2.13. In each case, the tunneling probability in the WKB approximation is given by

$$P(R_1 \rightarrow R_2) = \left| \frac{\Psi(R_2)}{\Psi(R_1)} \right|^2 \simeq e^{2i\Sigma_0[R_2 - R_1]}, \quad (4.34)$$

where $[R_2 - R_1]$ represents evaluation between the two turning points of the classical motion,

and Σ_0 is obtained by integrating Eq. 4.33. The plan of attack is to split the integral into three parts: one over the interior of the bubble, one over the exterior, and one in the neighborhood of the wall. We thus write:

$$i\Sigma_0 = F_I [R_2 - R_1] + F_O [R_2 - R_1] + F_w [R_2 - R_1]. \quad (4.35)$$

The integrals F_I and F_O are found by holding r_w and the geometry in the neighborhood of the wall fixed, while allowing nontrivial variation of L and R in the interior and exterior spacetimes. Following FMP, we will integrate L along a path of constant R to the boundary of the classically allowed/forbidden region, and then integrate along this boundary to the desired configuration of $L(r), R(r)$. The momenta vanish along this second leg, and so the integral will be of π_L over L

$$\begin{aligned} F_I &= \int_0^{\hat{r}} dr \int dL (\pm \pi_L) \\ &= \pm \int_0^{\hat{r}} dr \left[i\pi_L - RR' \cos^{-1} \left(\frac{R'}{La_{\text{ds}}^{1/2}} \right) \right]. \end{aligned} \quad (4.36)$$

Note that there is an ambiguity in the sign. This comes from the fact that the constraints (Eq. 4.26 and 4.27) are second order in the momenta, and so we must account for both the positive and negative roots. To keep track of this ambiguity, we will define a variable $\eta \equiv \pm 1$ with $\sqrt{\pi_L^2} = \eta\pi_L$. We shall have more to say about this issue later.

At the turning point, π_L vanishes. The integral evaluated between the two turning points is then

$$F_I [R_2 - R_1] = \eta \int_{R_1}^{R_2} dRR \cos^{-1} \left(\frac{R'}{La_{\text{ds}}^{1/2}} \right) \quad (4.37)$$

The integral outside the bubble wall ($r > r_w$) is given by

$$F_O = \eta \int_{r_w}^{\infty} dr \left[i\pi_L - RR' \cos^{-1} \left(\frac{R'}{La_{\text{ds}}^{1/2}} \right) \right] \quad (4.38)$$

which evaluated between the two turning point becomes

$$F_O [R_2 - R_1] = \eta \int_{R_1}^{R_2} dR R \cos^{-1} \left(\frac{R'}{L a_{\text{sds}}^{1/2}} \right) \quad (4.39)$$

At the turning point, R' inside and outside of r_w is given by solving Eqs. 4.26 and 4.27 for R' :

$$R'(r_w - \epsilon) = \pm L a_{\text{ds}}^{1/2}, \quad R'(r_w + \epsilon) = \pm L a_{\text{sds}}^{1/2}. \quad (4.40)$$

Therefore, the inverse cosine in the integrals of Eq. 4.37 and 4.39 are either 0 when R' is positive or π when R' is negative. To perform these integrals, imagine moving the wall along the tunneling hypersurface ($t = 0$) between the two turning points (for an example, see Fig. 4.1). The sign of β is positive if the coordinate radius r is increasing in a direction normal to the wall and negative if it is decreasing. Therefore, the sign of R' is equal to the sign of β as one moves along the tunneling hypersurface, and the integrals Eq. 4.37 and 4.39 will be zero in regions of positive β and π in regions of negative β .

Shown in table 4.1 are the values of F_O and F_I for all of the possible transitions where the unbound solution is to the left, on the conformal diagram, of the bound solution (for example, the process shown in Fig. 4.1), which in all cases but $B > 3(A - 1)$ with $M > M_S$ (the mass at which β_{sds} changes sign on the effective potential) occurs through a wormhole (for $B > 3(A - 1)$ with $M > M_S$, the most massive bound and unbound solutions can both be behind a worm hole). We will refer to these solutions as L(ef) tunneling geometries. These are the solutions studied by FGG and FMP, but we have seen above that there are actually many other allowed processes due to the non-compact properties of the SdS spacetime. These are tunneling processes where the unbound solution lies to the right of the bound solution on the conformal diagram, which we will refer to as R(ight) tunneling geometries. The values of the integrals F_I and F_O in this case are shown in table 4.2. In all cases except for $B > 3(A - 1)$ with $M > M_S$, the bubble wall exits the cosmological horizon (whereas the L tunneling geometries

went through a wormhole), as in Fig. 4.2 (for $B > 3(A - 1)$ with $M > M_S$, the bubble wall traverses a wormhole and cosmological horizon).

There still is one more integral to evaluate, which allows for the variation of the geometry at the position of the wall

$$F_w [R_2 - R_1] = \int_{R_1}^{R_2} dR_w R_w \left[\cos^{-1} \left[\frac{6M + 3k^2 R_w^3 - R_w^3 (\Lambda_- - \Lambda_+)}{6k R_w^2 a_{\text{ds}}} \right] - \cos^{-1} \left[\frac{6M - 3k^2 R_w^3 - R_w^3 (\Lambda_- - \Lambda_+)}{6k R_w^2 a_{\text{ds}}} \right] \right]. \quad (4.41)$$

We have been unable to find an analytic expression for this integral, and so have evaluated it numerically.

Putting everything together, we can evaluate the tunneling exponent for the various cases shown in tables 4.1 and 4.2. Shown in Fig. 4.3 is an example of $2i\Sigma_0$ for both the L (blue dashed line) and R (red solid line) tunneling geometries with $3(A - 1) < B < A + 3$ ($A = 1$, $B = 6$), where we have taken $\eta = +1$. The vertical dashed lines represent the mass scales M_D (left) and M_S . L tunneling geometries with $M < M_S$ correspond to tunneling through a wormhole. The magnitude of these tunneling exponents is fixed by the inverse bubble wall tension squared (k^{-2}), which in geometrical units ranges from $k^{-2} \simeq 10^{102}$ for a tension set by the Weak scale to $k^{-2} \simeq 1$ for a tension set by the Planck scale.

4.2.4 High- and low-mass limits

Note that as the mass increases, the width of the potential barrier that must be crossed decreases (see the potential diagrams in Fig. 2.8, 2.9, 2.10, and 2.11). We therefore expect that the tunneling exponent (for tunneling through the effective potential) goes to zero at the top of the barrier. However, the tunneling exponent is not always zero at the top of the potential, as can be seen from the tunneling exponent for the R tunneling geometry shown in Fig. 4.3 (red solid line). To see how this happens, consider a mass slightly below the maximum of the

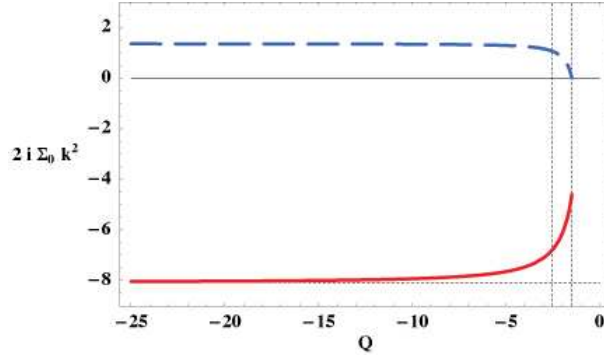


Figure 4.3: Tunneling exponent as a function of Q for $(A = 1, B = 6)$ (false vacuum bubbles). The blue dashed line is for the L tunneling geometries, while the red solid line is for the R tunneling geometries. The vertical dotted lines denote the mass scales M_D (left) and M_S (right) described in Tables 4.1 and 4.2. The horizontal dotted line is at the value of the CDL tunneling exponent (Eq. 4.42).

effective potential. The bound solutions are the same for both the L and R tunneling geometries (Solutions 1 or 2), but the unbound solutions to which we are tunneling differ. For a bound Solution 1, we are tunneling to one of the two versions (corresponding to the L or R tunneling geometry) of either Solution 6, 10, or 11 depending on the values of A and B . For a bound Solution 2, we are tunneling to one of the two versions of either Solution 8 or 9.

In the case where $B > 3(A - 1)$ (the situation pictured in Fig. 4.3), the most massive L tunneling geometry will have the bound and unbound solutions smoothly merge as the top of the potential barrier is approached. The most massive R tunneling geometry in this case will find the bound and unbound solutions separated by both a black hole and cosmological horizon, and so the tunneling exponent at the top of the potential well will be given by $2i\Sigma_0 = \pi (R_S^2 - R_C^2)$. This situation is reversed when $B < 3(A - 1)$, where the R tunneling geometry will possess the smooth high mass limit, and the most-massive L tunneling geometry will have a non-zero tunneling exponent.

Now consider the other end of the mass spectrum: the zero mass limit of the two different tunneling geometries. In either case, as the mass is taken to zero, the turning point of

the bound solution goes to zero, and the turning point of the unbound solution approaches the nucleation radius of a CDL bubble (see Eq. 2.13). Even so, there is a fundamental difference between these two solutions when the background spacetime is considered.

As the mass is taken to zero in the L tunneling geometry (corresponding to the FGG mechanism), the worm hole separating the background of the old phase and the bubble of the new phase disappears. This leaves a background spacetime in which absolutely nothing happens, along with a universe containing a CDL bubble which is created from nothing. At least in the zero-mass limit, this means that we are calculating Vilenkin's tunneling wave function for an inhomogenous universe [76, 77, 78] with the tunneling exponent equal in magnitude to the CDL instanton action (without the background subtraction term).

This situation is rather strange: if considered one physical system, we have seemingly created new degrees of freedom. It is therefore unclear how we should interpret the tunneling probability; what are we fluctuating out of, and probability per unit what? The massive case seems to create new degrees of freedom as well, since the region to the left of the worm hole (containing large regions of both the old and new phase) in Fig. 4.1 does not exist prior to the tunneling event. It is perhaps not so surprising then that Freivogel et. al. [69] have found that when a conformal field theory dual to FGG tunneling from AdS is constructed using the AdS/CFT correspondence, it corresponds to a non-unitary process.

The zero mass limit of the R tunneling geometry corresponds to the nucleation, in some background, of a CDL true- or false-vacuum bubble. The CDL tunneling exponent (including the background subtraction) can be written as [32, 79]

$$S_{\text{CDL}} = \frac{3\pi}{2} \left[\frac{1}{\Lambda_+} (1 - b\alpha_+) - \frac{1}{\Lambda_-} (1 - b\alpha_-) \right], \quad (4.42)$$

where

$$\alpha_{\pm} = \frac{\Lambda_+ - \Lambda_-}{6k} \mp \frac{k}{2}, \quad (4.43)$$

and

$$b = \sqrt{\frac{3}{\Lambda_- + 3\alpha_-^2}}. \quad (4.44)$$

The horizontal dotted line in Fig. 4.3 is the value of the CDL tunneling exponent for a particular choice of parameters, and it can be seen that the zero mass limit ($Q \rightarrow -\infty$) of the tunneling geometry with no wormhole asymptotes to this. Similar results were found in the case of *true*-vacuum bubbles by Ansoldi et. al. [80], who were able to reproduce the CDL tunneling exponent using a Hamiltonian formalism.

It can be seen in Fig. 4.3, that the tunneling exponent takes opposite signs for the two tunneling geometries (Fig. 4.1 and Fig. 4.2). For both tunneling probabilities to be less than one, η must take opposite signs in each case. We have found that the zero-mass limit of the L tunneling geometry (FGG mechanism) corresponds to creation of an inhomogenous universe from nothing. This perspective suggests that the sign choice we are forced to make is a reflection of some quantum-cosmological boundary conditions, since choosing the sign of η is tantamount to choosing the growing or decaying wave function in the region under the well. Taking linear combinations of the growing and decaying wave functionals would yield any one of the three existent sign conventions of Hartle and Hawking [81], Linde [82], and Vilenkin [76]. In contrast, the sign choice is rather straightforward for the R tunneling geometries. This process has a clear-cut interpretation in terms of a fluctuation between true- and false-vacuum regions. Thus, we might physically interpret the low CDL probability as the low probability for a downward entropy fluctuation in the background spacetime to occur [49].

If both tunneling geometries are allowed, we have two processes which correspond to tunneling under the same potential well Eq. 2.26. It is unclear exactly how one is to interpret this situation, but if it were the case that only one of these two interpretations were valid, there would be a number of important consequences. For example, if the FGG mechanism (L

Table 4.1: $F_I [R_2 - R_1]$ and $F_O [R_2 - R_1]$ for the tunneling geometries with the unbound final state lying to the left of the bound initial state (L tunneling geometries). The mass scales indicated can be located on the potential diagrams by identifying M_D as the point on the potential where β_{ds} changes sign, M_S with the point on the potential to the left of the max β_{sds} changes sign, and M_{SDS} with the point on the potential to the right of the max where β_{sds} changes sign.

A and B	M	$F_I [R_2 - R_1]$	$F_O [R_2 - R_1]$
$3(A - 1) < A + 3 < B$	$M < M_D$	$\frac{\pi}{2} (R_D^2 - R_2^2)$	$\frac{\pi}{2} (R_2^2 - R_S^2)$
$3(A - 1) < A + 3 < B$	$M_D < M < M_S$	0	$\frac{\pi}{2} (R_2^2 - R_S^2)$
$3(A - 1) < A + 3 < B$	$M > M_S$	0	$\frac{\pi}{2} (R_2^2 - R_1^2)$
$3(A - 1) < B < A + 3$	$M < M_S$	0	$\frac{\pi}{2} (R_2^2 - R_S^2)$
$3(A - 1) < B < A + 3$	$M > M_S$	0	$\frac{\pi}{2} (R_2^2 - R_1^2)$
$A + 3 < B < 3(A - 1)$	$M < M_D$	$\frac{\pi}{2} (R_D^2 - R_2^2)$	$\frac{\pi}{2} (R_2^2 - R_S^2)$
$A + 3 < B < 3(A - 1)$	$M_D < M < M_{SD}$	0	$\frac{\pi}{2} (R_2^2 - R_S^2)$
$A + 3 < B < 3(A - 1)$	$M < M_{SD}$	0	$\frac{\pi}{2} (R_C^2 - R_S^2)$
$B < A + 3 < 3(A - 1)$	$M < M_{SD}$	0	$\frac{\pi}{2} (R_2^2 - R_S^2)$
$B < A + 3 < 3(A - 1)$	$M > M_{SD}$	0	$\frac{\pi}{2} (R_C^2 - R_S^2)$
$A > B + 3$	$M < M_{CRIT}$	0	$\frac{\pi}{2} (R_C^2 - R_S^2)$
$A > \frac{B}{3} + 1$	$M < M_{SD}$	0	$\frac{\pi}{2} (R_2^2 - R_S^2)$
$A > \frac{B}{3} + 1$	$M > M_{SD}$	0	$\frac{\pi}{2} (R_2^2 - R_S^2)$
$A < \frac{B}{3} + 1$	$M < M_S$	0	$\frac{\pi}{2} (R_2^2 - R_S^2)$
$A < \frac{B}{3} + 1$	$M > M_S$	0	$\frac{\pi}{2} (R_2^2 - R_1^2)$

tunneling geometry) is in fact forbidden, then there would be no possible thin-wall false-vacuum bubble nucleation events in Minkowski space. We have also seen above that the bound and unbound solutions will merge into the monotonic solution at the top of the potential for *either* the L or R tunneling geometry, but never both. Since in the low mass limit only the R tunneling geometry matches the tunneling exponent for CDL bubbles, if one were to choose between the two mechanisms, either the low or the high mass end of the spectrum would be discontinuous for some range of parameters. We hope to explore these points further in future work.

Having developed the necessary tools to calculate the exponent for tunneling from bound to unbound vacuum bubbles, we now finish the development of a framework which will allow us to compare the relative likelihood for all thin-walled vacuum transitions to occur.

Table 4.2: $F_I [R_2 - R_1] + F_O [R_2 - R_1]$ for the tunneling geometries with the unbound final state lying to the *right* of the bound initial state (R tunneling geometries). The mass scales indicated can be located on the potential diagrams by identifying M_D as the point on the potential where β_{ds} changes sign, M_S with the point on the potential to the left of the max β_{sds} changes sign, and M_{SDS} with the point on the potential to the right of the max where β_{sds} changes sign.

A and B	M	$F_I [R_2 - R_1]$	$F_O [R_2 - R_1]$
$3(A - 1) < A + 3 < B$	$M < M_D$	$\frac{\pi}{2} (R_D^2 - R_2^2)$	$\frac{\pi}{2} (R_2^2 - R_C^2)$
$3(A - 1) < A + 3 < B$	$M_D < M < M_S$	0	$\frac{\pi}{2} (R_2^2 - R_C^2)$
$3(A - 1) < A + 3 < B$	$M > M_S$	0	$\frac{\pi}{2} (R_2^2 - R_1^2 + R_S^2 - R_C^2)$
$3(A - 1) < B < A + 3$	$M < M_S$	0	$\frac{\pi}{2} (R_2^2 - R_C^2)$
$3(A - 1) < B < A + 3$	$M > M_S$	0	$\frac{\pi}{2} (R_2^2 - R_1^2 + R_S^2 - R_C^2)$
$A + 3 < B < 3(A - 1)$	$M < M_D$	$\frac{\pi}{2} (R_D^2 - R_2^2)$	$\frac{\pi}{2} (R_2^2 - R_C^2)$
$A + 3 < B < 3(A - 1)$	$M_D < M < M_{SD}$	0	$\frac{\pi}{2} (R_2^2 - R_C^2)$
$A + 3 < B < 3(A - 1)$	$M > M_{SD}$	0	0
$B < A + 3 < 3(A - 1)$	$M < M_{SD}$	0	$\frac{\pi}{2} (R_2^2 - R_C^2)$
$B < A + 3 < 3(A - 1)$	$M > M_{SD}$	0	0
$A > B + 3$	$M < M_{\text{CRIT}}$	0	0
$A > \frac{B}{3} + 1$	$M < M_{SD}$	0	$\frac{\pi}{2} (R_2^2 - R_C^2)$
$A > \frac{B}{3} + 1$	$M > M_{SD}$	0	0
$A < \frac{B}{3} + 1$	$M < M_S$	0	$\frac{\pi}{2} (R_2^2 - R_C^2)$
$A < \frac{B}{3} + 1$	$M > M_S$	0	$\frac{\pi}{2} (R_2^2 - R_1^2 + R_S^2 - R_C^2)$

4.3 Comparison of the Tunneling Exponents

Assuming that the FGG mechanism exists (the L tunneling geometries), and that we can choose the overall tunneling exponent to be negative for both the L and R tunneling geometries, we now venture to directly compare the tunneling rates for these two processes. In a cosmological setting, we must fluctuate the bound solution which will expand to its turning point and possibly tunnel to one of the unbound solutions. In the absence of a detailed theory of the nature of these fluctuations, we assume that the probability of fluctuating a solution of a given mass is given by the exponential of the entropy change due to the change in the area of the exterior dS horizon in the presence of a mass [83, 8]

$$P_{\text{seed}} = \exp \left[-\pi \left(\frac{3}{\Lambda_+} - R_C^2 \right) \right], \quad (4.45)$$

where R_C is the radius of curvature of the cosmological horizon in SdS.

Once the bound solution has been fluctuated, it must survive until it reaches the turning point of the classical motion. The authors have shown [14] that any solution with a turning point is unstable against non-spherical perturbations. Even quantum fluctuations present on the bubble wall at the time of nucleation will go nonlinear over some range of initial size and mass. Presumably, these asphericities will affect the tunneling mechanism discussed in the previous section, and may be a significant correction to these processes. Seed bubbles can, however, avoid this instability by forming as near-perfect spheres very near the turning point; in the spectrum of possible fluctuations, there will inevitably be some such events.

Assuming that the seed bubble is still reasonably spherically symmetric when it reaches the turning point, the probability to go from empty dS to the spacetime containing an expanding vacuum bubble is given by the product

$$P \simeq CP_{\text{seed}} e^{2i\Sigma_0} \equiv Ce^{-S_E}. \quad (4.46)$$

Shown in Fig. 4.4 is $-S_E$ as a function of Q for $(A = 1, B = 6)$, normalized to k^{-2} , for both the L tunneling geometries (blue dashed line) and R tunneling geometries (red solid line). In this case, it can be seen that the L tunneling geometries (which pass through the worm hole) are always more probable than R tunneling geometries (which pass through the cosmological horizon). Also, note that the zero mass ($Q \rightarrow \infty$) solution is in both cases the most probable, even though the width of the potential barrier is largest in this limit.

We can locate and match the tunneling exponent for thermal activation [32] in Fig. 4.4 as the most massive R tunneling geometry (the solution resting on top of the potential in Fig. 2.9), which is denoted by the dot at the far right of the red solid curve. These solutions are bubbles which form in unstable equilibrium between expansion and collapse. We find, in agreement with Garriga and Megevand [32], that thermal activation is always sub-dominant to CDL.

We have seen above that the R tunneling geometry possesses a smooth high-mass limit only for $B < 3(A - 1)$. The post-tunneling spacetime for this range of parameters is Solution 16 (see Fig. 2.15). However, our picture of the spacetime for $B > 3(A - 1)$ is somewhat different than Solution 17 of Fig. 2.15, which is the post-tunneling spacetime found in Ref. [32]. We find instead that the bubble nucleates outside the cosmological horizon (in the process removing a large section of the background de Sitter) as opposed to behind a worm hole (which leaves the background de Sitter space intact).

We have studied examples of the tunneling exponent for all of the possible situations listed in Tables 4.1 and 4.2. The zero mass solution is always the most probable for both the L and R tunneling geometries. Depending on the values of A and B , either the L or R tunneling geometries can dominate. Shown in Fig. 4.5 is an example of a true-vacuum bubble with $(A = 9, B = 20)$; in this case the R tunneling geometries dominate. We can solve for the regions of parameter space where one geometry or another dominates by looking at the zero mass limit. The zero mass limit of the R tunneling geometry is CDL, and the tunneling exponent is given by Eq. 4.42 (this includes the background subtraction). The zero mass limit of the L tunneling geometry (FGG) corresponds to the creation from nothing of a universe of the old phase containing a CDL bubble. The tunneling exponent in this case is numerically equal to $3\pi/\Lambda_+ - S_{CDL}$. Taking the difference of the two tunneling exponents, we find that the L tunneling geometries will be dominant when $2S_{CDL} > 3\pi/\Lambda_+$.

Depending on the values of the interior and exterior cosmological constant, the picture of vacuum transitions can be very complicated. For comparable cosmological constants, the situation is the most complicated, with both tunneling geometries and all mass scales having tunneling exponents of the same order of magnitude. While one mechanism will dominate, it may not overwhelm the slightly less probable possibilities. In the case where $\Lambda_+ \ll \Lambda_-$, the zero mass limit of the L tunneling geometry (creation of a universe from nothing containing a

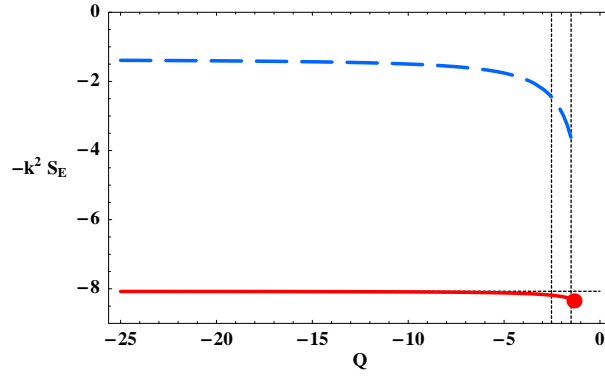


Figure 4.4: The exponent for the creation of a false-vacuum bubble from empty de Sitter as a function of Q for $(A = 1, B = 6)$. The blue dashed line is for the L tunneling geometries, while the red solid line is for the R tunneling geometries. The horizontal dotted line is the CDL tunneling exponent. The vertical dotted lines denote the Q corresponding to M_D (left) and M_S (right).

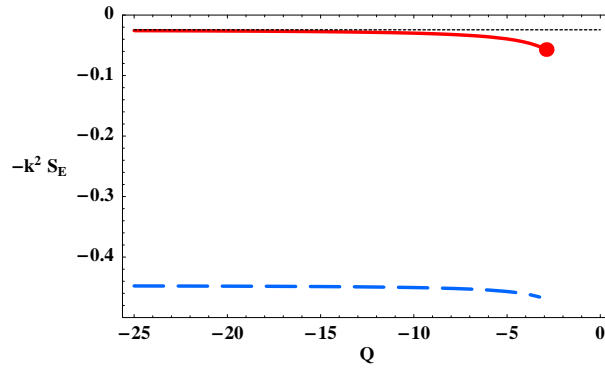


Figure 4.5: Tunneling exponent as a function of Q for $(A = 9, B = 20)$ (true-vacuum bubbles). The blue dashed line is for the L tunneling geometries, while the red solid line is for the R tunneling geometries.

CDL bubble) dominates. In the case where $\Lambda_+ \gg \Lambda_-$, the zero mass limit of the R tunneling geometry (CDL true-vacuum bubbles) will dominate.

4.4 The bottom line

In the context of the junction condition potentials Figs. 2.8, 2.9, 2.10, and 2.11, we now have a very organized picture of the types of vacuum transitions which are allowed. At one extreme, corresponding to $Q \rightarrow -\infty$ ($M \rightarrow 0$), we have *both* CDL bubble nucleation or the creation of a bubble spacetime from nothing. Moving up the potential in Q , we have the L tunneling geometries (FGG mechanism) and/or the R tunneling geometries. These are two-step processes, involving both a thermal fluctuation of the bound solution and a quantum tunneling event through the potential. At the top of the potential, we have the thermal activation mechanism, which is a one step, entirely thermal process. This completes our picture of the possible vacuum transitions, but still leaves unclear which processes actually occur.

The semi-classical picture that we have assembled has raised a number of important questions in this regard. For instance, we have seen in the derivation of the tunneling exponent that the L and R tunneling geometries require different sign conventions to ensure a well-defined transition amplitude. Since the zero-mass limit of the L tunneling geometry describes the creation of a universe from nothing, this sign choice indicates a connection with quantum cosmology. However, there does not seem to be any well defined reason to choose one sign convention over the other, or to allow both.

There is also the question of how to reconcile the high- and low mass-limits of the L and R tunneling geometries. We have seen that the zero-mass limit of the R tunneling geometry always describes the nucleation of true- or false-vacuum CDL bubbles. It is therefore tempting to use this as evidence that the L tunneling geometries are not allowed. However, in a number

of cases the high-mass limit of the R tunneling geometry is discontinuous in the sense that the pre-tunneling bound solution does not approach the post-tunneling unbound solution as the top of the effective potential is reached. In these cases, the high-mass limit of the L tunneling geometry *is* continuous. Thus, even though the low-mass limit of the L tunneling geometry is rather strange (the creation of a universe from nothing), the high-mass limit seems completely reasonable. This complicates any hope of ruling out all L or all R tunneling geometries based on the reasonableness of the high- and low-mass limits of the effective potential.

There is also the problem that the L tunneling geometry is never a manifold [20, 40]. That is, the Euclidean interpolating geometry between the pre- and post-tunneling states always has a degenerate metric. It is unclear that such metrics should be included in the path integral, and a better understanding of the true theory of quantum gravity might indicate that both, either, or neither the L and/or R tunneling geometries are allowed. It is nevertheless an interesting question to ask if the R tunneling geometries suffer from this pathology as well, and complete analysis of the L and R tunneling geometries will be treated in a future publication.

4.5 Conclusions

The effective potentials of the junction condition formalism which were used to construct the solutions in Chapter 2 clearly indicate the existence of a region of classically forbidden radii separating bound solutions from unbound solutions. There are seemingly two processes which correspond to quantum tunneling through this same region, which we refer to as the L and R tunneling geometries. Both processes begin with a bound solution, which might be fluctuated by the background dS spacetime as we have assumed in Sec. 4.3. This bound solution then evolves to its classical turning point, where it has a chance to tunnel to an unbound solution, which is typically either through a wormhole in the case of the L tunneling geometries (the

Farhi-Guth-Guven, or FGG, mechanism) or through a cosmological horizon in the case of the R tunneling geometries.

The R tunneling geometries without a wormhole have a very clear interpretation in terms of the transition of a background spacetime to a spacetime of a different cosmological constant. Indeed, the zero-mass limit corresponds exactly to the nucleation of true- and false-vacuum CDL (Coleman-De Luccia) bubbles, correctly reproducing the radius of curvature of the bubble at the time of nucleation, as well as the tunneling exponent.

The L tunneling geometries (FGG mechanism) have a rather perplexing interpretation, which is most clearly seen by studying the zero mass limit. This corresponds to absolutely nothing happening in the background spacetime, while a completely topologically disconnected universe containing a CDL bubble of the new phase is created from nothing. The massive L tunneling geometries also have an element of this creation from nothing. Before the tunneling event, there is no wormhole, but after the tunneling event, there is a wormhole behind which is a large (eventually infinite) region of the old phase surrounded by a bubble of the new phase. It is unclear how we are to interpret this as the transition of a background spacetime to a spacetime of a different cosmological constant, since the background spacetime remains completely unaffected save for the presence of a black hole.

We have found that the sign of the Euclidean action is opposite for the L and R tunneling geometries, and while the second order constraints on the momenta introduce a sign ambiguity, it is unclear how to correctly fix the signs in light of the existence of two seemingly different processes for tunneling in the same direction through the same potential. A complete explanation of these processes will most likely rely on the resolution of some very deep problems in quantum cosmology.

The instability discussed in Chapter 2 also introduces complications into the use of the L and R geometries as a means of baby universe production. The existing calculations of

the tunneling rate rely heavily on the assumption of spherical symmetry. It is unclear how to perform a similar calculation for a (possibly non-linearly) perturbed bubble, as the number of degrees of freedom has drastically increased and the assumption of a minisuperspace of spherically symmetric metrics is no longer good. Further, the bubble interior will become filled with scalar gradient and kinetic energy and gravity waves, possibly upsetting the interior sufficiently to prevent vacuum energy domination. One might argue that in an eternal universe there is plenty of time to wait around for a fluctuation which is sufficiently spherical. However, to fully understand the importance of these mechanisms, one must both have a model of the scalar field fluctuations, which would predict the distribution of bubble shapes and masses, and also a model for tunneling in the presence of asphericities.

If we take the stance that the L and R tunneling geometries are in competition as two real descriptions of a transition between spacetimes with different cosmological constants, then we must directly compare their relative probabilities. We have shown in Section 4.3 that the zero-mass solution is always the most probable for either the L or R tunneling geometries, and that the L tunneling geometry will be dominant when $2S_{CDL} > 3\pi/\Lambda_+$. Therefore, if one is considering drastic transitions of the cosmological constant, the zero-mass FGG mechanism will be the dominant mechanism for upward fluctuations and the nucleation of true-vacuum CDL bubbles will be the dominant mechanism for downward fluctuations. This situation upsets the picture of fluctuations in the cosmological constant satisfying some kind of detailed balance [13, 49].

It does, however, help to explain how spawning an inflationary universe from a non-inflating region might be a feasible cosmology [8]. In the picture that we have presented, both the L and R tunneling geometries are constructed by carving some volume out of the background spacetime and filling it with the new phase. The size of this region is in some sense a measure of how special the initial conditions for inflation are. In the case of the R tunneling geometries, a

huge number of the states of the background spacetime must be put into the false vacuum at high cost in terms of the probability of such a fluctuation occurring [49]. The L tunneling geometries avoid this cost by fluctuating new states already in the false vacuum (this is of course a non-unitary process as discussed by Frievogel et. al. [69]), with the result that beginning inflation is no longer prohibitively difficult. The question of how much of the background spacetime must make the transition to the false vacuum is therefore crucial to determining exactly how special the initial conditions for inflation are. Unfortunately, detailed balance and the resolution of the paradoxes associated with the initial conditions for inflation are seemingly incompatible, but hopefully future work will yield further insight into the old but still interesting theory of vacuum transitions.

Part II

Eternal Inflation

Chapter 5

Measures for Eternal Inflation

The simplest example of a phenomenon known as eternal inflation occurs in the context of a scalar field potential with a positive energy false vacuum and a positive, zero, or negative energy true vacuum. The false vacuum is in this case considered to be the inflationary phase, and the true vacuum the post-inflationary phase. If the nucleation rate of true vacuum bubbles is smaller than one per false vacuum Hubble time, then the bubbles will not percolate. In this situation, collisions between bubble walls become very infrequent (though each bubble will eventually undergo an infinite number of collisions), and it will always be possible to define a time-slicing in which the three-volume of false vacuum increases without bound in the future. This type of eternal inflation will henceforward be denoted as "False Vacuum Eternal Inflation."

There is also a second type of eternal inflation, "Slow Roll Eternal Inflation," that occurs when the quantum diffusion of a scalar field with a very flat potential overwhelms the classical force on the field to roll to lower energy density. In this case, local (super-Hubble) fluctuations can occur which increase the energy density. On large scales, this produces a situation in which it is again possible to define a time-slicing such that the three-volume of the inflating phase (region of high energy density) increases without bound in the future.

In either type of eternal inflation, given the appropriate potential, there will be local regions which undergo reheating, structure formation, and cosmological evolution not unlike that which we observe. In light of this fact, it is tempting to assert that our observable universe is merely a tiny region of a much larger, eternally inflating multiverse (here defined as a spacetime which has local regions exhibiting different physical properties). Indeed, the realization that string theory predicts a Landscape of different vacua [84, 85, 86, 87], each potentially connected by transitions of the types expounded upon in previous chapters, has underscored the importance of understanding eternal inflation.

In this picture, there are seemingly many different low-energy theories consistent with the fundamental theory they were derived from (string theory), and a mechanism by which each of these low-energy theories is *actually realized* in different spatiotemporal regions of a large multiverse. In the simplest scenario, this leads to variation of physical constants, while the structure of low-energy physics remains the same (ie dimensionality, symmetry breaking scheme, etc.), though the topography of the landscape is far from being understood, and it is unclear that this picture is valid.

Considering the variation of the constants of nature presents us with a number of questions, of increasing ambition. One interesting proposal is to try to construct a map of the multiverse, asking the question: statistically, which regions will have which properties? The more ambitious proposal is to try to interpret the relevance of such a map to making predictions for the various constants of nature that we observe in our universe. We might be tempted to ask a question like: why do we observe the particular properties we see in the part of the universe we have access to?

As it stands, such a question is ill-defined; we need to be more specific. What we might hope for is a question like: "*What are the most probable values of various parameters that a randomly chosen object would observe?*" The relevant quantity to calculate would be the

probability, $\mathcal{P}_X(\alpha)$, that a randomly chosen X is in a region with properties α , where X is some “conditionalization object” such as a point in space, a baryon, a galaxy, or an “observer” that arguably makes \mathcal{P}_X relevant to what we will actually observe in some future experiment (see, e.g., [88, 89]). This probability is generally split into two components:

$$\mathcal{P}_X(\alpha) \propto P_p(\alpha)n_{X,p}(\alpha). \quad (5.1)$$

Here, P_p is a “prior” probability distribution defined in terms of some type of object p regardless of the conditionalization object X , and α is a vector of properties we might hope to compare to locally observed properties of our universe. For example, if p = “pocket universe” then $P_p(\alpha)$ describes the probability that a randomly chosen bubble has low-energy observable properties α . The factor $n_{X,p}$ conditions these probabilities by the requirement that some X -object exists; for example with X = “galaxy”, $n_{X,p}(\alpha)$ might count the (α -dependent) number of galaxies in a pocket with properties α .

If we associate ourselves with the randomly chosen X object, then we have made an assumption: the principle of mediocrity; we are typical among a given class of observers. Under this assumption, it becomes possible to make *statistical* prediction for the various constants of nature.

A very important component of the predictions outlined above are selection effects, that is to say, we must ask: what is it possible for the class of observers we are considering to observe? This is related to the anthropic principle (according to some authors, by anthropic [90], one is necessarily talking about human-like observers, here we take it to refer to whatever class of observers one is willing to discuss, and will interchange “anthropic” and “selection”): the conditions for observers to exist must be met in order for them to make observations. Note that selection effects are in many ways similar to considering conditional probabilities. For instance, by choosing the class of observers to be “carbon-based life existing in galaxies,” we

have conditioned on the fact that such observers could not exist outside of a certain window of density perturbations, strength of coupling constants, higgs vev, etc. Many of these selection effects are very strong, for instance if the strength of the strong interactions were different by less than one percent, then stable nuclei could not exist.

This conditionalization procedure is perhaps one of the most vexing problems for making predictions in eternal inflation. As emphasized by Linde [90, 91], most of the volume in an inflationary universe is "dead." That is, normal observers are produced only during a very short time after the end of inflation, since the energy density produced during reheating is diluted by the de Sitter expansion if the vacuum in question has a positive cosmological constant. One must now ask the question of how this dead volume might produce additional observers in the context of eternal inflation. If we consider the post-observer de Sitter space to be eternal de Sitter space (there will always be patches which never undergo additional tunneling events), then there are some puzzling features of such a cosmology as first pointed out by Dyson et. al. [67] and discussed in earlier chapters.

In essence, any fluctuation out of the eternal dS space corresponds to a downward fluctuation in entropy. There are a number of ways that one might imagine such a downward fluctuation in entropy could produce observers. For example, some patch might fluctuate into slow-roll inflation, and then produce observers via reheating. This is the hard way, a much easier route is to fluctuate a local region which already contains the conditions for observers to exist (for instance, a region with matter the size of our Local Group of galaxies, seeded with density fluctuations that are not too large or too small), or even the observers themselves (the so-called Boltzmann's Brains). Since we would like to think that we are not freak observers such as these, this is an example of the problems that may arise for making predictions in eternal inflation. The source of most problems such as this arises from the chosen regularization and comparison of infinite quantities [92, 93, 94, 8, 5, 90]: there are an infinite number of both freak

and ordinary observers.

In this chapter, we will outline the principles of false vacuum eternal inflation. We then discuss a number of difficulties with recent proposals for computing probabilities in false vacuum eternal inflation, and describe a new proposal for a probability measure on cosmological observables.

5.1 Desirable measure properties: a scorecard

To test a theory entailing eternal inflation with diverse post-inflationary predictions, we would like to know “what physical properties are most likely”, and compare them to our local observations. This question, however, is simply ambiguous – any answerable version of this question will entail a tacit choice of a conditionalization X , and calculation of \mathcal{P}_X as described above. The measures we will discuss correspond to different attempts to (at least implicitly) propose a plausible candidate for X , and to calculate the prior distribution P_p that might be used in calculating \mathcal{P}_X for that X .

A fundamental property that a well-defined measure should have is that its answer should be gauge-invariant, by which we simply mean that its answer can be calculated in any coordinate system we choose. This is distinct from “gauge-independence” as we shall discuss shortly.

Beyond this, it is important to consider what properties we might want a sensible measure to have. Some such desiderata, either stressed previously in the literature or first mentioned here, are given below. We note, however, that it is quite possible that the “correct” measure (if it exists) does not satisfy every item.

- Physicality – The p to which the measure applies, and the choice of P_p , should be such that (a) the probabilities do not appear to have been “picked out of a hat,” and (b)

$n_{X,p}$ is plausibly calculable. For example, we might choose p = “vacuum” and set P_p proportional to the tenth power of the hyperbolic tangent of the energy of the vacuum in Planck units. However, (a) this measure is obviously rather arbitrary, and (b) since there is no physical process behind the creation of regions described by the different vacua, the measure seems useless in calculating $n_{X,p}$ for, say X = “baryon.” Note, however, that different physically reasonable conditionalization objects may require different P_p – for example were X = “vacuum”, then the measure would still violate condition (a), but would satisfy condition (b) by definition.

- Gauge-independence – The relative probabilities should not depend on an arbitrary decomposition of spacetime into space and time. For instance, it has been shown [95, 96, 97, 98] that measures that weight based on the physical volume in a given state at late times give a result that depends sensitively on the assumed foliation of spacetime into equal-time hypersurfaces. In the absence of a strong physical reason for choosing a particular decomposition, such measures thus seem ambiguous.
- Ability to cope with varieties of transitions and vacua – The measure should be general enough to treat all of the types of vacua (e.g. positive, negative, or zero energy), and the various types of transitions between them.
- Independence of initial conditions – It is often argued that eternal inflation approaches a steady-state, and that essentially all observers exist “at late times,” so a physically reasonable measure should become independent of initial conditions. This criterion is not obviously necessary; although it may be appropriate for a particular conditionalization object (e.g. X = “a randomly chosen observer”), it may not be appropriate for others. For example, if one were interested in knowing what a *given* observer (or worldline) will experience in the future, then a dependence on initial conditions seems quite reasonable.

- Ability to cope with various and/or varying topological structures – The measure should potentially be applicable to spacetimes with non-trivial topological structures as may arise in eternal inflation (as discussed at length in Sec. 5.5).
- Accurate and robust treatment of “states” and “transitions” – this entails several sub-criteria:
 - General principles – the basic principles behind the measure should allow it to be used (in principle) for the complicated “spacetimes” of landscapes that cannot simply be encapsulated by transition rates between vacua.
 - Physical description of transitions – transition rates must be clearly linked to the physical process that describes the transition (e.g. Coleman-De Luccia bubble nucleation).
 - Reasonable treatment of “split” states – the measure should deal properly with very similar states and/or very large transition rates. (For example, a vacuum split by the insertion of a small potential barrier should, in the limit of an infinitesimal barrier, act just as a single vacuum.)
 - Continuity in transition rates – When transition rates are used, the measure should be continuous in these rates. For example, there should be no discontinuity in the probabilities between a stable vacuum and a metastable vacuum with a lifetime τ , in the limit $\tau \rightarrow \infty$.

We would argue that all of these potentially pleasing features are absent in at least one measure proposal in the literature, and that no extant proposal clearly fulfills them all.

5.2 False Vacuum Eternal Inflation

As discussed above, if a scalar field theory has a positive energy metastable minimum whose lifetime is greater than the background de Sitter expansion, then the consequent spacetime will exhibit false vacuum eternal inflation. Recent progress in string theory [87] indicates that de Sitter space must be metastable, perhaps making an understanding of false vacuum eternal inflation directly relevant to our universe. As discussed above, the existence of the string theory landscape¹ presents us with a situation where many different types of bubbles can form, each of which might have interiors with quite different properties. In the following description of false vacuum eternal inflation, we will assume that only the vacuum energy varies between minima in the landscape. Of course, this is not a complete or correct description, but it is an assumption we must make initially in order to make some progress with understanding how the mechanism of eternal inflation populates the various minima in the Landscape. We will see that even under this simplifying assumption, it is difficult to make progress.

The program we wish to undertake is a statistical description of how the process of bubble nucleation populates the universe with regions containing different vacuum energies. This amounts to a calculation of the prior discussed in Eq. 5.1, and there are a number of existing proposals for doing so, to which we now turn.

5.2.1 The Measures and their Properties

We now examine the various measures under consideration. It is useful to classify vacua as “terminal” or “recycling”: terminal vacua can be reached, but never exited; recycling vacua can exit to the state from which they originated, and may also transition to other states.

As a first step in this analysis, we can divide the measures into three categories: first,

¹While generally accepted, the string theory landscape has received a number of criticisms; see for example [99].

those that calculate volumes in different vacua on some equal-time surface; second, those that count individual bubbles; third, those that focus on the vacua experienced by an observer following a single worldline. The first category of measures is the oldest, beginning with work by Linde, Mezhlumian, Starobinsky, and Vilenkin [95, 57, 100]. The second and third category of measures consist of a number of more recent proposals (“gauge-independent” measures that do not depend on the choice of a time coordinate) [2, 101, 102, 103].

There are two basic volume-counting methods, counting either physical volume (i.e. p =“unit of physical volume”) or comoving volume (p =“unit of comoving volume”).

- *The Comoving Volume (CV) method:* Put forward by Garriga and Vilenkin [104], this method might be considered the counterpart for bubble nucleations (in comoving volume) to the work of Linde, Linde and Mezhlumian [95] in stochastic inflation. One starts with some region on an initial spacelike surface, and considers a congruence of hypersurface-orthogonal geodesics (the “comoving observers”) emanating from that region.

As a function of some global time coordinate t , the number of worldlines (to which the comoving volume fraction is defined to be proportional) in different vacua is calculated. Typically, the time variable is chosen to be the logarithm of the scale factor

$$t = \ln(a(\tau)), \tag{5.2}$$

where τ is the proper time of an observer. The fraction, $f_i(t)$, of comoving observers in a vacuum labeled by i at a time t can be calculated by solving a set of first order differential equations [1, 104]

$$\frac{df_i}{dt} = \sum_j \kappa_{ij} f_j - \kappa_{ji} f_i, \tag{5.3}$$

with the constraint that

$$\sum_i f_i(t) = 1 \tag{5.4}$$

for all t . Here, κ_{ij} corresponds to the rate of formation of bubbles of phase i in a background of j . This rate is typically estimated as that of the CDL or HM instanton that would mediate a transition from vacuum j to vacuum i . Recall that CDL bubbles approach a constant comoving size at late times. True vacuum bubbles grow asymptotically to a comoving *false vacuum* Hubble size, while false vacuum bubbles shrink to a comoving *true vacuum* Hubble size. The comoving Hubble size is related to the Hubble constant by the division of the scale factor $H_c = (Ha(t))$. Since the scale factor increases with time, the constant comoving size of bubbles nucleated at late times is smaller than the comoving size of bubbles nucleated at early times.

A number of assumptions are made in the derivation of Eq. 5.3. For instance, we must assume that details over a Hubble-sized 4-volume have been smoothed over, and therefore that CDL bubbles form at their asymptotic size. We must also assume that comoving worldlines never cross (ie there are no caustics), which may be violated due to the focusing effect of domain walls[105, 106].

The probability, P^{cv} , to be in a given vacuum is then defined to be proportional to the fraction of comoving volume (or number of worldlines), $f_i(t)$, in that pocket, in the $t \rightarrow \infty$ limit. Note that if there are terminal vacua, then as $t \rightarrow \infty$ all of the comoving volume will be distributed among the terminal vacua, except for a set of measure zero (albeit one that corresponds to infinite physical volume!). Metastable vacua are thus accorded zero weight. This measure depends heavily on initial conditions, because the fraction of comoving volume in a given terminal vacuum can only increase with time ².

The next two methods, rather than counting total relative volume in different bubble types, count relative total *numbers* of bubbles, i.e. p =“bubble”.

²Note that this is worse than it may sound, because the *same spacetime* might be sliced with different initial surfaces so as to lead to completely different probability distributions.

- *The Comoving Horizon Cutoff (CHC) method:* In the proposal of Garriga et al. [102], the measure is defined by directly counting bubbles of a given phase. We follow the most recent description of this procedure as given by Vilenkin [105]. First, just as in the CV method, a spacelike hypersurface in the spacetime is chosen, and a congruence of geodesics is extended from this hypersurface. The geodesics are followed arbitrarily far into the future, passing into any bubbles they may encounter. These lines are used to project bubbles in the spacetime back onto the initial hypersurface as “colored shadows”. The relative frequency of bubbles of different colors is defined to be the ratios of their shadow numbers on the initial hypersurface. The shadows are very clumped, gathering around the rare regions where inflation continues longest, with an arbitrarily large number of arbitrarily small overlaid shadows surrounding the set (of measure zero) of points on the surface where inflation continues forever. Thus, all counts are infinite numbers and require regularization to be well-defined. The authors propose only counting shadows larger than a size ϵ , and then take the limit $\epsilon \rightarrow 0$. This measure is argued to be independent of initial conditions on the surface and applies to terminal and recycling vacua. It also has the important feature of giving metastable states non-zero weight. While the idea of “counting bubbles at future infinity” is intuitively clear, it is somewhat unclear that the “shadow counting” used to actually implement the cutoff is particularly physical.

Moreover, converting this – relatively clear – idea into an actual calculation is a subtle matter. To date, such calculations have been performed in a rate-equation framework in which one follows the fractions of comoving volume in the various vacua and then effectively “divides through” by the bubble volume in order to obtain the bubble count. The shadow-size cutoff is then implemented by imposing a *set* of late-time cutoffs, one for each bubble type out of which the counted bubbles are nucleated (on the assumption

that this determines the “comoving size” of the nucleated bubbles, and thus the size of the shadow, to which the cutoff applies). This is depicted in Fig. 5.1, where the comoving bubble distribution produced by a two-well landscape is shown. The bubbles are assumed to be produced at their asymptotic comoving size (a comoving hubble length as defined by the background phase). The scale-factor time cutoff, $t_{AB}^{(\epsilon)}$ ($t_{BA}^{(\epsilon)}$), for transitions out of vacuum B (A) into vacuum A (B), is given by [102]

$$t_{AB}^{(\epsilon)} = -\ln(\epsilon H_B), \quad t_{BA}^{(\epsilon)} = -\ln(\epsilon H_A) \quad (5.5)$$

where ϵ can be identified as the comoving hubble size in the background phase at the cutoff time. This choice is meant to ensure that when bubbles intersecting the cutoff surface are projected back onto the initial surface, only bubbles of size exceeding ϵ will be obtained. This procedure is shown for the middle cluster of bubbles in Fig. 5.1. However, it is not completely clear that this procedure is entirely consistent.

For example, the formalism allows the situation depicted on the left side of Fig. 5.1, where the bubble of A is counted while its parent bubble of B is not. The bubble of A has a larger asymptotic comoving size than its parent (we thank Alex Vilenkin and Delia Schwartz-Perlov for discussions of this point), and so makes the cut, but it is unclear that the nucleation of bubbles larger than their parent actually occurs (this is certainly not mediated by any known instanton). True vacuum bubbles must grow to a true vacuum hubble size (which takes roughly a hubble time) before a false vacuum bubble will fit inside ³. This, along with the ordering of the cutoff surfaces, indicates that this effect occurs only for false vacuum bubbles.

Taking the viewpoint that the counting of such events is an error, we are systematically overcounting false vacuum bubble nucleation events. Further, this error may be rather

³While the standard procedure is to smear over a few hubble times, the cutoff procedure is sensitive to effects on smaller timescales

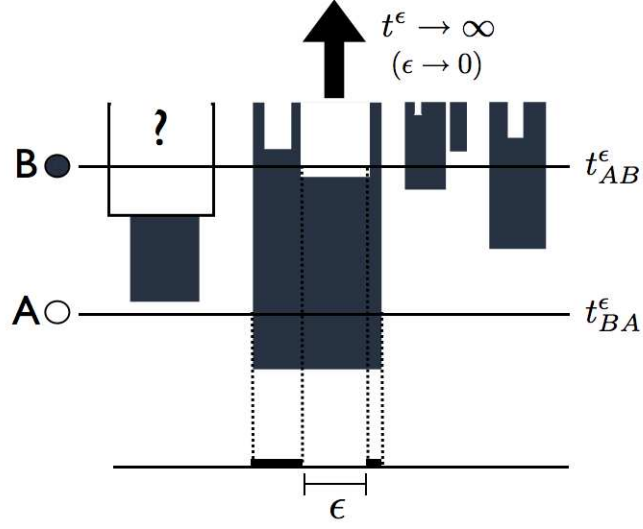


Figure 5.1: A depiction of the cutoff scheme imposed in the CHC method for a two-well landscape. There are two spacelike cutoff surfaces, $t_{AB}^{(\epsilon)}$ and $t_{BA}^{(\epsilon)}$ for each parent vacuum A (light) and B (dark). Bubbles which nucleate out of the parent vacuum before the cutoff time are larger than the indicated comoving size ϵ and are therefore counted. The bubbles are drawn with their asymptotic comoving sizes (in comoving coordinates, true vacuum bubbles grow to this size whereas false vacuum bubbles shrink to it [1]). The asymptotic size of the bubble is projected as a shadow onto the initial surface at $t = 0$ (bottom). Note the puzzling situation that the bubble of A nucleating out of B on the left is larger than its parent, and so would be counted while its parent is not.

large since the ratio of 4-volume between the cutoff surfaces to the 4-volume before the cutoffs goes like $\sim (H_A/H_B)^3 > 1$ as $t_{AB}^{(\epsilon)} \rightarrow \infty$. Of course, only the portion of this 4-volume in phase B will produce bubbles of A , but there will still be more 4-volume in phase B between the cutoffs than before them.

- *The Worldline (W) method:* Easter et al. [101], whose measure we denote the Worldline (W) method, assume that at some initial time (defined by a spacelike hypersurface), the universe is in some places in a non-terminal vacuum. They then suggest considering a finite number of randomly chosen points on this initial data surface and following forward

worldlines with randomly chosen velocities⁴ from these initial data points. Only bubbles that are encountered by at least one of these worldlines are counted in determining the relative bubble abundance (no bubble is counted more than once, even if multiple worldlines enter it). One then takes the total number of worldlines to infinity. Like CHC, this measure is claimed to be essentially independent of initial conditions as long as inflation is eternal. It was argued in [102] that the CHC and W methods of bubble counting yield identical answers for terminal landscapes (the W method is ill-defined for fully recycling landscapes as discussed in [103]).

The remaining two measures focus on the transitions between vacua experienced by a single eternal worldline, and accord a probability to a vacuum that is proportional to the relative frequency with which it is entered (p = “segment of a worldline between vacuum transitions”).

- *The Recycling Transition (RT) method:* The proposal of Vanchurin and Vilenkin [103], which we will refer to as the Recycling Transition (RT) method, is to follow the evolution of a given geodesic observer and set the probability to be in a given vacuum proportional to the frequency with which this vacuum is entered, in the limit where the proper time elapsed goes to infinity. As presented, the method only applies to landscapes with no terminal vacua, and was argued to be equivalent to the CHC method in that case [103].
- *The Recycling and Terminal Transition (RTT) method:* The Bousso proposal [2], which we denote the Recycling and Terminal Transition (RTT) method, covers the cases of terminal and recycling vacua. Here, one chooses an initial condition for the worldline (the predictions of this measure are dependent on initial conditions), and considers the relative probabilities of the worldline entering various other vacua, averaging over possible

⁴It is unclear the extent to which the velocities of individual points can be chosen at random, as discussed by Vilenkin in [105]

realizations. This is equivalent to the RT measure in the case where there are no terminal vacua.

The focus in RTT on the worldline of an observer is presented as being motivated by holography and the desire to only consider regions of spacetime that an observer can signal to and receive signals from (the “causal diamond”). However, this viewpoint makes essentially no difference to the mathematics and – as mentioned below – the time average over histories for Bousso’s observer could equally well be thought of as spatial averages over widely-separated worldlines in any of the above approaches. A similar observation is made in [90]. Of course, a holographic point of view might lead one to strongly disfavor further possible weighting factors to apply such as volume weighting.

Although we will not treat them further, let us also mention some other approaches to asking about predictions in eternal inflation. In [98], Tegmark advances a simple and direct possible answer to the question of the relative numbers of different vacuum regions: because eternal inflation should produce a countably infinite number of each type of vacuum region, and because all countable infinities are equal in the sense of being relatable by a one-to-one mapping, each vacuum should be assigned equal weight. In [107], the authors put a measure on the space of classical FRW solutions to the Einstein plus scalar field equations. If this could be extended to allow for quantum jumps analogous to bubble nucleations, it might help address the distribution of vacua within and amongst solutions. In [108], the authors focus on histories that might be/might have been observed, in the context of single-field inflation with a monotonic potential.

5.2.2 Relations between the measures

Although the methods, both in their motivation and in their presentation here, have been categorized into “volume counting”, “bubble counting” and “worldline following”, there are relations between them that cross these divisions, so that in fact there are actually very few essentially different measures under consideration.

Some of the relations between measures (as presented by their authors) have been mentioned above (e.g. the equality of CHC and W for terminal landscapes, and the equality of CHC and RT for “fully recycling” landscapes with no terminal vacua). More, however, exist.

In particular, the RTT method accords the same relative probabilities to terminal vacua as does the CV method (though the methods differ for non-terminal vacua, which have zero probability in CV and nonzero probability in RTT). To see this, consider a congruence of comoving worldlines starting in some vacuum. Now, as $t \rightarrow \infty$, every worldline that will eventually end up in a terminal vacuum will do so (by definition); moreover, each terminal vacuum will only be entered once (also by definition). Since RTT accords relative probability to two terminal vacua A and B equal to the the relative probability of a worldline entering them, this will in turn be equal to the relative numbers of worldlines terminating in A versus B, which is in turn equal to the relative $t \rightarrow \infty$ comoving volume fractions as defined in the CV method. In appendix C, we show this correspondence by directly comparing the results of the RTT and CV methods in the context of a specific model. More generally, the results of the RTT method, for terminal as well as recycling landscapes, can be obtained by integrating the incoming probability current into the various vacua [90, 1].

These relations between the measures (as formulated in the original papers) are summarized in Fig. 5.2. It also appears possible to use what is understood about these connections to devise some hybrid or generalized versions of the methods.

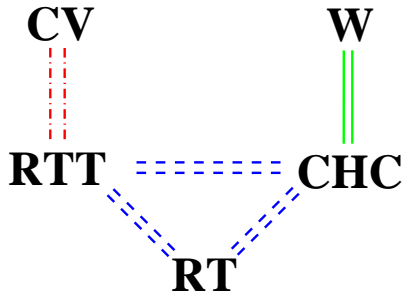


Figure 5.2: A summary of the connections between the various measures. Solid green lines indicate equivalence between the measures for a terminal landscape. Dashed blue lines indicate equivalence in the case of a fully recycling landscape. Dashed-dotted red lines indicate that the measures assign the same relative weights to terminal vacua.

For example, take the CV procedure, where only a single late-time hypersurface is considered, and attempt to count the number of bubbles intersecting this surface from the volume distribution and some appropriately defined cutoff. This is *not* quite the CHC method since, as described above, the CHC calculation requires a different time cutoff for bubbles formed in different parent vacua. But this CV-CHC “hybrid” prescription does not seem any less reasonable to us. One could also generalize the CHC prescription to obtain an infinite number of related measures by altering the limiting procedure: rather than only counting shadows larger than a size independent of the bubble type, one could instead only count shadows larger than a given size relative to, say, some function of their Hubble radius. It would be interesting to investigate how (in)sensitive the probabilities are to the choice of a particular cutoff procedure. Having described the various bubble counting measures and their connections, we now use a set of sample landscapes to illustrate some of their predictions.

5.3 Some Sample Landscapes

Consider the related one-dimensional landscapes pictured in Fig. 5.3. They all contain both terminal and recycling vacua (where we assume here that a vacuum is terminal if and only

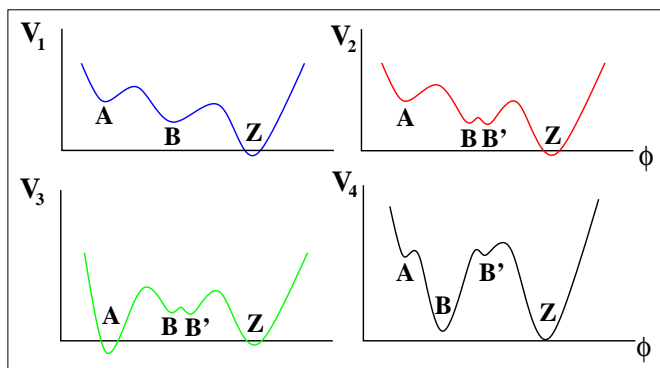


Figure 5.3: Some sample landscapes. Potential V_1 depicts the ABZ example discussed by Bousso [2]. V_2 splits the B vacuum by introducing a small barrier. Potential V_3 lowers the A vacuum to zero or negative energy, so that it becomes terminal. The potential V_4 has a low energy minimum with high-energy neighbors that have short lifetimes (relative to other vacua in the landscape).

if its energy is zero or negative), and we now discuss the predictions made by the RTT method for each. In light of the close connections between the measures, many of the conclusions drawn from these calculations will hold more generally.

Following Bousso, we define the relative probability μ_{NM} to transition from vacuum M to vacuum N as

$$\mu_{NM} \equiv \frac{\kappa_{NM}}{\sum_P \kappa_{PM}} \quad (5.6)$$

where P is summed over all decay channels out of M , and κ_{NM} is the probability per unit time of tunneling from vacuum M to vacuum N . Note that all summations in this paper are expressly indicated. κ_{NM} typically takes the form of a three-volume times a nucleation rate per unit four-volume, the latter being calculated using semiclassical instanton techniques. Note that $\sum_P \mu_{PM} = 1$ if M is metastable and $\mu_{PM} = 0$ if M is terminal, and also that $\mu_{MN} \neq \mu_{NM}$ in general. Bousso introduces the concepts of trees and pruned trees in order to calculate the prior distribution in the RTT method. He also presents a matrix formulation, which we develop further in appendix C.

It will be important for what follows to obtain an indication of the magnitudes of tunneling rates in a typical landscape. We model this landscape by a single scalar field ϕ with a potential $V(\phi)$ expressed as $V(\phi) = \mu^4 v(\phi/m)$. We further assume that v is a smooth function that varies over a range of order unity as its argument changes by order unity, and μ sets the energy scale. For the semi-classical approximation that we are working in to make sense, we must have $\mu^4 \ll M_{Pl}^4$, where M_{Pl} is the Planck Mass. For Coleman–De Luccia instantons to exist, m must be less than some $O(1)$ multiple of M_{Pl} . See [16] for more on the motivation for this form of the potential.

As mentioned above, we will estimate tunneling rates between the potential minima using semiclassical instanton techniques, notwithstanding thorny issues of interpretation, particularly for upward transitions. Then $\kappa_{NM} \propto e^{-(S_{(NM)} - S_M)}$, the bracketed exponential factor being the difference between the action $S_{(NM)}$ of the Coleman-De Luccia or Hawking-Moss instanton linking the two vacua and the action S_M of the Euclidean four-sphere corresponding to the tunneled-from spacetime. Note that the same instanton applies to uphill and downhill transitions (hence the use of symmetrising brackets in its label). Using the Euclidean equations of motion, $S_{(NM)}$ can be written as

$$S_{(NM)} = - \int \sqrt{g} V(\phi) d^4x \quad (5.7)$$

where the integral is performed over the Euclidean manifold of the instanton. The background subtraction term (which is negative and larger in magnitude than the instanton action) is given by the same expression and evaluates to

$$S_M = - \frac{3M_{Pl}^4}{8V(\phi_M)}, \quad (5.8)$$

where $V(\phi_M)$ is the value of the potential of the pre-tunneling vacuum M at $\phi = \phi_M$.

From these formulae we can immediately deduce two important facts. First, we can compare uphill and downhill rates between two vacua. In the ratio of the rates the instanton

part cancels out, and only the background parts are left. If $V(\phi_M) = V(\phi_N) + \Delta V$, then

$$\frac{\kappa_{MN}}{\kappa_{NM}} \sim \exp \frac{-3M_{Pl}^4}{8} \frac{\Delta V}{V^2(\phi_M)} = \exp \frac{-3}{8} \frac{\Delta v}{v_M^2} \left(\frac{M_{Pl}}{\mu} \right)^4. \quad (5.9)$$

So, unless Δv is tuned to be much smaller than v , the uphill rate is exponentially smaller than the downhill rate.

Second, we can compare the rates to two vacua N and P from the same parent vacuum M . This time the background parts cancel and we are left with the exponential of the difference of the instanton actions:

$$\frac{\kappa_{PM}}{\kappa_{NM}} \sim \exp -(S_{(PM)} - S_{(NM)}). \quad (5.10)$$

Both instanton actions will be of order $(M_{Pl}/\mu)^4$, so we typically expect the tunneling rates to differ exponentially. In particular, if V_N and V_M are somewhat atypically similar, and if there is only a small barrier between the two, then as long as V_P is not atypically close to V_M also, tunneling from M to P will be exponentially disfavored relative to tunneling to N . This holds even if the tunneling from M to N is uphill and that from M to P is downhill. This difference in tunneling rates can be extreme: for a typical inflationary energy scale of $\mu \sim 10^{16}$ GeV, $\kappa_{PM}/\kappa_{NM} \sim e^{-10^{12}}$.

5.3.1 Coupled pairs dominate in terminal landscapes

We begin by considering the potential V_2 depicted in Fig. 5.3. We assume that the barrier separating B and B' is very small, so that rapid transitions occur between the two wells. Thus we take $\kappa_{B'B} \gg \kappa_{AB}$ and $\kappa_{BB'} \gg \kappa_{ZB'}$. Using the results of appendix C, in the limit we

obtain:

$$\begin{pmatrix} P_A^{A,B,B'} \\ P_B^{A,B,B'} \\ P_{B'}^{A,B,B'} \\ P_Z^{A,B,B'} \end{pmatrix} \propto \begin{pmatrix} \kappa_{BB'}\kappa_{AB} \\ \kappa_{BB'}\kappa_{B'B} \\ \kappa_{BB'}\kappa_{B'B} \\ \kappa_{B'B}\kappa_{ZB'} \end{pmatrix} \quad (5.11)$$

where P_N^M is the “prior” probability of Eq. 5.1 (with subscript p dropped) to be in the vacuum N , given an initial state in vacuum M . A multiple superscript indicates that the same distribution applies to the listed initial states for the transition rates under consideration.

There are a number of interesting points to note here. First

$$\frac{P_B^{A,B,B'}}{P_A^{A,B,B'}} = \frac{\kappa_{B'B}}{\kappa_{AB}} \gg 1 \quad (5.12)$$

$$\frac{P_B^{A,B,B'}}{P_Z^{A,B,B'}} = \frac{\kappa_{BB'}}{\kappa_{ZB'}} \gg 1. \quad (5.13)$$

These ratios hold independent of initial conditions. Vacuum B' is similarly weighted relative to A and Z . We therefore see that (as might be expected in a measure that counts transitions) metastable vacua participating in fast transitions with their neighbors are weighted very heavily. Such regions certainly exist in a landscape with sufficient complexity, and it is these regions that the prior distribution in the RTT method will favor. From our above estimates of typical transition rates in regimes with energies somewhat below the Planck scale, factors of order $e^{10^{12}}$ should be commonplace.

Of course, *arbitrarily* fast transitions between B and B' (which give arbitrarily high weighting to both vacua) are unrealistic. In reality, bubble collisions will become important, and at high enough nucleation rates there will be percolation. In this limit, there should then be a transition to a treatment in terms of field rolling and diffusion. In this regard, it would be desirable to treat field diffusion as described by the stochastic formalism and bubble nucleation (with collisions taken into account) in a unified way (see [1] for work in this direction).

Although the CHC measure is inequivalent to the RTT measure in landscapes with terminal vacua, it (and hence the W method) nevertheless gives similar qualitative predictions. We can see this by analyzing the “FABI” model of [102], which, in the limit where $\kappa_{B'B} \gg \kappa_{AB}$ and $\kappa_{BB'} \gg \kappa_{ZB'}$, gives the same ratios as Eqs. 5.12 and 5.13. Thus the CHC and W proposals weight fast-transitioning states exponentially more than others in exactly the same way the RTT method does. The weighting can easily be large enough to dominate any volume factors, which appear in the full probability defined using the CHC method [102], unless the number of e-folds during the slow-roll period after a transition is extreme.

We have seen that pairs of vacua undergoing fast transitions in both directions are weighted very heavily, but what about transitions that are fast in one direction only? For example, consider V_4 in Fig. 5.3, where there are quick transitions into B , but transitions out of B are strongly suppressed. Requiring only $\kappa_{BB'} \gg \kappa_{ZB'}$ in the probability tables from appendix C yields:

$$\begin{pmatrix} P_A^{A,B,B'} \\ P_B^{A,B,B'} \\ P_{B'}^{A,B,B'} \\ P_Z^{A,B,B'} \end{pmatrix} \propto \begin{pmatrix} \kappa_{BB'} \kappa_{AB} \\ \kappa_{BB'} (\kappa_{AB} + \kappa_{B'B}) \\ \kappa_{BB'} \kappa_{B'B} \\ \kappa_{B'B} \kappa_{ZB'} \end{pmatrix}. \quad (5.14)$$

It is apparent that vacuum B will be the most probable vacuum in this sample landscape. The relative weight of A to B' is very sensitive to the details of the potential since, as shown above, there is an exponential dependence on the difference in instanton actions (which itself tends to be quite large). In the absence of extremely fine-tuned cancellation in this difference (which would be required to make $\kappa_{AB} \sim \kappa_{B'B}$), one of the two will be vastly more probable than the other. We have already considered the case where vacuum B' is much more likely than vacuum A with landscape V_2 above. So the other generic alternative is for vacua A and B to have probabilities very close to one-half, vacuum B' to be exponentially suppressed and vacuum Z

to be even more suppressed.

These two examples together make it clear that in order to obtain the large weighting observed for potentials V_2 and V_3 , there must be pairs of vacua which undergo fast transitions in *both* directions. This allows for closed loops that produce large numbers of bubbles of each of the vacua in the pair; in such cases the probabilities of both vacua scale with the product of the transition rates between them.

5.3.2 Coupled pairs dominate in cyclic landscapes

As one might expect, the extreme weighting of coupled pairs persists if we raise the height of the Z well of V_2 in Fig. 5.3 so that it is no longer terminal. From the calculations in appendix C, we find:

$$\frac{P_B^{A,B,B',Z}}{P_A^{A,B,B',Z}} \simeq \frac{\kappa_{B'B}}{\kappa_{AB}} \quad (5.15)$$

$$\frac{P_B^{A,B,B',Z}}{P_Z^{A,B,B',Z}} \simeq \frac{\kappa_{BB'}}{\kappa_{ZB'}} \quad (5.16)$$

with the same results for the ratios of $P_{B'}$ in place of P_B to P_A and P_Z . This is of special interest because for cyclic landscapes the predictions of the RTT method agree with those of the CHC and RT methods (see Fig. 5.2). Thus all of these measures will weight rapidly transitioning vacua heavily.

5.3.3 Splitting vacua

A closely related “test” to which we can put the RTT method to is to consider the situation where potential V_2 is obtained from potential V_1 (The “ABZ” example of [2]) by inserting a small potential barrier in the middle (B) well. The ratio of weights in the A and Z wells in potential V_1 is given by:

$$\frac{P_A^{A,B}}{P_Z^{A,B}} = \frac{\kappa_{AB}}{\kappa_{ZB}}, \quad (5.17)$$

which can be found from the result of [2] by substituting $\epsilon = \kappa_{AB}/(\kappa_{AB} + \kappa_{ZB})$ and $1 - \epsilon = \kappa_{ZB}/(\kappa_{AB} + \kappa_{ZB})$. Now let us insert the barrier in such a way that the transition rates into and out of the A and Z wells remain unaffected. After the insertion, the relative weights of vacuum A and Z (in potential V_2) are then found from Eq. 5.11 to be

$$\frac{P_A^{A,B,B'}}{P_Z^{A,B,B'}} = \frac{\kappa_{BB'} \kappa_{AB}}{\kappa_{B'B} \kappa_{ZB'}}. \quad (5.18)$$

Now we can consider two cases. First, if there is no symmetry as B is interchanged with B' , then we see that inserting the barrier has changed *both* the absolute probabilities (which are now strongly weighted toward B and B'), and also the *relative* weights of the other vacua. Second, if the problem is symmetric under interchange of B and B' (so that $\kappa_{BB'} = \kappa_{B'B}$ and $\kappa_{ZB'} = \kappa_{AB}$), then the relative weights of A and Z are unaffected; however, the absolute weights of both are still altered drastically by this decomposition of B into two identical vacua with fast transitions between them. This is somewhat disturbing, and again points to the need for a smooth connection between “vacuum transitions” and “field evolution.”

5.3.4 Continuity of predictions

The next sample landscape we wish to consider is the most simple – a double well potential, where we consider both the terminal and recycling cases. In this example, the predicted ratio of weights in vacuum A to that in Z (in the case of full recycling) is identical for the CHC, RT, and RTT methods, with $P_A/P_Z = 1$, independent of the relative lifetimes of the states. The ratio of weights predicted by the CV method is [103] $P_A/P_Z = (H_A/H_Z)^4 e^{S_A - S_Z}$, where $H_{A,Z}$ is the Hubble constant and $S_{A,Z}$ the entropy of vacuum A and Z respectively. The difference is due to the fact that the CHC, RT, and RTT methods count the frequency of transitions while the CV method weights according to the time spent in a given vacuum [103].

Now consider shifting the entire potential down, such that the lower well becomes a

terminal vacuum. The predictions of the CHC, RT, and RTT methods will remain identical until the lower well is exactly terminal, at which point the CHC and RTT methods (the RT method breaks down when the lower well becomes terminal) predict $P_A = 0$, $P_Z = 1$ ⁵. Were this a correct description of relevant probabilities, it would be very important in making predictions to know if the energy of a minimum were zero or different from zero by one part in $10^{10^{100}}$. The CV method will predict this distribution as well, but will approach it in a *continuous* manner ($S_Z \rightarrow \infty$, sending the ratio P_A/P_Z to zero). The predictions of the CV method are for this reason much more robust under small changes of the potential.

One possible way to avoid this discontinuity might be to reverse the order of limits $t \rightarrow \infty$ and $\kappa_{AZ}^{-1} \rightarrow \infty$. All of the measures discussed in this paper take the $t \rightarrow \infty$ limit first, but one could perhaps define a measure where the duration in time is held finite while $\kappa_{AZ}^{-1} \rightarrow \infty$. Applying this to the two-well example, as the lifetime of the lower well goes to infinity, the expectation value of the number of transitions observed would smoothly go to zero. Alternatively, it may be the case that there are no truly terminal vacua (with strictly zero probability of being tunneled from)⁶. Finally, it may be that there is simply something conceptually flawed in the way bubble-counting measures treat the borderline between a vacuum being terminal and non-terminal.

5.4 Consequences for predictions in a landscape

The previous section pointed out some interesting features of bubble-counting measures (all the measures here save CV) as somewhat abstract procedures applied to small “toy”

⁵It is worth noting that that this is completely independent of the ratio of the lifetimes of the states, which might be arbitrarily large [16].

⁶For example, if the “L” process describe below in Sec. 5.5 occurs, it might mediate transitions away from negative or zero-energy vacua. A heuristic argument in favor of tunneling from negative “big crunch” vacua was given in [15]. Finally, we note that after tunneling to a negative vacuum, the spacetime is an open FRW model with energy density. Thus there may conceivably be tunneling before the “crunch” even if such tunneling is impossible from pure AdS or Minkowski space.

landscapes. What might these features imply for predictions (in the form of P_p or \mathcal{P}_X) in a more realistic landscape with many, many vacua and transitions connecting them?

Without a well-specified model of such a landscape this is a difficult question to answer; however the strong preference for pairs of fast-transitioning vacua does suggest some general – and possibly troubling – predictions. Within a landscape, imagine the set of all pairs of neighboring vacua (M, N) with similar pairs of energies (V_M, V_N) , and suppose that for each pair, the barrier between M and N is independent of the barriers separating M and N from other nearby vacua. Then we might expect that members of different pairs will be accorded exponentially differing probabilities depending on the details of the barrier. In Sec. 5.3 we found in our sample landscapes that the probabilities for the vacua in a fast-transitioning pair (N, M) are approximately proportional to the product $\kappa_{NM}\kappa_{MN}$ of the transition rates between them. What determines this product? We fix V_M and V_N , and imagine the possible potentials v in-between (i.e. consider we consider many pairs in the landscape). We have

$$\kappa_{MN}\kappa_{NM} \sim e^{-2S_{(MN)}(v)} e^{S_M+S_N}, \quad (5.19)$$

where $S_{(MN)}(v)$ is the instanton action of Eq. 5.7 and $S_{M,N}$ are the background subtractions for vacua M and N , given by Eq. 5.8. With S_M and S_N fixed, the product then depends just on $S_{(MN)}$. As argued above, this action will be of order $(M_{\text{Pl}}/\mu)^4$, and vary by order unity as the parameters governing the potential v are varied. Thus the weightings of the members of each pair do appear to be exponentially sensitive to the shape of the potential in-between.

Now imagine that our vacuum is one tunnel away from one of the vacua with energy V_N . All other things being equal, we should be likely to come from any given one according to its weight. The evolution towards our vacuum depends on the shape of the potential, and because v is smooth this will not be independent of the shape of the potential between the endpoints of the instanton. If an observable α depends on the shape of the potential as our vacuum is

approached, then this raises the possibility of it having an exponentially varying prior over an observationally relevant range. A good example might be the number of post-tunneling e-folds, which might possess a prior exponentially favoring a particular number.

One might hope to compensate the prior probabilities P_p favoring cosmologies unlike ours using a conditionalization factor $n_{X,p}$ that disfavors them (e.g. conditionalizing on the existence of a galaxy). In some cases, this seems plausible. For example, if we consider the cosmological constant Λ and (unrealistically) assume that all other cosmological parameters stay fixed to our observed values, then $n_{X,p}(\Lambda)$ decreases as an exponential in $\Lambda/\xi^4 Q^3$, where $Q \sim 10^{-5}$ is the fluctuation amplitude and $\xi \sim 10^{-28}$ is the matter mass per photon in Planck masses (e.g., [109]). Because this scale is so much smaller than the scale over which the parameters of the potential vary (i.e. $\xi^4 Q^3 \ll M$), the exponential variations of $P_p(\Lambda)$ are likely to be nearly constant over a range of order $\xi^4 Q^3$, so $n_{X,p}(\Lambda)$ would be effective in forcing \mathcal{P}_X to give most weight to a region of parameter space near to what we observe [110, 111]. But in other cases this is far from clear; for example, the number of inflationary e-folds is determined by the *high energy* structure of the potential at and near tunneling, and the number of e-folds is linked to the field value to which tunneling occurs, which is in turn linked to the instanton solution and hence the tunneling rate. Thus $n_{X,p}$ and P_p might easily vary over the same scale in the parameters governing the landscape potential, and the conditionalization may be ineffective at forcing \mathcal{P}_X to peak in the observed range.

5.5 Observers in Eternal Inflation

Measures relying on properties experienced by a local “observer” (generally equated with a causal worldline) require that observers can actually transition between the different vacua. It is not, however, clear that this is always the case. In [17], two of the authors found

that in semi-classical Hamiltonian descriptions of thin-wall tunneling, there are always two qualitatively different types of transitions described by the same formalism.

One, called the “R” tunneling geometry, is a generalization of Coleman-De Luccia [12]/Lee-Weinberg [13] (CDL/LW) true and false vacuum bubbles. It corresponds to the fluctuation of a bubble of the new phase which is always in causal contact with the background region, in the sense that worldlines in the old phase can both “tunnel with” the bubble, and also enter the bubble of new phase soon after it forms.

In the other, which was called the “L” tunneling geometry (a generalization of the Farhi-Guth-Guven mechanism [20]), the bubble of new phase lies behind a wormhole separating it from the original background spacetime. In this case, no causal curve from the original phase can enter the new phase after the tunneling event (in marked contrast to the usual picture of an expanding bubble of new phase, or to the R mechanism). Some rare worldlines might “tunnel with” the bubble, but the physical connection between pre-and post-tunneling phases represented by such worldlines is obscure at best; moreover such worldlines do not exist in the (highest probability) limit in which the bubble has zero mass.

If both L and R processes occur, then the L mechanism is the most probable path by which regions of *higher* vacuum energy emerge, while the R geometry dominates decay to a lower vacuum [17]; both processes are dominated by the lowest-mass bubbles.

At the semi-classical level of these calculations, the authors of [17] found no convincing reason that one but not the other of these two tunneling processes would occur. Holographic considerations would seem to conflict with the L geometries (at least for transitions to higher vacuum energy), and [69] argued using AdS/CFT (see [75] for another treatment of L tunneling geometries using AdS/CFT) that such events tunneling from AdS to dS would correspond to non-unitary processes; however the question has not been settled with any clarity. In this section we will therefore consider how the L-tunneling process would impact eternal inflation, and the

measures as applied to it.

Let us consider an initial parcel of comoving volume in a metastable state residing in an arbitrary potential landscape. This is shown at the bottom of Fig. 5.4. As time goes on, bubbles of either higher or lower vacuum energy will nucleate by either the L or R tunneling geometries. Since low-mass bubbles are most probable, most downward transitions will be CDL bubbles (the R geometry in the zero mass limit), and most upward transitions will be L-geometry tunneling events corresponding to a very small mass black hole forming in the background spacetime. Such small black holes affect the background spacetime in a completely negligible way as long as the nucleation rate is rather small ⁷. In particular, these upward nucleations remove zero comoving volume from the old phase.

The pre-and post-tunneling spacetimes in an L-tunneling event are described comprehensively in, e.g., [17]; the portion of the post-tunneling spacetime existing behind the wormhole consists of regions with both new and old vacuum energy separated by a thin wall, and in the zero-mass limit is just the Lorentzian CDL bounce geometry. Both vacuum regions are larger than their corresponding Hubble radii and so will unavoidably continue to inflate, independent of the precise details of the initial nucleated space (i.e. how the instanton is “sliced” to be continued into Lorentzian space; see [1] ⁷ for the corresponding issue concerning the CDL instanton).

The result is that an entirely new “branch” of eternal inflation is created, with some initial physical volume, having essentially no effect on the original spacetime. If a comoving volume is assigned to this physical volume using the “scale factor time” of the background geometry near the nucleation event, then the effect will be to create *new comoving volume* ⁸.

The new branch will in turn spawn more branches – and more comoving volume – via L-events,

⁷In fact even more probable is the zero-mass limit in which there is no black hole at all, which also clearly does not affect the background spacetime.

⁸How to actually define “comoving volume” in the new phase is very unclear; comoving volume is related to a particular coordinatization of a spacetime, and its definition is tied to a congruence of geodesics; here no such congruence continues through the nucleation to fill the initial slice.

so that the comoving volume appears to actually grow exponentially (though in what “time” this occurs is unclear since there is no foliation of the entire spacetime). This process is shown in Fig. 5.4.

How do the measures we have been discussing connect with this new picture? Consider first the measures RTT, RT and W that explicitly follow causal worldlines. As formulated, these measures would essentially “ignore” L transitions. This seems quite artificial, however, as regions with high vacuum energy (reached by upward transitions) would almost all arise from this process; put another way, choosing a random point in the entire spacetime (including the tree of new universes formed by the L tunneling geometry) and projecting any geodesic back, it would almost certainly hit an L-geometry nucleation surface in the past rather than the assumed initial slice.

Now consider the CV and CHC prescriptions. As stated, the idea is to count the relative comoving volume or number of bubbles of different types “on future null infinity”. But as described in Sec. 5.2.1 and in [104, 102, 105], these measures are actually *calculated* with very strong reliance on a congruence of geodesics emanating from an initial surface; thus as calculated in this formulation they would be as unaffected by L-geometry events as RTT, RT, and W. It is interesting, however, to speculate about taking these prescriptions seriously as counting bubbles on future infinity, as this would actually include the bubbles in the other branches created by L-events.

Consider, then, a volume \mathcal{V}_i nucleated by an L-event (with the subscript i labeling the particular region under consideration), and imagine a congruence of geodesics emanating from it, denoting by $\mathcal{J}^+(\mathcal{V}_i)$ the part of the spacetime’s future null infinity reachable by these geodesics. Then we might “count bubbles of comoving size exceeding ϵ ” (for CHC) or “count comoving volume” (for CV) on $\mathcal{J}^+(\mathcal{V}_i)$, to define a set of relative probabilities $P^{\mathcal{V}_i}$.

Now, it is very unclear how precisely to combine the $P^{\mathcal{V}_i}$ in all of the branches i formed

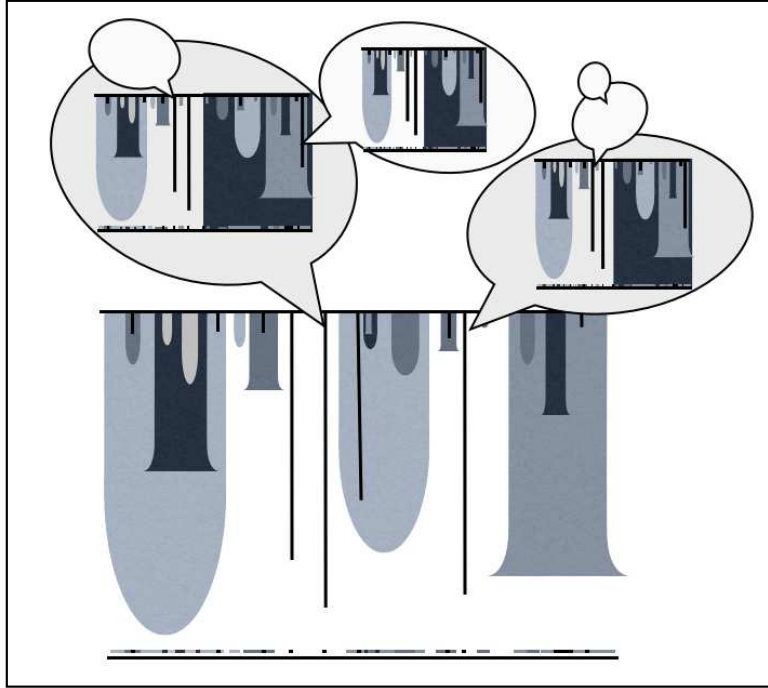


Figure 5.4: A picture of an eternally inflating universe which takes into account both L and R tunneling geometries. At the bottom, there is an “original” parcel of comoving volume (defined by the horizontal spacelike slice at the bottom of the figure), which evolves in time (vertically). True and false vacuum bubble nucleation events occur via the R geometry in this volume, denoted by the shaded regions which in the case of true vacuum bubbles grow to a comoving Hubble volume and in the case of false vacuum bubbles shrink to a comoving Hubble volume. The vertical black lines denote the black holes formed during L geometry tunneling events. On the other side of a wormhole (inside the captions), the initial distribution, which is fixed by the tunneling geometry, undergoes L and R tunneling events as well, spawning more disconnected parcels of volume in which this process repeats. The original parcel of comoving volume will spawn an infinite amount of new comoving volume via L geometry tunneling events. Shown on the bottom of each parcel is the set of bubble shadows that might be used in the CHC method to calculate probabilities $P^{\mathcal{V}_i}$ for each region \mathcal{V}_i .

from L-tunnelings out of both the original spacetime, and out of the future of \mathcal{V}_i , and from the descendants of these branches, etc. Nonetheless, some general statements might be made even in the absence of such precision.

Consider first CHC. Since its probabilities are essentially independent of \mathcal{V}_i , it seems that $P^{\mathcal{V}_i}$ will be the same in all branches, so it is hard to see how anything else could result from combining them.

Now consider CV, which *is* dependent on the initial conditions for \mathcal{V}_i . Here, the “initial” conditions for a branch are not provided by the original spacetime, but rather by the dynamics of the L-tunneling process, with a different set corresponding to each pair of vacua between which the nucleations can occur. Whatever way we calculate all of the $P^{\mathcal{V}_i}$, it seems likely that the original spacetime’s initial conditions will be completely overwhelmed by those of all of the branches in the infinite self-similar tree depicted in Fig. 5.4. One might then imagine that the total prior distribution P is given by a weighted sum of these separate distributions, and is independent of the initial conditions of the original spacetime.

We also point out that these questions may apply to “stochastic” eternal inflation as well. It is generally implicitly assumed in these models that the global spacetime is causally connected, but this is far from proven. Indeed, large fluctuations generically cause a large back reaction, and it is not obvious that the large stochastic fluctuations driving eternal inflation do not cause the production of universes behind a wormhole (this is suggested by singularity theorems [33, 35, 14]). This discussion is also relevant for hypothetical transitions out of negative energy minima. While no instanton has been constructed for such a transition (see [15] for a proposal concerning the probability of such a process), if one exists then (considering thin-wall constructions [69]) it would have to be an L geometry. Based on the considerations above, it is unclear how or if including such transitions would change the predictions of extant measures.

5.6 Discussion and Conclusions

Property	CV	CHC	W	RT	RTT
Physicality	P	P	P	P	P
Gauge independence	P	Y	Y	Y	Y
Independence of initial conditions	N	Y	Y	Y	N
Copes with varieties of transitions and vacua	P	Y	N	N	Y
Copes with nontrivial topologies	P	P	N	N	N
Treatment of states and transitions:					
– General principles	P	P	P	P	P
– Physical description of transitions	P	P	P	N	N
– Reasonable treatment of split states	Y	N	N	N	N
– Continuity in transition rates	Y	N	N	N	N

Table 5.1: Properties of bubble counting measures – Y=yes, N=no, P=partial.

We have analyzed a number of existing measures for eternal inflation, exploring connections that exist between them, and highlighting some generic predictions that they make. With this perspective, let us return to the list of desiderata presented in Sec. 5.1. Shown in Table 5.1 is a “scorecard” detailing which of the measures, in at least a majority of the authors’ humble and irresolute opinions, satisfy the properties listed in Sec. 5.1.

First, which measures are “physical”, in the sense of providing a non-arbitrary prior probability P_p , for some “counting object” p , useful for calculating \mathcal{P}_X ? Physical volume weighting (discussed little here) would seem quite physical but appears to lead to gauge dependence [96, 95], and incorrect predictions in at least some gauges (see [97, 98]). The related CV (p =“unit of comoving volume”) method may avoid some of this difficulty, but at some cost to physicality: comoving volumes are generally meaningful only insofar as they are re-converted to physical ones, or if there are conserved objects (baryons, galaxies, etc.) with fixed density per unit comoving volume. The latter may be true after reheating, but it is unclear to us that comoving volume is as meaningful *during* a complex, inhomogenous inflationary period. Another option is to weight according to the integrated incoming probability current [91, 90]

across reheating surfaces, which can be found directly from volume distributions. This proposal, which is tied more closely to the conditionalization, avoids the gauge dependence and spurious predictions of standard volume weighting (as discussed above, this prescription can reproduce the results of the RTT method [90, 1]).

The CHC and W methods have $p = \text{“bubbles,”}$ which might be tied to conditionalization objects associated with the various reheating surfaces (though this involves considerable uncertainty since those reheating surfaces are generically infinite). However, the objects (worldlines and shadows) actually used to arrive at a bubble count seem rather less physical, particularly as they demand a cutoff prescription that – while natural – also seems as if it could easily be different. The RT and RTT methods use $p = \text{“segment of a worldline between vacuum transitions,”}$ and has been suggested as an appropriate measure if we identify $X = \text{“unit of entropy production”}$ [2, 92]. This connection is not entirely compelling, however, as the results of these “holographic” measures can be found by considering an ensemble of observers (as noted in Sec. 5.2.1 and by [90]). These connections suggest that CV, RT, and RTT are very closely related, but with a consistent and appropriate physical interpretation somewhat lacking.

Consider now gauge independence. Physical volume weighting is gauge dependent, but the other measures appear gauge-independent, albeit with some caveats. For RT, RTT, W, and CHC, gauge-independence stems from their counting of objects (bubbles) or events (transitions); in CV it occurs via use of a congruence of geodesics, which are also then “counted” to obtain comoving volume. The caveats stem from subtleties – connected with a time variable choice – in defining cutoffs, transitions rates, and initial conditions, and we hope to elucidate some of these further in future work. (We single out CV as partially gauge-dependent because the results will depend on the time slicing used to characterize the initial value surface.)

Drawing on the description of the various measures presented in Sec. 5.2.1, we can see that not all of the measures under discussion have the ability to cope with all types of transitions

and vacua. For instance, the CV method accords zero weight to metastable minima (particularly disturbing as we may live in one), and the RT method in its current formulation is not able to describe a landscape with terminal vacua. We also note that the CV and RTT methods are dependent on initial conditions.

In Sec. 5.5, we argued that it is possible – if certain types of “L” bubble nucleation events occur – for different regions of the eternally inflating multiverse to be separated by wormholes, and therefore causally disconnected. None of the evaluated measures are, as formulated, equipped to deal with such spacetimes in a reasonable way. The “philosophy” behind CV and CHC – of counting bubbles or volume on future infinity – might reasonably apply to such spacetimes, and if this could be implemented technically we argued that in this case CV would probably become independent of initial conditions. The philosophy behind RTT and RT would suggest simply ignoring these events (as indeed those measures effectively do) but it is rather unclear to us that this is appropriate. Accounting for such tunneling events in measure prescriptions is very difficult – but this merely highlights the possible importance of such transitions, and of determining whether or not they occur.

Even thornier problems might arise from considering transitions in greater generality. All of the measures considered rely on a congruence of worldlines and a fairly straightforward spacetime structure. Were we to include transitions between different string/M theory flux vacua, including even different numbers of large spacetime dimensions, it is unclear whether the principles of extant measures would apply. Without having a well-defined description of such transitions this is difficult to assess, hence we do not consider this in our table.

But even confining our attention to (relatively) well-understood spacetime evolution in a general scalar potential landscape, the measures differ somewhat in how generally and robustly they treat “vacua” and “transitions”. All of the measures under discussion have been applied to the brand of eternal inflation driven by metastable minima. However, it would be desirable to

include the effects of all the dynamics of an eternally inflating universe, and the effective scalar fields that are imagined to drive it. This includes a description of the diffusion and classical rolling of the field that will occur. There has been work extending CV and CHC methods to these cases, but little so far in making such an extension to RT or RTT.

In terms of connecting transition rates to physical transitions, all of the measures ignore the small-scale details of vacuum transitions (i.e. within a few Hubble volumes). This may be relatively benign, but bears investigation. For example in RTT “transitions” are thought of as something that occurs to a worldline within its causal diamond – but these transitions could occur via the encounter of a bubble formed in a nucleation process *outside* the causal diamond.

More trouble occurs when we consider nearby vacua separated by a small barrier. The main observations of this paper centered around a study of the sample landscapes shown in Fig. 5.3 using the RTT method. In Sec. 5.3.1 it was found that pairs of vacua that undergo fast transitions will be very strongly weighted. Using order of magnitude estimates of the transition rates, we argued that the probability ratio of such pairs to other vacua in the sample landscape can be exponentially large. This effect occurs in both terminal and recycling landscapes. Using the equivalences between the various measures noted in Sec. 5.2.2 (for a summary, see Fig. 5.2), and an explicit example for the CHC method, we have shown that the weighting of fast-transitioning pairs occurs in the CHC, W, and RT methods as well. As discussed in Sec. 5.3.3, because of this effect, by inserting a small barrier in an intermediate state, the absolute weight assigned to each vacuum is affected drastically. Therefore, the RTT, RT, W, and CHC methods are only partially robust in their definition of transitions; the undivided-well distribution is not recovered as the barrier disappears. This situation might be remedied if, as bubble collisions become more and more important, the diffusion analysis replaces bubble nucleation (giving further impetus to generalizing the measures to treat this). In contrast, the CV method *does* approach the undivided-well weight as the small barrier disappears.

Lastly, we considered continuity in transition rates, which was studied using a two-well landscape in Sec. 5.3.4. It was noted that the predictions of the CHC, RT, and RTT methods change discontinuously as a recycling vacuum is deformed into a terminal vacuum. This discontinuity makes the *exact* properties of vacua in a landscape important. Such a discontinuity could be avoided if the order of limits in the cutoff procedure were modified.

Most of the discussion – and all of the scorecard – has focused on issues of principle concerning the measures as abstract procedures. Some of the discussed features have implications for what such assumed measures would mean *observationally*. In particular, we saw in Sec. 5.4 that the exponential dependence of the prior distribution P_p on the details of the potential implies that making predictions using bubble counting measures may be very hard. This problem is particularly acute when, for some parameter α , the factors $P_p(\alpha)$ and $n_{X,p}(\alpha)$ (these are the prior and conditionalization factors needed to produce a prediction in the form of Eq. 5.1) vary appreciably over the same range in α . This may be the case, for example, when α is related to the number of e-folds during inflation. If the observation that fast-transitioning pairs are exponentially weighted generalizes to more complicated landscapes, then bubble-counting measures may in some cases lead to strongly exponential prior probabilities that would overwhelm any conditionalization factor $n_{X,p}(\alpha)$. This would lead to very strong predictions, which might be successful, or disastrous. More generally, this exponential dependence suggests that current measures seem to potentially call for a complete knowledge of the fine details of the entire landscape, a Herculean requirement.

Perhaps not surprisingly, we come to the conclusion that while progress has been made towards predicting our place in the multiverse, we are far from finished. It would be desirable to find and explore other measures, and see if they fall victim to any of the same problems that we have outlined.

Chapter 6

Measures on transitions for cosmology from eternal inflation

6.1 Introduction

”Cosmic inflation”, the idea that the early universe underwent an epoch of accelerated expansion, was developed to account for the universe’s observed uniformity, geometric near-flatness, absence of GUT monopoles, and required small density inhomogeneities. But while inflation grants these wishes, it, like the proverbial genie let out of the bottle, is difficult to contain. In nearly any model in which the scalar field potential driving inflation has multiple minima, the very exponential expansion responsible for inflation’s predictive successes also prevents a global end to inflation: the expansion shields still-inflating regions from the encroaching effect of those where inflation has ended. Such models can be fairly described as ”eternal” because a time foliation exists in which the physical inflating volume expands exponentially forever, and inflation only ends *locally* in regions where the field settles into a particular, low energy, potential minimum or “vacuum”.

Moreover, developing understanding of metastable states in string theory seems to be pointing towards a vast, interconnected, many-dimensional web or “landscape” of many, many such vacua. Populated by eternal inflation, this would lead to an ensemble of “bubble universes” with diverse properties, making predictions of low-energy observables probabilistic. A major open question is how – even in principle – this probability distribution should be calculated, and significant effort has been expended in finding methods to assign probabilities $P(v_k)$ to different vacua v_k using, e.g., bubble abundances, frequencies of vacuum entries, and probability currents (e.g., [96, 105, 104, 2, 103, 102, 101, 90]).

We argue here that such $P(v_k)$ are insufficient: while many particle-physics-type observables may depend on the vacuum alone, many cosmological observables depend not just on what vacuum a region is in at some time, but also on *the history of that region*. Thus, what is actually required in principle is a measure over *histories* rather than over vacua. Putting measures over histories is not a new concept (e.g., [108, 107]), but counting full histories to determine low-energy observables is probably overkill if significant inflation occurs after most transitions that lead to low energy vacua. The final transition type will typically determine the slow-roll inflationary history down to a low energy state, and hence answer most cosmological and low-energy particle physics questions. Thus a measure over *transitions* should be sufficient (and much simpler to calculate) for most purposes.

6.2 Transitions rather than vacua

In the “multiverse” picture suggested by eternal inflation, the 20-odd parameters α_i defining both a “standard model” of particle physics and a cosmology since inflation’s end (see, e.g. [109] for a listing) might be described by a 20-odd dimensional joint probability distribution $\mathcal{P}_X(\alpha_i)$, where X is some “conditionalization object” such as a point in space, baryon, galaxy, or

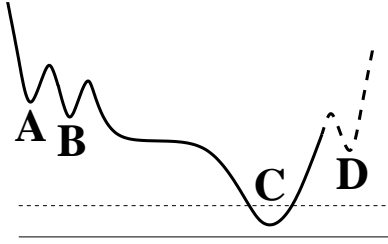


Figure 6.1: A simple potential landscape. We consider both a positive and negative energy C -well, with the zeros in energy density denoted by the solid or dotted line. In the text, we discuss both three-well (composed of (A, B, C)) and four-well (composed of (A, B, C, D)) landscapes.

“observer”, and $\mathcal{P}_X(\alpha_i)$ governs the chance – given no other information – that an “X” inhabits a region with parameters described by α_i [89, 88].

How can $\mathcal{P}_X(\alpha_i)$ be calculated? A method based on vacua, as is generally done, might run as follows. Suppose there is a unique set $\alpha_i(w_k)$ of parameter values and a fixed number $N_X(w_k)$ of X-objects associated with each w_k , where each w_k is equated with a particular vacuum v_k . Then for each i we might calculate:

$$\mathcal{P}_X(\alpha_i) = \int d\alpha'_i \sum_k N_X(w_k) P(w_k) \delta(\alpha'_i - \alpha_i(w_k)), \quad (6.1)$$

normalize, and smooth the distribution if desired.

However, both α_i and N_X often depend not just on the vacuum v_k , but also on how that vacuum was reached – that is, there is a one-to-many mapping from vacua v_k to observables α_i . For example, consider the potential $V(\phi)$ in Fig. 6.1. Bubbles of vacuum C can form via Coleman-De Luccia transitions [12] from either the B or D vacua. The endpoint of tunneling from B would lie on the flat region of the potential, whereas the endpoint of tunneling from D might be very near C ’s minimum. The number N_e of inflationary e-folds between tunneling and reheating then depends on which of these two transitions took place.

Clearly, each vacuum will not correspond to a unique set of α_i for inflationary predictions like N_e , the tensor/scalar ratio, the curvature scale, the perturbation amplitude, the

reheating temperature, etc.¹ Instead, each vacuum maps to a set of possibilities that may be large, given that in a many-dimensional landscape there might be hundreds of directions from which to tunnel. It is possible that some non-inflationary predictions could depend on the vacuum tunneled from as well.

Even if a parameter $\alpha_{(i)}$ does depend on just the vacuum v_k (for instance the late-time vacuum energy), the “counting factor” N_X very likely will not. For example, X choices of “a unit volume on the reheating surface” (e.g., [104]) or “a galaxy” (e.g., [112, 109]) or “a unit of entropy generation” [2] would all seem to depend on (at least) N_e .² Thus even if $\alpha_{(i)}$ is merely *correlated* in N_X or P with an observable that depends on the predecessor vacuum, properly predicting $\alpha_{(i)}$ using \mathcal{P}_X requires accounting for the transition history.

These considerations suggest that we may still use Eq. 6.1 to calculate $\mathcal{P}_X(\alpha_i)$, but that each w_k should correspond to a *transition* between two vacua, which will (in most cases) map directly both to a unique set of observables α_i and to a unique counting factor N_X . We stress here that fully labeling a transition requires specification of both a “before” and an “after” vacuum.

It is also quite possible that the transition rates and mechanisms themselves depend on the transition history. For example, Tye [113] has recently argued that in a landscape like Fig. 6.1, very fast “resonant” tunneling from $A \rightarrow C$ can occur if (a) the (non-resonant) $B \rightarrow C$ transition rate approximately equals the $A \rightarrow B$ rate, and (b) the shape of the potential near vacuum B satisfies a “resonance condition” (see also [114]). Such tunneling in a general landscape can be accounted for consistently, but only if one allows the $B \rightarrow C$ transition rate to depend upon whether or not the previous transition was $A \rightarrow B$.

As another example, consider the case where the C -well in Fig. 6.1 has negative energy.

¹This dependence can be seen “in action” in Tegmark’s study [98] of inflationary predictions for random one-dimensional potentials.

²In fact, N_X will often be infinite and require regularization; we will not pursue that thorny difficulty here.

A transition $D \rightarrow C$ might (if the potential is suitably chosen) yield no post-tunneling inflation and lead quickly to a big-crunch in bubble’s interior, so that the tunneling rate out of C would either be extremely suppressed or even vanish identically. But after a tunneling from $B \rightarrow C$, transitions back to B might occur during the near-de Sitter phase during slow roll toward C .³

6.3 Transitions on a single worldline

We now develop a transition-based analogue of Bousso’s “holographic probability” measure for vacua [2].⁴ Consider a worldline that passes through spacetime regions described by different vacua. If we denote by NM the transition from vacuum M to N , then we can denote by p_i^α , with $\alpha = NM$, the probability that the i th transition experienced by the worldline is NM .

If we now assume that the probability that a transition β is followed by a transition α is independent of transitions before β , and denote this probability (or “branching ratio”) by μ_{β}^{α} , then the p_i^α form a Markov chain, with

$$p_{i+1}^\alpha = \sum_{\beta} \mu_{\beta}^{\alpha} p_i^{\beta}. \quad (6.2)$$

Note that if $\alpha = NM$ and $\beta = LK$ then μ_{β}^{α} is nonzero only for $L = M$, and that in general $\mu_{\beta}^{\alpha} \neq \mu_{\alpha}^{\beta}$. Also, normalization of the probabilities requires that $\sum_{\alpha} \mu_{\beta}^{\alpha} = 1$ if transition β ends in a metastable vacuum; if β ends instead in a “terminal” vacuum (which cannot be transitioned out of), μ_{β}^{α} vanishes for all α .

Now, if we start with some initial condition p_0^α , and write \mathbf{p} as a vector and $\boldsymbol{\mu}$ as a matrix (with entries labeled by the greek indices), then $\mathbf{p}_i = (\boldsymbol{\mu})^i \mathbf{p}_0$, and the expected number n_j^α of transitions of type α after j steps (excluding the “zeroth” transition) is:

³This distinction would be critical in measures that yield very different probabilities depending on whether transitions are allowed – with whatever probability – out of a vacuum or not; see [18].

⁴Indeed, the dependence of entropy production on the parent vacuum, and the necessity to introduce a formalism such as that presented here, was anticipated in the conclusions of the pre-print versions of [2].

$$\mathbf{n}_j = \sum_{i=1}^j \mathbf{p}_i = \mathbf{S}_j \mathbf{p}_0, \quad (6.3)$$

where $\mathbf{S}_j \equiv \sum_{i=1}^j (\boldsymbol{\mu})^i$.

The sum can be performed exactly if the landscape is terminal, and must be regulated in the case of a fully recycling landscape (we refer the reader to the Appendix of [18] for analogous details). In either case, in the $j \rightarrow \infty$ limit the number of transitions is proportional to

$$\mathbf{n}_\infty \propto \{\text{adj}(\mathbf{1} - \boldsymbol{\mu})\} \boldsymbol{\mu} \mathbf{p}_0, \quad (6.4)$$

where adj denotes the adjoint matrix operation (i.e. the transpose of the matrix of cofactors of the matrix in question). Normalizing \mathbf{n}_∞ yields probabilities for the various transitions in the model.

To illustrate this method, consider a landscape with three vacua (A, B, C), with vacuum energies $V_C < V_A, V_B$ (solid curve in Fig. 3.47), that can experience nearest-neighbor transitions only. If $p_i^\alpha = (p_i^{AB}, p_i^{BA}, p_i^{CB}, p_i^{BC})$, we obtain

$$\boldsymbol{\mu} = \begin{pmatrix} 0 & \mu_{BA}^{AB} & 0 & \mu_{BC}^{AB} \\ \mu_{AB}^{BA} & 0 & 0 & 0 \\ 0 & \mu_{BA}^{CB} & 0 & \mu_{BC}^{CB} \\ 0 & 0 & \mu_{CB}^{BC} & 0 \end{pmatrix}. \quad (6.5)$$

Imposing the normalization condition on the columns, we obtain $\mu_{AB}^{BA} = 1$, $\mu_{BA}^{AB} = \epsilon$, $\mu_{BA}^{CB} = 1 - \epsilon$, $\mu_{BC}^{AB} = \delta$, $\mu_{BC}^{CB} = 1 - \delta$, and $\mu_{CB}^{BC} = 0$ (resp. $\mu_{CB}^{BC} = 1$) if C is terminal (resp. recycling), with free parameters $\epsilon, \delta < 1$.

As an example, if the fictitious zeroth transition is BA (i.e. $p_0^\alpha = (0, 1, 0, 0)$), starting us in vacuum B , the expected number of transitions for the terminal case ($\mu_{CB}^{BC} = 0$) is $\mathbf{n}_\infty =$

$(\epsilon/(1-\epsilon), \epsilon/(1-\epsilon), 1, 0)$. Normalizing, the transition probabilities are given by

$$\begin{aligned} P(AB) &= \frac{\epsilon}{1+\epsilon}, & P(BA) &= \frac{\epsilon}{1+\epsilon}, \\ P(CB) &= \frac{1-\epsilon}{1+\epsilon}, & P(BC) &= 0. \end{aligned} \tag{6.6}$$

Using any initial condition, we can compute the number of transitions in the recycling case ($\mu_{CB}^{BC} = 1$), yielding $\mathbf{n}_\infty \propto (\delta, \delta, 1-\epsilon, 1-\epsilon)$. Normalizing, the probabilities assigned to the various transitions are then:

$$\begin{aligned} P(AB) &= P(BA) = \frac{\delta}{2(1-\epsilon+\delta)}, \\ P(CB) &= P(BC) = \frac{(1-\epsilon)}{2(1-\epsilon+\delta)}. \end{aligned} \tag{6.7}$$

6.3.1 Recovery of one-point statistics

Let us quantify the extent to which the transition counting measure presented above is a generalization of Bousso's [2] measure for vacua. In [2], one considers n_v vacua with transitions between them, the rates of which depend only upon the starting and ending vacuum. Describing these transitions requires $n_v(n_v - 1)$ transition rates with n_v normalization conditions, hence $n_v(n_v - 2)$ independent numbers must be specified. In contrast, there are $n_v(n_v - 1)^2$ possible transitions between transitions, with $n_v(n_v - 1)$ normalization conditions, hence $n_v(n_v - 1)(n_v - 2)$ independent parameters. There is thus $n_v - 1$ times as much freedom, essentially corresponding to the $n_v - 1$ ways a vacuum might be entered.

Now let us see how probabilities for states can be reproduced. Thinking in terms of states rather than transitions suggests two things: (1) assuming that transition rates depend only upon the initial and final states (that is, for a given α , μ_{β}^{α} is identical for all β that end in the same state) and (2) that we are interested primarily in the probability accorded to each vacuum M . To obtain this probability, we simply sum \mathbf{n} over all transitions that end in M , do likewise for all other vacua, then normalize.

Probabilities for the states A , B and C in the examples above can be found by setting $\delta = \epsilon$ (assumption (1) above) and summing over the two transitions that end in B to obtain results in agreement with those of [2].

It is worth noting that under assumption (1), one can calculate the relative frequencies $p(NM)$ of the different transitions by first calculating the relative frequencies $p(M)$ of different parent vacua (but now including the starting transition in \mathbf{n}_j), then multiplying by the “branching ratio” μ_M^N , which is the (normalized) probability that M transitions into N . In cases where assumption (1) holds, this can provide a simpler procedure.

6.3.2 Higher moments and longer histories

In principle it is possible that either (a) we might desire probabilities for strings of three or more transitions, or (b) transition rates might depend on the last two or more transitions. Probabilities for long chains are simple if transition rates depend only on at most the previous transition. Then, if we wish to count chains $PON\dots MLK$ along a worldline, we simply multiply $p(LK)$ by a string of branching ratios: $p(PON\dots MLK) = \mu_{ON}^{PO}\dots\mu_{LK}^{ML}p(LK)$.

If transition rates *do* depend on two or more previous transitions, it is still straightforward to generalize the counting to longer histories (groups of transitions). Focusing on the count along a single worldline, if we set $\alpha = PO\dots LK$, $\beta = NM\dots JI$, then μ_β^α implements transitions from the transition group $I \rightarrow \dots \rightarrow N$ into the group $K \rightarrow \dots \rightarrow P$. This allows the transition rate to a new vacuum to depend on a history of transitions of arbitrary length. To accomplish this, we set $\mu_\beta^\alpha = 0$ unless $\alpha = QNM\dots J$ for some Q ; that is, we only allow transitions such as $CBA \rightarrow DCB$ or $DCB \rightarrow EDC$ but not, e.g. $CBA \rightarrow EDC$ (which would allow the DC transition rate to depend on what transition occurs *after* DC). With this setup, we can calculate $p(N\dots M)$, using the same Markov chain techniques described above.

6.4 Counting total transition numbers

The measure discussed in the previous sections assigns weight to various transitions occurring on a single worldline. It is also possible to define a measure based on the total number of transitions occurring in the eternally inflating spacetime. Consider the method of Garriga et al. [102], which follows the evolution of a congruence of hypersurface-orthogonal geodesics extending from some initial spacelike slice. The formalism first calculates the fraction of geodesics in a given phase as a function of time. To extend this method, we must keep track of the fraction f^{NM} of these “comoving observers” in vacuum N that came from vacuum M , such that $\sum_{N,M} f^{NM} = 1$. The dynamics are determined by the rate equations

$$\frac{df^{NM}}{dt} = - \left(\sum_P \kappa_{NM}^{PN} f^{NM} \right) + \left(\sum_L \kappa_{ML}^{NM} f^{ML} \right), \quad (6.8)$$

where κ_{BA}^{CB} are the transition rates.

The state-based rate-equation formalism can be recovered by assuming that rates do not depend on the previous transition ($\kappa_{NM}^{PN} \rightarrow \kappa_N^P$), and then summing over M ($f^N \equiv \sum_M f^{NM}$) to yield

$$\frac{df^N}{dt} = \sum_P -\kappa_N^P f^N + \sum_M \kappa_M^N f^M. \quad (6.9)$$

Note that there are n_v equations for f^N , but $n_v(n_v - 1)$ equations for f^{NM} , reproducing the fact that there are $(n_v - 1)$ more degrees of freedom in a transition-based framework.

The procedure given by [102] for counting the total number of bubbles of type N nucleated in a background M before some (NM -dependent) time cutoff can be generalized straightforwardly: the number of such bubbles formed per unit time would be given by the formation rate $\sum_L \kappa_{ML}^{NM} f^{ML}$ of comoving volume fraction f^{NM} , divided by the asymptotic comoving volume of bubbles of N . f^{NM} itself can be calculated by formulating Eq. 6.8 as a matrix problem, in a manner similar to that for the standard rate equations presented in [102].

Bubble-counting measures may be extended to longer histories (of bubbles within bubbles within bubbles...) in a similar manner as for transitions along a worldline.

6.5 Conclusions

Many cosmological observables depend upon how the inflaton evolves to the minimum of its potential, which in turn depends on how that minimum's basin of attraction was entered. We have therefore argued that a measure for eternal inflation should assign weights to *transitions* between vacua, as opposed to existing measures that count vacua regardless of how they were reached. Moreover, a measure on transitions is a more natural way to apply many of the “anthropic” conditionalizations being considered today (baryons, galaxies, entropy produced, etc.), since these also generally depend upon the transition type rather than simply the vacuum considered.

We showed how two proposed measures – counting either vacuum entries by a worldline, or the total number of bubbles of different vacua in an eternally inflating spacetime – could be modified to count transitions as opposed to vacua, as well as how the transition formalism could be extended to allow for history-dependent transition rates, and to provide probabilities for longer histories.

Chapter 7

Towards observable signatures of other bubble universes

7.1 Introduction

Cosmological inflation never ends globally when driven by an inflaton potential with long-lived metastable minima. This was discovered in the very first models of inflation as a failure of “true” (lower) vacuum bubbles in a “false” vacuum background to percolate [115]. It was later recognized as a special case of “eternal inflation” in which our observable universe would lie within a single nucleated bubble [116] while inflation continues forever outside of this bubble (e.g., [115, 117]).

While important for any sufficiently complicated inflaton potential, this issue has become prominent lately with the realization that stabilized string theory compactifications appear to correspond to minima of a many-dimensional effective potential “landscape” [85, 118] that would drive just this sort of eternal inflation and thus create “pocket” or “bubble” universes with diverse properties. This has raised a number of very thorny questions regarding which properties

to compare to our local observations (e.g. [88, 119]), as well as debates as to whether these other “universes” have any meaning if they are unobservable, as is the conventional wisdom.

But what if they *are* observable, so that the processes responsible for eternal inflation can be directly probed? What is the chance we could actually see such bubbles, and how would they look on the sky? These are the questions that the present paper begins to explore.

It would seem that for us to observe bubble collisions in our past, three basic and successive criteria must be met:

1. *Compatibility*: A bubble collision must allow standard cosmological evolution including inflation and reheating – and hence be potentially compatible with known observations – in at least part of its future lightcone.
2. *Probability*: Within a given “observation bubble” (seen as a negatively-curved Friedmann-Robertson-Walker (FRW) model by its denizens) a randomly chosen point in space should have a significant probability of having (compatible) bubbles to its past.
3. *Observability*: The effects of compatible bubbles to the past must not be diluted away by inflation into unobservability, nor affect a negligible area of the observer’s sky.

Although a rigorous analysis of these issues does not yet exist, several recent studies suggest – in contrast to previous thinking – that it is actually plausible that these three criteria may be met.

First, studies of bubble collisions “boosted” so that one bubble forms much “earlier” than the other indicate that the older bubble may see the younger bubble as a small perturbation that does not disrupt its overall structure [120], even if the younger bubble contains a big-crunch singularity [121]. Second, straightforward arguments (see below), inspired by the results of Garriga, Guth & Vilenkin [122] (hereafter GGV), indicate that a random position in the

FRW space within a bubble should (with probability one) have a bubble nucleation event to its past. Third, in a complex inflaton potential with many minima, the number of e-foldings within a randomly chosen bubble can become a random variable with some probability distribution. Suppose that this distribution favors a small number of e-foldings, and yet – either to match our observations or for “anthropic” reasons – we focus only on the subset of bubbles with $< N_{\min} \sim 50 - 60$ e-foldings. Then we might expect that our region underwent close to N_{\min} e-foldings [98, 123]. Thus it is plausible that just enough inflationary e-foldings occurred to explain the largeness and approximate flatness of the universe; and since the CMB perturbations on the largest scales formed $\sim N_{\min}$ e-foldings before the end of inflation, perturbations at the beginning of inflation may then be detectable.

None of these studies have actually addressed whether bubble collisions might be observable, however, and leave many key questions unresolved. The bulk of the present paper aims to help answer several of these questions by calculating, given an observer at an arbitrary spacetime point in an bubble, the expected differential number

$$\frac{dN}{d\psi d(\cos\theta)d\phi} \tag{7.1}$$

of bubble collisions on the observer’s bubble wall, seen on the sky by the observer with angular scale ψ and direction (θ, ϕ) .

We will see that for small nucleation rates, this distribution is interesting for two cases. First, very late-time observers might observe a nearly-isotropic distribution of bubbles with tiny angular scales. Second, for a typical position inside the bubble, many bubbles enter the past lightcone at early times and with large angular scales (i.e., each collision will affect the majority of the observer’s sky), nearly all from a particular direction on the sky. While we can only speculate as to how these bubbles would look observationally, the detection of either signal would offer direct observational evidence that we inhabit a universe undergoing false-vacuum

eternal inflation, and would bolster support for fundamental theories that may drive this type of cosmological evolution.

We proceed as follows. In Sec. 7.2 we discuss the dS background and the structure of a bubble universe inside it, then outline the calculation to be performed and the simplifying assumptions we will employ. In Sec. 7.3 we display the calculation. The basic results and their implications are summarized in Sec. 7.4, and readers uninterested in the details of the computations can skip from Sec. 7.2 to this section. Finally, in Sec. 7.5 we conclude.

7.2 Setting up the problem

The system we will study consists of a de Sitter spacetime (dS) supported by a false-vacuum energy, containing nucleated Coleman-de Luccia (CDL) [12, 10, 11] bubbles of true vacuum. We work in the approximation where all bubbles are nucleated with vanishing size, expand at the speed of light, and have an infinitely thin wall. Bubble walls then correspond to spherically symmetric null shells.

The geometry of the bubble interior, the background de Sitter space, and the wall between them can all be visualized and understood in terms of a 5D embedding space with coordinates X^μ , $\mu = 0\dots 4$, and Minkowski metric $ds^2 = \eta_{\mu\nu}dX^\mu dX^\nu$. In this embedding, pure dS is a hyperboloid defined by $\eta_{\mu\nu}X^\mu X^\nu = H^{-2}$, where $H^2 = 8\pi\rho_\Lambda/3$ in terms of the vacuum energy density ρ_Λ .

In formulating the problem we employ the “flat slicing” coordinates (t, r, θ, ϕ) to describe the dS (with $H = H_F$) outside of the bubble. In the embedding space, these coordinates

are given by

$$X_0 = H_F^{-1} \sinh H_F t + \frac{H_F}{2} e^{H_F t} r^2 \quad (7.2)$$

$$X_i = r e^{H_F t} \omega_i$$

$$X_4 = H_F^{-1} \cosh H_F t - \frac{H_F}{2} e^{H_F t} r^2,$$

with $(\omega_1, \omega_2, \omega_3) = (\cos \theta, \sin \theta \cos \phi, \sin \theta \sin \phi)$, $0 \leq r < \infty$, $-\infty < t < \infty$. This induces the metric:

$$ds^2 = -dt^2 + e^{2H_F t} [dr^2 + r^2 d\Omega_2^2], \quad (7.3)$$

which covers half of the de Sitter hyperboloid.

Turning now to the bubble, the exact form of the post-nucleation bubble interior is found from the analytic continuation of the CDL instanton [12], with the details largely dependent on the form of the inflaton potential. The null cone, which in our approximation traces the wall trajectory, more generally corresponds to the post-tunneling field value.¹ Inside of this null cone, the metric is that of an open FRW cosmology

$$ds^2 = -d\tau^2 + a^2(\tau) [d\xi^2 + \sinh^2 \xi d\Omega_2^2]. \quad (7.4)$$

This metric is induced by the embedding

$$X_0 = a(\tau) \cosh \xi \quad (7.5)$$

$$X_i = a(\tau) \sinh \xi \omega_i$$

$$X_4 = f(\tau),$$

where $0 \leq \xi < \infty$, $0 < \tau < \infty$, and where $f(\tau)$ solves $f'^2(\tau) = a'^2(\tau) - 1$. If we set $a(\tau) = H_T^{-1} \sinh(H_T \tau)$, we have $f(\tau) = H_T^{-1} \cosh(H_T \tau)$, and we recover the usual “open slicing” of dS.

¹At late times, the identification of the null cone with the position of the bubble wall becomes an increasingly accurate approximation, and we can safely neglect the portion of the spacetime encompassing the wall.

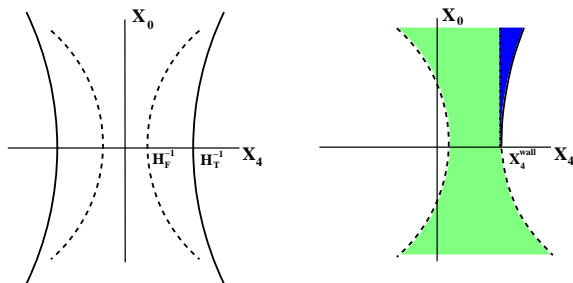


Figure 7.1: On the left is the embedding of two dS spaces of different vacuum energy in 5-D Minkowski space (three dimensions suppressed). The construction obtained by matching these two hyperboloids along a plane of constant X_4 , as shown on the right, corresponds to the one-bubble spacetime shown in Fig. 7.2 in the limit where the bubble interior is pure dS. The light shaded (green) region represents the false vacuum exterior spacetime, while the dark shaded (blue) region represents the interior spacetime.

Now these two spacetimes can be “glued together” across the bubble wall.² In the limit where the bubble interior is pure dS, this corresponds to gluing two dS hyperboloids in the embedding space, and breaks the original $SO(4,1)$ symmetry of empty de Sitter space to $SO(3,1)$, since we must choose an axis (here, we choose X_4) along which to do the pasting. This procedure is shown schematically in Fig. 7.1. For a more general interior $a(\tau)$ the picture is similar but with the “scale” of the hyperboloid varying with $X_4 > X_4^{\text{wall}}$.

The basic setup of the problem we wish to consider is shown in Fig. 7.2, which is the conformal diagram for de Sitter space containing a true vacuum bubble. In this model our observable universe resides within the “observation bubble.” The spacelike slices inside this bubble correspond to surfaces of constant- τ that, by the homogeneity of the metric Eq. 7.4, are also surfaces of constant curvature and density. These slices correspond to the various epochs of cosmological evolution inside of the bubble: the beginning of inflation (near the tunnelled-to field value), the end of inflation at the failure of slow-roll, reheating, the recombination epoch, etc., up until the present time.³

²Even in the thin-wall limit this is only an approximate solution to the coupled Einstein and scalar field equations (for the full solution, see eg [1]), corresponding to the limit where the initial bubble radius vanishes.

³We note that it is difficult to construct inflaton potentials (without considerable fine tuning) giving rise to a

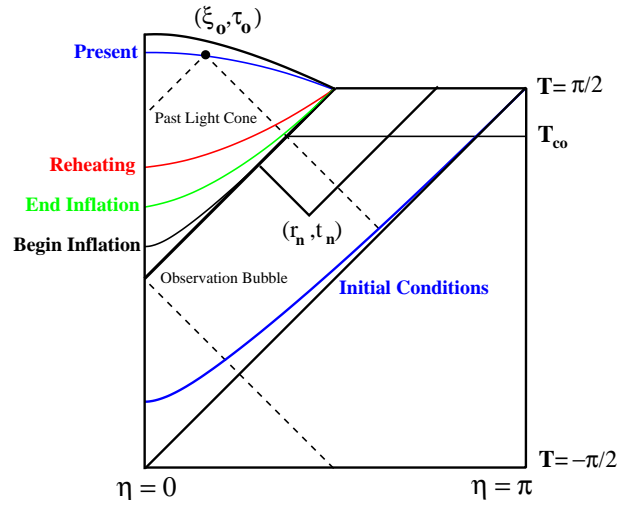


Figure 7.2: The conformal diagram for a bubble universe. We imagine an observer at some position $(\xi_o, \tau_o, \theta_o)$ inside of the observation bubble, which is assumed to nucleate at $t = 0$ and expand at the speed of light. The foliation of the bubble interior into constant density, negative curvature, hyperbolic slices is indicated by the solid lines. These spacelike slices denote epochs of cosmological evolution in the open FRW cosmology inside of the bubble. The past light cone of the observer is indicated by the dashed lines. There is a postulated no-bubble surface at some time to the past of the nucleation of the observation bubble. Also shown is a $(\theta = \theta_n, \phi = \phi_n)$ slice of a) colliding bubble that nucleated at some position $(t_n, r_n, \theta_n, \phi_n)$, and intersects the bubble wall within the past light cone of the observer.

If the nucleation rate λ (per unit physical 4-volume) of true-vacuum bubbles is small compared to H_P^4 , the observation bubble will be one of infinitely many that form as part of what either is or approaches a “steady-state” bubble distribution wherein there is a foliation of the background dS in which the bubble distribution is statistically independent of both position and time (see [124], and also [117, 125].) An infinite subset of these will actually collide with the observation bubble.

If we now assume that our bubble experiences what a “typical” bubble in the steady-state distribution does, then we can follow the strategy of GGv and consider the bubble to exist at $t = 0$, model the background as having an initial pure false-vacuum surface at $t = t_0$ (indicated in Fig. 7.2), then send $t_0 \rightarrow -\infty$. (By doing this, GGv explicitly showed that there is a “preferred frame” in the model of eternal inflation they treated, which coincides with comoving observers in the “steady-state” foliation, and is related to the initial false-vacuum surface; observers with different boosts with respect to this frame see bubble collisions at different rates.)

Given an observer at time τ_o and hyperbolic radius ξ_o inside the bubble, we can define a two-sphere by the intersection of the observer’s past lightcone (dashed lines in Fig. 7.2) with another equal- τ surface (i.e. corresponding to a portion of the recombination surface or the bubble wall). The question we now wish to address is: **what is the number of bubbles observed in a given direction (θ, ϕ) with a given angular size on the two-sphere (the observer’s “sky”)?** This quantity could provide the basis for a calculation of the impact on the observer’s CMB of incoming bubbles that distort the recombination (or reheating, etc.) surface.

In the next section we calculate this quantity under the following assumptions:

1. We assume that bubbles start at zero radius and expand at lightspeed at all times. We also

cosmological evolution inside of the bubble similar to our own.

assume that the bubbles do not back-react, i.e. one bubble will not alter the trajectory of a subsequent bubble. This may be important for directions on the sky hit with multiple bubbles, but requires a careful treatment of bubble collisions and is reserved for future work.

2. We assume that no bubbles form within bubbles, and that there are no transitions from true to false vacuum. We comment on the implications of including these features in Sec. 7.4
3. We assume that structure of the observation bubble is unaffected by the incoming bubbles, and that the observed equal- τ surface is at $\tau \rightarrow 0$, coinciding with the bubble wall. The first – rather strong – assumption is discussed below in Sec. 7.4; the second should be reasonable insofar as we are hoping to assess the incoming bubbles’ impact on the first few e-foldings of inflation.

Within this setup, let us examine why it is plausible for a typical observer to have one or more bubble nucleations within their past lightcone. Because bubbles expand as lightcones and nucleate with some rate λ per unit 4-volume, the expected number of bubbles in an observer’s past lightcone is just λV_4 , where V_4 is the 4-volume of the exterior spacetime contained in the past light cone of the observer, bounded by the initial value surface, the bubble wall, and the past light cone of the nucleation site of the observation bubble (which enforces the no bubbles-within-bubbles approximation). This 4-volume depends on the position of the observer inside of the bubble and the epoch of observation.

Now, the spatial volume in a coordinate interval $d\xi$ goes as $dV_3 \propto 4\pi \sinh^2 \xi d\xi$, thus the volume is exponentially weighted towards large ξ . If observers inside of the bubble are uniformly distributed on a given constant- τ surface, we would expect most of them to exist at large ξ . But as shown by [122], on any constant- τ surface, the 4-volume relevant for bubble nucleation

diverges for large ξ as $V_4 \propto \xi$. Thus even for a tiny nucleation rate⁴ most observers have a huge 4-volume to their past and should therefore expect bubbles in their past.⁵

We now proceed to calculate the distribution of collisions on our observer’s sky. Readers uninterested in the details of this calculation can proceed to Sec. 7.4 for a summary of the results.

7.3 Computations

Consider an observer at coordinates $(\xi_o, \tau_o, \theta_o)$ in the observation bubble. There is nothing breaking the symmetry in ϕ , so we are free to choose $\phi = \text{const}$.

1. First, we compute the angular scale ψ and direction θ_{obs} on the sky of the triple-intersection of the observer’s past lightcone, the bubble wall (the $\tau \rightarrow 0$ surface), and the wall of a bubble nucleated at some point in the background spacetime.
2. We then find the differential number (Eq. 7.1) of bubbles of angular size ψ in the direction θ_{obs} by integrating the volume element for the exterior spacetime over all available nucleation points on a surface of constant ψ and θ_{obs} and multiplying by the bubble nucleation rate λ .

Both items can be computed in two different frames that we shall denote the “unboosted” and the “boosted” frames. In the original “unboosted” frame, where the observer is at $(\xi_o, \tau_o, \theta_o)$, we compute the locations of triple-intersections on the 2-sphere of the observer’s sky, then convert these locations to an observed angle θ_{obs} and angular scale ψ on the sky (see Sec. 7.3.1 and Appendix D). While this frame is most straightforward, the calculations are much more tractable using a trick suggested by GVV: given the symmetries of dS, a boost in

⁴We might expect a typical nucleation rate to be of order $\lambda \sim e^{-S_F}$, where S_F is the entropy of the exterior de Sitter space.

⁵If the interior vacuum energy is much lower than the exterior one, this only increases the 4-volume accessible to the observer.

the embedding space changes none of the physical quantities we are interested in (see below for elaboration). Thus we can choose a boost such that the observer lies at $\xi=0$, so that (a) θ_{obs} coincides with the coordinate angle θ_n at which the bubble nucleates, and (b) the bubble's angular scale is just given by the angular coordinate separation of the two triple-intersection points. The cost of this simplification is that the initial false-vacuum surface is boosted into a more complicated surface. In the results to follow, we will employ both the boosted and unboosted viewpoints, but will focus on the boosted frame for the calculation of the distribution function.

7.3.1 Angles according to the unboosted observer

The triple-intersection between the observation bubble, the colliding bubble, and the past light cone of the observer represent the set of events that form a boundary to the region on the observer's sky affected by the collision. Working in a plane of constant ϕ , these will correspond to two events, and the angle between geodesics emanating from these two events and reaching the observer at $(\tau_o, \xi_o, \theta_o)$ gives the observed angle on the sky. In the particular case where the bubble interior is dS with $H_T = H_F$, Appendix D gives the explicit solution to this problem, although a similar (necessarily more complicated) procedure can be applied to the more general case.

Let us visualize this by focusing now on the inside of the observation bubble which (as discussed in Sec. 7.2) is described by an open FRW cosmology. We can use the Poincaré disk representation to describe the hyperbolic equal- τ surfaces in this spacetime. Suppressing one of the spatial dimensions, the metric on a spatial slice of Eq. 7.4 becomes

$$ds^2 = 4a(\tau) \frac{dz^2 + z^2 d\theta^2}{(1 - z^2)^2}. \quad (7.6)$$

Since there are collision events that disrupt large angular scales, we find it useful for visualization purposes to let polar angle θ assume also negative values $-\pi < \theta < \pi$ and limit the range of ϕ

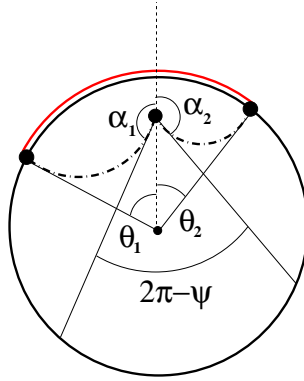


Figure 7.3: A time lapse picture of the null rays reaching an observer from the boundary of the region affected by a collision event in the Poincaré disk representation. The boundaries are located at angles $\theta_{1,2}$ from the center of the disk, and at angles $\alpha_{1,2}$ from the location of the observer. The total angular scale of the collision event as recorded by the observer, which affects the region of the disc indicated by the double lines, is given by ψ .

accordingly. Scaling by $a(\tau)^{-1}$ gives the disk unit radius, with $z = 1$ corresponding to the wall of the observation bubble, as depicted in Fig. 7.3.

This figure shows the time-lapse of a collision event from the perspective of an interior observer on the Poincaré disk. The angles θ_1 and θ_2 are the triple-intersection points. The broken lines from these points trace the path of null rays that reach the observer at $(\xi_o, \tau_o, \theta_o = 0)$, where we have used the remaining symmetry of the problem to place the observer at $\theta_o = 0$.

Analyzing this geometry, the angular position of an intersection from the perspective of an interior observer is given by

$$\cos \alpha_{1,2} = \frac{\tanh \xi_o - \cos \theta_{1,2}}{\tanh \xi_o \cos \theta_{1,2} - 1} \quad (7.7)$$

Notice that the denominator never vanishes unless $\xi \rightarrow \infty$ (the boundary) where $\cos \alpha = -1$, independent of θ . Using the above results, we conclude that the observer will see a collision as having an angular scale of

$$\psi = \alpha_1 - \alpha_2 \quad (7.8)$$

where one has to take some care choosing the correct branch of the cosine function in the process

of solving for α using Eq. 7.7, see Fig. 7.3.

Because of the hyperbolic nature of the spatial slices, an observer at large- ξ_o can record an angle α that is very different from θ . To examine this limit, transform to the Euclidean coordinates (z, θ) on the disc, and expand Eq. 7.7 near the boundary at $z = 1 - \epsilon$

$$\cos \alpha_{1,2}(z, \theta) = -1 + \frac{1}{2} \cot^2\left(\frac{\theta_{1,2}}{2}\right)\epsilon^2 + \mathcal{O}(\epsilon^3). \quad (7.9)$$

Accordingly, any given angle θ gets mapped to $\alpha = \pm\pi$ the closer we approach the boundary ($\epsilon \rightarrow 0$). On the other hand, regardless of how close to the wall we are, there are always small enough angles $\theta < \epsilon$ that will be mapped by Eq.7 to small hyperbolic angles α .

In the first case, choosing the branch of the cosine in Eq. 7.7 determines whether the angular size is $\psi \simeq \pi - \pi$ or $\psi \simeq \pi + \pi$. Studying a few examples, it is easy to see that in this limit intersections where $\theta_{1,2}$ have opposite signs get mapped to $\psi \sim 2\pi$, and intersections where $\theta_{1,2}$ have the same sign get mapped to $\psi \sim 0$.

We will see in the following sections that most of the phase space for bubble nucleation comes from *very small angles* $\theta_{\text{obs}} \sim 0$, typically yielding one intersection in the upper half and one in the lower half of the disk. In this frame, we also expect the angular scale $|\theta_1 - \theta_2|$ to be small, since the majority of colliding bubbles form at very late times, and therefore have a tiny asymptotic comoving size. All of this information taken together suggests that typical collision events will appear to take up *either* very large or very small angular scales on the observer's sky, depending on where the observer is situated inside of the bubble.

7.3.2 The boosted view

We now go on to discuss the boosted frame. We will again exploit the symmetry of the problem to position the observer at $\theta_o = 0$, and define the following transformation in the

embedding space:

$$X'_0 = \gamma(X_0 - \beta X_1), \quad (7.10)$$

$$X'_1 = \gamma(X_1 - \beta X_0),$$

$$X'_{2,3,4} = X_{2,3,4}.$$

This is simply a boost in the X_1 -direction of the embedding space, and respects the $\text{SO}(3,1)$ symmetry of the one-bubble spacetime, since it is in a direction perpendicular to the "surface of pasting" described in Sec. 7.2. If $\gamma = \cosh \xi_o$ and $\beta = \tanh \xi_o$, the observer at ξ_o is translated to the origin. More generally, in terms of the open coordinates inside of the observation bubble (with arbitrary scale factor), this boost is equivalent to a translation (see Appendix E for an explicit demonstration of this).

Points outside of the observation bubble are also affected by the boost. We will be particularly concerned with the effects on the initial value surface at $t_0 \rightarrow 0$, since this determines the available 4-volume to the past of our observer. The boost will push portions of this initial value surface into regions of the de Sitter manifold not covered by the flat slicing coordinates (see Eq. 7.3). It is therefore useful to employ the third foliation of dS, into positively curved spatial sections, which cover the entire manifold. Using a conformal time variable, these coordinates (T, η, θ, ϕ) are defined by:

$$X_0 = H_F^{-1} \tan T \quad (7.11)$$

$$X_i = H_F^{-1} \frac{\sin \eta}{\cos T} \omega_i$$

$$X_4 = H_F^{-1} \frac{\cos \eta}{\cos T},$$

where $-\pi/2 \leq T \leq \pi/2$ and $0 < \eta < \pi$, and the ω_i are the same as in Eq. 7.5. This induces the metric

$$ds^2 = \frac{1}{H_F^2 \cos^2 T} [-dT^2 + d\eta^2 + \sin^2 \eta d\Omega_2^2]. \quad (7.12)$$

The transformation between the boosted and unboosted frames in terms of the global coordinates is given by

$$\tan \theta' = \frac{\sin \eta \sin \theta}{\gamma (\sin \eta \cos \theta - \beta \sin T)} \quad (7.13)$$

$$\tan T' = \gamma \left(\tan T - \beta \frac{\sin \eta \cos \theta}{\cos T} \right) \quad (7.14)$$

$$\cos \eta' = \cos T' \frac{\cos \eta}{\cos T}. \quad (7.15)$$

We now apply this transformation to the initial value surface at $t_0 \rightarrow -\infty$. In terms of the embedding coordinates, we can define this (null) surface by $X_0 + X_4 = 0$ ($T = \eta - \pi/2$), which boosts to

$$X'_0 + \beta X'_1 = -\frac{X'_4}{\gamma}. \quad (7.16)$$

Substituting with the global coordinates, we arrive at the relation

$$\sin T' = -\left(\frac{\cos \eta'}{\gamma} + \beta \sin \eta' \cos \theta' \right). \quad (7.17)$$

Henceforward we will drop the prime on the boosted coordinates unless explicitly noted.

The boosted initial value surface Eq. 7.17 is a function of the coordinate angle, accounting for the dependence on θ_{obs} of the past 4-volume for an unboosted observer. This is displayed for a variety of angles on the dS conformal diagrams in the upper cell of Fig. 7.4.

The effects of the boost on a slice of constant $(\phi, \theta = 0)$ in the background spacetime is shown in the lower cell of Fig. 7.4. Even for this rather modest boost (here we use $\xi_o = 2$), it can be seen that most of the points in the unboosted frame are condensed into the wedge between the past light cone of the nucleation event and the boosted initial value surface.

One may be worried that the presence of colliding bubbles, which break the $\text{SO}(3,1)$ symmetry of the one-bubble spacetime, invalidates our procedure. In fact, to calculate the quantities we are interested in, we only need a consistent description of the spacetime outside of the colliding bubbles. We assume that the colliding bubbles are null and since $\text{SO}(3,1)$ symmetry

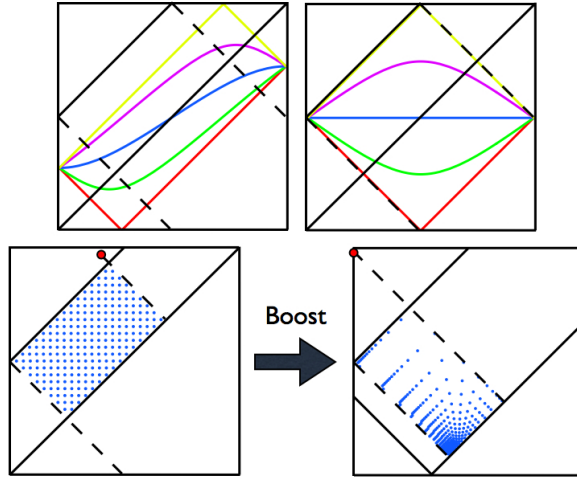


Figure 7.4: The effects of the boost. The top cell shows the boosted initial value surface (at $t_0 \rightarrow -\infty$ in the unboosted frame) for small (left) and large (right) ξ_o for a variety of angles (with the bottom curve (red) corresponding to $\theta = 0$, the top (yellow) corresponding to $\theta = \pi$, and other lines corresponding to intermediate angles at intervals of $\pi/4$). The bottom cell shows the effects of the boost on points in the exterior spacetime on a slice of constant $(\phi, \theta = 0)$. Note that even for this very modest boost ($\xi_o = 2$), most of the points are condensed into the wedge created by the past light cone of the nucleation event and the boosted initial value surface.

transformations keep points inside their light cones, it follows that the spacetime outside bubbles is mapped to itself. While it may be true that such transformation may e.g. violate causality *inside the colliding bubbles* this effect does not affect the analysis we perform here.

7.3.3 Angles according to the boosted observer

We can now calculate the angular scale of a collision on the boosted observer's sky. To do so, we must confront the non-Euclidean geometry of spatial slices in the global coordinates: constant- T slices are 3-spheres of radius $1/H_F \cos T$. We can visualize a timeslice of bubble evolution by suppressing one dimension, embedding in a 3 dimensional Euclidean space, and scaling the spheres to unit radius. The polar angle on this two-sphere is given by η and the azimuthal angle by θ (recall that we take the range $-\pi < \theta < \pi$).

A bubble wall appears as an evolving circle on the unit 2-sphere. Allowing for arbitrary

bubble interiors, and continuing the global coordinate equal time slices ($X_0 = \text{const.}$ in the embedding) into them, a spatial slice is not quite a two sphere, but rather a two sphere with divets and bumps describing the varying curvature of the spacetime inside of the bubbles. For colliding bubbles, these structures – no matter how extreme – are irrelevant, as we will only employ information about the bubble wall.

But the observation bubble requires more care, since we are ultimately interested in a description of collision events from the perspective of an inside observer. Whatever form the embedding of the bubble interior may take, by symmetry, the bubble wall will be a latitude on the background two-sphere. It will have $\eta = T$ (since it nucleates at $T = 0$), and span all θ from $-\pi$ to π . For $T < \pi/2$ it looks like a circle, with the bubble interior the portion of the sphere bounded by this circle. At $T = \pi/2$ the circle is a great circle and the bubble exterior a hemisphere. If we had chosen a frame in which the observation bubble was formed at some $T_n < 0$, then for $T - T_n > \pi/2$ the bubble wall would again become a “small” circle, with the portion of the sphere bounded by this circle corresponding to the bubble *exterior*. By homogeneity of the space a bubble nucleated elsewhere would appear similarly.

In the spherically symmetric, open FRW coordinates that describe the interior of the observation bubble, the boosted observer lies at the origin, which coincides with $X_i = 0$ in the embedding space. Because of the spherical symmetry of this metric, radial incoming null rays from the bubble wall follow trajectories of constant θ and ϕ , and the angle on the sky is identical to the angle we would find if the bubble interior were replaced by a continuation of the background dS. In terms of calculating the observed angle, we can therefore largely ignore the hyperbolic geometry of the bubble interior, and visualize the collision between the observation bubble and an incoming bubble as the intersection of two circles on the $T = \text{const.}$ sphere, as shown in Fig. 7.5.

In analyzing the geometry it is helpful to perform a stereographic projection onto a

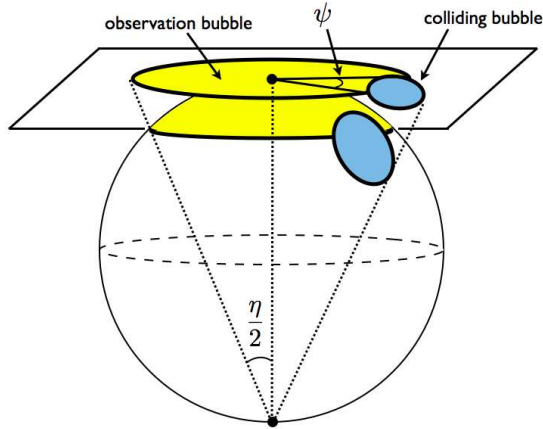


Figure 7.5: A spatial slice in the global foliation of the background de Sitter space, and its stereographic projection. The observation bubble is shaded light (yellow) and the colliding bubble is shaded dark (blue). The angle ψ is indicated in the plane of projection.

plane tangent to the north pole of the two-sphere ($\eta = 0$) as shown in Fig. 7.5. This projection maps circles on the 2-sphere to circles in the plane, and also preserves angles since the map is conformal.

Examining the projection, there are three cases to consider. Colliding bubbles with an interior that does not cut out the south pole appear as filled circles in the projection (upper-left panel of Fig. 7.6, where the light (yellow) disc represents the observation bubble and the dark (blue) disc represents the colliding bubble). On the time slice when a bubble wall intersects the south pole, the wall appears as a line in the projection, bisecting the plane into a region inside, and outside, the bubble (upper-right panel of Fig. 7.6). If the bubble interior cuts out the south pole, it projects to a circle whose interior corresponds to the region *outside* of the bubble (see the lower panel of Fig. 7.6).

Now consider a bubble nucleated at arbitrary coordinates (T_n, η_n, θ_n) . Ingoing and outgoing radial null rays from the center of this bubble (corresponding to the location of the

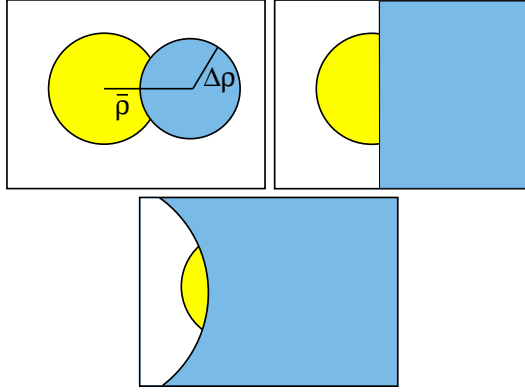


Figure 7.6: The three cases of bubble intersection in the plane of projection. The top left cell displays the case where the bubble interior does not encompass the south pole of the projected two-sphere, the top right cell displays the case where the bubble wall intersects the south pole, and the lower cell displays the case where the bubble interior includes the south pole.

bubble wall) obey:

$$\eta = \eta_n \pm (T - T_n) \equiv \eta_n \pm \eta_T. \quad (7.18)$$

We are interested in the projection of this bubble at the global time-slice T_{co} (and bubble coordinate time $\tau_{\text{co}} \rightarrow 0$) when the observer's past lightcone intersects the observation bubble wall (see Fig. 7.2). If we follow the past lightcone of the observer we find

$$\xi = \int_{\tau}^{\tau_o} d\tau/a(\tau). \quad (7.19)$$

To determine T_{co} , a valid junction between the interior and exterior spacetimes requires that the physical radius of two-spheres (the coefficients of $d\Omega_2$ in Eq. 7.4 and 7.12) at the location of the wall match, and gives

$$T_{\text{co}} = \arctan \left[H_F \lim_{\tau \rightarrow 0} a(\tau) \sinh \left(\int_{\tau}^{\tau_o} d\tau/a(\tau) \right) \right]. \quad (7.20)$$

In the case where the interior is pure dS (where $a(\tau) = H_T^{-1} \sinh H_T \tau$), this works out to $T_{\text{co}} = \arctan[(H_F/H_T) \tanh(H_T \tau_o/2)]$. As we send $\tau_o \rightarrow \infty$, it can be seen that this ranges between $T_{\text{co}} = \pi/4$ for $H_T = H_F$ and $T_{\text{co}} = \pi/2$ for $H_T \ll H_F$.

Viewed in the projected plane using polar coordinates $(\rho, \phi_{\text{proj}})$, the incoming bubble has a center at $\bar{\rho} = (\rho_2 + \rho_1)/2$, and a radius $\Delta\rho = (\rho_2 - \rho_1)/2$ as shown in the upper left panel of Fig. 7.6. Then, since the projection of an arbitrary point gives $\rho = 2 \tan \eta/2$ (this can be seen by analyzing the geometry of Fig. 7.5), we can work out:

$$\bar{\rho} = \frac{2 \sin \eta_n}{\cos \eta_n + \cos \eta_T}, \quad \Delta\rho = \frac{2 \sin \eta_T}{\cos \eta_n + \cos \eta_T}. \quad (7.21)$$

Finally, on the plane we can find the angle ψ between the two radial null rays that come to the observer from the two intersection points, which is given by:

$$\cos\left(\frac{\psi}{2}\right) = -\cot \eta_n \cot T_{\text{co}} + \frac{\cos(T_n - T_{\text{co}})}{\sin \eta_n \sin T_{\text{co}}}. \quad (7.22)$$

At $\xi = \eta = 0$, observers at rest in the open and closed coordinates are in the same frame, so ψ is the actual angular scale on the sky of the bubble’s “sphere of influence”, as seen by the observer.

We can now foliate the background spacetime into surfaces of constant ψ , as shown in Fig. 7.7. From the symmetries of the boosted frame, this foliation is independent of θ and ϕ (although the angular dependence of the boosted initial value surface will play an important role in defining the statistical distribution of collisions). This provides a map between the nucleation site of a colliding bubble and the observed angular scale of the collision. The number of collisions of a given angular scale can be found by examining how the exterior four-volume is distributed in the causal past of the observer.

In the $\xi_o \rightarrow \infty$ limit, there is a *divergent* 4-volume containing nucleation sites that correspond to $\psi \sim 2\pi$ and $\theta_n \simeq 0$ (in the corner near past null infinity enclosed by the shaded boxes of Fig. 7.7, the left panel of which shows the $H_T \sim H_F$ case). Considering the time evolution of an observer starting from $\tau \simeq 0$, most of the 4-volume in this region will come into the observer’s past light cone at very early times. The observer will therefore see new bubble

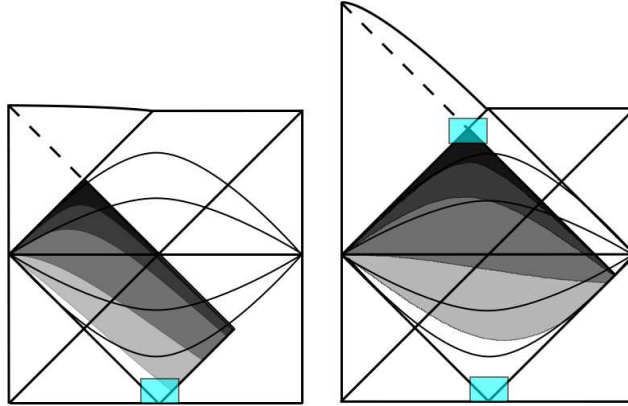


Figure 7.7: The foliation of the exterior de Sitter space into surfaces of constant ψ for junctions with $H_T \sim H_F$ (left) and $H_T \ll H_F$ (right). Dark regions correspond to small ψ and light regions correspond to large ψ . Superimposed on this picture is the boosted initial value surface for various θ_n in the limit of large- ξ_o .

collisions at a rate that is very high at first (formally divergent as $\xi \rightarrow \infty$), and decreases with time⁶.

In the limit where $H_T \ll H_F$, for all ξ_o , there is also a very large 4-volume containing nucleation sites that correspond to $\psi \sim 0$ (in the corner near future null infinity enclosed by the shaded box), though the observer will not have access to these collisions until late times. In this late-time limit (and even for $\xi_o \rightarrow \infty$), the boosted initial value surface cuts into the relevant phase space only when $\theta_{\text{obs}} \sim \pi$, so the distribution is nearly isotropic.

Assembling this information, we predict that the distribution function has two potentially large peaks: one at $\psi \sim 2\pi$ and $\theta_n = 0$, for large ξ_o , and one at $\psi \sim 0$ and all angles, for large τ_o ; both are in complete agreement with the analysis of the unboosted frame. Collisions with $\psi \sim 2\pi$ are recorded at very early observation times, while those with $\psi \sim 0$ are recorded at very late observation times. We now directly confirm these predictions by explicitly calculating

⁶Surfaces of constant ξ are nearly null at early times, so this effect can be viewed as due to time dilation in the boosted frame.

the distribution function in the boosted frame.

7.3.4 Angular distribution function

We now calculate $\frac{dN}{d\psi d\cos\theta_{\text{obs}}d\phi_{\text{obs}}}$, the differential number of bubbles with an observed angular scale ψ in a direction on the sky given by $(\theta_{\text{obs}}, \phi_{\text{obs}})$. In Sec. 7.3.3 we found a mapping (Eq. 7.22) between the position at which a colliding bubble nucleates and the observed angular scale ψ as seen by an observer situated at the origin (for which $\theta_{\text{obs}} = \theta_n$, $\phi_{\text{obs}} = \phi_n$). We can therefore calculate the distribution function by determining the density of nucleation events on surfaces of constant ψ and θ_n . (The symmetry in ϕ implies that the distribution is independent of ϕ_n .)

The differential number of bubbles nucleating in a parcel of 4-volume somewhere to the past of the observation bubble is:

$$dN = \lambda dV_4 = \lambda H_F^{-4} \frac{\sin^2 \eta_n}{\cos^4 T_n} dT_n d\eta_n d(\cos \theta_n) d\phi_n. \quad (7.23)$$

A more complete analysis would include the probability that a given nucleation site is not already inside of a bubble. Under our assumption that bubble walls are null, this probability is given by $f_{\text{out}} = e^{-\lambda V_4^{\text{past}}(\eta_n, T_n, \theta_n)}$ [126], where $V_4^{\text{past}}(\eta_n, T_n, \theta_n)$ is the 4-volume to the past of a given nucleation point. Consider some parcel of 4-volume from which bubbles might nucleate. At late times, in the unboosted frame, a straightforward calculation shows that the 4-volume to the past of any point is proportional to t , the flat slicing time. This yields a differential number of nucleated bubbles:

$$\frac{dN}{dt dr d(\cos \theta) d\phi} = \lambda r^2 e^{(3-\lambda H^{-4})Ht} \simeq \lambda r^2 e^{3Ht}, \quad (7.24)$$

where we have used the fact that in any model of eternal inflation $\lambda H^{-4} \ll 1$. The total number of bubbles is found by integrating, and it can be seen (essentially for the same reason

that inflation is eternal in these models) that including f_{out} only minutely affects both the differential and total bubble counts. We will therefore neglect this correction in our calculation.

Returning to Eq. 7.23, changing variables from T_n to ψ using Eq. 7.22, and integrating η_n at constant $\psi(\eta_n, T_n)$, we obtain the distribution function:

$$\begin{aligned} \frac{dN}{d\psi d(\cos\theta_{\text{obs}})d\phi_{\text{obs}}} &= \frac{dN}{d\psi d(\cos\theta_n)d\phi_n} \\ &= \lambda H_F^{-4} \left[\int_0^{\eta_{\text{max}}(\xi_o, \psi, \theta_n)} d\eta_n \frac{\sin^2 \eta_n}{\cos^4(T_n(\psi, \eta_n, T_{\text{co}}))} \left| \frac{\partial T_n(\psi, \eta_n, T_{\text{co}})}{\partial \psi} \right| \right], \end{aligned} \quad (7.25)$$

with the Jacobian given by

$$\begin{aligned} \left| \frac{\partial T_n(\psi, \eta_n, T_{\text{co}})}{\partial \psi} \right| &= \frac{1}{2} \sin \eta_n \sin T_{\text{co}} \sin \left(\frac{\psi}{2} \right) \times \\ &\quad \left[1 - \left(\cos \left(\frac{\psi}{2} \right) + \cot \eta_n \cot T_{\text{co}} \right)^2 \sin^2 \eta_n \sin^2 T_{\text{co}} \right]^{-1/2}. \end{aligned} \quad (7.26)$$

The lower limit of integration at $\eta_n = 0$ can be understood by tracing the surfaces of constant ψ in Fig. 7.7 and also by noting that for all ψ and T_{co} , Eq. 7.22 yields $T_n(\psi, \eta_n = 0, T_{\text{co}}) = 0$. The upper limit of integration, $\eta_{\text{max}}(\xi_o, \psi, \theta_n)$, is found by determining the intersection of the surfaces of constant- ψ with the boosted initial value surface; this intersection depends position on θ_n and ξ_o (due to the boosted initial value surface Eq. 7.4), reflecting the dependence of the past 4-volume on the position of the observer.

The properties of the observation bubble enter this calculation through the determination of T_{co} via Eq. 7.20. Recall that for late-time observers ($\tau_o \rightarrow \infty$), T_{co} can range from $\frac{\pi}{4}$ for $H_T = H_F$ to $\frac{\pi}{2}$ for $H_T \ll H_F$.

We first examine the behavior of the distribution function Eq. 7.25 for an observer at the origin, $\xi_o = 0$. In this limit, the distribution is isotropic, and based upon the discussion surrounding Fig. 7.7, we expect it to have a large peak around $\psi = 0$ as $T_{\text{co}} \rightarrow \pi/2$ ($H_T/H_F \rightarrow 0$ and $\tau_o \rightarrow \infty$). Integrating Eq. 7.25, we see in Fig. 7.8 that this behavior is indeed observed. For fixed H_T/H_F , the amplitude of the distribution function approaches a constant maximum

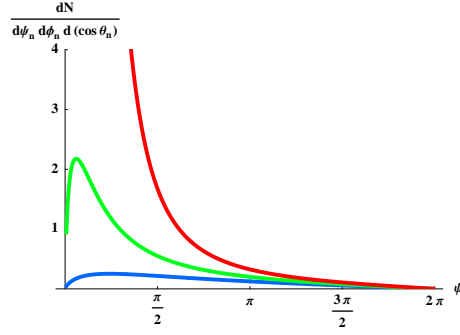


Figure 7.8: The distribution function Eq. 7.25 for an observer at $\xi_o = 0$ with varying T_{co} (corresponding to a varying H_T), factoring out the overall scale λH_F^{-4} . (This factor will in general be astronomically small, but we choose this convention to more clearly display the functional behavior of the distribution function.) This function is independent of θ_n for this observer. As $T_{co} \rightarrow \pi/2$ ($H_T/H_F \rightarrow 0$), a divergent peak around $\psi = 0$ develops.

value as $\tau_o \rightarrow \infty$ (T_{co} approaches its maximum). We will see in the next section that the total number of observable collisions at late times is bounded, reflecting the behavior of the distribution function.

From the analysis of the boosted initial value surface in Sec. 7.3.2, we predicted that in the limit of large- ξ_o , the distribution function Eq. 7.25 should be anisotropic, peaking around $\theta_n = 0$. Fig. 7.9 shows a number of constant- (θ_n, ϕ_n) slices through the distribution function for $T_{co} = \frac{\pi}{4}$ and $\xi_o = 25$, where we see that this behavior is indeed present. The peak at large ψ , which was predicted to arise based upon the analysis in both the unboosted (Sec. 7.3.1) and boosted frames (Sec. 7.3.3), is present in this example as well. Finally, we observe that as $\theta_n \rightarrow 0$, the distribution peaks at progressively larger ψ . This feature can be predicted from Fig. 7.7 by noting that as $\theta_n \rightarrow 0$, an increasing fraction of the 4-volume above the boosted initial value surface corresponds to nucleation sites that produce a large ψ (the shaded box near past null infinity in Fig. 7.7).

Focusing on a slice through the distribution function with $(\theta_n = 0, \phi_n = \text{const.})$ – for which the amplitude is largest – we can study the effects of varying T_{co} and ξ_o . Fig. 7.10

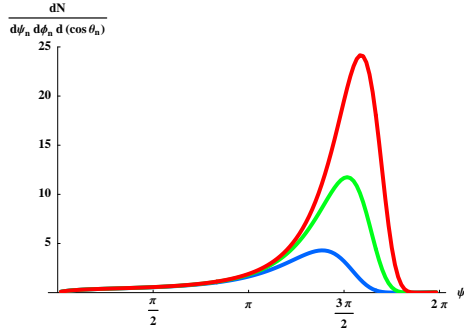


Figure 7.9: The distribution function Eq. 7.25 for an observer at $\xi_o = 25$, with $T_{co} = \frac{\pi}{4}$, for $\theta = \frac{\pi}{10}, \frac{\pi}{15}, \frac{\pi}{20}$, factoring out the overall scale λH_F^{-4} . As $\theta_n \rightarrow 0$, the position of the peak shifts to larger ψ , and increases in amplitude, displaying the predicted anisotropic peak about large angular scales.

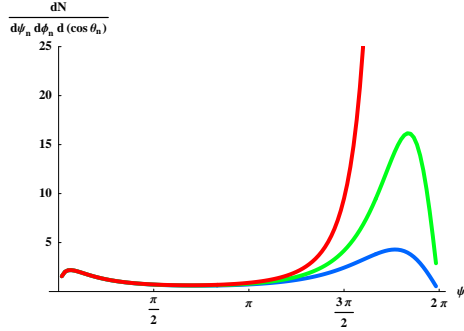


Figure 7.10: The distribution function Eq. 7.25 with $\theta_n = 0$ and $\tau_{co} = \frac{3\pi}{8}$ for $\xi_o = (1.5, 2, 100)$, factoring out the overall scale λH_F^{-4} . As ξ_o gets large, the peak near $\psi \sim 2\pi$ grows, while the peak near $\psi \sim 0$ remains of constant amplitude.

shows the distribution function for fixed $\theta_n = 0$ and $T_{co} = \frac{3\pi}{8}$ with varying ξ_o . As ξ_o increases, the amplitude of the peak at large ψ increases, while the peak at small ψ remains unaffected. This can be understood from Figs. 7.4 and 7.7 by recognizing that as ξ_o grows, the phase space near past null infinity – corresponding to nucleation points producing $\psi \sim 2\pi$ – grows, while the phase space near the intersection of the past light cone and the observation bubble wall – corresponding to nucleation points producing $\psi \sim 0$ – remains constant.

Finally, Fig. 7.11 shows the evolution of the distribution function produced by fixing

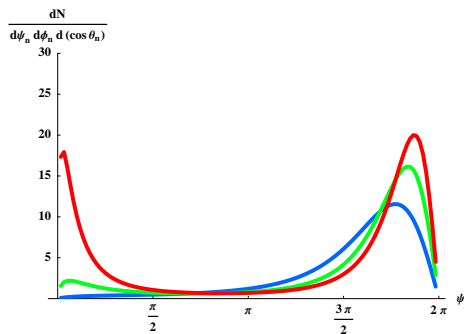


Figure 7.11: The distribution function Eq. 7.25 with $\theta_n = 0$ and $\xi_o = 2$ for $T_{co} = (\frac{\pi}{4}, \frac{3\pi}{8}, \frac{7\pi}{16})$, factoring out the overall scale λH_F^{-4} . As T_{co} grows, the bimodality of the distribution becomes more and more pronounced. Both the peak about $\psi \simeq 0$ and $\psi \simeq 2\pi$ grow, with the growth of the $\psi \simeq 0$ peak eventually overtaking the growth of the $\psi \simeq 2\pi$ peak. The position of the peaks shift as well, with one peak approaching $\psi = 0$ and the other $\psi = 2\pi$ as $T_{co} \rightarrow \frac{\pi}{2}$.

$\theta_n = 0$ and position $\xi_o = 2$ and increasing T_{co} (corresponding to the actual time-evolution of the distribution function seen by this observer). Here, the bimodality of the distribution becomes apparent. Based on Fig. 7.7, we determined that bubbles with large angular scales form at early (open slicing) observation times, and bubbles with small angular scales form at late times. This can be seen in the distribution function of Fig. 7.11. As T_{co} increases, the peak near $\psi \simeq 0$ becomes more and more pronounced, overtaking the amplitude of the $\psi \simeq 2\pi$ peak, whose growth eventually stagnates. The positions of the peaks also shift, moving towards $\psi = 0$ and $\psi = 2\pi$, respectively, as T_{co} increases.

7.3.5 Behavior of the distribution near $\psi \simeq 2\pi$ and $\psi \simeq 0$

Since the distribution function (as displayed in the figures) is multiplied by $\lambda H_F^{-4} \ll 1$, it must have a very large amplitude for our hypothetical observer to hope to see any collisions. We have seen that the distribution function is largest for $\psi \simeq 2\pi$ (corresponding to collisions occurring at small τ) in the large- ξ_o , small- θ_n limit as well as for $\psi \simeq 0$ (corresponding to collisions occurring at large τ) in the limit where $H_T \ll H_F$. The origin of these peaks was

discussed in Sec. 7.3.3, but now we assess them quantitatively.

7.3.5.1 The peak at $\psi \sim 0$

The total number of late-time collisions can be found by evaluating λ times the 4-volume $V_4^{\psi \sim 0}$ in the exterior spacetime corresponding to small angles. Assuming that the bubble interior and exterior are pure dS and taking the limit of large τ_o with $H_T \ll H_F$, we obtain

$$N^{\psi \sim 0} = \frac{4\pi\lambda}{3H_T^2 H_F^2} \tanh^2\left(\frac{H_T \tau_o}{2}\right) + \mathcal{O}\left(\log \frac{H_F}{H_T}\right). \quad (7.27)$$

For fixed H_T this approaches a fixed number as $\tau_o \rightarrow \infty$, but this number can be arbitrarily large if $H_T \rightarrow 0$. We see also that for $N^{\psi \sim 0} > 0$, we require both $H_T < \lambda^{1/2} H_F^{-1}$, and $\tau_o > H_F \lambda^{-1/2}$.

The angular scale of late-time collisions decreases with τ_o , as exhibited by Fig. 7.11; one might then ask what total angular area on the sky is affected. This can be found by evaluating:

$$\Omega = \lambda \int dV_4 \psi^2 \quad (7.28)$$

over the volume outside of the observation bubble available for the nucleation of colliding bubbles, where ψ is a function of the exterior spacetime coordinates as in Eq. 7.22. As it turns out, the decrease in angular scale nearly cancels the growth in $N^{\psi \sim 0}$, so while the latter scales as $(H_F/H_T)^2$, the maximal sky fraction is nearly logarithmic in H_F/H_T , as shown in Fig. 7.12. Since $\lambda H_F^{-4} \ll 1$, the total angular area is very small unless H_T is essentially zero (and τ_o absurdly large); thus for any realistic scenario the bubble distribution should be considered a set of point sources with infinitesimal total solid angle.

7.3.5.2 The peak at $\psi \sim 2\pi$

Let us now consider the large- ξ_o , small- θ_n limit. To do so, we take $\psi = 2\pi - \epsilon$ with $\epsilon \ll 1$ and look at $T_{\text{co}} = \pi/4$ (the amplitude of the peak would only be larger if we were to take $T_{\text{co}} > \pi/4$, so this gives a lower bound). Keeping terms to first order in ϵ , we can simplify the

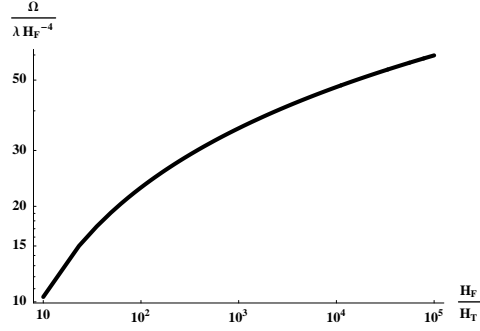


Figure 7.12: A log-log plot (calculated numerically) of the total angular area on the sky taken up by late-time collisions with $\psi \simeq 0$.

various objects in Eq. 7.25 immensely: T_n along constant ψ surfaces is given approximately by $T_n = -\eta_n$, and the Jacobian reduces to

$$\left| \frac{\partial T_n(\psi, \eta_n)}{\partial \psi} \right| = \frac{\epsilon}{4} \frac{\sin \eta_n}{\sqrt{1 + \sin(2\eta_n)}} \quad (7.29)$$

yielding a distribution

$$\frac{dN}{d\psi d\phi_n d(\cos \theta_n)} = \frac{\lambda H_F^{-4} \epsilon}{4} \times \int_0^{\eta_{\max}} \frac{(\tan \eta_n)^3}{\cos \eta_n \sqrt{1 + \sin(2\eta_n)}} d\eta_n. \quad (7.30)$$

In the limiting case under discussion, we can solve for η_{\max} from the simplified form of the initial value surface (obtained from Eq. 7.17)

$$\sin \eta_{\max} = \frac{\cos \eta_{\max}}{\gamma} + \beta \sin \eta_{\max} \quad (7.31)$$

yielding

$$\eta_{\max} = \sec^{-1} \left(e^{\xi_o} \sqrt{1 + e^{-2\xi_o}} \right), \quad (7.32)$$

where we have not yet taken ξ_o large. Integrating Eq. 7.30, substituting with η_{\max} , and taking $\xi_o \gg 1$, we obtain:

$$\frac{dN}{d\psi d\phi_n d(\cos \theta_n)} = \frac{\lambda H_F^{-4} \epsilon}{12} e^{3\xi_o}, \quad (7.33)$$

which diverges as $\xi_o \rightarrow \infty$.

7.4 Summary of results and implications

7.4.1 Properties of the distribution function

Given an observer at some point in their bubble defined by $(\tau_o, \xi_o, \theta_o = 0)$, we have calculated the expected number, angular size, and direction $(\theta_{\text{obs}}, \phi_{\text{obs}})$ of regions on the sky affected by bubble collisions, under the assumption that those collisions merely perturb the observation bubble.

Three key features of this distribution $dN/d\psi d(\cos \theta_{\text{obs}}) d\phi_{\text{obs}}$ are:

- For observers at $\xi_o \neq 0$ inside bubbles with $H_T \ll H_F$, the distribution is bimodal, with peaks at $\psi \simeq 0$ and $\psi \simeq 2\pi$ forming at late and early observation times respectively.
- For early-time collisions with $\psi \simeq 2\pi$, the distribution is strongly anisotropic as $\xi_o \rightarrow \infty$, with the overwhelming majority of collision events originating from $\theta_{\text{obs}} \simeq 0$, while the distribution of collision events with $\psi \simeq 0$ becomes isotropic at late-times.
- For a given H_T , H_F , and τ_o , the peak at $\psi \simeq 2\pi$ diverges as $\exp(3\xi_o)$; the peak at $\psi \simeq 0$ has fixed amplitude, with the total number of such collisions bounded by $N^{\psi \sim 0} < \lambda H_T^{-2} H_F^{-2}$.

Although different observers see qualitatively different bubble distributions, we can focus on two key classes: those at large ξ_o and those at very late times τ_o .

Because the bubble interior is naturally foliated into a set of homogeneous spaces that accord no particular preference to $\xi_o = 0$, we might imagine observers distributed uniformly over these spaces. In this case (as argued in Sec. 7.2) a “typical” observer would be at large ξ_o , and have causal access to a large number of collision events (as long as $\xi_o > H_F^4 \lambda^{-1}$). If such collisions are Compatible (with our observations), we should therefore expect that they exist to our past.

At very late times, observers at any position ξ_o will have access to nearly the same distribution of collisions. We have seen that such an observer would typically record the first collision at exponentially late times (of order $\tau_o \sim \lambda^{-1/2} H_F$), with tiny angular scale. Thereafter, the number of collisions would grow to asymptotically approach $\sim H_T^{-2} H_F^{-2}$, and the distribution would become nearly isotropic. Note that this analysis is relevant to the suggestion by [127, 128] that an observer residing at $\xi_o = 0$ inside of a bubble with $H_T = 0$ (the “census taker” of [128]) could be used to define a measure over the pocket universes in eternal inflation; it may also be relevant for evaluating the quantum-gravitational degrees of freedom of an eternally-inflating de Sitter space [129]. In terms of *our* observations, if we fix H_T to be the vacuum energy we currently observe, and $\tau_o \sim H_T^{-1}$, late-time, small angular scale collisions could be observable if $\lambda H_F^{-4} > 10^{-100}$. While perhaps an atypically large tunneling rate, this is well within the limit $\lambda H_F^{-4} \ll 1$ required for eternal inflation in our parent vacuum.

Because all observers might potentially ‘see’ bubbles at late times (for sufficiently large λ), and essentially (except for a set of measure zero) all should ‘see’ collisions at early times, it is interesting to ask what potential observational effects might exist.

7.4.2 A classification of collision events

Unfortunately, assessing any potentially observational effects of this scenario requires a good understanding of the outcome of bubble collisions under a variety of circumstances, which is presently lacking. As a preliminary step, we can qualitatively survey the general types of collision events that might occur in a universe undergoing false-vacuum eternal inflation; after this we return to what these collision types could imply observationally.

Each cell of Fig. 7.13 depicts two bubbles near future null infinity in the eternally inflating background dS. Cell A depicts the situation considered thus far, of two colliding true vacuum bubbles (“downward-bubbles” for present purposes). Others show also transitions *up-*

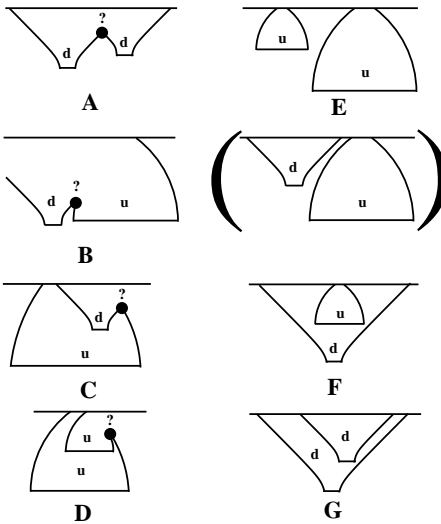


Figure 7.13: A general set of situations which might involve collisions between two bubbles in an eternally inflating spacetime. Each cell represents a region near future null infinity (horizontal solid line) of an eternally inflating background dS. True vacuum bubbles form at very small radius and expand, while false vacuum bubbles form larger than the exterior horizon size, and contract. Collisions are denoted by filled circles, with the uncertainty of the post-collision spacetime indicated by a question mark.

ward from the false vacuum (“upward-bubbles”); the structure of such bubbles is very different: they collapse due to the inward pressure gradient [13], so if they contain a finite region of future null infinity, then they form must with super-(exterior) horizon size⁷ (e.g., [14]).

The first column (A-D) shows situations where bubbles actually collide; the right-hand column shows cases in which they do not. Cell A shows the collision between two downward-bubbles (which may or may not be of the same vacuum energy). Downward-bubbles can also collide with upward bubbles (cell B), but because the latter accelerate inward, and have strongly suppressed formation rates relative to downward-bubbles, such collisions should be extremely rare. Collisions of type C, between nested bubbles, occur if a downward-bubble quickly nucleates within an upward-bubble, our observation bubble is unlikely to be such an early bubble when infinitely many form later within the same false-vacuum bubble. Finally, nested upward-bubbles

⁷Or form on the other side of an Einstein-Rosen bridge.

may collide (cell D), but only very rarely.

This general survey of two-bubble collision events, indicates that the focus on situation A alone is quite justified: all other possible collision events should be negligibly rare.

Determining the detailed aftermath of a collision event between two vacuum bubbles of arbitrary vacuum energy is a very complicated problem, most likely involving numerical relativity. Previous numerical and analytic studies have treated cases where the vacuum energy inside both bubbles vanishes [130, 120], cases where both bubbles have negative vacuum energy [131], and cases where a zero and negative vacuum energy bubble collide [121].

In the absence of detailed computations, but based on these studies, we can outline a few generic possibilities. For collisions between bubbles of the same vacuum, the disturbed intersection region might radiate away much of the wall's energy, then be smoothed out by subsequent inflation. For bubbles of different vacuum field value, wall energy may still radiate away (as demonstrated in [130, 131]), but a domain wall must remain, and would presumably accelerate into the bubble of higher vacuum energy.

In terms of the effect on an observation bubble, it would seem that collisions resulting primarily in a domain wall accelerating away from an observer are likely to be “Compatible” (in the terminology of Sec. 6.1) over a significant part of the collision's future. Even if considerable energy is released, it will be red-shifted by the epoch of inflation within the bubble, perhaps resulting in only a minor perturbation of the interior cosmology. On the other hand, a domain wall accelerating *towards* the observer will almost certainly be catastrophic (and hence not Compatible). In between, bubbles of the same vacuum (where there is no domain wall), or collisions resulting in a timelike domain wall (as in [121]), may or may not be Compatible (for all or just a portion of the causal future of the collision) depending on the details of the collision.

Returning to Fig. 7.13, cells A-C depict collision events potentially relevant to the observation bubble. In each case, if the vacuum energy of the observation bubble is lower than

the vacuum energy of both the background dS and the colliding bubble, it seems likely that the collision is Compatible over most of its future. A or C could alternatively be fatal if the incoming bubble (in cell A) or the background space (in cell C) are at lower vacuum energy than the observation bubble. However, the finer details will need to be studied to provide a definitive classification of these collision events and to what degree they satisfy the Compatibility condition.

7.4.3 Observational implications

What does all of this mean for making predictions starting from a fundamental theory that drives eternal inflation? The above discussion of the possible results of bubble collisions suggests a spectrum ranging from what might be called “Fatal” collisions to “Perturbative” ones. Fatal collisions would destroy all observers to their future, while Perturbative collisions would merely “paint” their effect on the observation bubble. Realistic collisions would fall in between these extremes.

Consider first a scenario in which Fatal (downward) bubbles can form at rate λ_{fatal} and collide with our observation bubble. Focusing on the $\tau = \tau_o$ spatial slice, on which we presumably exist now, we must be at a position that has not yet experienced such a collision. The unaffected volume fraction will be $f_{\text{OK}} = \exp[-\lambda_{\text{fatal}}V_4(\xi_o)]$ (where V_4 measures the available past 4-volume for nucleations, which for $\xi_o \gg 1$ is $V_4(\xi_o) \simeq 4\pi\xi_o H_F^{-4}/3$), and as discussed in Sec. 7.2, the 3-volume element goes as $dV_3 = 4\pi H_T^{-3} \sinh^2(\xi_o)d\xi_o$. Combining these, the distribution in ξ_o , for $\xi_o \gg 1$, of volume unaffected by fatal bubbles goes as

$$dV_3 f_{\text{OK}} \propto \exp\left[\left(2 - \frac{4\pi}{3}\lambda_{\text{fatal}}H_F^{-4}\right)\xi_o\right] d\xi_o,$$

For $\lambda_{\text{fatal}}H_F^{-4} < \frac{3}{2\pi}$ (which will be satisfied for any theory of eternal inflation) this diverges as $\xi_o \rightarrow \infty$, so we would expect *even the surviving regions* to be dominated by the largest ξ_o .

Now, *if we assume* ourselves to be in a typical surviving region, there are two cases of interest. If we are in a bubble with $H_T < \lambda_{\text{fatal}}^{1/2} H_F^{-1}$, then as time increases, we will have an increasing risk of being hit by Fatal bubble (as discussed in Sec. 7.3.3), and would expect such a collision after a cosmological time of order $\tau_o \sim \lambda_{\text{fatal}}^{-1/2} H_F$. Even if $H_T = 0$, for exponentially small nucleation rates this can easily be a reassuringly long time;⁸ conversely, we can use our survival to rule out scenarios that include Fatal bubbles with $\lambda_{\text{fatal}}^{-1/2} H_F > 10$ Gyr. If, instead, $H_T > \lambda_{\text{fatal}}^{1/2} H_F^{-1}$, then all of the collision events likely to ever affect us happened in the distant past, and we will safely inhabit our unaffected region of the observation bubble, oblivious to the fact that fatal collisions may have occurred elsewhere.

Let us consider collisions that are Compatible but not Fatal, so that we might exist in at least part of the collision's future. If this part is relatively small, or excludes the region that we are likely to be in, we might treat these bubbles as Fatal, and simply assume that we are not in the future of any of them. If, on the other hand, we might exist in essentially all of the collision's future, we might treat them as Perturbative. If a theory predicts that at least one collision type is effectively Perturbative, then we can simply assume ourselves to be in a region unaffected by non-Perturbative bubbles, but should still expect to see Perturbative collisions to our past, following our derived distribution function. Determining whether a Compatible collision is effectively Fatal or Perturbative will be difficult, as it requires a detailed understanding of the collision's aftermath, and may also involve 'measure' issues to determine whether or not the (putative) observers in question are likely be in the perturbed or the destroyed part of the collision result. (One cause for concern in this regard is that the $\xi_o \rightarrow \infty$ observers likely to see many collisions are very highly "boosted". Therefore even if an incoming bubble is almost perfectly Perturbative, this perturbation might be extremely dangerous to such a highly-boosted

⁸This analysis agrees with that of GGv, who essentially assumed that collisions are all Fatal and then found that we are unlikely to hit by such a bubble soon.

worldline. Another way to see this is to note that most collisions observed at early times by the “boosted” observer in Fig. 7.7 come from very early cosmological times.)

In our analysis, we have concentrated on determining the region of the observer’s sky that is *in principle* affected by (a set of) collision events. Further, we have used the bubble wall as the surface upon which the observer is examining the effects of collisions. This has allowed us to avoid making any assumptions about how collision products may travel inside of the observation bubble. However, the most relevant calculation is to determine the effects of bubble collisions on the post-tunneling equal-field surface, then in turn the observable effect on the last-scattering surface (and therefore in the CMB). This will necessarily involve a better understanding of the physics involved in bubble collisions, an investigation that we reserve for future work.

That being said, we might speculate that the gross features of the distribution function on the last scattering surface will be similar to the analysis we have carried out, suggesting that bubble collisions would produce anisotropies and features on large angular scales in the CMB. Because of the bimodality of the distribution function, the subdominant peak around $\psi \simeq 0$ might also produce observable effects akin to point sources, but only if $\lambda > (H_T H_F)^{-2}$ for some bubble type. These speculations must be put on much firmer ground before any conclusions can be drawn from current or future data.

7.5 Discussion

In Sec. 6.1, we outlined three conditions that must be met for there to be observable effects of bubble collisions in false-vacuum eternal inflation: Compatibility, Probability, and Observability. What do our results imply about these?

We have not gone beyond the general arguments concerning Compatibility given in

Sec. 6.1, except to note that incoming bubbles of higher vacuum energy are likely to be separated from us by a domain wall that accelerates away from us, greatly enhancing the likelihood that they will merely perturb the “observation bubble.” We have *not*, however, actually shown that bubbles with the requisite level of Compatibility are expected; it will be necessary to extend previous bubble-collision analyses [130, 120, 131, 121] to answer this question decisively, as well as to assess the result of multiple bubble collisions affecting a single point inside the observation bubble.

Our main result is a calculation of the statistical distribution of collisions coming from a direction (θ_n, ϕ_n) that can affect an angular scale ψ on the 2-sphere defined by the portion of the bubble wall causally accessible to an observer at some instant in time, *assuming* that the incoming bubbles merely perturb the observation bubble. The properties of this distribution function depend upon the location of the observer inside of the observation bubble. We have evaluated it in complete generality, but there are two interesting cases.

Our main result is a calculation of the statistical distribution of collisions coming from a direction (θ_n, ϕ_n) that can affect an angular scale ψ on the 2-sphere defined by the portion of the bubble wall causally accessible to an observer at some instant in time, *assuming* that the incoming bubbles merely perturb the observation bubble. The properties of this distribution function depend upon the location of the observer inside of the observation bubble, which we have evaluated in complete generality, but there are two limiting cases of interest.

First, if we sit very far from the finite “unaffected” region near the center of the bubble (defined by $\xi_o < \lambda H_F^{-4}$ in terms of the false-vacuum Hubble parameter H_F), then our results show that most collisions come from the direction of the bubble wall, happen at early observation times, and have a *large* angular scale $\psi \simeq 2\pi$. If such bubble collisions are compatible with our observations, there is no reason to expect that they are not causally accessible to us.

Second, for an observer at any ξ_o , bubbles can potentially be encountered (or come

into view) at late times $\tau_o \sim \lambda^{-1/2} H_F$ if $H_T < \lambda^{1/2} H_F^{-1}$. (Note that such values of λ are large compared to typical exponentially suppressed nucleation rates, but still small compared to values that would allow percolation and thus preclude eternal inflation.)

Now consider Observability. One might have guessed that even if an infinite number of bubbles collide with ours, they might be of infinitesimal angular size on the sky, perhaps even taking up small total sky fraction. Indeed this appears to be true for the small scale, late-time collisions, but is *not* the case for the early-time collisions – which take up large angular scales – implying that the Observability criterion is at least partly satisfied.

Now consider Observability. One might have guessed that even if an infinite number of bubbles collide with ours, they might be of infinitesimal angular size on the sky, perhaps even taking up small total sky fraction. Indeed this appears to be true for the small scale, late-time collisions, but is *not* the case for the early-time collisions, which take up large angular scales, implying that the Observability criterion is at least partly satisfied.

Assessing the other half of Observability (that the effects of the collisions must survive inflation within the bubble) would, in the context of eternal inflation, require both an accurate model of the inflaton potential, and also a measure over transitions within this potential so as to give a probability distribution over e-foldings [19]. Neither is in hand but the present results increase the importance of making progress in this area.

In some sense, bubble collisions are the most generic prediction made by false vacuum eternal inflation, independent of the properties of the fundamental theory that may drive it. While connecting this prediction to real observational signatures will entail both difficult and comprehensive future work (and probably no small measure of good luck), it appears worth pursuing. For a confirmed observational signature of other universes, while currently speculative even in principle, and probably far-off in practice, would surely constitute an epochal discovery.

Appendix A

Spacetimes with a cosmological constant

In this section, we outline the properties of a number of spherically symmetric spacetimes with a cosmological constant. We will describe the de Sitter (henceforward referred to as dS), Anti-de Sitter (AdS), Schwarzschild de Sitter (SdS), and Schwarzschild Anti de Sitter (SAdS) spacetimes in detail.

A.1 The FRW metric

The Friedmann Robertson Walker (FRW) metric is derived by assuming that spatial slices are homogeneous and isotropic: the spatial slices are maximally symmetric, and therefore spherically symmetric, which greatly constrains the form of the metric. Spatial slices at different times are allowed to have some dynamics in the form of an overall scale factor. The FRW metric is given by

$$ds^2 = -dt^2 + a(t)^2 \left[\frac{dr^2}{1 - kr^2} + r^2 d\Omega_2 \right], \quad (\text{A.1})$$

where $k = 0, \pm 1$.

The different values that k can take correspond to spacetimes with constant positive

($k = +1$), negative ($k = -1$), or zero ($k = 0$) curvature. This can be seen by examining the metric in each of these three cases. The simplest is $k = 0$, where the metric on a spatial slice at time t is given by

$$d\gamma^2 = a(t)^2 [dr^2 + r^2 d\Omega_2], \quad (\text{A.2})$$

which can be recognized as being conformal to 3 dimensional, flat Euclidean space. The metric on a spatial slice in the case of positive curvature ($k = +1$) becomes

$$d\gamma^2 = a(t)^2 \left[\frac{dr^2}{1-r^2} + r^2 d\Omega_2 \right]. \quad (\text{A.3})$$

If we introduce a new coordinate $r \equiv \sin(\chi)$, this metric becomes

$$d\gamma^2 = a(t)^2 [d\chi^2 + \sin^2(\chi) d\Omega_2] = a(t)^2 d\Omega_3, \quad (\text{A.4})$$

which is conformal to the surface of a 3-sphere. The metric on a spatial slice in the case of negative curvature is

$$d\gamma^2 = a(t)^2 \left[\frac{dr^2}{1+r^2} + r^2 d\Omega_2 \right]. \quad (\text{A.5})$$

Defining $r = \sinh(\chi)$, we obtain a metric which is conformal to a hyperbolic surface

$$d\gamma^2 = a(t)^2 [d\chi^2 + \sinh^2(\chi) d\Omega_2]. \quad (\text{A.6})$$

A.1.1 Friedmann Equations

The matter content of the FRW spacetime is taken to be a perfect fluid, whose energy momentum tensor is given by

$$T_{\mu\nu} = (p + \rho) U_\mu U_\nu - p g_{\mu\nu}, \quad (\text{A.7})$$

where p is the pressure and ρ is the energy density of the fluid. The quantity U_ν is the four-velocity of the fluid, which in the comoving frame is just

$$U_\mu = (1, 0, 0, 0). \quad (\text{A.8})$$

In this frame, the energy momentum tensor is given by

$$T_{\nu}^{\mu} = \text{diag}(-\rho, p, p, p), \quad (\text{A.9})$$

where we might split up the total density and pressure into contributions from fluids with different equations of state ($\rho \rightarrow \sum_i \rho_i$, $p \rightarrow \sum_i p_i$).

Substituting the metric and energy momentum tensor into Einstein's equations

$$R_{\mu\nu} = 8\pi \left(T_{\mu\nu} - \frac{1}{2} g_{\mu\nu} T \right), \quad (\text{A.10})$$

yields the Friedmann equations

$$\frac{\ddot{a}}{a} = - \sum_i \frac{4\pi}{3} (\rho_i + 3p_i) \quad (\text{A.11})$$

$$\left(\frac{\dot{a}}{a} \right)^2 = \sum_i \frac{8\pi}{3} \rho_i + \frac{k}{a^2}, \quad (\text{A.12})$$

which together with energy conservation

$$0 = \nabla_{\nu} T^{\nu}_0 = \sum_i -\dot{\rho}_i - 3 \frac{\dot{a}}{a} (\rho_i + p_i) \quad (\text{A.13})$$

fully determines the evolution of the scale factor. The scale factor as a function of time for a fluid with equation of state $p = w\rho$:

$$a(t) = a_0 t^{\frac{2}{3(1+w)}} \quad (\text{A.14})$$

where

$$\begin{aligned} w = 0; & \quad \text{dust,} \\ w = 1/3; & \quad \text{radiation,} \\ w = -1/3; & \quad \text{curvature,} \\ w = -1; & \quad \text{cosmological constant.} \end{aligned} \quad (\text{A.15})$$

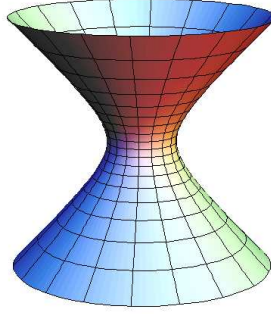


Figure A.1: 4 dimensional de Sitter space can be visualized as a hyperboloid embedded in 5 dimensional Minkowski space.

A.2 de Sitter Space

De Sitter space is a maximally symmetric spacetime, with $SO(4,1)$ symmetry. It belongs to the Friedman, Robertson, Walker (FRW) class of spherically symmetric, homogenous, and isotropic metrics. The stress energy tensor that generates de Sitter space is a perfect fluid (see Eq. A.7) possessing an equation of state $p = -\rho$ ($w = -1$).

It is possible to visualize de Sitter space as the surface of a hyperboloid embedded in a 5-dimensional Minkowski space, as shown in Fig. A.1. The surface is defined by the equation

$$-X_0^2 + X_1^2 + X_2^2 + X_3^2 + X_4^2 = H^{-2} \quad (\text{A.16})$$

where $H^2 \equiv \Lambda/3$. We will find it convenient to express the various coordinates of interest in terms of these embedding coordinates, as it allows for easy transformations between them.

Static Slicing

The first coordinate system we will discuss is the static foliation, described by the metric

$$ds_-^2 = -a_{\text{ds}} dt^2 + a_{\text{ds}}^{-1} dR^2 + R^2 d\Omega_2^2, \quad (\text{A.17})$$

$$a_{\text{ds}} = 1 - H^2 R^2. \quad (\text{A.18})$$

This metric has a coordinate singularity at $R = H^{-1}$, indicating the presence of an event horizon, henceforward referred to as the cosmological horizon. This coordinate system does not cover the entire manifold, we must work with alternate coordinates or multiple patches to discuss the behavior of the spacetime across the horizon. The amount of covering can be determined by looking at the embedding coordinates

$$X_0 = H^{-1} \sqrt{1 - H^2 R^2} \sinh Ht, \quad (\text{A.19})$$

$$X_i = R\omega_i \quad i = 1, 2, 3, \quad (\text{A.20})$$

$$X_4 = H^{-1} \sqrt{1 - H^2 R^2} \cosh Ht, \quad (\text{A.21})$$

where the ω_i parametrize an S^2

$$\omega_1 = \cos \theta_1, \quad (\text{A.22})$$

$$\omega_2 = \sin \theta_1 \cos \theta_2, \quad (\text{A.23})$$

$$\omega_3 = \sin \theta_1 \sin \theta_2, \quad (\text{A.24})$$

and the coordinates take the range $-\infty < t < \infty$, $0 < R < H^{-1}$. It can be seen that these coordinates do not cover the entire manifold, for example excluding values of X_i larger than H^{-1} . We can cover the entire manifold by using four coordinate patches, given by

$$X_0 = \sqrt{1 - H^2 R^2} \sinh \left(Ht + \frac{in\pi}{2} \right), \quad (\text{A.25})$$

$$X_i = R\omega_i \quad i = 1, 2, 3, \quad (\text{A.26})$$

$$X_4 = \sqrt{1 - H^2 R^2} \cosh \left(Ht + \frac{in\pi}{2} \right), \quad (\text{A.27})$$

where

$$n = 0, 2; \quad -\infty < t < \infty; \quad 0 < R < H^{-1}, \quad (\text{A.28})$$

$$n = 1, 3; \quad -\infty < t < \infty; \quad H^{-1} < R < \infty. \quad (\text{A.29})$$

Flat Slicing

de Sitter space can be foliated by flat spatial slices, and in these coordinates the metric is given by

$$ds^2 = -dT + e^{2HT} d^3x. \quad (\text{A.30})$$

This can be recognized as an FRW metric (see Eq. A.2) with a scale factor $a(T) = e^{HT}$, and $k = 0$. These coordinates extend across the cosmological horizon, but they do not cover the entire manifold. In terms of the embedding, they can be defined by

$$X_0 = H^{-1} \sinh(HT) + \frac{H}{2} \mathbf{x}^2 e^{HT}, \quad (\text{A.31})$$

$$X_i = x_i e^{HT}, \quad (\text{A.32})$$

$$X_4 = H^{-1} \cosh(HT) - \frac{H}{2} \mathbf{x}^2 e^{HT}. \quad (\text{A.33})$$

Null Coordinates

A useful foliation of de Sitter space is in terms of null rays. Looking at the flat slicing metric Eq. A.30, we can see that ingoing null rays will be parametrized by

$$G = r + H^{-1} e^{-HT}, \quad (\text{A.34})$$

and outgoing null rays will be parametrized by

$$F = r - H^{-1} e^{-HT}. \quad (\text{A.35})$$

The collection of ingoing and outgoing null rays is sufficient to foliate the portion of the manifold covered by the flat slicing coordinates, and we can perform a coordinate transformation from (r, t) to (F, G)

$$ds^2 = H^{-2} \left[\frac{1}{(G-F)^2} (dF dG + dG dF) + \frac{(G+F)^2}{(G-F)^2} d\Omega^2 \right]. \quad (\text{A.36})$$

From the metric Eq. A.36, we must have $G > F$, which translates into a requirement that the outgoing and ingoing light cones intersect in the portion of the manifold covered by the flat

slicing coordinates. Continuing across the coordinate singularity in the metric to regions where $G < F$, we can cover the entire manifold. The embedding coordinates are given by

$$X_0 = \frac{H^{-2} + GF}{G - F}, \quad (\text{A.37})$$

$$X_i = H^{-1} \frac{G + F}{G - F} \omega_i, \quad (\text{A.38})$$

$$X_4 = \frac{H^{-2} - GF}{G - F}. \quad (\text{A.39})$$

To get an idea of how null rays look in the embedding picture, we can solve for $X_0(X_4, F)$ and $X_0(X_4, G)$, yielding

$$\begin{aligned} X_0(X_4, G) &= \frac{H^{-2} + G^2}{H^{-2} - G^2} X_4 - H^{-2} \frac{2G}{H^{-2} - G^2} \\ X_0(X_4, F) &= \frac{H^{-2} + F^2}{H^{-2} - F^2} X_4 + H^{-2} \frac{2F}{H^{-2} - F^2} \end{aligned} \quad (\text{A.40})$$

Shown in Fig. A.2 is a projection of the de Sitter embedding (the hyperboloid in Fig. A.1) onto the X_0 - X_4 plane. The foliation of this spacetime into lines of constant F and G , found from Eq. A.40, is shown. Adding an extra dimension to this picture, we find that null rays are given by the intersection of the hyperboloid with a plane. Lines of constant F and G form the boundaries of the past and future light cones from their point of intersection.

Open Slicing

de Sitter space can also be foliated by open spatial slices, with the metric

$$ds^2 = -d\tau^2 + H^{-2} \sinh^2(H\tau) [d\xi^2 + \sinh^2 \xi d\Omega^2]. \quad (\text{A.41})$$

The embedding coordinates are given by

$$X_0 = H^{-1} \cosh \xi \sinh(H\tau), \quad (\text{A.42})$$

$$X_i = H^{-1} \sinh \xi \sinh(H\tau) \omega_i, \quad (\text{A.43})$$

$$X_4 = H^{-1} \cosh(H\tau). \quad (\text{A.44})$$

Closed Slicing

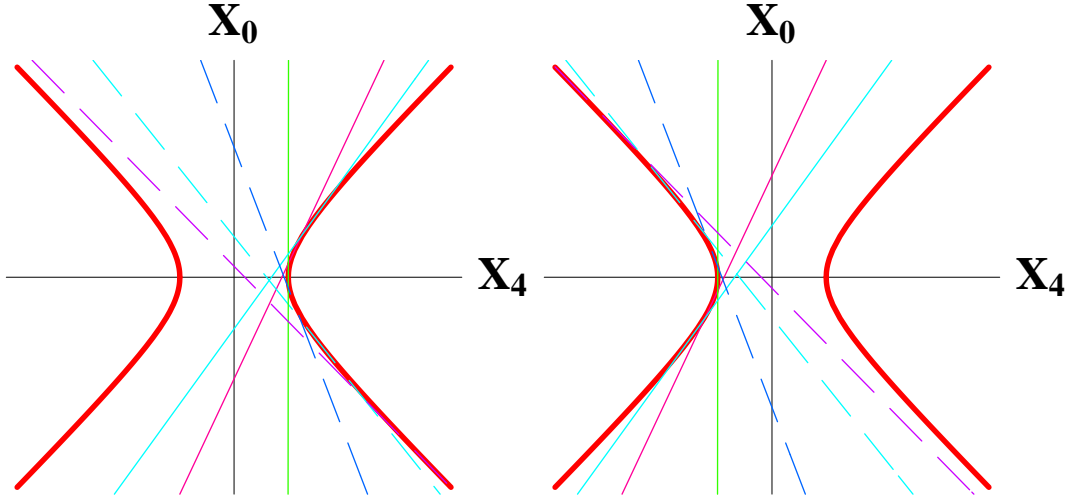


Figure A.2: A projection in the X_0 - X_4 plane of the embedding for de Sitter space. Shown on the left are lines of constant G , and on the right are lines of constant F . Dashed lines correspond to $F, G > 1$, and solid lines correspond to $F, G < 1$.

The foliation of de Sitter space by closed spatial slices can be accomplished with the embedding [60]

$$X_0 = H^{-1} \cos(Hz), \quad (\text{A.45})$$

$$X_4 = H^{-1} \sin(Hz) \sinh \chi, \quad (\text{A.46})$$

$$X_i = H^{-1} \sin(Hz) \cosh \chi \omega_i, \quad (\text{A.47})$$

$$(\text{A.48})$$

The metric is given by

$$ds^2 = dz^2 + H^{-2} \sin^2(Hz) [-d\chi^2 + \cosh^2 \chi d\Omega_2^2] \quad (\text{A.49})$$

Global Coordinates

A set of coordinates can be defined that covers the entire de Sitter manifold, in terms of which the metric is given by

$$ds^2 = -d\tau^2 + H^{-2} \cosh^2(H\tau) [d\eta^2 + \sin^2(\eta) d\Omega_2^2]. \quad (\text{A.50})$$

The embedding is given by

$$X_0 = H^{-1} \sinh(H\tau) \tag{A.51}$$

$$X_i = H^{-1} \cosh(H\tau) \sin(\eta)\omega_i \tag{A.52}$$

$$X_4 = H^{-1} \cosh(H\tau) \cos(\eta). \tag{A.53}$$

Conformal Coordinates

The global coordinates can be used to define a set of coordinates that are conformal to the Einstein Static Universe, which is a cylinder ($\mathbf{R} \times S^3$). Defining a new variable τ' such that

$$\cosh(H\tau) = \frac{1}{\cos \tau'}, \tag{A.54}$$

the metric becomes

$$ds^2 = \frac{1}{H^2 \cos^2 \tau'} (-d\tau'^2 + d\eta^2 + \sin^2(\eta)d\Omega_2^2). \tag{A.55}$$

with $-\pi/2 < \tau' < \pi/2$ and $0 < \eta < \pi$. Performing a conformal transformation to the Einstein Static Universe, and unwrapping the cylinder, we obtain the conformal diagram for de Sitter space shown in Fig. A.3. Each point on this diagram corresponds to a two-sphere with a radius equal to the proper radius R in the static slicing. A number of features can be located on this diagram. The vertical dotted lines on the left and right are the north and south poles, corresponding to spheres of zero radius. Recall that conformal transformations preserve null rays, which will travel on 45 degree lines. The top and bottom of the diagram can therefore be identified as future and past null infinity respectively (denoted J^\pm). The intersecting null lines denote the location of the cosmological horizon at $R = H^{-1}$. The foliation of the spacetime into surfaces of constant static time t is shown, with the circulating arrows indicating the direction of increasing coordinate time in each of the four static patches required to cover the entire dS manifold (note that $t \rightarrow \infty$ as an event horizon is approached, and then jumps to $t = -\infty$ in the next patch).

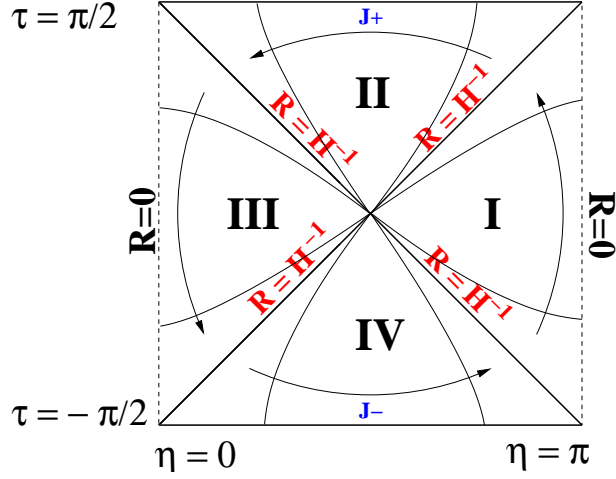


Figure A.3: Conformal diagram for the de Sitter geometry.

A.3 Anti-de Sitter space

The Anti de Sitter spacetime is also maximally symmetric, with $SO(3,2)$ symmetry. It describes a spacetime filled with dust possessing negative energy density, which can be parametrized by a negative cosmological constant. Like dS, AdS can also be viewed as the surface of a hyperboloid embedded in 5 dimensional Minkowski space, defined by

$$-X_0^2 - X_4^2 + X_1^2 + X_2^2 + X_3^2 = -H^{-2} \quad (\text{A.56})$$

where $H^2 \equiv |\Lambda|/3$.

Global Coordinates

A set of coordinates can be introduced that covers the entire AdS manifold. The embedding is given by

$$X_0 = H^{-1} \cosh(H\eta) \cos(\tau) \quad (\text{A.57})$$

$$X_i = H^{-1} \sinh(H\eta) \omega_i \quad (\text{A.58})$$

$$X_4 = H^{-1} \cosh(H\eta) \sin(\tau). \quad (\text{A.59})$$

The metric is given by

$$ds^2 = -H^{-2} \cosh^2(H\eta) d\tau + d\eta^2 + H^{-2} \sinh^2(H\eta) d\Omega^2 \quad (\text{A.60})$$

Defining a new coordinate θ such that $\tan \theta = \sinh(H\eta)$ ($0 \leq H\eta \leq \pi/2$), we see that this metric is conformal to the Einstein Static universe

$$ds^2 = \frac{1}{H^2 \cos^2 \theta} (-d\tau^2 + d\theta^2 + \sin^2 \theta d\Omega^2.) \quad (\text{A.61})$$

Since the coordinate θ only ranges between $0 \leq \theta \leq \pi/2$, then we see that AdS maps to half of the ESU cylinder. Unwrapping, the conformal diagram for AdS is shown in Fig. A.4. The red dashed line in this figure represents a future-directed null ray emitted from the origin at $\tau = 0$. In a time $\tau = \pi$, this null ray returns to the origin after reflecting off of the boundary at $\theta = \pi/2$ ($\eta = \infty$). The blue dotted line is a timelike geodesic. No timelike geodesics starting at the origin can reach the boundary of the AdS spacetime.

Static Coordinates

A set of static coordinates can be defined in analogy with the static coordinates in de Sitter space. The embedding is given by

$$X_0 = H^{-1} \sqrt{1 + H^2 R^2} \sin Ht, \quad (\text{A.62})$$

$$X_i = R\omega_i \quad i = 1, 2, 3, \quad (\text{A.63})$$

$$X_4 = H^{-1} \sqrt{1 + H^2 R^2} \cos Ht, \quad (\text{A.64})$$

where $H^2 \equiv |\Lambda|$. The metric is given by

$$ds^2 = -(1 + H^2 R^2) dt^2 + (1 + H^2 R^2)^{-1} dR^2 + R^2 d\Omega^2. \quad (\text{A.65})$$

Comparing with the global coordinates of Eq. A.60, we see that

$$t = H^{-1} \tau, \quad (\text{A.66})$$

$$R = H^{-1} \sinh(H\eta) = \tan \theta. \quad (\text{A.67})$$

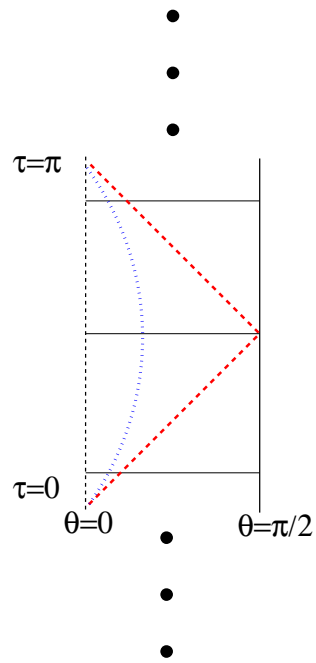


Figure A.4: Conformal diagram for the Anti de Sitter geometry. Horizontal solid lines denote surfaces of constant static time t . The red dashed line represents a null ray emitted from the origin, traveling out to the boundary, and back to the origin. The blue dotted line represents a timelike geodesic.

Shown in Fig. A.4 are surfaces of constant t , where the left and right boundaries correspond to the origin at $R = 0$ and $R = \infty$ respectively.

A.4 Schwarzschild de Sitter

The Schwarzschild-de Sitter (SdS) spacetime describes a spherically symmetric point mass in a spacetime with a positive cosmological constant. Using Birkhoff's theorem, it is possible to construct the metric in a static slicing

$$ds^2 = -a_{\text{sds}} dt^2 + a_{\text{sds}}^{-1} dR^2 + R^2 d\Omega^2, \quad (\text{A.68})$$

$$a_{\text{sds}} = 1 - \frac{2M}{R} - \frac{\Lambda}{3} R^2. \quad (\text{A.69})$$

Fixing Λ , there are three qualitatively different casual structures characterized by the value of M (see [132]), due to the nature of the three roots of $a_{\text{sds}}(R)$.

For $3M < \Lambda^{-1/2}$, there are three distinct real roots of form:

$$R_n = 2(\Lambda)^{-1/2} \cos\left(\frac{\theta}{3} + \frac{2\pi n}{3}\right), \quad (\text{A.70})$$

where

$$\cos\theta = -3M(\Lambda)^{1/2}, \quad (\text{A.71})$$

and $\pi < \theta < 3\pi/2$. We can label them as

$$R_{BH} \equiv R_0, \quad R_- = R_1, \quad R_C = R_2,$$

where the range of θ means that they lie in the ranges $R_- < 0 < 2M < R_{BH} < 3M < R_C$. The two positive roots correspond to the black hole (R_{BH}) and cosmological (R_C) horizons.

We can re-write the metric coefficient as

$$a(R) = -\frac{\Lambda}{3R} (R - R_-)(R - R_{BH})(R - R_C), \quad (\text{A.72})$$

and using the above definitions, there are a number of identities among the horizon radii

$$R_- + R_{BH} + R_C = 0 \quad (\text{A.73})$$

$$\frac{3}{\Lambda} = R_{BH}^2 + R_{BH}R_C + R_C^2 \quad (\text{A.74})$$

$$\frac{6M}{\Lambda} = R_{BH}R_C(R_{BH} + R_C) \quad (\text{A.75})$$

For $3M = \Lambda^{-1/2}$, there are also three real roots: a double positive root R_h and a negative R_- , given by:

$$R_h = \Lambda^{-1/2}, \quad R_- = -2\Lambda^{-1/2}. \quad (\text{A.76})$$

This mass is known as the Nariai mass, and in this spacetime there is only one horizon at the positive root. For $3M > \Lambda^{-1/2}$, there is one real negative root, and therefore no horizons in the spacetime.

The static patch of SdS given by the metric A.68 covers a spatial region between the black hole and cosmological event horizons only. There are coordinate singularities at the horizons, and it is desirable to remove these by a change of coordinates. In the process, we will extend the coordinates to cover the entire SdS manifold. We will work with values of the cosmological constant and mass satisfying $3M < \Lambda^{-1/2}$, and define a tortoise coordinate

$$R^* = \int a_{sds}(R)^{-1} dR \quad (\text{A.77})$$

The integral can be evaluated using the form of the metric coefficient given by Eq. A.72, yielding

$$R^* = \frac{1}{2k_{BH}} \ln(R - R_{BH}) - \frac{1}{2k_C} \ln(R_C - R) + \left(\frac{1}{2k_C} - \frac{1}{2k_{BH}} \right) \ln(R + R_{BH} + R_C), \quad (\text{A.78})$$

where $k_{BH,C}$ are the surface gravities of the black hole and cosmological horizons

$$k_{BH,C} = \frac{1}{2} \left| \frac{da_{sds}}{dR} \right|_{R_{BH,C}}, \quad (\text{A.79})$$

$$k_{BH} = \frac{\Lambda}{6R_{BH}} (2R_{BH} + R_C) (R_C - R_{BH}), \quad (\text{A.80})$$

$$k_C = \frac{\Lambda}{6R_C} (2R_C + R_{BH}) (R_C - R_{BH}). \quad (\text{A.81})$$

It can be seen that R^* goes to infinity at the horizons R_{BH} and R_C . We now introduce a set of null coordinates defined by

$$u = t - R^*, \quad v = t + R^*, \quad (\text{A.82})$$

after which the metric becomes

$$ds^2 = -a_{sds} dudv + R^2 d\Omega^2. \quad (\text{A.83})$$

In these coordinates, the horizons are both located at $u, v = \pm\infty$ (because of R^*). We can lift this degeneracy by introducing two coordinate patches, one covering the vicinity of each horizon. The location of the horizons can be pulled in from infinity by defining the following two sets of coordinates

$$u_{C,BH} = \pm e^{\pm k_C, BH u}, \quad v_{C,BH} = \mp e^{\mp k_C, BH v}. \quad (\text{A.84})$$

The metric in these coordinates takes the form

$$ds_{C,BH}^2 = -f_{C,BH} du_{C,BH} dv_{C,BH} + R^2 d\Omega^2 \quad (\text{A.85})$$

where $f_{C,BH}$ is defined as

$$f_C = \frac{\Lambda}{3k_C^2 R} (R - R_{BH})^{1+k_C/k_{BH}} (R + R_{BH} + R_C)^{2-k_C/k_{BH}}, \quad (\text{A.86})$$

$$f_{BH} = \frac{\Lambda}{3k_{BH}^2 R} (R_C - R)^{1+k_{BH}/k_C} (R + R_{BH} + R_C)^{2-k_{BH}/k_C}. \quad (\text{A.87})$$

It can be seen that we have eliminated all of the coordinate singularities in the original system since this metric is perfectly regular as the horizons are approached. The BH patch is good for all $R < R_C$, and the C patch is good for all $R > R_{BH}$. Together, these two patches cover $0 < R < \infty$ and $-\infty < t < \infty$.

We now define the following two coordinates

$$U_{C,BH} = \frac{1}{2}(u_{C,BH} - v_{C,BH}) \quad (\text{A.88})$$

$$V_{C,BH} = \frac{1}{2}(u_{C,BH} + v_{C,BH}) \quad (\text{A.89})$$

which cast the metric in the form

$$ds_{C,BH}^2 = f_{C,BH}(-dV_{C,BH} + dU_{C,BH}) + R^2 d\Omega^2 \quad (\text{A.90})$$

and it can be seen that the $(U_{C,BH}, V_{C,BH})$ plane is conformal to Minkowski space. These coordinates are related to the original (t, R) coordinate system by:

$$\begin{aligned} \pm U_{C,BH}^2 \mp V_{C,BH}^2 &= e^{\mp 2k_{C,BH}R^*} = \\ &= (R - R_{BH})^{-\frac{k_{C,BH}}{k_{BH}}} (R_C - R)^{\frac{k_{C,BH}}{k_C}} (R + R_{BH} + R_C)^{\left(\frac{k_{C,BH}}{k_C} - \frac{k_{C,BH}}{k_{BH}}\right)} \end{aligned} \quad (\text{A.91})$$

In the BH coordinate patch the origin is at R_{BH} , and in the C coordinate patch the origin is at R_C . The R -coordinate then corresponds to hyperboloids in the $(U_{C,BH}, V_{C,BH})$ plane. We can solve for the t coordinate by taking the ratio

$$t = \frac{1}{k_{C,BH}} \tanh\left(\pm \frac{V_{C,BH}}{U_{C,BH}}\right) \quad (\text{A.92})$$

We will find the $(U_{C,BH}, V_{C,BH})$ coordinates useful when we Euclideanize the SdS metric for the construction of instantons in Chapter 4. Presently, we move on to discuss the causal structure of the SdS spacetime.

The $(U_{C,BH}, V_{C,BH})$ patches can be sewn together to cover the entire SdS manifold, and as discussed in [133], they can be used to define a global set of coordinates¹. From this set of coordinates, we can explicitly construct the conformal diagram shown in Fig. A.5. In this diagram, surfaces of constant coordinate time t are drawn as solid lines, with the circulating

¹It is possible to construct the conformal diagram for any spacetime which admits spacelike slices of the form $ds_2^2 = -f dt^2 + f^{-1} dR^2$ without finding the explicit form of the global coordinates [134]. This is a very useful construction technique in cases where global coordinates are difficult or impossible to define.

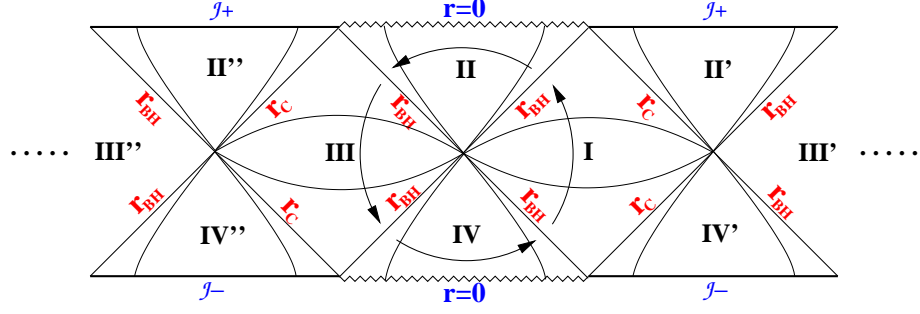


Figure A.5: Conformal diagram of the Schwarzschild de Sitter geometry for $3M < \Lambda_+$.

arrows denoting the direction of increasing t . Note that the conformal diagram is periodic, reflecting the fact that spacelike slices in SdS are noncompact.

The conformal diagram for the Nariai spacetime, $3M = \Lambda^{-1/2}$, is shown in the upper panel of Fig. A.6 [132]. There is also a time-reverse solution, starting at past null infinity and ending at $R = 0$. For $3M > \Lambda^{-1/2}$, there is one real negative root, and therefore no horizons in the spacetime. The conformal diagram for this case is shown in the lower cell of Fig. A.6.

A.5 Schwarzschild Anti-de Sitter

The Schwarzschild Anti-de Sitter (SAdS) spacetime describes a spacetime with a negative cosmological constant containing a spherically symmetric point mass. As with the SdS spacetime, the metric can be constructed using Birkhoff's theorem, and can be foliated by static slices with a metric given by

$$ds^2 = -a_{sads} dt^2 + a_{sads}^{-1} dR^2 + R^2 d\Omega^2 \quad (\text{A.93})$$

where

$$a_{sads} = 1 - \frac{2M}{R} + \frac{|\Lambda|}{3} R^2. \quad (\text{A.94})$$

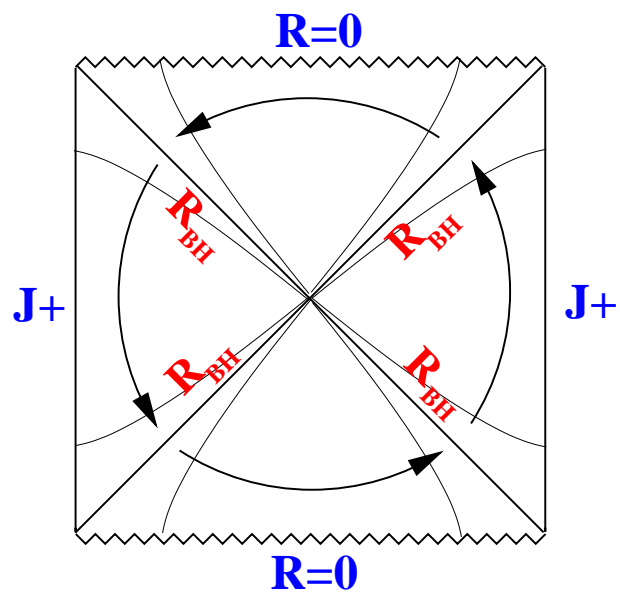


Figure A.7: Conformal diagram for the Schwarzschild Anti de Sitter geometry.

Appendix B

Covariant Entropy Bound and Singularity Theorems

In this appendix, we briefly discuss the covariant entropy bound and the Penrose singularity theorems. We will restrict ourselves to spherically symmetric spacetimes, and concentrate on the practical issues of their application rather than their technical details, for which we refer the reader to the original literature. Our presentation of the covariant entropy bound will rely heavily on the review of Bousso [135], which can be consulted for further references.

B.1 Covariant Entropy Bound

We can state the covariant entropy bound as:

The entropy on any light sheet L of a surface B will not exceed the area of B ,

$$S(L_B) < \frac{A(B)}{4}. \tag{B.1}$$

The light sheet of a surface is defined by following null rays from the surface (there are always two directions) back to a focal point (a caustic). There are in fact four orthogonal null

directions emanating from any surface B, as shown in Fig. B.1. In this figure, the conformal diagram for Minkowski space is shown (we will work with conformal diagrams, as this will be the most economical way to apply the covariant entropy bound to the spherically symmetric spacetimes we will be interested in), and the light sheet emanating from an S^2 of some radius (the point labeled B) is indicated by the blue and red dashed lines. In this case, the covariant entropy bound states that the entropy on the future directed ingoing and past directed ingoing null surfaces is bounded by the area of the S^2 labeled B.

In flat space, null rays can only focus at the origin. For example, the future directed incoming null rays in Fig. B.1 are focusing as they approach B (the radius of the S^2 at each point on the curve is getting smaller). Continuing this past B, we would see that after passing through the origin, the null rays are now future directed outgoing, which diverge (pass through S^2 of increasing radius along the curve). However, there are situations in curved spacetime where null rays can focus without passing through the origin. In light of this fact, we will find it useful to classify the various types of surfaces that can exist in a curved spacetime.

To do so, we will use the rays from past directed ingoing and outgoing null directions. A normal surface will be defined as one in which the past directed ingoing null rays are focusing and the past directed outgoing null rays are defocusing (as the curves are followed back from the surface). A trapped surface will be defined as one which has both the past directed ingoing and outgoing null rays defocusing. An anti-trapped surface will be defined as one which has both the past directed ingoing and outgoing null rays focusing. Examples of each of these types of surfaces can be found in the time symmetric Schwarzschild geometry as shown in Fig. B.2.

Looking at the representative points in Fig. B.2, it can be seen that the light sheet of a normal surface will be composed of the past directed and future directed null directions. The situation is different for trapped and anti-trapped surfaces. The light sheet for trapped surfaces will be composed of the future directed ingoing and outgoing null directions, and the

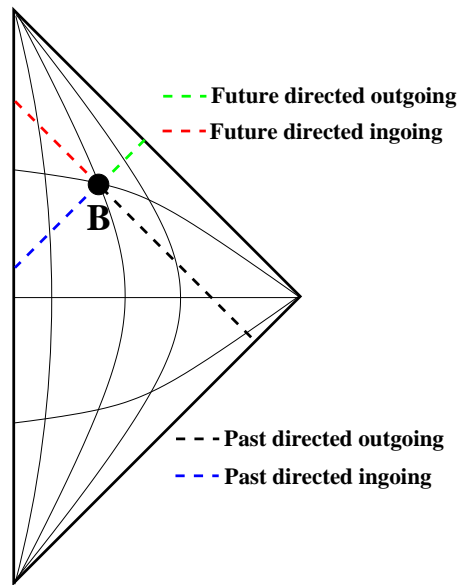


Figure B.1: Shown in this figure is the conformal diagram for Minkowski space. The point labeled **B** is in fact the surface of an S^2 , and the four orthogonal null directions from this surface are indicated by the dashed lines. The light sheet for **B** in this example is composed of the future directed ingoing and past directed ingoing null surfaces indicated by the red and blue dashed lines respectively.

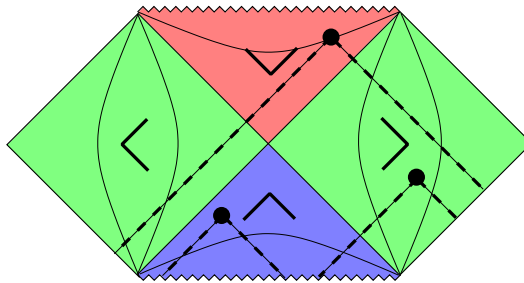


Figure B.2: The conformal diagram for the time symmetric Schwarzschild spacetime. Points in the green shaded regions are normal surfaces, points in the red shaded region are trapped surfaces, and points in the blue shaded region are anti-trapped surfaces. Representative surfaces and their past directed null rays are shown in each type of region. The wedges in each region represent the direction of the light sheet corresponding to surfaces in that region.

light sheet for anti-trapped surfaces will be composed of the past directed ingoing and outgoing null directions. The light sheet structure is denoted by the wedges shown in Fig. B.2.

Having defined the covariant entropy bound and introduced the concept of light sheets, we must now clarify how such a bound relates to real matter systems. The relation is most clear in situations where we are interested in a surface that completely encloses a weakly gravitating system. In this case, the future directed light sheet will "sweep out" the volume of the system, and therefore bounding the entropy on the light sheet is tantamount to bounding the entropy of the system. In situations where gravity is important, the presence of matter will cause light sheets to focus. In systems where there is a correspondence between the statistical entropy of a system and its energy, then the consequent focusing effects have been shown in all studied cases to uphold the bound.

There is much evidence to interpret the bound as a fundamental statement about the degrees of freedom that a quantum theory of gravity might possess. This leads one to conjecture that a Holographic Principle will apply to the as-yet-unknown theory of quantum theory of gravity. As stated in [135], the Holographic Principle is:

The covariant entropy bound is a law of physics which must be manifest in an underlying theory. This theory must be a unified quantum theory of matter and space- time. From it, Lorentzian geometries and their matter content must emerge in such a way that the number of independent quantum states describing the light-sheets of any surface B is manifestly bounded by the exponential of the surface area:

$$\mathcal{N}[L(B)] < e^{A(B)/4} \tag{B.2}$$

It will be of particular use for the material discussed in thesis to apply the holographic principle to spacetimes with a positive cosmological constant. This is related to the N-bound [136], which states that spacetimes with a finite positive cosmological constant will

have an observable entropy less than $N = 3\pi/\Lambda$.

Qualifying what is meant by observable entropy will lead to the identification of the causal diamond of an observer as an object of fundamental importance. Consider two time-like separated points, p and q , with p to the past of q . These points might represent the state of some measuring device at two instants of time. Signals could conceivably intersect the worldline between p and q if they are emitted somewhere in the causal past of p . However, all matter that is present in this light cone must have passed through the boundary of the causal future of q . Any entropy in the causal past of q that lies outside of the causal future of p is not considered to be observable entropy. That is, observable entropy must be locally accessible to the measuring device on the worldline between p and q . *For two points p and q on a timelike curve, the causal diamond is defined as the intersection of the causal future of p and the causal past of q .*

If one considers a fundamental theory describing the experiments done inside of the causal diamond, then such a theory must have a number of degrees of freedom commensurate with the observable entropy. Therefore, an application of the Holographic Principle along with the N-Bound, implies that the number of degrees of freedom in a spacetime with positive cosmological constant is bounded by $3\pi/\Lambda$. In the context of a stable de Sitter space, this claim was originally made by Banks and Fischler [66]. It is possible to formulate a quantum theory of stable de Sitter space [65], and the relation of such a theory to the topics discussed in this thesis is presented in Chapter 3.

B.2 Penrose Singularity Theorems

We can state the singularity theorems as [24]

If:

1. The spacetime is connected.

2. There exists a non-compact cauchy surface.
3. The null energy condition ($R_{\mu\nu}k^\mu k^\nu \geq 0$ for all null k^μ) holds everywhere.
4. There exists a trapped surface (anti-trapped surface).

Then, there exists a singularity to the future (past).

More precisely, the conditions above imply the existence of at least one past-directed null geodesic which cannot be extended beyond some finite affine parameter. The null energy condition (also known as the "null convergence condition") implies that matter focuses light, and in a spacetime filled with a perfect fluid of pressure p and energy density ρ , requires that $\rho \geq -p$.

Appendix C

Matrix Calculations and Snowman

Diagrams

In this appendix we present a quick way of calculating normalized probabilities for terminal and cyclic landscapes in a unified manner, which also sheds light on the nature of the regularizing limit taken in the cyclic case.

First, assemble the relative transition probabilities μ_{NM} into a matrix $\boldsymbol{\mu}$ (equivalent to Bousso's η matrix). Starting in an initial state represented by a vector \mathbf{q} with components q_N ($\sum_N q_N = 1$), after one transition the mean number of entries (or “raw probability”) for each vacuum will be given by $\boldsymbol{\mu}\mathbf{q}$. At the second transition an additional $\boldsymbol{\mu}^2\mathbf{q}$ entries will occur and so on. After n transitions the raw probability will be given by $(\boldsymbol{\mu} + \boldsymbol{\mu}^2 + \dots + \boldsymbol{\mu}^n)\mathbf{q}$. If we set $\mathbf{S}_n \equiv \boldsymbol{\mu} + \boldsymbol{\mu}^2 + \dots + \boldsymbol{\mu}^n$, then $(\mathbf{1} - \boldsymbol{\mu})\mathbf{S}_n = \boldsymbol{\mu}(\mathbf{1} - \boldsymbol{\mu}^n)$. In the terminal case we can invert $(\mathbf{1} - \boldsymbol{\mu})$ and take the $n \rightarrow \infty$ limit to obtain \mathbf{S}_∞ directly ($\boldsymbol{\mu}^n \rightarrow 0$ since asymptotically all the probability goes into the terminal vacua and so fewer and fewer vacuum entries occur). In the cyclic case $\det(\mathbf{1} - \boldsymbol{\mu}) = 0$ and $\boldsymbol{\mu}^n$ does not tend to zero, and things are not so simple. It is convenient to proceed by replacing $\boldsymbol{\mu}$ by $(1 - \varepsilon)\boldsymbol{\mu}$, which can be inverted. Neglecting the

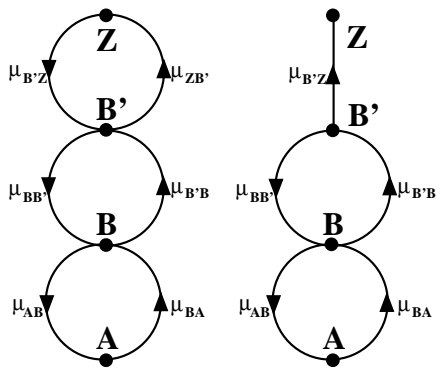


Figure C.1: Examples of “snowman diagrams” summarizing relative transition probabilities μ_{NM} . The one on the left is for a recycling landscape and the one on the right is for a terminal landscape.

troublesome determinant factor (since we shall be later normalizing to obtain probabilities from numbers of vacuum entries anyway), we take the limits $n \rightarrow \infty$ and $\varepsilon \rightarrow 0$ in that order, and for both terminal and recycling landscapes obtain the simple expression:

$$\mathbf{S}_\infty \propto \mathbf{T} \equiv (\text{adj}(\mathbf{1} - \boldsymbol{\mu})) \boldsymbol{\mu} \quad (\text{C.1})$$

where adj denotes the adjoint matrix operation (i.e. the transpose of the matrix of cofactors of the matrix in question). Multiplying \mathbf{T} into \mathbf{q} and normalizing yields the probabilities for the vacua given the initial state in question.

This procedure yields exactly the same results as the pruned tree method. We thus see that the latter procedure is equivalent to considering sequences of transitions up to some length n and then taking the limit $n \rightarrow \infty$.

The μ_{NMS} in question can conveniently be depicted in snowman-like diagrams such as those shown in Fig. C.1, which apply to the calculations in Sec. 5.3. In fact we treat both cases at once by leaving $\mu_{ZB'}$ arbitrary and only set it to 1 or 0 as appropriate after having calculated \mathbf{T} . We also allow for the possibility of vacuum A being terminal in the same manner.

Suppressing the normalizing factor for clarity, we obtain

$$\begin{pmatrix} P_A^{A,B,B',Z} \\ P_B^{A,B,B',Z} \\ P_{B'}^{A,B,B',Z} \\ P_Z^{A,B,B',Z} \end{pmatrix} \propto \begin{pmatrix} \mu_{AB}(1 - \mu_{B'Z}\mu_{ZB'}) \\ 1 - \mu_{B'Z}\mu_{ZB'} \\ \mu_{B'B} \\ \mu_{B'B}\mu_{ZB'} \end{pmatrix} \quad (\text{C.2})$$

in the recycling case with the full set of superscripts indicating that the results are independent of initial conditions.

In the terminal case we can only start in states A , B or B' and we obtain:

$$\begin{pmatrix} P_A^A \\ P_B^A \\ P_{B'}^A \\ P_Z^A \end{pmatrix} \propto \begin{pmatrix} \mu_{AB} \\ 1 \\ \mu_{B'B} \\ \mu_{ZB'}\mu_{B'B} \end{pmatrix}, \quad (\text{C.3})$$

$$\begin{pmatrix} P_A^B \\ P_B^B \\ P_{B'}^B \\ P_Z^B \end{pmatrix} \propto \begin{pmatrix} \mu_{AB} \\ \mu_{AB}\mu_{BA} + \mu_{BB'}\mu_{B'B} \\ \mu_{B'B} \\ \mu_{B'B}\mu_{ZB'} \end{pmatrix} \quad (\text{C.4})$$

and

$$\begin{pmatrix} P_A^{B'} \\ P_B^{B'} \\ P_{B'}^{B'} \\ P_Z^{B'} \end{pmatrix} \propto \begin{pmatrix} \mu_{AB}\mu_{BB'} \\ \mu_{BB'} \\ \mu_{BB'}\mu_{B'B} \\ \mu_{ZB'}(1 - \mu_{AB}\mu_{BA}) \end{pmatrix}. \quad (\text{C.5})$$

The relative transition probabilities are related to the transition rates by

$$\mu_{BA} = 0 \text{ or } 1 \tag{C.6}$$

$$\mu_{AB} = \frac{\kappa_{AB}}{\kappa_{AB} + \kappa_{B'B}} \tag{C.7}$$

$$\mu_{B'B} = \frac{\kappa_{B'B}}{\kappa_{AB} + \kappa_{B'B}} \tag{C.8}$$

$$\mu_{BB'} = \frac{\kappa_{BB'}}{\kappa_{ZB'} + \kappa_{BB'}} \tag{C.9}$$

$$\mu_{ZB'} = \frac{\kappa_{ZB'}}{\kappa_{ZB'} + \kappa_{BB'}} \tag{C.10}$$

where $\mu_{BA} = 0$ if A is terminal and $\mu_{BA} = 1$ if it isn't. Substituting these expressions into equations C.3, C.4, and C.5, we can then take the limits discussed in Sec. 5.3 to produce the appropriate probability tables.

In the case where vacuum A is terminal ($\mu_{AB} = 0$), there are a number of ratios of interest. The probabilities assigned by the CV method to this sample landscape were calculated in [102] (the ‘‘FABI’’ model), and using these results, we can directly compare the results of the CV and RTT methods. For initial conditions in B or B' , we find:

$$\frac{P_A^B}{P_Z^B} = \frac{\kappa_{AB} (\kappa_{BB'} + \kappa_{ZB'})}{\kappa_{B'B} \kappa_{ZB'}} \tag{C.11}$$

$$\frac{P_A^{B'}}{P_Z^{B'}} = \frac{\kappa_{AB} \kappa_{BB'}}{\kappa_{ZB'} (\kappa_{AB} + \kappa_{B'B})} \tag{C.12}$$

As expected given the argument of Sec. 5.2.2, these results agree with the predictions of the CV method.

Appendix D

Triple intersection in the unboosted frame

In this appendix we solve directly for the coordinate angles denoting the boundaries of a collision on the Poincaré disk. We specialize to the case $H_T = H_F = H$, where it is possible to foliate the bubble interior with the flat slicing. Working in a plane of constant- ϕ ,¹ we are attempting to find the triple-intersection between three circles representing the observation bubble, the colliding bubble, and the past light cone of the observer, whose radii are given by

$$r_{obs} = 1 - e^{-Ht}, \quad (\text{D.1})$$

$$r_{coll} = e^{-Ht_n} - e^{-Ht}, \quad (\text{D.2})$$

$$r_{plc} = e^{-Ht} - e^{-Ht_o}. \quad (\text{D.3})$$

Using up the remaining symmetry of the problem we can assume that the observer is at $\theta_o = 0$. The free parameters that must be specified are then the position at which the colliding bubble

¹As before, we work with the convention where $-\pi < \theta < \pi$ to cover full circles.

is nucleated (t_n, r_n, θ_n) and the position of the observer (t_o, r_o) in terms of the flat slicing coordinates. The transformation between the open and flat slicing location of the observer is given by

$$r_o = \frac{H^{-1} \sinh \xi_o \sinh \tau_o}{\cosh \tau_o + \cosh \xi_o \sinh \tau_o} \quad (\text{D.4})$$

$$t_o = H^{-1} \log(\cosh \tau_o + \cosh \xi_o \sinh \tau_o).$$

The observation bubble introduces no new free parameters, since it is centered around the origin, and nucleates at $t = 0$.

We find it useful to parameterize time with $x \equiv 1 - e^{-Ht}$ (this way $r = x$ is the observation bubble). It is straightforward to conclude that the three light-cones are the set of points $(r(x, \theta), x, \theta)$ parameterized as follows:

- Observation Bubble future lightcone:

$$(r = x, x, \theta) \quad 0 \leq x \leq 1, \quad -\pi \leq \theta \leq \pi \quad (\text{D.5})$$

- Observer's past lightcone:

$$(r_o \cos \theta \pm \sqrt{(x - x_o)^2 - r_o^2 \sin^2 \theta}, x, \theta) \quad (\text{D.6})$$

$$x \leq x_o, \quad |\theta| \leq |\arcsin(\frac{x - x_o}{r_o})|$$

- New bubble future lightcone:

$$(r_n \cos(\theta - \theta_n) \pm \sqrt{(x_n - x)^2 - r_n^2 \sin^2(\theta - \theta_n)}, x, \theta) \quad (\text{D.7})$$

$$x_n \leq x, \quad |\theta - \theta_n| \leq |\arcsin(\frac{x_n - x}{r_n})|$$

The triple intersection is the set of points belonging to all three groups. Demanding first that $1 - x = r_o \cos \theta \pm \sqrt{(x - x_o)^2 - r_o^2 \sin^2 \theta}$ and repeating for $1 - x = r_n \cos(\theta - \theta_n) \pm \sqrt{(x_n - x)^2 - r_n^2 \sin^2(\theta - \theta_n)}$, then solving for $x(\theta)$ we obtain

$$2x = \frac{r_o^2 - x_o^2}{r_o \cos \theta - x_o} = \frac{r_n^2 - x_n^2}{r_n \cos(\theta - \theta_n) - x_n}, \quad (\text{D.8})$$

giving an equation for θ :

$$\begin{aligned}
A \cos \theta + B \sin \theta + C &= 0, \quad \text{where} \\
A &= r_o(x_n^2 - r_n^2) - \cos \theta_n r_n(x_o^2 - r_o^2) \\
B &= -\sin \theta_n r_n(x_o^2 - r_o^2) \\
C &= x_n(x_o^2 - r_o^2) - x_o(x_n^2 - r_n^2).
\end{aligned} \tag{D.9}$$

There are two solutions² to Eq. D.9,

$$\cos \theta_{1,2} = -\frac{\left(AC \pm B\sqrt{A^2 + B^2 - C^2}\right)}{A^2 + B^2}. \tag{D.10}$$

One can now solve for the time of the intersection by plugging $\theta_{1,2}$ into eq. D.8. This gives the coordinates of the two desired intersection events in the flat slicing where the angle is measured from the origin. By spherical symmetry, these angles are the same as the coordinate angles measured from the origin of the of the bubble interior as described by the open slicing coordinates. We can then use the angles $\theta_{1,2}$ to define the angle as measured by the observer sitting at some open slicing coordinates $(\xi_o, \tau_o, \theta_o = 0)$ via Eq. 7.7.

²The denominator $A^2 + B^2$ never vanishes because the observer and the nucleated bubble never sit on the observation bubble wall. Also, notice that the symmetry in ϕ is reflected in the fact that the positive solution for a given θ_n is the negative solution for $-\theta_n$.

Appendix E

Effects of boosts on the bubble

In Sec. 7.3.2, we used the symmetries of the one-bubble spacetime to justify performing a boost that would bring us to a frame where the observer is at the origin. Here, we explore the effects of this boost on the interior spacetime in greater detail.

In terms of the embedding coordinates, the transformation is given by Eq. 7.11. The first important property to note is that the X_4 coordinate is invariant. In the open slicing, surfaces of constant X_4 are surfaces of constant τ , and so we see that the boost preserves the open slicing time. The second important property is that the observer at $(\xi_o, \tau_o, \theta_o = 0)$ is translated to the origin $(\xi'_o = 0, \tau'_o = \tau_o, \theta'_o = 0)$ of the boosted frame. From the relation for X'_0 in Eq. 7.11,

$$\cosh \xi'_o = \cosh \xi_o (\cosh \xi_o - \tanh \xi_o \sinh \xi_o) = 1, \quad (\text{E.1})$$

and therefore $\xi'_o = 0$.

In Sec. 7.3, we derived a formula for the observed angular scale of a collision event in both the boosted and unboosted frames. We now establish the invariance of this quantity by directly applying the transformation to Eq. 7.7. The angle θ in this equation corresponds to the angular position of the intersection on the null wall of the observation bubble (as defined by the

origin in the unboosted frame), so using $\eta = T$, the boosted angle from Eq. 7.13 is:

$$\tan \theta' = \frac{\sin \theta}{\gamma(\cos \theta - \beta)}. \quad (\text{E.2})$$

In this frame, θ' can be identified as α , the actual observed angle at which the boundary of the collision lies (which is used to find the total angular scale of the collision in Eq. 7.7). Solving for $\cos \theta'$,

$$\cos \theta' = \frac{\sinh \xi_o - \cos \theta \cosh \xi_o}{\sqrt{\sin^2 \theta + (\sinh \xi_o - \cos \theta \cosh \xi_o)^2}}, \quad (\text{E.3})$$

and expanding into exponentials reveals that this expression is in fact equal to Eq. 7.7, as evidenced by:

$$\cos \alpha = \cos \theta' \quad (\text{E.4})$$

$$= -\frac{1 + 2e^{i\theta} + e^{2i\theta} + e^{2i\xi_o} - 2e^{i\theta+2\xi_o} + e^{2i\theta+2\xi_o}}{1 + 2e^{i\theta} + e^{2i\theta} - e^{2i\xi_o} + 2e^{i\theta+2\xi_o} - e^{2i\theta+2\xi_o}}$$

In the Poincaré disk representation, using the hyperbolic law of cosines, this implies that all of the angles in the triangle composed of (and therefore the lengths between) the observation point, the unboosted position of the origin, and the edge of the collision, remain invariant under the boost. More generally, the distance between any two points on the disc will be invariant under the boost (as one can check on a point-by-point basis), and so we can identify the boost as a pure translation in the open coordinates.

Bibliography

- [1] J. Garriga and A. Vilenkin, *Recycling universe*, *Phys. Rev.* **D57** (1998) 2230–2244, [astro-ph/9707292].
- [2] R. Bousso, *Holographic probabilities in eternal inflation*, *Phys. Rev. Lett.* **97** (2006) 191302, [hep-th/0605263].
- [3] A. H. Guth, *The inflationary universe: A possible solution to the horizon and flatness problems*, *Phys. Rev.* **D23** (1981) 347–356.
- [4] S. M. Carroll and J. Chen, *Spontaneous inflation and the origin of the arrow of time*, hep-th/0410270.
- [5] T. Banks, *Entropy and initial conditions in cosmology*, hep-th/0701146.
- [6] R. Penrose, *Difficulties with inflationary cosmology*, *Annals N. Y. Acad. Sci.* **571** (1989) 249–264.
- [7] S. Hollands and R. M. Wald, *An alternative to inflation*, *Gen. Rel. Grav.* **34** (2002) 2043–2055, [gr-qc/0205058].
- [8] A. Albrecht and L. Sorbo, *Can the universe afford inflation?*, *Phys. Rev.* **D70** (2004) 063528, [hep-th/0405270].

- [9] Y.-S. Piao, *Entropy of microwave background radiation in observable universe*, *Phys. Rev. D* **74** (2006) 047301, [gr-qc/0606024].
- [10] S. R. Coleman, *The fate of the false vacuum. 1. semiclassical theory*, *Phys. Rev. D* **15** (1977) 2929–2936.
- [11] J. Callan, Curtis G. and S. R. Coleman, *The fate of the false vacuum. 2. first quantum corrections*, *Phys. Rev. D* **16** (1977) 1762–1768.
- [12] S. R. Coleman and F. De Luccia, *Gravitational effects on and of vacuum decay*, *Phys. Rev. D* **21** (1980) 3305.
- [13] K.-M. Lee and E. J. Weinberg, *Decay of the true vacuum in curved space-time*, *Phys. Rev. D* **36** (1987) 1088.
- [14] A. Aguirre and M. C. Johnson, *Dynamics and instability of false vacuum bubbles*, *Phys. Rev. D* **72** (2005) 103525, [gr-qc/0508093].
- [15] T. Banks and M. Johnson, *Regulating eternal inflation*, hep-th/0512141.
- [16] A. Aguirre, T. Banks, and M. Johnson, *Regulating eternal inflation. ii: The great divide*, *JHEP* **08** (2006) 065, [hep-th/0603107].
- [17] A. Aguirre and M. C. Johnson, *Two tunnels to inflation*, *Phys. Rev. D* **73** (2005) 123529, [gr-qc/0512034].
- [18] A. Aguirre, S. Gratton, and M. C. Johnson, *Hurdles for recent measures in eternal inflation*, hep-th/0611221.
- [19] A. Aguirre, S. Gratton, and M. C. Johnson, *Measures on transitions for cosmology in the landscape*, *Phys. Rev. Lett.* **98** (2006) 131301, [hep-th/0612195].

- [20] E. Farhi, A. H. Guth, and J. Guven, *Is it possible to create a universe in the laboratory by quantum tunneling?*, *Nucl. Phys.* **B339** (1990) 417–490.
- [21] S. K. Blau, E. I. Guendelman, and A. H. Guth, *The dynamics of false vacuum bubbles*, *Phys. Rev.* **D35** (1987) 1747.
- [22] R. Penrose, *The question of cosmic censorship*, *J. Astrophys. Astron.* **20** (1999) 233–248.
- [23] L. F. Abbott and S. R. Coleman, *The collapse of an anti-de sitter bubble*, *Nucl. Phys.* **B259** (1985) 170.
- [24] R. Penrose, *Gravitational collapse and space-time singularities*, *Phys. Rev. Lett.* **14** (1965) 57–59.
- [25] B. Freivogel and L. Susskind, *A framework for the landscape*, *Phys. Rev.* **D70** (2004) 126007, [[hep-th/0408133](#)].
- [26] R. Bousso, *Cosmology and the s-matrix*, *Phys. Rev.* **D71** (2005) 064024, [[hep-th/0412197](#)].
- [27] R. Bousso and B. Freivogel, *Asymptotic states of the bounce geometry*, *Phys. Rev.* **D73** (2006) 083507, [[hep-th/0511084](#)].
- [28] A. Aurilia, M. Palmer, and E. Spallucci, *Evolution of bubbles in a vacuum*, *Phys. Rev.* **D40** (1989) 2511.
- [29] H. Sato, *Motion of a shell at metric junction*, *Prog. Theor. Phys.* **76** (1986) 1250.
- [30] V. A. Berezin, V. A. Kuzmin, and I. I. Tkachev, *Dynamics of bubbles in general relativity*, *Phys. Rev.* **D36** (1987) 2919.
- [31] A. Gomberoff, M. Henneaux, C. Teitelboim, and F. Wilczek, *Thermal decay of the cosmological constant into black holes*, *Phys. Rev.* **D69** (2004) 083520, [[hep-th/0311011](#)].

- [32] J. Garriga and A. Megevand, *Decay of de sitter vacua by thermal activation*, *Int. J. Theor. Phys.* **43** (2004) 883–904, [[hep-th/0404097](#)].
- [33] E. Farhi and A. H. Guth, *An obstacle to creating a universe in the laboratory*, *Phys. Lett.* **B183** (1987) 149.
- [34] S. Dutta and T. Vachaspati, *Islands in the lambda-sea*, *Phys. Rev.* **D71** (2005) 083507, [[astro-ph/0501396](#)].
- [35] T. Vachaspati and M. Trodden, *Causality and cosmic inflation*, *Phys. Rev.* **D61** (2000) 023502, [[gr-qc/9811037](#)].
- [36] F. C. Adams, K. Freese, and L. M. Widrow, *Evolution of nonspherical bubbles*, *Phys. Rev.* **D41** (1990) 347.
- [37] J. Garriga and A. Vilenkin, *Perturbations on domain walls and strings: A covariant theory*, *Phys. Rev.* **D44** (1991) 1007–1014.
- [38] J. Guven, *Covariant perturbations of domain walls in curved space- time*, *Phys. Rev.* **D48** (1993) 4604–4608, [[gr-qc/9304032](#)].
- [39] W. Fischler, D. Morgan, and J. Polchinski, *Quantum nucleation of false vacuum bubbles*, *Phys. Rev.* **D41** (1990) 2638.
- [40] W. Fischler, D. Morgan, and J. Polchinski, *Quantization of false vacuum bubbles: A hamiltonian treatment of gravitational tunneling*, *Phys. Rev.* **D42** (1990) 4042–4055.
- [41] V. A. Berezin, N. G. Kozimirov, V. A. Kuzmin, and I. I. Tkachev, *On the quantum mechanics of bubbles*, *Phys. Lett.* **B212** (1988) 415.
- [42] S. Khlebnikov, *A dual description of decoherence in de sitter space*, *JHEP* **03** (2003) 059, [[hep-th/0301103](#)].

- [43] J. Garriga and A. Vilenkin, *Quantum fluctuations on domain walls, strings and vacuum bubbles*, *Phys. Rev.* **D45** (1992) 3469–3486.
- [44] T. Vachaspati and A. Vilenkin, *Quantum state of a nucleating bubble*, *Phys. Rev.* **D43** (1991) 3846–3855.
- [45] A. Ishibashi and H. Ishihara, *Equation of motion for a domain wall coupled to gravitational field*, *Phys. Rev.* **D60** (1999) 124016, [[gr-qc/9802036](#)].
- [46] A. Ishibashi and H. Ishihara, *Bubble wall perturbations coupled with gravitational waves*, *Phys. Rev.* **D56** (1997) 3446–3458, [[gr-qc/9704058](#)].
- [47] R. Bousso, B. Freivogel, and M. Lippert, *Probabilities in the landscape: The decay of nearly flat space*, *Phys. Rev.* **D74** (2006) 046008, [[hep-th/0603105](#)].
- [48] D. A. Samuel and W. A. Hiscock, *Effect of gravity on false vacuum decay rates for $o(4)$ symmetric bubble nucleation*, *Phys. Rev.* **D44** (1991) 3052–3061.
- [49] T. Banks, *Heretics of the false vacuum: Gravitational effects on and of vacuum decay. ii*, [hep-th/0211160](#).
- [50] M. Cvetič, *Stability of vacua and domain walls in supergravity and superstring theory*, [hep-th/9210006](#).
- [51] M. Cvetič, S. Griffies, and S.-J. Rey, *Static domain walls in $n=1$ supergravity*, *Nucl. Phys.* **B381** (1992) 301–328, [[hep-th/9201007](#)].
- [52] M. Cvetič, S. Griffies, and H. H. Soleng, *Nonextreme and ultraextreme domain walls and their global space-times*, *Phys. Rev. Lett.* **71** (1993) 670–673, [[hep-th/9212020](#)].
- [53] M. Cvetič, S. Griffies, and H. H. Soleng, *Local and global gravitational aspects of domain wall space-times*, *Phys. Rev.* **D48** (1993) 2613–2634, [[gr-qc/9306005](#)].

- [54] A. D. Linde, *Particle Physics and Inflationary Cosmology*. Harwood Academic, 1990.
- [55] G. V. Dunne and H. Min, *Beyond the thin-wall approximation: Precise numerical computation of prefactors in false vacuum decay*, *Phys. Rev.* **D72** (2005) 125004, [[hep-th/0511156](#)].
- [56] S. W. Hawking and I. G. Moss, *Supercooled phase transitions in the very early universe*, *Phys. Lett.* **B110** (1982) 35.
- [57] A. A. Starobinsky, *Stochastic de sitter (inflationary) stage in the early universe*, . In *De Vega, H.j. (Ed.), Sanchez, N. (Ed.): *Field Theory, Quantum Gravity and Strings**, 107-126.
- [58] J. C. Hackworth and E. J. Weinberg, *Oscillating bounce solutions and vacuum tunneling in de sitter spacetime*, *Phys. Rev.* **D71** (2005) 044014, [[hep-th/0410142](#)].
- [59] U. Gen and M. Sasaki, *False vacuum decay with gravity in non-thin-wall limit*, *Phys. Rev.* **D61** (2000) 103508, [[gr-qc/9912096](#)].
- [60] D. Lindley, *The appearance of bubbles in de sitter space*, *Nucl. Phys.* **B236** (1984) 522–546.
- [61] R. Basu, A. H. Guth, and A. Vilenkin, *Quantum creation of topological defects during inflation*, *Phys. Rev.* **D44** (1991) 340–351.
- [62] T. Tanaka and M. Sasaki, *False vacuum decay with gravity: Negative mode problem*, *Prog. Theor. Phys.* **88** (1992) 503–528.
- [63] S. J. Parke, *Gravity, the decay of the false vacuum and the new inflationary universe scenario*, *Phys. Lett.* **B121** (1983) 313.

- [64] A. Ceresole, G. Dall'Agata, A. Giriyavets, R. Kallosh, and A. Linde, *Domain walls, near-bps bubbles, and probabilities in the landscape*, *Phys. Rev.* **D74** (2006) 086010, [[hep-th/0605266](#)].
- [65] T. Banks, *More thoughts on the quantum theory of stable de sitter space*, [hep-th/0503066](#).
- [66] T. Banks, *Cosmological breaking of supersymmetry or little lambda goes back to the future. ii*, [hep-th/0007146](#).
- [67] L. Dyson, M. Kleban, and L. Susskind, *Disturbing implications of a cosmological constant*, *JHEP* **10** (2002) 011, [[hep-th/0208013](#)].
- [68] R. Penrose, *A complete guide to the laws of the universe*, . London, UK: Vintage (2005) 1099 p.
- [69] B. Freivogel *et al.*, *Inflation in ads/cft*, *JHEP* **03** (2006) 007, [[hep-th/0510046](#)].
- [70] T. Banks and W. Fischler, *The holographic approach to cosmology*, [hep-th/0412097](#).
- [71] T. Banks and W. Fischler, *Holographic cosmology*, [hep-th/0405200](#).
- [72] T. Banks and W. Fischler, *Holographic cosmology 3.0*, *Phys. Scripta* **T117** (2005) 56–63, [[hep-th/0310288](#)].
- [73] T. Banks and W. Fischler, *An holographic cosmology*, [hep-th/0111142](#).
- [74] J. Garriga, *Nucleation rates in flat and curved space*, *Phys. Rev.* **D49** (1994) 6327–6342, [[hep-ph/9308280](#)].
- [75] G. L. Alberghi, D. A. Lowe, and M. Trodden, *Charged false vacuum bubbles and the ads/cft correspondence*, *JHEP* **07** (1999) 020, [[hep-th/9906047](#)].

- [76] A. Vilenkin, *Creation of universes from nothing*, *Phys. Lett.* **B117** (1982) 25.
- [77] A. Vilenkin, *Quantum creation of universes*, *Phys. Rev.* **D30** (1984) 509–511.
- [78] A. Vilenkin, *The wave function discord*, *Phys. Rev.* **D58** (1998) 067301, [gr-qc/9804051].
- [79] J. L. Feng, J. March-Russell, S. Sethi, and F. Wilczek, *Saltatory relaxation of the cosmological constant*, *Nucl. Phys.* **B602** (2001) 307–328, [hep-th/0005276].
- [80] S. Ansoldi, A. Aurilia, R. Balbinot, and E. Spallucci, *Classical and quantum shell dynamics, and vacuum decay*, *Class. Quant. Grav.* **14** (1997) 2727–2755, [gr-qc/9706081].
- [81] J. B. Hartle and S. W. Hawking, *Wave function of the universe*, *Phys. Rev.* **D28** (1983) 2960–2975.
- [82] A. D. Linde, *Quantum creation of the inflationary universe*, *Nuovo Cim. Lett.* **39** (1984) 401–405.
- [83] G. W. Gibbons and S. W. Hawking, *Cosmological event horizons, thermodynamics, and particle creation*, *Phys. Rev.* **D15** (1977) 2738–2751.
- [84] A. Strominger, *Superstrings with torsion*, *Nucl. Phys.* **B274** (1986) 253.
- [85] L. Susskind, *The anthropic landscape of string theory*, hep-th/0302219.
- [86] R. Bousso and J. Polchinski, *Quantization of four-form fluxes and dynamical neutralization of the cosmological constant*, *JHEP* **06** (2000) 006, [hep-th/0004134].
- [87] S. Kachru, R. Kallosh, A. Linde, and S. P. Trivedi, *De sitter vacua in string theory*, *Phys. Rev.* **D68** (2003) 046005, [hep-th/0301240].

- [88] A. Aguirre and M. Tegmark, *Multiple universes, cosmic coincidences, and other dark matters*, *JCAP* **0501** (2005) 003, [[hep-th/0409072](#)].
- [89] A. Aguirre, *Universe or Multiverse*, ch. On making predictions in a multiverse: Conundrums, dangers, and coincidences. Cambridge University Press, In Press 2006. [[astro-ph/0506519](#)].
- [90] A. Linde, *Sinks in the landscape, boltzmann brains, and the cosmological constant problem*, *JCAP* **0701** (2007) 022, [[hep-th/0611043](#)].
- [91] J. Garcia-Bellido, A. D. Linde, and D. A. Linde, *Fluctuations of the gravitational constant in the inflationary brans-dicke cosmology*, *Phys. Rev.* **D50** (1994) 730–750, [[astro-ph/9312039](#)].
- [92] R. Bousso and B. Freivogel, *A paradox in the global description of the multiverse*, [[hep-th/0610132](#)].
- [93] A. Vilenkin, *Freak observers and the measure of the multiverse*, *JHEP* **01** (2007) 092, [[hep-th/0611271](#)].
- [94] D. N. Page, *Is our universe decaying at an astronomical rate?*, [[hep-th/0612137](#)].
- [95] A. D. Linde, D. A. Linde, and A. Mezhlumian, *From the big bang theory to the theory of a stationary universe*, *Phys. Rev.* **D49** (1994) 1783–1826, [[gr-qc/9306035](#)].
- [96] S. Winitzki, *On time-reparametrization invariance in eternal inflation*, *Phys. Rev.* **D71** (2005) 123507, [[gr-qc/0504084](#)].
- [97] A. H. Guth, *Inflation and eternal inflation*, *Phys. Rept.* **333** (2000) 555–574, [[astro-ph/0002156](#)].

- [98] M. Tegmark, *What does inflation really predict?*, *JCAP* **0504** (2005) 001, [astro-ph/0410281].
- [99] T. Banks, M. Dine, and E. Gorbatov, *Is there a string theory landscape?*, *JHEP* **08** (2004) 058, [hep-th/0309170].
- [100] A. Mezhlumian and A. A. Starobinsky, *Stochastic inflation: New results*, astro-ph/9406045.
- [101] R. Easther, E. A. Lim, and M. R. Martin, *Counting pockets with world lines in eternal inflation*, *JCAP* **0603** (2006) 016, [astro-ph/0511233].
- [102] J. Garriga, D. Schwartz-Perlov, A. Vilenkin, and S. Winitzki, *Probabilities in the inflationary multiverse*, *JCAP* **0601** (2006) 017, [hep-th/0509184].
- [103] V. Vanchurin and A. Vilenkin, *Eternal observers and bubble abundances in the landscape*, *Phys. Rev.* **D74** (2006) 043520, [hep-th/0605015].
- [104] J. Garriga and A. Vilenkin, *A prescription for probabilities in eternal inflation*, *Phys. Rev.* **D64** (2001) 023507, [gr-qc/0102090].
- [105] A. Vilenkin, *A measure of the multiverse*, hep-th/0609193.
- [106] A. Vilenkin, *Gravitational field of vacuum domain walls and strings*, *Phys. Rev.* **D23** (1981) 852–857.
- [107] G. W. Gibbons and N. Turok, *The measure problem in cosmology*, hep-th/0609095.
- [108] S. Gratton and N. Turok, *Langevin analysis of eternal inflation*, *Phys. Rev.* **D72** (2005) 043507, [hep-th/0503063].
- [109] M. Tegmark, A. Aguirre, M. Rees, and F. Wilczek, *Dimensionless constants, cosmology and other dark matters*, *Phys. Rev.* **D73** (2006) 023505, [astro-ph/0511774].

- [110] S. Weinberg, *Anthropic bound on the cosmological constant*, *Phys. Rev. Lett.* **59** (1987) 2607.
- [111] D. Schwartz-Perlov and A. Vilenkin, *Probabilities in the bouso-polchinski multiverse*, *JCAP* **0606** (2006) 010, [[hep-th/0601162](#)].
- [112] J. Garriga and A. Vilenkin, *Testable anthropic predictions for dark energy*, *Phys. Rev.* **D67** (2003) 043503, [[astro-ph/0210358](#)].
- [113] S. H. H. Tye, *A new view of the cosmic landscape*, [hep-th/0611148](#).
- [114] J. Baacke and N. Kevlishvili, *Tunneling in a quantum field theory on a compact one-dimensional space*, *Nucl. Phys.* **B745** (2006) 142–164, [[hep-th/0505118](#)].
- [115] A. H. Guth and E. J. Weinberg, *Could the universe have recovered from a slow first order phase transition?*, *Nucl. Phys.* **B212** (1983) 321.
- [116] J. R. Gott, *Creation of open universes from de sitter space*, *Nature* **295** (1982) 304–307.
- [117] A. Vilenkin, *Did the universe have a beginning?*, *Phys. Rev.* **D46** (1992) 2355–2361.
- [118] M. R. Douglas, *The statistics of string / m theory vacua*, *JHEP* **05** (2003) 046, [[hep-th/0303194](#)].
- [119] J. B. Hartle, *Anthropic reasoning and quantum cosmology*, *AIP Conf. Proc.* **743** (2005) 298–304, [[gr-qc/0406104](#)].
- [120] R. Bousso, B. Freivogel, and I.-S. Yang, *Eternal inflation: The inside story*, *Phys. Rev.* **D74** (2006) 103516, [[hep-th/0606114](#)].
- [121] B. Freivogel, G. T. Horowitz, and S. Shenker, *Colliding with a crunching bubble*, [hep-th/0703146](#).

- [122] J. Garriga, A. H. Guth, and A. Vilenkin, *Eternal inflation, bubble collisions, and the persistence of memory*, [hep-th/0612242](#).
- [123] B. Freivogel, M. Kleban, M. Rodriguez Martinez, and L. Susskind, *Observational consequences of a landscape*, *JHEP* **03** (2006) 039, [[hep-th/0505232](#)].
- [124] A. Aguirre and S. Gratton, *Inflation without a beginning: A null boundary proposal*, *Phys. Rev.* **D67** (2003) 083515, [[gr-qc/0301042](#)].
- [125] A. Aguirre and S. Gratton, *Steady-state eternal inflation*, *Phys. Rev.* **D65** (2002) 083507, [[astro-ph/0111191](#)].
- [126] A. H. Guth and E. J. Weinberg, *Cosmological consequences of a first order phase transition in the $su(5)$ grand unified model*, *Phys. Rev.* **D23** (1981) 876.
- [127] A. Maloney, S. Shenker, and L. Susskind to appear.
- [128] S. Shenker, *Lectures at kitp*, .
- [129] N. Arkani-Hamed, S. Dubovsky, A. Nicolis, E. Trincherini, and G. Villadoro, *A measure of de sitter entropy and eternal inflation*, [arXiv:0704.1814](#) [[hep-th](#)].
- [130] S. W. Hawking, I. G. Moss, and J. M. Stewart, *Bubble collisions in the very early universe*, *Phys. Rev.* **D26** (1982) 2681.
- [131] J. J. Blanco-Pillado, M. Bucher, S. Ghassemi, and F. Glanois, *When do colliding bubbles produce an expanding universe?*, *Phys. Rev.* **D69** (2004) 103515, [[hep-th/0306151](#)].
- [132] K. Lake and R. C. Roeder, *Effects of a nonvanishing cosmological constant on the spherically symmetric vacuum manifold*, *Phys. Rev.* **D15** (1977) 3513–3519.
- [133] T. R. Choudhury and T. Padmanabhan, *Concept of temperature in multi-horizon spacetimes: Analysis of schwarzschild-de sitter metric*, [gr-qc/0404091](#).

- [134] M. Walker, *Block diagrams and the extension of timelike two-surfaces*, *J. Math. Phys.* (1970), no. 11 2280.
- [135] R. Bousso, *The holographic principle*, *Rev. Mod. Phys.* **74** (2002) 825–874, [[hep-th/0203101](#)].
- [136] R. Bousso, *Positive vacuum energy and the n-bound*, *JHEP* **11** (2000) 038, [[hep-th/0010252](#)].